PROCEEDINGS OF THE 1995 ANTENNA APPLICATIONS SYMPOSIUM

19960617 115

Rome Laboratory
Air Force Materiel Command
Rome, New York

DISCLAIMER NOTICE

UNCLASSIFIED

Technical Report
distributed by

**DEFENSE
TECHNICAL
INFORMATION
CENTER**

DTIC Acquiring Information-
Imparting Knowledge

Cameron Station
Alexandria, Virginia 22304-6145

UNCLASSIFIED
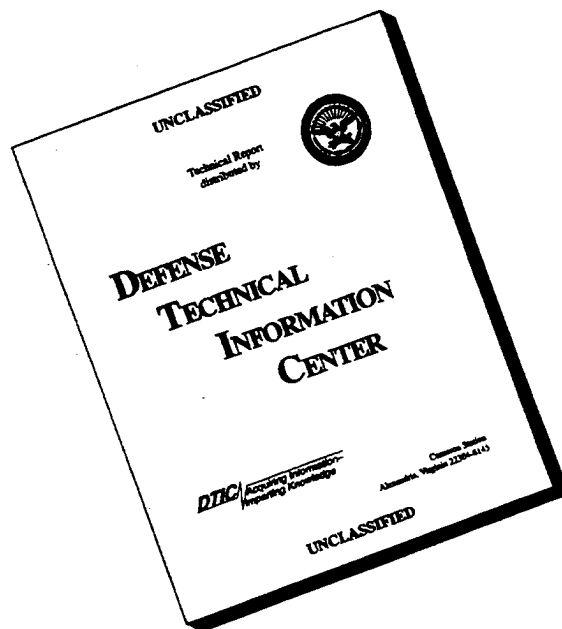
**THIS DOCUMENT IS BEST
QUALITY AVAILABLE. THE
COPY FURNISHED TO DTIC
CONTAINED A SIGNIFICANT
NUMBER OF PAGES WHICH DO
NOT REPRODUCE LEGIBLY.**

Title of Report: PROCEEDINGS OF THE 1995 ANTENNA APPLICATIONS
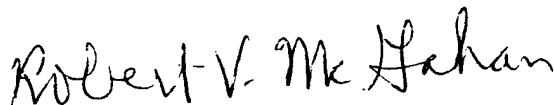   SYMPOSIUM

PUBLICATION REVIEW

This report has been reviewed and is approved for publication.

APPROVED:

DANIEL J. JACAVANCO
Chief, Antennas & Components Division
Electromagnetics and Reliability Directorate

APPROVED:

ROBERT V. McGAHAN
Acting Director
Electromagnetics and Reliability Directorate

REPORT DOCUMENTATION PAGE		*Form Approved* *OMB No. 0704-0188*

1. AGENCY USE ONLY *(Leave blank)*	2. REPORT DATE May 1996	3. REPORT TYPE AND DATES COVERED Scientific Interim

4. TITLE AND SUBTITLE

PROCEEDINGS OF THE 1995 ANTENNA APPLICATIONS SYMPOSIUM

5. FUNDING NUMBERS

PE: 62702F
PR: 4600
TA: 460014
WU: 460014PP

6. AUTHOR(S)

Daniel H. Schaubert, et al

7. PERFORMING ORGANIZATION NAME(S) AND ADDRESS(ES)

Rome Laboratory/ERAA
31 Grenier Street
Hanscom AFB, MA 01731-3010

8. PERFORMING ORGANIZATION REPORT NUMBER

RL-TR-96-100

Volume I

9. SPONSORING/MONITORING AGENCY NAME(S) AND ADDRESS(ES)

10. SPONSORING/MONITORING AGENCY REPORT NUMBER

11. SUPPLEMENTARY NOTES

Volume I consists of pages 1 through 351.
Volume II consists of pages 352 through 671.

12a. DISTRIBUTION/AVAILABILITY STATEMENT

Approved for Public Release; Distribution Unlimited

12b. DISTRIBUTION CODE

13. ABSTRACT *(Maximum 200 words)*

The Proceedings of the 1995 Antenna Applications Symposium is a collection of state-of-the-art papers relating to phased array antennas, multibeam antennas, satellite antennas, microstrip antennas, reflector antennas, HF, VHF, UHF and various other antennas.

14. SUBJECT TERMS

Antennas	Microstrip	Multibeam Antennas
Satellite Antennas	Reflector	Array Antennas
Broadband Antennas	HF, VHF, UHF	

15. NUMBER OF PAGES
358

16. PRICE CODE

17. SECURITY CLASSIFICATION OF REPORT	18. SECURITY CLASSIFICATION OF THIS PAGE	19. SECURITY CLASSIFICATION OF ABSTRACT	20. LIMITATION OF ABSTRACT
UNCLASSIFIED	UNCLASSIFIED	UNCLASSIFIED	SAR

Standard Form 298 (Rev. 2-89)
Prescribed by ANSI Std. Z39-18
298-102

PROGRAM FOR
1995 ANTENNA APPLICATIONS SYMPOSIUM

WEDNESDAY, SEPTEMBER 20, 1995

I. MILITARY AND COMMERCIAL COMMUNICATIONS

* Not included in this volume.

II. REFLECTORS AND DF ANTENNAS

THURSDAY, SEPTEMBER 21, 1995

III. NEW TECHNIQUES AND CONCEPTS

IV. ANALOG AND DIGITAL BEAMFORMING

FRIDAY, SEPTEMBER 22, 1995

V. ARRAY THEORY AND TECHNOLOGY

TRI-BAND FLYAWAY ANTENNAS FOR WORLDWIDE COMMUNICATIONS

Nicholas Moldovan

Prodelin Corporation

1700 NE Cable Drive

Conover, NC 28613

ABSTRACT

The Department of Defense (DOD) is rapidly moving toward Commercial-Off-The-Shelf (COTS) Flyaway Tri-Band Satellite Ground Terminals to provide worldwide communications with spacecraft such as DCSC, DOMESTIC SATELLITE ORGANIZATION (DOMSAT), INTELSAT, ORION, PANAMSAT, etc. A critical element in the ground terminal is the communication antenna. The complexity of multi-band of operation (C, X, and Ku), high reliability, low cost, transportation/packaging requirements, and international compliance to numerous operational specifications for satellite accessing (certifications) has placed challenging requirements on the antenna. This paper describes three (3) antennas with aperture sizes of 1.2, 1.8, and 2.4 meters specifically developed for such applications.

1.0 INTRODUCTION

During the past ten years there have been increasingly widespread applications for cost-effective satellite communication systems offering the end user two-way voice, data, or video transmission. This technology has been identified as Very Small Aperture Terminal (VSAT) and is currently in use by private industry and federal agencies. Typically, these fixed remote antennas are 2.4 meters in aperture size or less and connect to a central antenna hub/switching facility to create the network.

This technology first started domestically, operating in the Ku- frequency band (receive: 11.7 - 12.2 GHz and transmit: 14.0 - 14.5 GHz). Typical rules and regulations as it pertained to the VSAT antenna was and still is covered by the FCC. However, as VSAT technology spread throughout the world, the VSAT antenna underwent changes by providing cost-effective components which configured the antenna to operate over a variety of C and Ku-band satellites.

Because of the growth in global communication traffic, increased demands were placed upon satellite capacity and limited available frequency bands. Newly constructed satellites offered extended frequency bands, along with unique

2

polarizations. Complicating the issue, each satellite agency or organization contains specific performance specifications in order to access the satellite.

Today, the VSAT antenna is configured, and in some cases, licenced in just about every frequency band and polarization required for world-wide satellite accessing. Figure 1.0-1 illustrates the wide variety of configurations available.

However, during the past three years a new market of flyaway VSAT antennas has emerged for such applications as: emergency back-up to the already in-place networks, and temporary communications. The design and development of these flyaway VSAT antennas added a new challenge in addressing and meeting the transportability requirements. Although developed for commercial applications, multi-frequency VSAT flyaway antenna systems which will provide world-wide communications with spacecrafts such as DCSC, DOMSAT, INTELSAT, ORION, PANAMSAT, etc. are also requested by the Department of Defense (DOD).

The following paragraphs present four (4) flyaway antennas with aperture sizes of 1.2, 1.8, and 2.4 meter.

C-Band Circular Polarized
Rx 3.625 - 4.200 GHz   Tx 5.850 - 6.425 GHz
(Intelsat Type Approved "STD G" Feed)

C-Band Circular (Co and X-Pol)
Rx 3.625 - 4.200 GHz   Tx 5.850 - 6.425 GHz
(Domsat, Brazilsat, Panamsat, Morelos . .)

Extended C-Band Linear
Rx 4.5 - 4.8 GHz   Tx 6.725 - 7.025 GHz
(Insat Satellite)

Ku-Band
Rx 10.95 - 12.75 GHz   Tx 14.00 - 14.50 GHz
(Intelsat Type Approved Feed, Domsat, Orion, . .)

2.4 Meter C-Band Rx/Tx
Intelsat STD G
Type Approved Antenna

NASA ACTS
20/30 GHz

L-Band, C.P.

Figure 1.0 - 1   Fixed VSAT Antenna with Various Feeds for World Wide Satellite Accessing   08/02/95

4

2.0   FLYWAY TRIBAND ANTENNA DESIGNS

Figure 2.0-1 presents four (4) antennas developed for both commercial and military applications. Criteria for their designs are listed below.

1. High efficiency across each frequency band.

2. Capable of meeting appropriate specifications (FCC, Intelsat, DSCS, Panamsat...).

3. Utilized high volume in production components.

4. Logically defined real transportability requirements (weights and sizes).

2.1   REFLECTOR DESIGNS

The reflectors used in fabricating the 1.2 and 1.8 meter antennas are production single piece high-volume compression molded reflectors that were sectionalized. Compression molded reflectors' unique property of zero residual stresses allowed cutting the reflector in multi-pieces without changing the surface rms.

A novel method of attaching interface flanges with self-aligning fasteners to each reflector section provided the required method of reassembling the reflector.
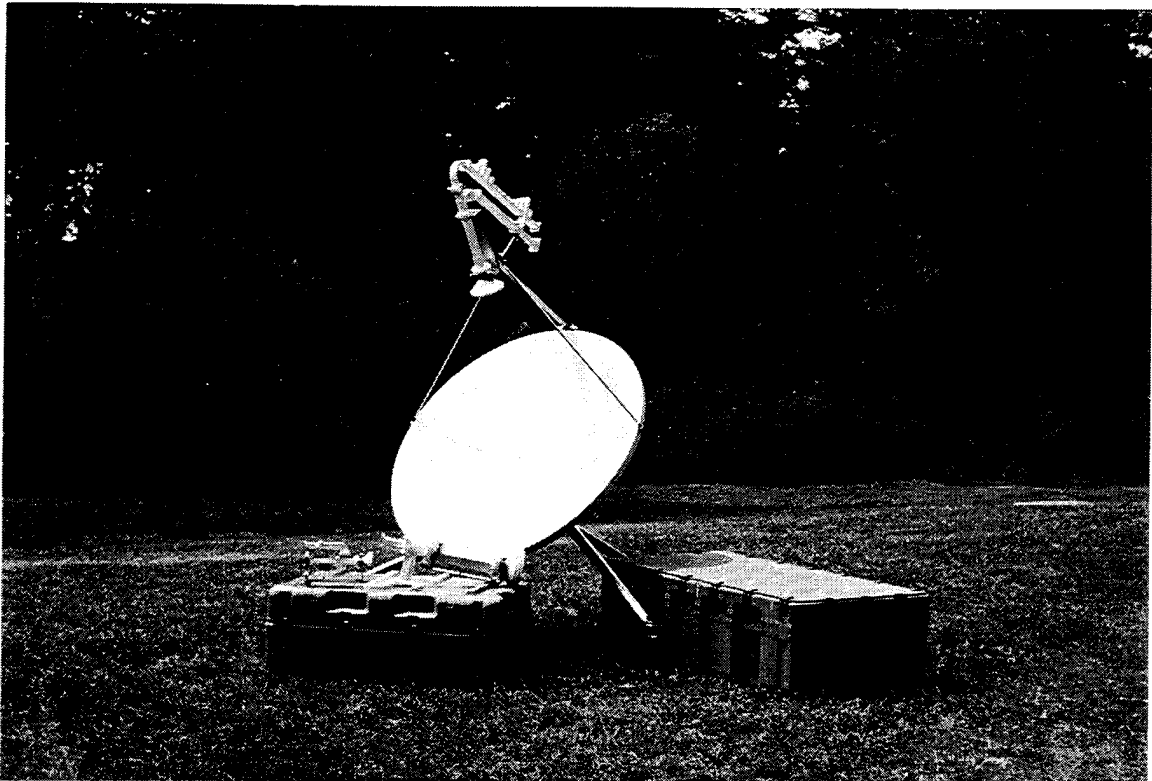
1.2 M Antenna with Triband Feeds (2-piece Reflector, X-band shown)
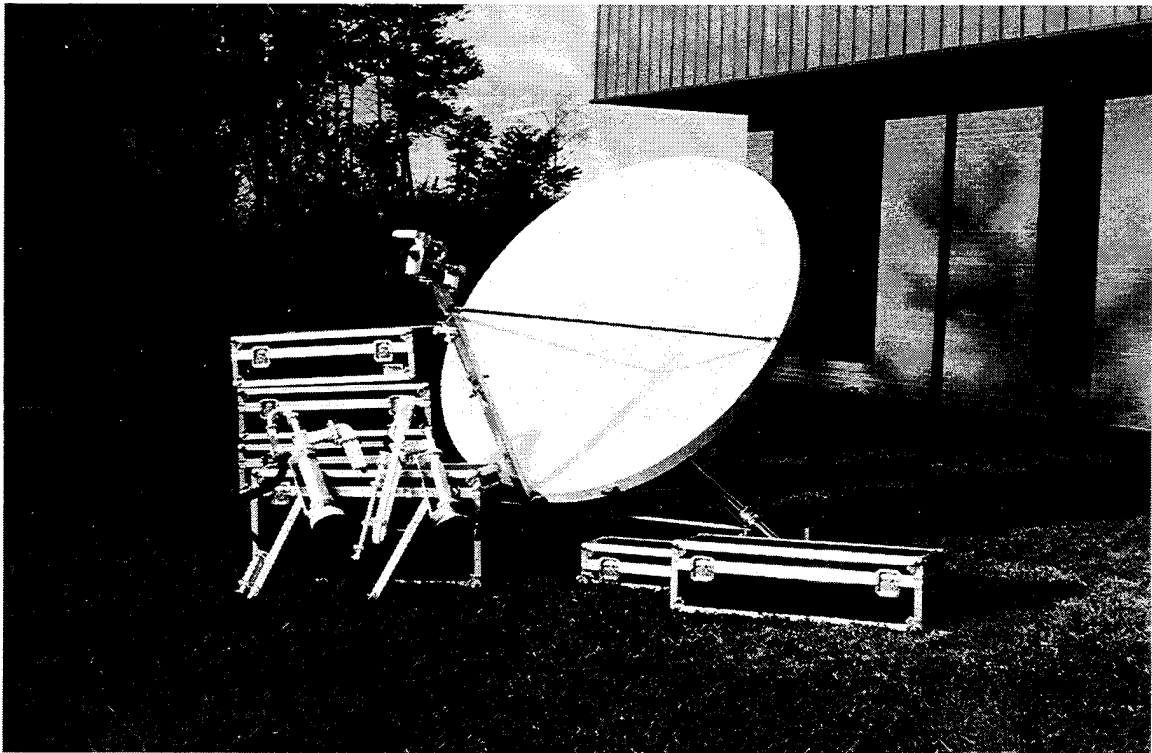
1.8 M Antenna with Triband Feeds (9-piece Reflector, Ku-band shown)

Figure 2.0-1 Flyaway Antennas for Commercial and Military Applications
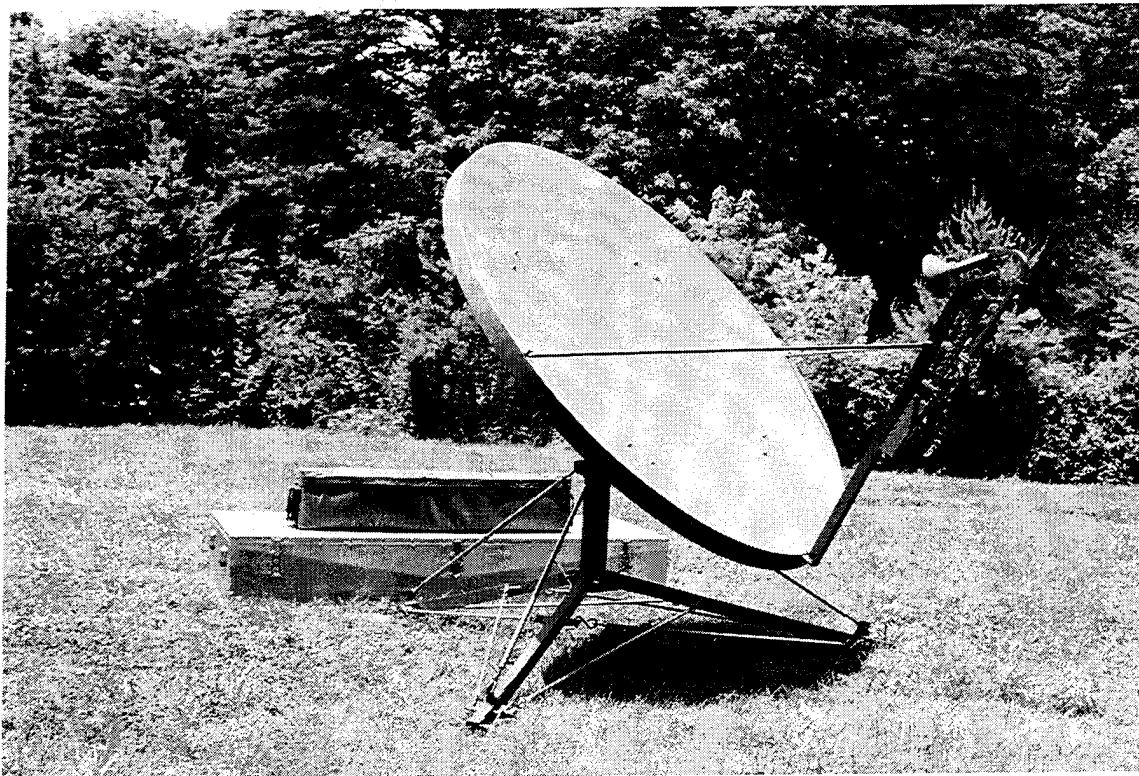
1.8M Antenna with Triband Feeds (2-piece Reflector, X-band shown)
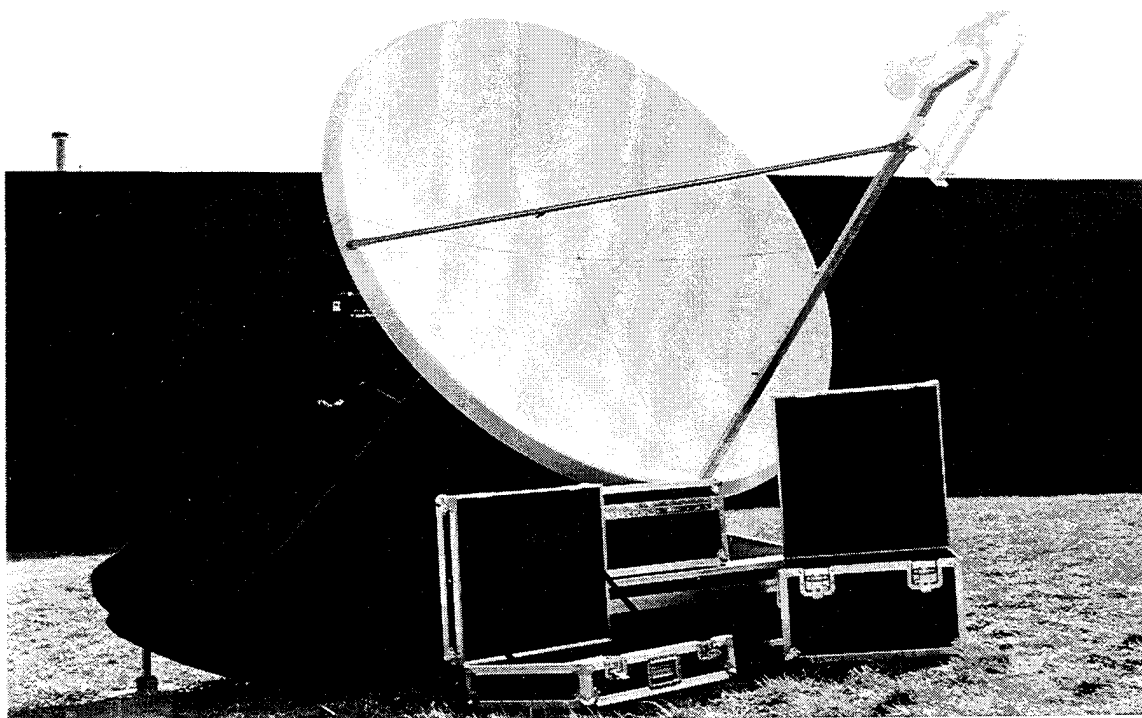
2.4 M Antenna with Triband Feeds (4-piece Reflector, X-band shown)

Figure 2.0-1 Flyaway Antennas for Commercial and Military Applications

The 2.4 meter reflector is a standard tooled compression molded four-piece reflector used for both transportable and fixed antennas.

2.2   TRIBAND FEED SYSTEMS

Figure 2.2-1 shows typical triband feed systems. Each feed assembly is designed to plug into a common reflector feed support. The following paragraphs summarize the key features of each feed assembly.

2.2.1   C-BAND FEED SYSTEM

The C-band feed system consists of three major assemblies: feed horn, polarizer, and OMT. This single feed system provides all the required polarizations necessary (Intelsat circular pol, X-pol linear, and co-pol linear). The feed horn employed consists of a corrugated conical horn manufactured in a single piece die casting. The circular polarizer is a square waveguide iris design that is manufactured as a single piece investment casting. Depending on the feeding
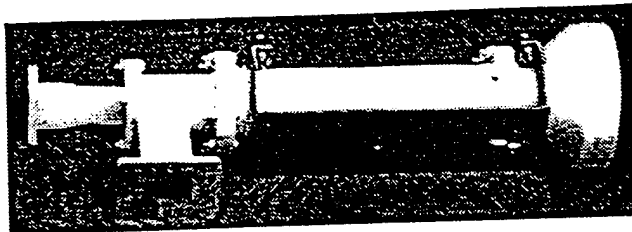
C-Band Feed
- Cross Polarized Linear
- Co-Polarized Linear
- Intelsat Circular Polarized (extended band)
- Integrated Band Pass and Band Reject Filters (located in OMT)
- Type N or CPR 137 TX Interfaces
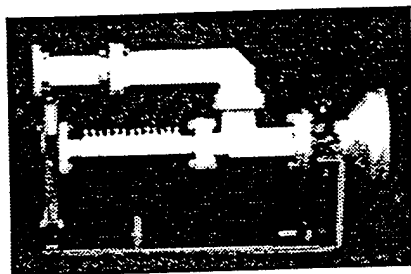
Ku-Band Feed
- World Wide Frequencies (Rx: 10.95 - 12.75 GHz) Tx: 14.0 - 14.5 GHz)
- Integrated Assemblies (Horn, OMT, and Band Reject Filter)
- Cradle Assembly for Ease of Polarization Adjustment
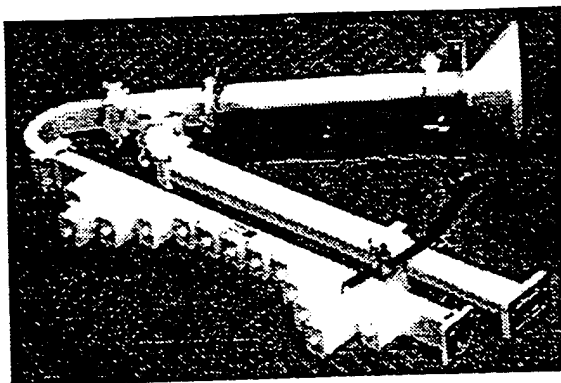
X-Band Feed
- Operates over DSCS at X-Band
- Integrated Assemblies (Horn, Polarizer, OMT, Band Pass, and Band Reject Filters)
- Low Axial Ratio: 1.0 dB max.
- Low VSWR and Insertion Loss

Figure 2.2-1   Tri-Band Feed Systems

9

orientation of a linear polarized electric field at the input of the polarizer, a right

hand or a left hand circular polarized field is generated through the polarizer. In

addition, the polarizer will also propagate linear polarization when rotated with

respect to the OMT. Completing the feed system, an OMT is required. The OMT

is a novel design since it is capable of providing the following:

- Cross polarization linear

- Co-polarization linear

- Integrated filters (band pass and band reject)

- Manufactured in three (3) pieces in diecasting.

Field polarization changes are accomplished by rotating the OMT with respect to

the polarizer and rotating the OMT through port with respect to the OMT

common port.

2.2.2   KU-BAND FEED SYSTEM

The Ku-band feed system provides simultaneous operation across the receive

(10.95 - 12.75 GHz) and transmit (14.0 - 14.5 GHz) frequency bands with linear

polarization. Each component making up the feed asssembly is manufactured by die casting with the exception of the filters.

2.3.3 X-BAND FEED SYSTEM

The X-band feed system consists of a horn, polarizer, OMT, waveguide bends, and filters. The polarizer is a square iris waveguide design. The complete assembly is well matched resulting in excellent VSWR (1.25:1) and axial ratio (.75 dB max.).

3.0 ANTENNA PATTERN CHARACTERISTICS

To illustrate the typical performance characteristics of each antenna, transmit co-polarized secondary radiation patterns are presented in Figures 3.0-1, 3.0-2, and 3.0-3.

4.0 CONCLUSION

This paper describes three flyaway tri-band antenna systems developed specifically for commercial and military satellite communications. The presented antennas utilize cost-effective, high-volume tool components from commercial VSAT fixed

The following labels appear within the radiation pattern charts:

29-25 Log θ

1.2M 2-PC.
6.425 GHz
+/- 9°

29-25 Log θ

1.2M 2-PC.
8.15 GHz
+/- 9°

29-25 Log θ

1.2M 2-PC.
14.25 GHz
+/- 9°
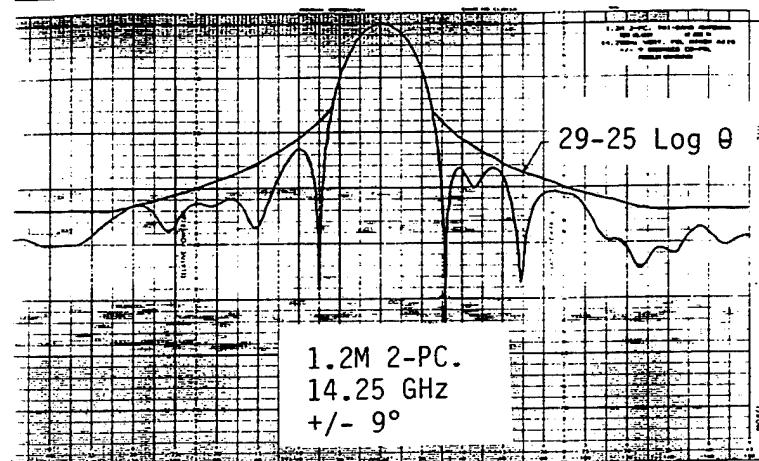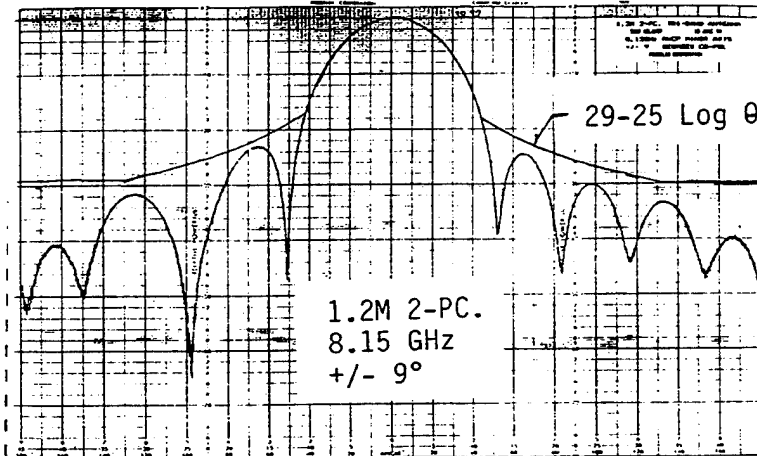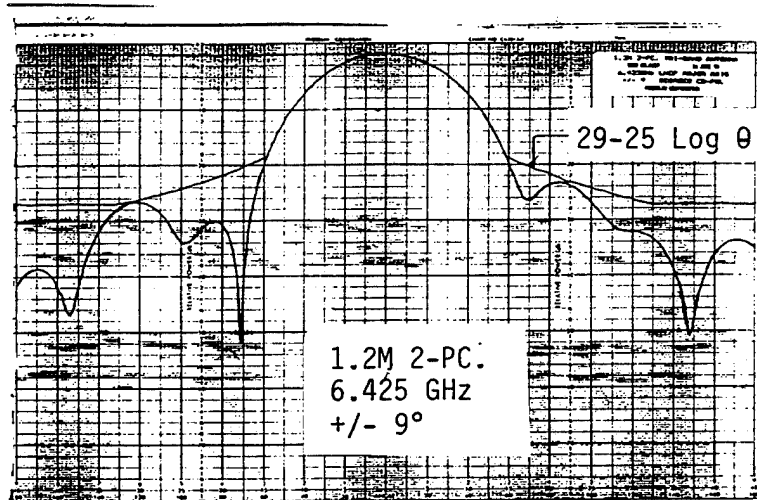
Figure 3.0-1 1.2M Radiation Patterns

29-25 Log θ

1.8M 9-PC.
6.425 GHz
+/- 4.5°

29-25 Log θ

1.8M 9-PC.
8.150 GHz
+/- 9°

29-25 Log θ

1.8M 9-PC.
14.25 GHz
+/- 9°
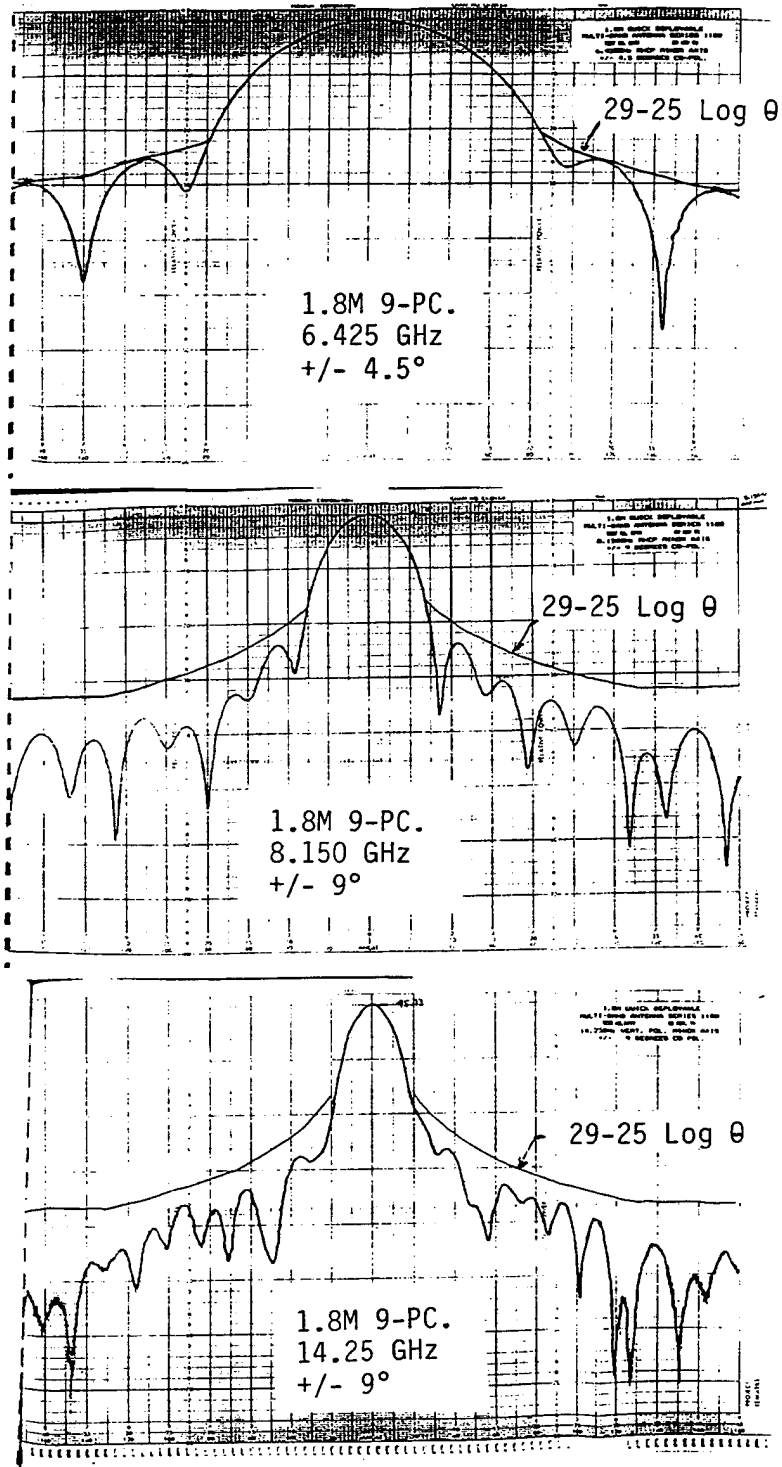
Figure 3.0-2 1.8M Radiation Patterns

13

32-25 Log θ

2.4M 4-PC.
6.425 GHz
+/- 9°

32-25 Log θ

2.4M 4-PC.
8.15 GHz
+/- 9°

29-25 Log θ

2.4M 4-PC.
14.25 GHz
+/- 9°
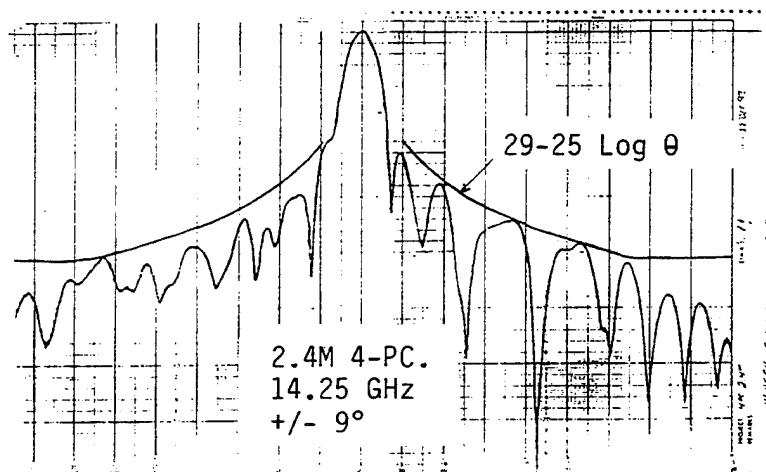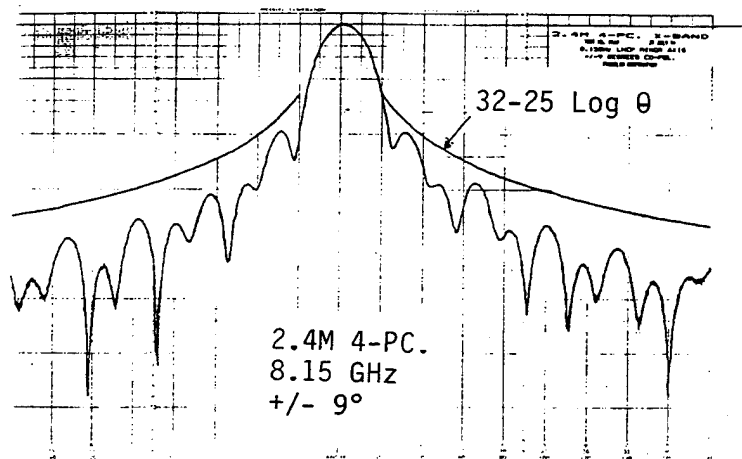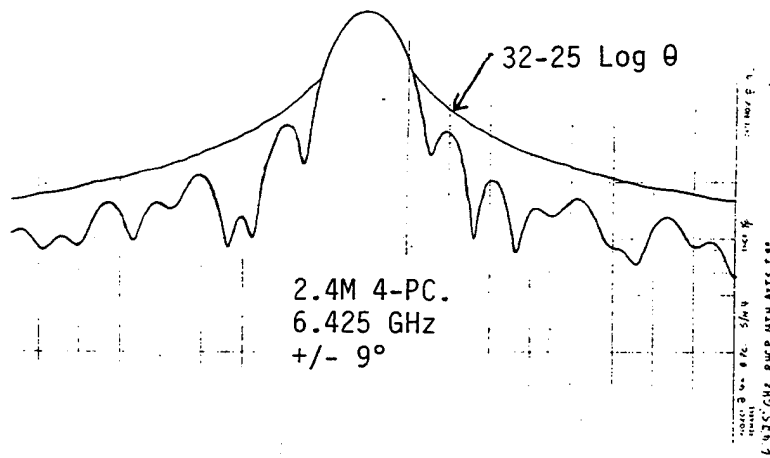
Figure 3.0-3 2.4M Radiation Patterns

antenna systems. Feed component configurations which provide tri-band

frequency compliance and selected transmit co-polarized secondary radiation

patterns are present.

A VEHICULAR ANTENNA FOR MOBILE SATELLITE SERVICE

Charles D. McCarrick
Seavey Engineering Associates, Inc.
135 King Street
Cohasset, Massachusetts 02025

Christopher J. Mosher
Seavey Engineering Associates, Inc.
135 King Street
Cohasset, Massachusetts 02025

1.0 INTRODUCTION

Plans are underway for a Mobile Satellite Communications Service which will provide seamless coverage to fixed and mobile earth terminal users within the Continental United States. This service will be rendered via a geostationary satellite system incorporating a RHCP L-band link. Consequently, equipment manufacturers are pressed to provide compact, low cost mobile terminals suitable for a commercial market. A major element in the success of this service is the mobile antenna and how it integrates both functionally and visually with the mobile equipment. In order for a mobile vehicular antenna to gain social acceptance, it must appear unobtrusive to the end user. However, medium gain circularly polarized antennas operating at L-band frequencies tend to be large in size. Hence the main design objective lies in overcoming the non aesthetic nature of such an antenna.

Development efforts have led to the realization of a production version medium gain mobile satellite antenna commonly referred to as the "mast". This multiturn quadrifilar helical antenna is designed for installation on a mobile platform, such as an automobile or cruise ship, where beam adjustment is critical for maintaining a RF transmission link with a geostationary satellite. In particular, the mast antenna permits its main radiation beam to be manually adjusted from twenty-five to seventy degrees above horizon while maintaining omnidirectional coverage in the azimuthal plane.

The mast is a mature product and currently the sole antenna to successfully undergo type approval by OPTUS, the SATCOM service provider in Australia. Together with the NEC Australia Pty. Ltd. mobile satellite telephone, the mast antenna offers seamless voice, data, and fax coverage to OPTUS users throughout Australia and its surrounding waters.

This paper provides a basic understanding of the quadrifilar, its operation, and modeling techniques. More importantly, it describes the design, construction, and electrical performance of the mast antenna. With the launching of satellites here in the United States by SATCOM service provider AMSC, antennas with unique features such as the beam steerable mast will gain particular attention as service requirements begin to unfold.

2.0 DESCRIPTION OF THE QUADRIFILAR AND ITS OPERATION

A quadrifilar helical antenna consists of four helical elements physically rotated by 90° in space with respect to one another while sharing a common axis. The helical elements themselves are conducting wires which serve as the radiating portion of the antenna. The two ends of the helix are referred to as the distal and proximal ends. Generally the distal end of a vertically mounted antenna is that end furthest from the ground plane, formed in this case by the vehicle body.

The quadrifilar is a versatile antenna in that its feed point may be located at either the proximal or distal end. At the feed point the four helical elements are fed in phase quadrature with equal amplitude. The antennas polarization sense depends upon the direction in which the helical elements are wound. To achieve right hand circular polarization for a proximal fed quadrifilar, each helical element must ascend in a counter-clockwise fashion as viewed from the proximal end.

The three dimensional shape of a helix defines the surface of a cylinder which has associated with it the dimensions of length and diameter. These dimensions are respectively referred to as the axial length and helix diameter. As a wire element is wound about a constant diameter to generate a uniform helix, an angle is formed between the helix element and the plane normal to that of the central axis. This angle is called the pitch angle and it is dependent upon the number of helix turns for a given axial length. The pitch, not to be confused with pitch angle, is defined as the axial length required for the helix to complete one full turn about its axis.

The pitch and helix diameter each play a role in determining the radiation characteristics of the antenna. Decreasing either parameters' dimension form an arbitrary reference dimension will cause the radiation beam in the elevation plane to scan towards zenith. Conversely, an increase in parameter dimensions will cause the beam to scan towards horizon. As with all traveling wave antennas, there exists a distinct shift in the angle of peak radiation at two separate frequencies for a set of constant helix parameters. More specifically, an increase or decrease in operating frequency elicits an inverse response in elevation angle. This behavior is commonly denoted as "frequency scanning".

3.0 MODELING TECHNIQUES

The Numerical Electromagnetic Code (NEC) software is of moderate utility. This software can quickly evaluate the radiation characteristics and input impedance of a wire structure in three dimensional space. Using NEC, one can successfully model various wire antennas including quadrifilars.

Radiation characteristics are evaluated with the quadrifilar suspended in free space. As described above, it is the proper selection of helix parameters which yields the desired coverage. Intuition and experience are employed to determine an initial set of parameters. An iterative approach is then adopted. To great success, several generator programs have been created which interface with the NEC software to allow for rapid manipulation of the helix parameters.

As discussed, the quadrifilar is fed in phase quadrature with equal amplitude. Hence, measuring the terminal impedance of each helical element is not straightforward. Fortunately however, NEC can predict the terminal impedance with reasonable accuracy when arranged in the proper format.

Due to mutual coupling between helical elements, alteration of the helix parameters strongly affects the input impedance of the quadrifilar. Thus the impedance must be carefully monitored throughout the iterative process. In fact, fulfilling the coverage requirements while maintaining a reasonable match is the most challenging aspect of the design.

4.0 MAST ANTENNA DESIGN

The mast antenna is a multiturn quadrifilar helical antenna fed in phase quadrature at the proximal end. Feeding is accomplished via a covered microstrip power combiner of cylindrical form. Attached to the feed network are conductive elements of fixed undeveloped length which ascend in a helical manner to the distal end. Along the way the elements are delicately supported to provide stability under vibration conditions. At the distal end the elements are attached to a rotatable knob. The complete assembly is housed within a tapered fiberglass radome and attached to a low loss coaxial cable. Please refer to Figure 1 for an outline drawing of the mast antenna with reference dimensions.

4.1 Adjustment Mechanism

The mast's radiation pattern is omnidirectional in azimuth with directive beams in the elevation plane. By proper selection of helix parameters it is possible to achieve 8dBic of antenna gain. However, gains of this magnitude yield an elevation beam which is too directive to provide complete elevation coverage using a fixed set of helix parameters. To that end a mechanical feature has been incorporated into the mast design to allow for manual variation of these parameters.

Turning the rotatable knob in one direction or the other increases or decreases the number of turns in the antenna depending upon the direction of rotation. Any change in the number of turns over a fixed axial length results in an inversely proportional change in the helix diameter and pitch. The final result is a shift in the angle of maximum radiation. Hence the rotatable knob is the source of beam adjustment for the user. Calibration markings on the knob provide an approximate location of the radiation beam in degrees above horizon for a vertical mast. In this manner one can steer the radiation beam to any angle between twenty-five and seventy degrees as dictated by his/her geographical location.

The method of adjustment explained here can be described as manually mechanical. However, a manually electrical adjustment is also available. In fact, there currently exists a motorized version of the mast antenna which allows the user to adjust the mast from a remote location such as inside the vehicle. In the fullness of time system costs will decrease resulting in a higher demand for luxury options. Paralleled with advances in mobile terminal technology, it is envisioned that the motorized mast will operate in a "hands off" mode where beam adjustment is controlled entirely by the mobile terminal equipment.

4.2 Feed Network

Under normal circumstances, the phase quadrature required to feed a quadrifilar would be accomplished via two 3dB hybrids. Moreover, the isolated port of each hybrid would be terminated in a load of characteristic impedance. In such a configuration a portion of the power reflected at each input terminal of the volute is redirected into a load where it is dissipated.

The feed network employed here is a four way covered microstrip power combiner which does not incorporate hybrids or resistive loads. Instead it uses 90° and 180° line lengths to achieve phase quadrature. This arrangement offers several advantages such as ease of assembly and reduced physical size. However, feeding the mast in this manner requires a proper impedance match at the feed/volute interface for all parameter variations. Otherwise, an amplitude unbalance will occur between the four helical arms causing a substantial degradation in back lobe performance and gain. The rational behind this is best understood through a transmission line analysis of such a feed network.

4.3 Frequency Scanning

The frequency scanning characteristics of the mast can potentially jeopardize its utility as a medium gain antenna if not properly accounted for. Frequency scanning results in an unfortunate reduction in antenna gain between the transmit and receive modes of operation. This reduction is often referred to as "crossover loss". Recent developments have led to an improved version of the mast antenna with significantly reduced frequency scanning behavior.

5.0 MAST ANTENNA CONSTRUCTION

5.1 Helical Elements and Power Combiner Circuit

The microstrip power combiner and four helical elements form a continuous printed circuit of copper on 5 mil Mylar film. After etching, the circuit is die cut into the form shown in Figure 2. An important feature of the Mylar film is its ability to maintain a uniform helical shape along the central axis during adjustment.

5.2 Base Assembly

The power combiner portion of the circuit is sandwiched between inner and outer sections of polypropylene tubing which form the microstrip sub and superstrates respectively. To complete the microstrip circuit, the entire assembly is fitted over a brass rod which acts as a ground plane. A coaxial cable enters the brass rod and engages the lower tail of the power combiner forming a coaxial-to-microstrip transition. This low loss cable is 8.2' long, 0.29" in diameter, and terminates in a TNC male connector. A rubber grommet is also provided to facilitate cable passage through the skin of the vehicle if required. A 2.6" long by 0.94" diameter stainless steel spring is attached to the bottom of the brass rod to absorb shock on impact between the antenna and low objects (i.e. garage doors, tree limbs, etc.). The opposite end of the spring is tapped with M8 x 1.0 female threads for use with most commercially available mounts such as trunk, gutter, and universal ball mounts.

5.3 Radome

Both the feed network and the helical elements are housed within a black fiberglass radome. This tapered radome is 33.8" long and varies from 0.57" to 0.85" in diameter. The radome is secured to the base assembly near the location of the coaxial cable entry. A protective sheath affixed to the radome provides a tamper resistant transition at the cable/radome interface.

5.4 Adjustment Knob Assembly

The adjustment knob assembly consists of a knurled rotatable knob and a travel limiting nut. The threaded shaft of the knob and the limiting nut are contained within a clear polycarbonate housing. The entire assembly is fashioned to the top of the radome at which point the helical elements engage the rotatable knob.

Turning the adjustment knob alters the height of the limiting nut within the clear housing. In short, the nut is raised or lowered depending upon the direction of rotation. When properly calibrated, the location of the limiting nut provides insight as to the direction of maximum radiation. As such, calibration markings have been laser etched into the clear housing which provide the user with six adjustment settings over the range of 25° to 70°. Mechanical stops exist within the assembly which prevent the user from twisting the helical elements beyond their practical limits. Upon completion of final assembly the mast is fully environmentally sealed and water immersion tested on a 100% basis.

6.0 MEASURED ELECTRICAL PERFORMANCE

Tables 1 through 3 summarize the gain and VSWR performance for elevation settings of 30°, 50°, and 70° respectively. The frequencies listed here correspond to the low, middle, and high end of the Australian receive and transmit bands. Similar performance is obtained over the designated United States bands which are somewhat lower in frequency.

TABLE 1 - ELECTRICAL PERFORMANCE AT 30° EL

FREQUENCY (MHz)	GAIN (dBic)	VSWR
1545	7.9	1.42:1
1552	7.8	1.40:1
1559	7.7	1.37:1
1646.5	7.7	1.24:1
1653.5	7.7	1.39:1
1660.5	7.6	1.59:1

TABLE 2 - ELECTRICAL PERFORMANCE AT 50° EL

FREQUENCY (MHz)	GAIN (dBic)	VSWR
1545	8.0	1.23:1
1552	8.1	1.21:1
1559	7.9	1.21:1
1646.5	8.0	1.05:1
1653.5	7.8	1.20:1
1660.5	7.6	1.36:1

TABLE 3 - ELECTRICAL PERFORMANCE AT 70° EL

FREQUENCY (MHz)	GAIN (dBic)	VSWR
1545	8.1	1.33:1
1552	8.2	1.27:1
1559	8.3	1.21:1
1646.5	8.0	1.25:1
1653.5	7.8	1.40:1
1660.5	7.8	1.54:1

Figure 1   Mast Antenna Outline Drawing

34.6" REF. (879 MM)

2.6" (66 MM) REF.

TNC MALE CONNECTOR

2.5 METER COAXIAL CABLE

CALIBRATION MARKINGS

FIBERGLASS RADOME

RUBBER GROMMET

.57 DIA. REF (14.5 MM)

.85 DIA. REF (21.6 MM)

.94 DIA. REF (23.8 MM)

M8 X 1.0 FEMALE THREADS

ADJUSTMENT KNOB ASSEMBLY

STAINLESS STEEL SPRING
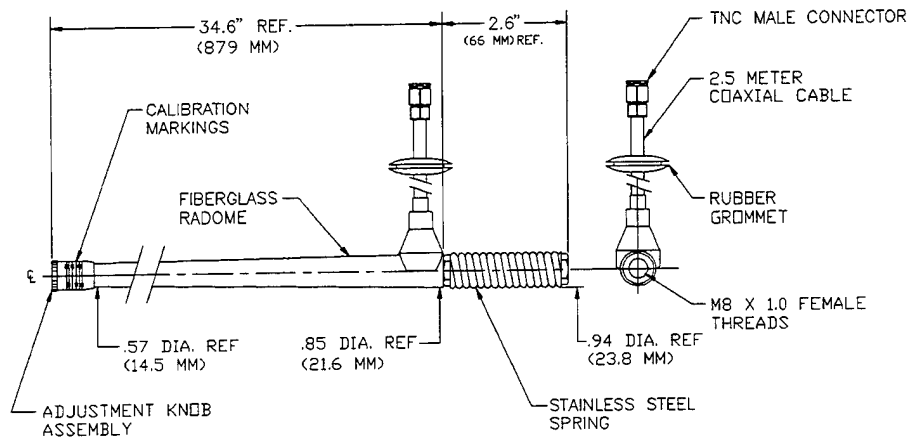
Figure 2   Helical Elements and Power Combiner Circuit
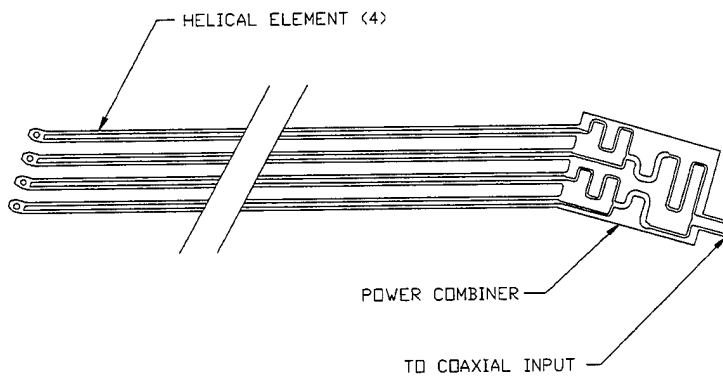
HELICAL ELEMENT (4)

POWER COMBINER

TO COAXIAL INPUT

25

LOW COST MILLIMETER WAVE PHASED ARRAY ANTENNA

Patrick PONS
Christian RENARD

DASSAULT ELECTRONIQUE
55, Quai Marcel Dassault
92214 - SAINT-CLOUD - FRANCE

LOW COST MILLIMETER WAVE
PHASED ARRAY ANTENNA

Patrick PONS

Christian RENARD

DASSAULT ELECTRONIQUE
55, Quai Marcel Dassault
92214 - SAINT-CLOUD - FRANCE

ABSTRACT

The design of a mechanically fixed antenna with electronical scanning of a narrow beam is usually a complex technical problem, and it becomes a real challenge when the antenna, operating in millimetric frequency band, is to be affordable (i.e. low cost).

This presentation is going to address the subject of an original antenna concept, intended for Radar application, with two-axis electronical scanning of the radiated beam.

The complex, cumbersome and costly use of a large number of mmw phase shifters in order to operate 3-D scan in a broad field of vision is replaced in this design by a combined use of frequency scan and beam switch, compatible with Radar specifications.

This presentation will describe the architecture used in this concept, with the constitutive elements designed to satisfy the overall technical goals.

FOREWORD

The scope of this presentation is the system and technical assessment for the definition of an antenna for a future Radar system operating in millimetric frequency band, and capable of electronic scanning of the beam while ensuring low cost goal.

Radar systems in millimetric frequencies are well adapted to close-range applications on mobile platforms, in order to produce high resolution Radar images <1>. Moreover, the choice of millimetric frequencies enables the use of small dimensions for the scanning antenna, while ensuring wide bandwidths not available at lower frequencies.

However, the utilization of the millimetric frequency range must still overcome several problems and limitations among which is the lack of low-cost, low power consumption components for antennas.

BACKGROUND - STATE OF THE ART

A passive reflector or an array mechanically scanned is a solution not adequate for flush-mounted/low visibility requirement.

The benefits of a fixed array antenna with electronic beam steering include :

    -- beam agility and flexibility, as the direction of radiation is not dependant on mechanical constraints (motorization)

    -- conformation and low observability, as the whole system can be implemented inside the host structure with the antenna positioned as a window upon it.

Array antennas with electronic beam scanning, active or passive in transmission or reception are well documented <2> and, in some cases, are in the stage of mass production, particularly in the telecommunications field <3>

These antennas in a general manner make use of an array of radiating elements connected to a microwave power divider realizing the generation of the amplitude illumination pattern ensuring the required characteristics in terms of radiation pattern.

The electronic scanning function is achieved with modules associated with each radiating elements and inserted between these radiators and the power divider. These modules generate the phase illumination pattern on the radiating aperture, typically from the use of coaxial or printed diode phase shifters, from waveguide or printed ferrite phase shifters, or from digitally controlled line lengths for wide-band phased arrays.

These techniques have already been transposed in the millimetric frequency range, and technological demonstrators have been developed and tested e.g. in the civil (20-30 GHz) or military (20-44 GHz) telecommunications band <4>, and in some frequency bands allocated to Radar.

However, these techniques lead to various problems and limitations following the fact that a narrow beam requires a great number of elements, increasing with the maximum scanning angle. This can be illustrated by the following example:

-- a fixed array antenna with the main beam presenting a half power width $2°x4°$, and scanning in an extended area $120°x30°$ requires approximately 1,500 radiating elements for the array.

A classical architecture for electronic scanning based on the use of individual phase shifters would then necessitate 1,500 phase shifters and a power dividing device of 1 to 1,500, generating the following constraints:

-- critical layout (connections between radiators and modules, between modules and power divider, mechanical and thermal layout), all the more complicated as the frequency goes up, i.e. as the inter-element spacing is reduced.

-- high cost, according to the number of phase shifter modules and radiating elements.

This problem is even more complex when the radar monopulse signals (azimuth and elevation differences) are to be generated.

The architecture described hereafter solves in a specific way the limitations listed above: the operation of the radar antenna is based on frequency scanning in one direction of scan, and beam direction switching based on Rotman lens in the other direction of scan.

FREQUENCY SCANNING

The principle made use of here involves the variation with frequency of the phase difference between the radiating elements of a linear array, fed through propagation lines of different

lengths.[5]

This may be implemented in two different ways:

-- by feeding the elements in series connection with a
sinuous, or serpentine, propagation line coupled to radiators,
where the electric distance s between adjacent elements separated
by a distance d is fixed in such a way that any frequency shift
modifies the phase difference between adjacent elements, hence
the angle of scan, in a definite way. The scan angle counted
from broadside is Θ_m such that $\sin\Theta_m = s\, \lambda/d\,(1/\lambda g - 1/\lambda gm)$ where
λ and λg are respectively the wavelengths in the air and at the
work frequency, and λgm corresponds to the frequency where s is
an integer number times this wavelength.

THE ROTMAN LENS

In general the role of a lens is to focus an incoming plane wave
toward a specific point for this direction called focus.

The Rotman lens[6] is a two dimensional device designed to align
the radiating elements of a linear array along various wave
fronts, hence generating various scanned directions, determined
from the positions of the input ports. The Rotman lens is a
parallel-plate constrained lens: it makes use of the
electromagnetic propagation between two parallel plates with
input ports (E), or beam ports, corresponding to the directions
of the radiated beam, and the output ports connected to the
radiating elements of the linear array with lines of specific
lengths.

The Rotman lens consists of a circular focal arc on which
multiple feeds are arranged, three of them being of perfect
focus, one on axis and two symmetrically displaced from the axis:
the feeds radiate into the parallel-plate area, the radiated wave
being picked up by probes arranged on a specific curve and
connected to the radiators.

The operation is independent of frequency when the propagation
mode is a TEM mode. The choice of the direction of radiation,
i.e. of the beam port on the input side of the lens, is made with
a switch matrix.

ARCHITECTURE OF THE RADAR ANTENNA

The radar antenna making use of frequency scanning and beam

switch with Rotman lens is divided in parallel vertical columns.

The number of columns and the spacing between them are determined by the frequency band, the azimuth beamwidth and the maximum azimuth scan angle.

Each column is a frequency scanned linear array where the inter-element spacing d and the electric distance s between them are designed to scan the radiated beam in the required angle range in elevation plane.

The elevation monopulse signal is generated by dividing each column into halves.

The horizontal scan is realized by beam switch. A Rotman lens makes use of the signals generated by the linear array of vertical columns and ensures the azimuth scan: this lens has as many beam ports as directions to create, and as many antenna ports as vertical columns to feed. The azimuth direction is chosen through a switch matrix connecting the adequate beam port to the Radar transmitter/receiver.

The azimuth monopulse signal is generated by dividing the linear array of vertical columns into a left and a right half.

The orientation of the radiated beam is then accomplished with a combination of a choice of a specific frequency on the one hand, and the choice of a beam azimuth direction port on the other hand.

This architecture emphasizes the advantages reached in comparison with more classical architectures, to the prejudice of a more elaborated Radar signal processing:

-- diminution and simplification of inter-element connecting problem: the radiating array is really a horizontal array of frequency scanned elements. In the example shown above, a 1,500 element rectangular array antenna is reduced to a linear array of approximately 60 frequency scanned elements.

-- reduction and simplification of the layout of the beam pointing devices. In the example shown above, a set of 1,500 phase shifters is replaced by electric line lengths and a set of one to four Rotman lenses with the associated switch matrix.

-- reduction and simplification of the layout of the feeding system and the command and control of these elements which become crucial at high frequencies.

-- hence following from these characteristics and the reduction of complexity, the cost of the antenna is obviously reduced compared with solutions based on the use of phase shifters.

TECHNICAL APPROACH FOR THE CONSTITUTIVE ELEMENTS

The frequency scanned vertical columns may be designed in printed technology (e.g. in suspended substrate form capable of low loss and power handling or coplanar waveguide with printed elements as V-shaped dipoles, notches,...).

An alternative is to design the parallel columns in waveguide technology as a cascade of couplers made from rectangular windows or Bethe holes with waveguide slots as radiating elements; powerful software programs have been developed to analyze these waveguide slot arrays[8]. Automatic milling machines are used to manufacture these elements.

Rotman lenses have been designed in printed technology and in waveguide technology. This last form is mechanically simple, as it consists of two parallel metallic plates, with beam and radiator ports being either processed as standard rectangular waveguide, or made compatible with coaxial connections through the use of probes in the lens.

Finally, switch matrices may be designed at mm frequencies using ferrite devices as elementary switch elements.

CONCLUSIONS

An architecture design has been described for a new kind of two dimensional phase array at millimetric frequencies.

The architecture brings into operation a combination of frequency scan and beam switch with Rotman lenses.

This concept opens the possibility of low cost antennas at millimetric frequencies as the architecture:

 -- reduces the number of phase commands in the antenna, roughly from one element per radiator to one command per column in a rectangular array.

 -- drastically reduces the number of interconnections in the array.

REFERENCES

<1>   Glockler, R.; "Phased Array for Millimeter Wave Frequencies", <u>International Journal of Infrared and Millimeter Waves</u>.   vol. XI, no.2

<2>   Silvy, O., Renard, C.; "Testing An Airborne Phased Array Antenna with Aramis"; 12th AMTA Symposium, Philadelphia, 1990.

<3>   Freyssinier, P., Medard, J.; "Antennes Reseau Plaquées Bi-Fréquences en Polarisation Circulaire", <u>L'Onde Electrique</u>, vol. 73, no.1, 1993.

<4>   <u>Aviation Week and Space Technology</u> sept.12, 1994 p.64

<5>   Lo, Y., Lee, S.; <u>Antenna Handbook</u>, Van Nostrand Reinhold, 1988.

<6>   Rotman, W., Turner, R.; "Wide Angle Microwave Lens for Line Source Applications", <u>IEEE Tr. AP</u>, Nov.1963, p.623.

<7>   Mailloux, R.J.; <u>Phased Array Antenna Handbook</u>, Artech House, 1994.

<8>   Renard, C., Clerc, F.; "A Computer Package for the Study of Electromagnetic Radiation", Antenna Application Symposium, University of Illinois, 1989.

FREQUENCY
SCAN

BEAM SWITCH
SCAN

V

Fmax

H

Fmin

Elevation
scan angle

20

0

−10

Fmin   Fmax
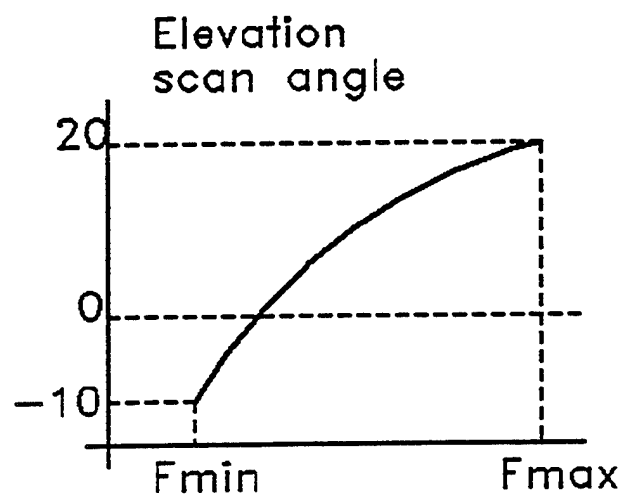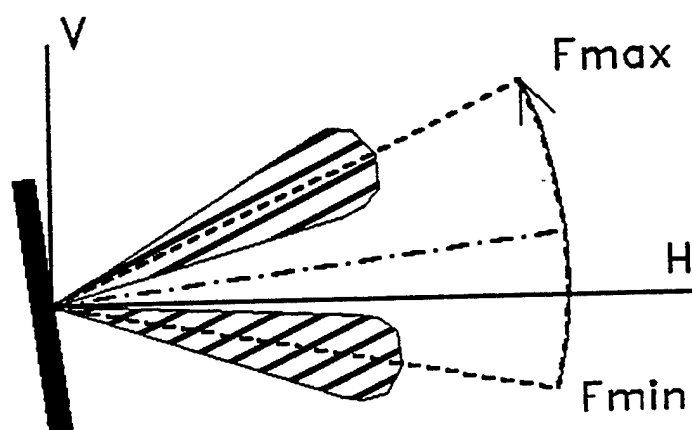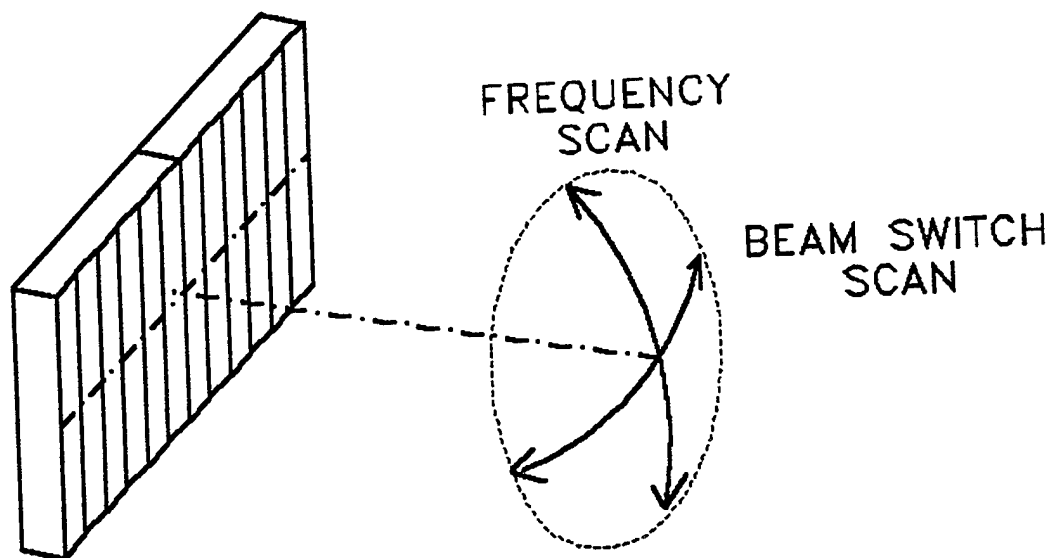
EL. PLANE   F. SCAN   WAVEGUIDE FED SLOTTED BARS
AZ. PLANE   E. SCAN   ROTMAN LENS

$N_{EL} = 22$

$N_{AZ} = 64$

SLOTTED WAVEGUIDE ANTENNAS
$1408 = 64 \times 22$

AZIMUTH ROTMAN LENS
4

AZIMUTH SWITCH MATRIX
4

BEAMFORMING NETWORK
$(\Sigma, \Delta_{AZ}, \Delta_{EL})$

R_R^U 50×32

R_L^U 50×32

R_R^D 50×32

R_L^D 50×32

SM_R^U $1/50$

SM_L^U $1/50$

SM_R^D $1/50$

SM_L^D $1/50$

B.F.N.

Σ

Δ_{AZ}

Δ_{EL}
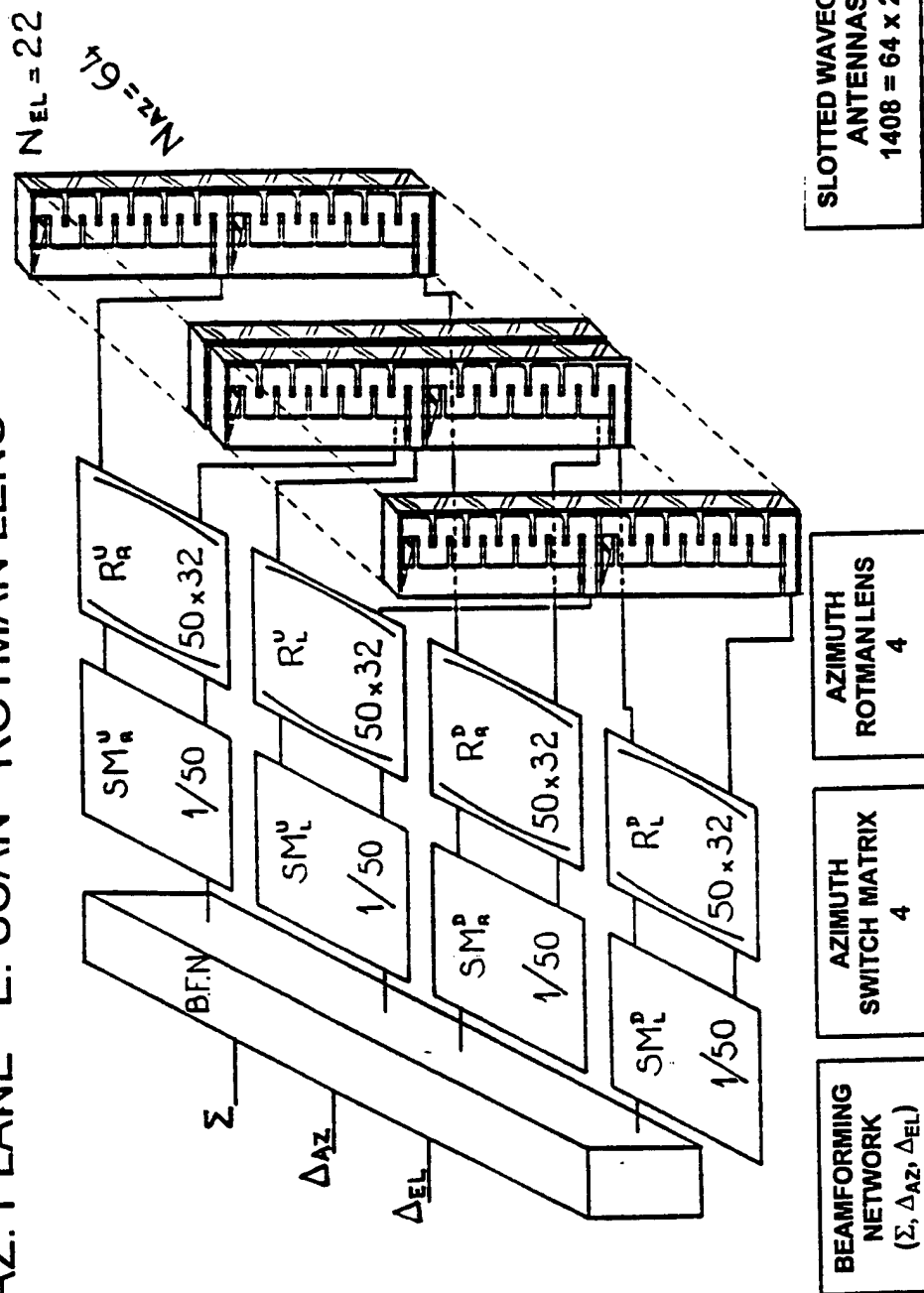
PERFORMANCE ANALYSIS FOR A CONCEALED

AUTOMOBILE ENTERTAINMENT RADIO ANTENNA SUB-SYSTEM

by

Andrew Adrian
Automotive Components Division
Ford Motor Company
Dearborn, MI

ABSTRACT.

AM/FM mobile broadcast reception for many years has been very pragmatic in its use of antenna sub-systems. The primary antenna element of choice has been the vertical, 92 MHz, quarter wave fixed mast or the vertical, 92 MHz, telescoping quarter wave mast. Each are mounted using the vehicle sheetmetal as the ground plane. Location of the mast has always been primarily driven by styling input. From the element, low capacitance coaxial cable is utilized to propagate the signal to the radio receiver. Performance of this type of antenna sub-system is very consistent with little electrical engineering effort required to maximize signal transfer from the antenna to the radio.

Although quarter wave mast type systems do not require extensive electrical engineering efforts, they do have significant disadvantages. The mast detracts from overall styling of the vehicle. It is also very susceptible to mechanical damage during the life of an automobile. This is especially true for telescoping masts. Finally, as automobiles have become more aerodynamic and have a quieter ride, wind whistle from the mast that was previously masked be the automobile is now audible and leads to customer dissatisfaction and complaints. For these reasons, concealed antenna sub-systems are a very desirable feature for automobiles.

Implementation of a concealed automotive antenna sub-system for AM/FM reception requires significantly more electrical engineering effort than a conventional quarter wave mast type antenna subsystem. Because of the increased electrical complexity of the design, design tools have been developed to predict the performance of concealed antenna sub-systems. The following presents the architecture and an electrical model of a concealed automotive antenna sub-system with comparisons to experimental testing.

1.0 DESIGN REQUIREMENTS

When designing a concealed automotive entertainment radio antenna
sub-system for production and public sale, customers must not be
able to discern any difference between AM/FM radio reception
performance using a conventional quarter wave mast antenna sub-
system or a concealed antenna sub-system.

1.1 AM Design Requirements.

The AM frequency band of operation is 530 to 1710 KHz. Since at
AM frequencies the maximum dimension of any vehicle utilizing an
antenna sub-system for AM reception is less than 0.04λ, the
antenna is nothing more than an electrically small field probe.
Due to the significant reactance associated with such a small
element, the most effective method to characterize the antenna
sub-system's ability to transform electromagnetic radiation into a
usable signal at the antenna sub-system's terminals is the
measurement of the antenna factor, K.

$$K = \frac{E}{V} \tag{1}$$

where E is the electric field, of the desired polarization,
expressed in volts/meter and V is the voltage at the antenna
terminals with a defined load being driven by the antenna.

For a concealed antenna sub-system on a vehicle, frequency by
frequency, over the AM frequency band of operation, the antenna
factor for the vertical polarization, measured with the radio

37

receiver as the load shall be no less than the antenna factor for the vertical polarization, of a quarter wave mast antenna sub-system on the same vehicle, measured into the same receiver load. The receiver load impedance is illustrated in Figure 1.

Additionally, frequency by frequency, over the AM frequency band of operation, the vertically polarized antenna patterns at the horizon elevation of the concealed antenna sub-system shall have no more variation than the corresponding patterns for a quarter wave mast antenna sub-system on the same vehicle.

1.2 FM Design Requirements.

The frequency band of operation is 87.9 to 107.9 MHz. At these frequencies, the antenna sub-system has resonant dimensions and an effective broadband match to the receiver can be achieved. Consequently, antenna power gain measurements are used as the figures of merit to describe the antenna sub-system's ability to transform electromagnetic radiation into a usable signal at the antenna terminals. The gain reference that is utilized is a resonant dipole. All expressions of gain are in dBld (deci-Bell relative to a linearly polarized dipole.)

Frequency by frequency, over the FM frequency band of operation, the average vertically polarized gain at the horizon elevation of any concealed antenna sub-system as installed on a vehicle shall be greater than -10dBld (including mismatches into the receiver.) The receiver impedance that the antenna sub-system must drive is

illustrated in Figure 2.

2.0 MEASUREMENT TECHNIQUES

All measurements of AM antenna factor, FM gain, and impedance of
the antenna sub-system are performed as installed on the vehicle.

2.1 AM Measurements

Using a calibration antenna with a calibrated antenna factor, a
gain substitution method is used to determine the antenna factor
of the antenna sub-system with a high impedance
amplifier/transformer. This antenna factor is referred to as
$K_{A/T}$. The amplifier/transformer, always presents a constant
impedance to the receiving test equipment while presenting a very
high impedance to the antenna sub-system. At AM frequencies,
variation is negligible, so the measurements are made with the
vehicles under test in a stationary position.

Two port measurements of the amplifier/transformer over the AM
band of operation are then used to determine the voltage gain from
a source with the same impedance as the antenna sub-system through
the amplifier/transformer to the load of the receiving test
equipment. This gain is referred to as $g_{A/T}$ (Figure 3a.) Another
gain is also computed from a source with the same impedance as the
antenna sub-system to the AM receiver load (Figure 1.) This gain
is referred to a g_{RL} (Figure 3b.) Since the antenna factor is a
directly proportional to voltage, the antenna factor of the
antenna sub-system into the receiver load, K_{RL}, can be computed

from the following equation:

$$K_{RL} = K_{A/T} \cdot \left(\frac{g_{RL}}{g_{A/T}} \right) .$$ (2)

This is most easily facilitated by using a good circuit analysis program.

Antenna patterns to determine variation are also taken through a high impedance amplifier/transformer.

For all of the AM measurements listed, the sources for the vertically polarized electric fields are the AM broadcast stations.

2.2 FM Measurements

Antenna sub-system gain at FM is determined by measuring azimuth patterns in the desired polarization. 50Ω receiver equipment is connected to the output of the antenna sub-system and the received power data is recorded every degree of azimuth per frequency. The power data is converted to linear voltage units, v_i at each angle of measurement. The area of the triangle A_i, in square voltage units, defined by the consecutive voltage measurements, v_i and v_{i+1}, and the origin, is determined by the equations:

$$A_i = \frac{1}{2} b_i \cdot h_i$$ (3)

where

$$b_i = v_{i+1}, \tag{4}$$

$$h_i = v_i \cdot \sin\phi, \tag{5}$$

and ϕ is the angular resolution of the data, in this case, 1 degree. A_i is summed over 360 degrees to calculate the total square voltage area, A_T, of each antenna pattern:

$$A_T = \sum_{i=1,360} A_i. \tag{6}$$

Of course when i is 360, i+1 is 1. This calculation is illustrated graphically in Figure 4. A_T is then set equal to the area of a circle and the unknown radius is solved to yield the average voltage, V_a, of the antenna pattern:

$$V_a = \sqrt{\frac{A_T}{\pi}}. \tag{7}$$

V_a is converted back to power units and compared to the power from a tuned dipole, P_d, at the frequency of measurement to obtain the average gain into the 50Ω test equipment,

$$G_{a(Z_0=50)} = \frac{V_a^2}{P_d}. \tag{8}$$

Knowing the reflection coefficient $\Gamma_{Z0=50}$ of the antenna ($Z_0=50$), the maximum available gain of the antenna subsystem, MAG, can be computed:

$$MAG = \frac{G_a}{1 - |\Gamma_{Z_0 = 50}|}.$$

The reflection coefficient of the antenna sub-system can then be computed relative to the entertainment receiver, Γ_{REC}, and the average gain, G_{aREC}, of the antenna sub-system into the entertainment receiver can be determined.

3.0 SYSTEM CONFIGURATION

The concealed antenna sub-system architecture is illustrated in Figure 5 [1]. The AM receive element is the rear window defroster. FM receive is carried out through the art work above the rear window defroster.

Both AM and FM signals are carried back to an antenna isolation module. This module decouples the defroster grid from the car vehicle at AM frequencies as well as multiplexes AM and FM onto one transmission line that propagates both sets of signals back to the entertainment radio receiver.

This module also passes the necessary D.C. current from the vehicle power supply to the defroster grid when the heating function is required. When heating current is required, a high power filter circuit in the isolation module filters unwanted signals from the heater current before the current passes to the portions of the antenna sub-system that are active at radio frequencies.

The internal circuitry of the antenna isolation module is depicted in Figure 6.

4.0 SYSTEM ANALYSIS and DESIGN

The system analysis begins by measuring the various components in the system and generating models for them. This begins with measurements of impedance and gain of the antenna elements and continues with circuit measurements of the lumped components in the module, the cabling and the interconnects. It is also necessary to measure the receiver input impedance.

S-parameter measurements are what is used to characterize and model the components. The components in the module are measured on the printed circuit board in the configuration that they are used, parallel or series. Models of the module lumped components at AM and FM frequencies were developed. Several of the module components are listed in Table 1. with their electrical model.

For the transformer and the interconnects, actual two port S-parameter measurements of the devices are used in the model. The measured antenna element impedances and receiver impedances were used as source and load impedances. Cable representations included the characteristic impedance, phase velocity, and attenuation factor.

4.1 Power Filter Analysis

The power filter model is illustrated in Figure 7. The question

here is how much detail is required in the representation of the power filter in the AM and FM system analysis. Examining the impedance across the $0.47\mu F$ capacitor (Figure 7) that the power filter presents to the transformer, it is seen that for all practical purposes the impedance is a short circuit. The worst case impedance has a magnitude of less than 2.6Ω at the end of the FM band (Figure 8.) Knowing this, the AM and FM models of the module portion of the system can drop the power filter. Therefore the system model reduces to the illustration in Figure 9.

4.2 AM Analysis and Design

In the AM band, the impedance that the heater grid presents to the isolator module (Figure 10) where the transformer meets the $0.015\mu F$ capacitor is measured as well as the impedance of the FM element (Figure 11) where it meets the coaxial transmission line. The K factor of each of these elements with the high impedance amplifier/transformer is also measured (Table 2.)

Using the two AM antenna impedances as source impedances, the system model from Figure 9, and the AM radio impedance from Figure 1, the voltage gain through the system from each receiving antenna element is calculated (Figure 12) as well as the AM impedance that the antenna sub-system presents to the radio receiver (Figure 13). From Figure 12 and Table 3, we conclude that the FM input to the isolator module does not provide any appreciable AM signal to the radio receiver and is well isolated.

44

4.3 FM Analysis and Design

As in the AM band, the FM impedance of the FM element is measured (Figure 14) as well as the FM impedance that the heater grid presents to the isolator module (Figure 15.) The MAG of each of these elements in the vertical polarization is also measured (Figures 16 and 17.)

Using the two antenna FM impedances as source impedances, the system model from Figure 9, and the FM radio impedance from Figure 2, the power gain (actually a loss) through the system is calculated (Figure 18) as well as the FM impedance that the antenna sub-system presents to the radio receiver (Figure 19). From Figures 17 and 18, we conclude that the heater grid does not provide any appreciable FM signal to the radio receiver and is well isolated.

Since the heater grid is isolated from the system at FM, the vertical polarized MAG less the power loss through the system results in the anticipated FM antenna sub-system gain (Figure 20.)

5.0 DESIGN VERIFICATION

Actual measurements of the complete concealed antenna sub-system have been made to verify that the requirements of the design have been met.

5.1 AM Measurements

For AM, K_{RL} of the concealed system must is greater than K_{RL} for a

45

quarter wave mast system on the same vehicle in the vertical polarization. Figure 21 graphically illustrates $K_{A/T}$ for the concealed and quarter wave antenna sub-system as well as K_{RL} for both.

Illustrated in Figure 22 are the antenna patterns for the vertical polarization for both types of systems. As can be seen from Figure 22, the pattern variation for the concealed antenna sub-system is virtually identical to the quarter wave antenna sub-system.

The measured impedance presented to the AM receiver and the calculated impedance from the system analysis are both plotted in Figure 23. The impedance model agrees very well with the measurements.

5.2 FM Measurements

Vertical and horizontal FM patterns for the concealed antenna sub-system are illustrated in Figure 24. Additionally, Figure 25 plots the MAG for the vertical polarization, the calculated average gain into the FM receiver for the vertical polarization, and the measured average gain into the FM receiver for the vertical polarization.

The measured impedance presented to the FM receiver and the calculated impedance from the system analysis are both plotted in Figure 26.

6.0 Conclusion

A concealed automobile entertainment radio antenna sub-system architecture has been presented with a system analysis capability to aid in the successful application of the architecture to different vehicles. This concealed antenna sub-system has been applied to several vehicle lines with success that is measured in decreased antenna sub-system field failures, lower cost, and higher overall customer satisfaction.

REFERENCES

[1] *1995 Town Car, Crown Victoria, Grand Marquis Service Manual*, p. 15-02-1, Ford Motor Company, 1994.

COMPONENT MODELS

COMPONENT	AM BAND MODEL	FM BAND MODEL
0.47μF Capacitor	0.47μF Capacitor	0.47μF Capacitor on the end of a 50Ω transmission line 5.1° long at 98 MHz
680pF Capacitor	680pF Capacitor	680pF Capacitor on the end of a 50Ω transmission line 4.7° long at 98 MHz
850nH Inductor	850nH Inductor	S-Parameter Measurement
120μF Capacitor	120μF Capacitor	120μF Capacitor on the end of a 50Ω transmission line 5.1° long at 98 MHz
330KΩ Resistor	330KΩ Resistor	330KΩ Resistor on the end of a 50Ω transmission line 3.8° long at 98 MHz
100pF Capacitor	100pF Capacitor	100pF Capacitor
1.8μH Inductor	1.8uH Inductor	1.8μH Inductor
0.015μF Capacitor	0.015uF Capacitor	0.015μF Capacitor
3.9KΩ Resistor	3600 Ω Resistor	3325Ω Resistor on the end of a 50Ω transmission line 8.8° long at 98 MHz
150nH Inductor	150nH Inductor	150nH Inductor
15pF Capacitor	15pF Capacitor	15pF Capacitor
Transformer	S-Parameter Measurement	S-Parameter Measurement
Interconnects	S-Parameter Measurements	S-parameter Measurements
Coaxial Cable	Z_0, 84% Velocity of Propagation, 8.9 dB/100m Loss Factor	Z_0, 84% Velocity of Propagation, 8.9 dB/100m Loss Factor

Table 1. Component models for AM and FM analysis.

AM K FACTORS

Frequency (KHz)	$K_{A/T}$ for Heater Grid (dB/m)	$K_{A/T}$ for FM Element (dB/m)
560	-28.9	-31.1
690	-32.6	-35.4
760	-32.1	-34.6
950	-30.3	-32.5
990	-30.6	-33.4
1310	-29.9	-33.2
1600	-31.7	-33.9

Table 2. $K_{A/T}$ for the Heater Grid and the FM Element.
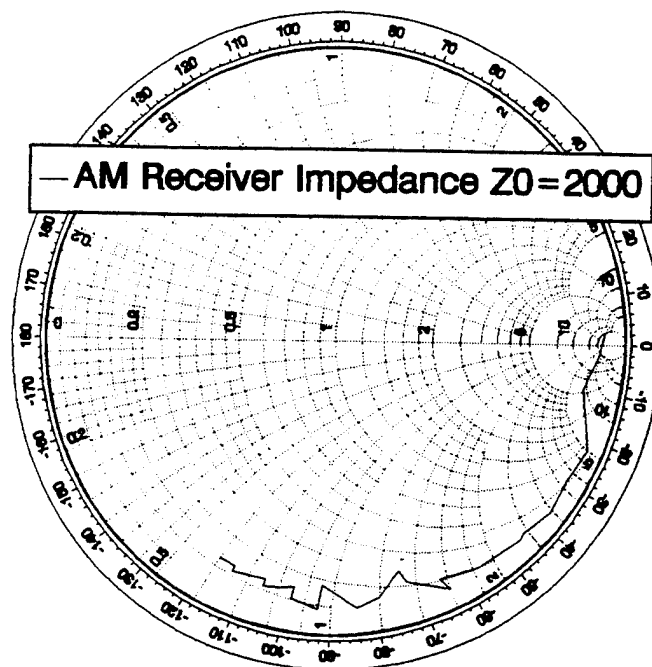
Figure 1.   AM receiver impedance normalized to 2000 ohms.
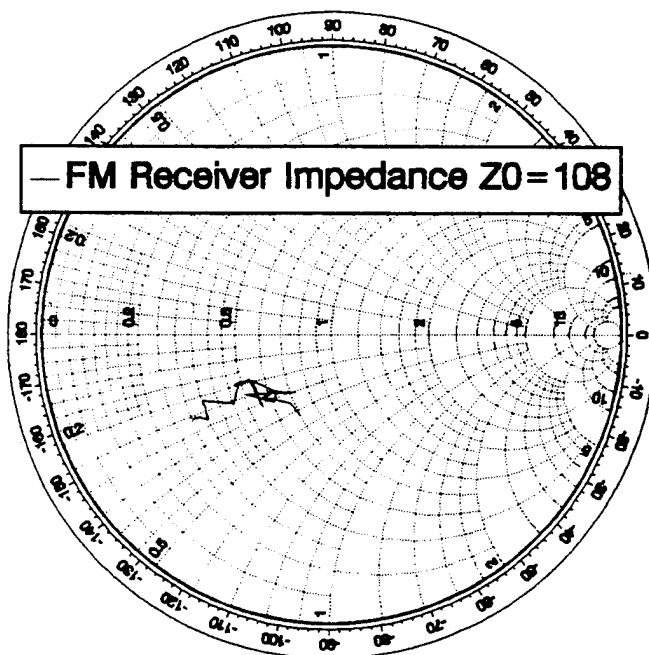
Figure 2.   FM receiver impedance normalized to 108 ohms.
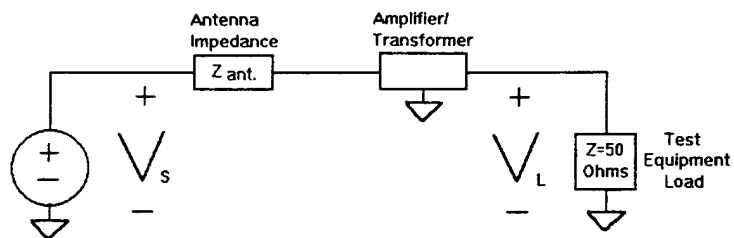
$$g_{A/T} = \frac{V_L}{V_s}$$

(a)
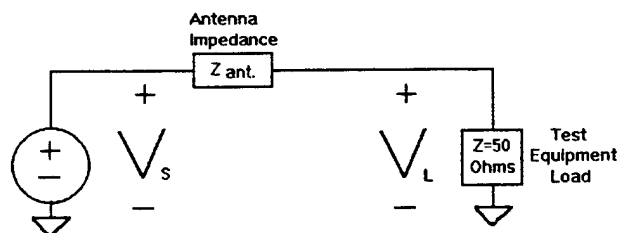
$$g_{RL} = \frac{V_L}{V_s}$$

(b)

Figure 3. (a) Voltage gain, $g_{A/T}$, from the antenna source to the test equipment load. (b) Voltage gain, g_{RL}, from the antenna source to the AM receiver.

$$\sum_i A_i = A_T$$
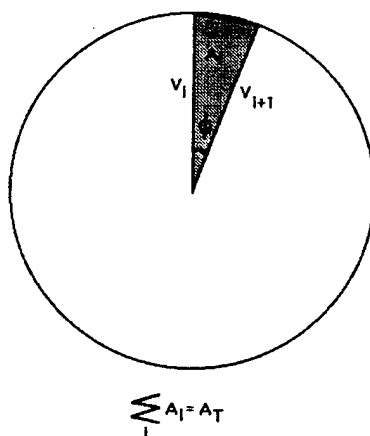
Figure 4. Graphical representation for the calculation of the square voltage area, A_T of an antenna pattern.
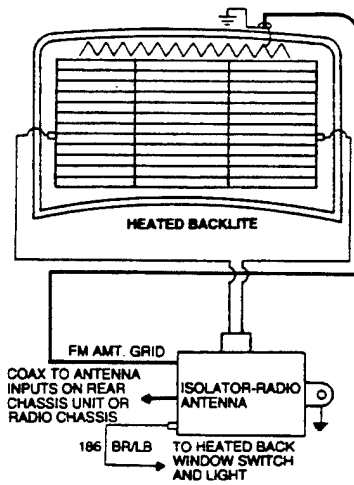
Figure 5. Concealed antenna sub-system architecture.
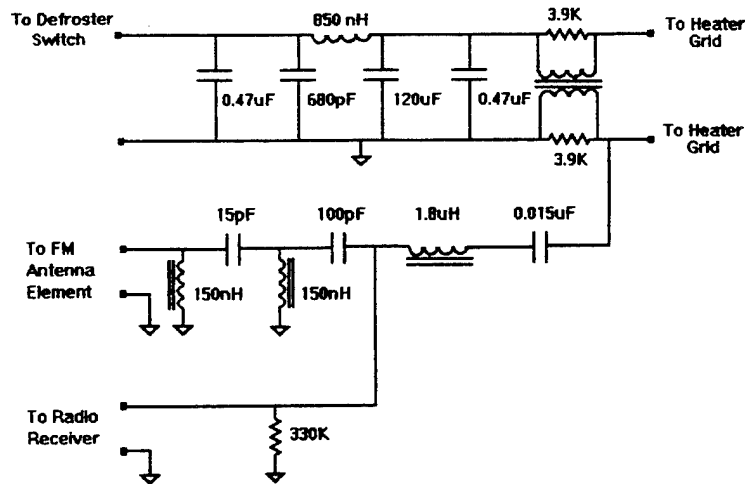
Figure 6. Internal circuitry of the antenna isolation module.
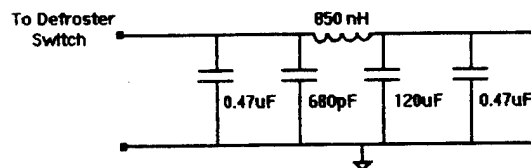
Figure 7. Power filter in the antenna isolator module.

52
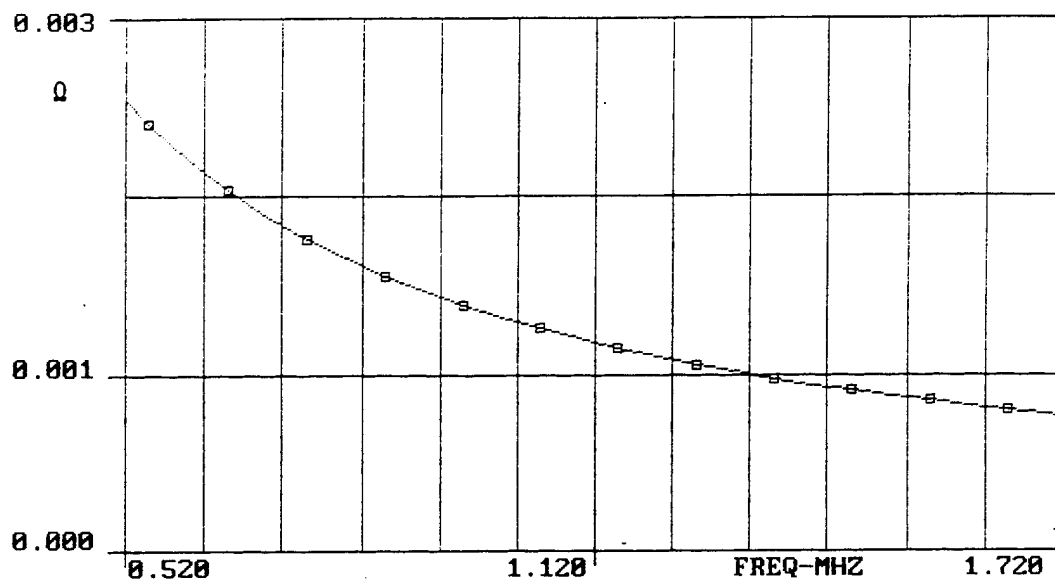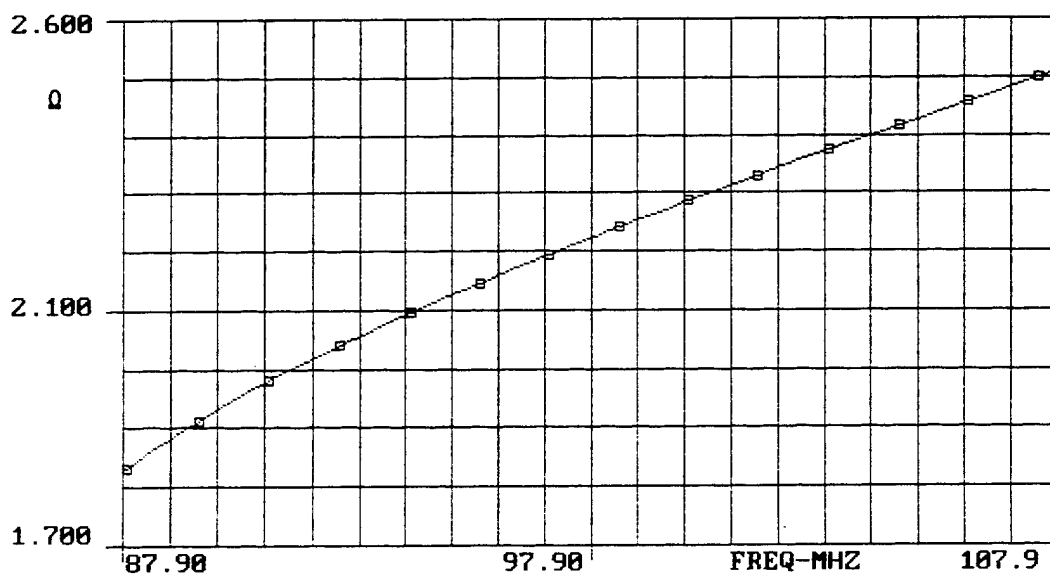
Figure 8. (a) Magnitude of the impedance across the $0.47\mu F$
capacitor of the power filter in the AM band. (b) Magnitude of
the impedance across the $0.47\mu F$ capacitor of the power filter in
the FM band.

53
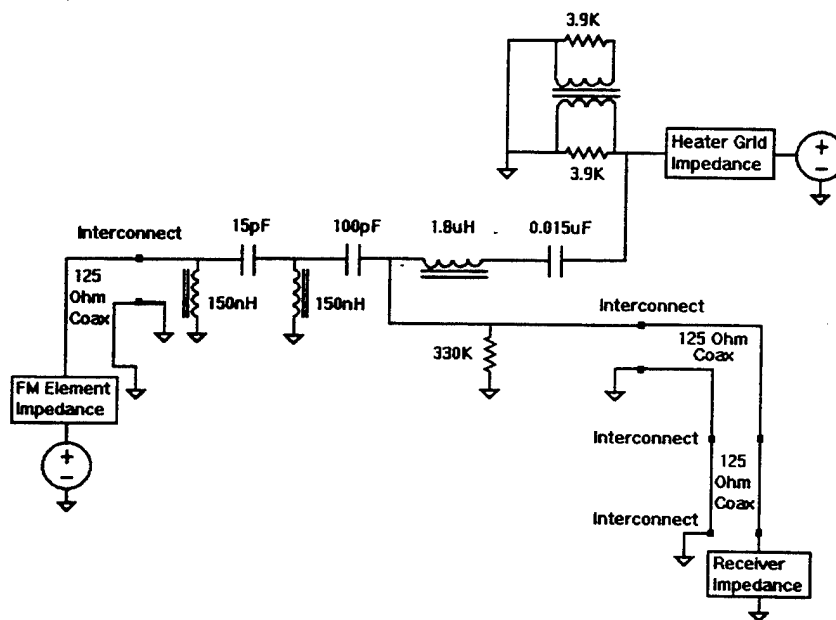
Figure 9.   Concealed antenna sub-system model.
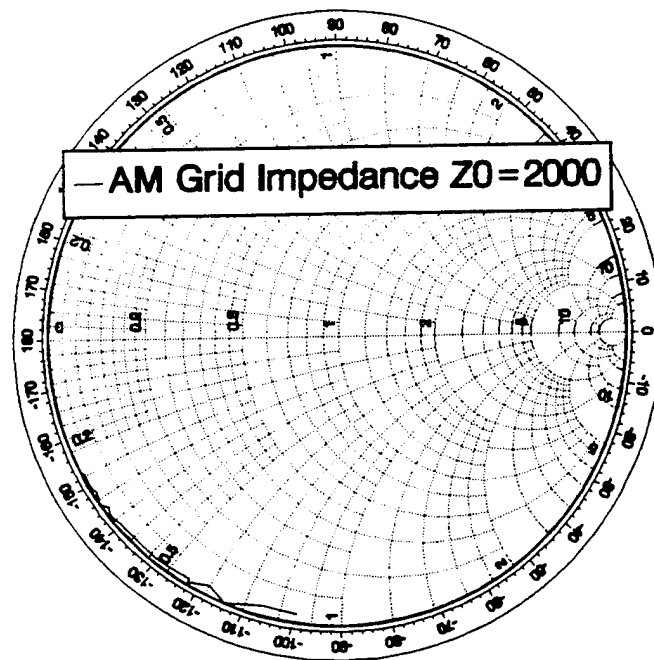
Figure 10. AM heater grid impedance normalized to 2000 ohms.
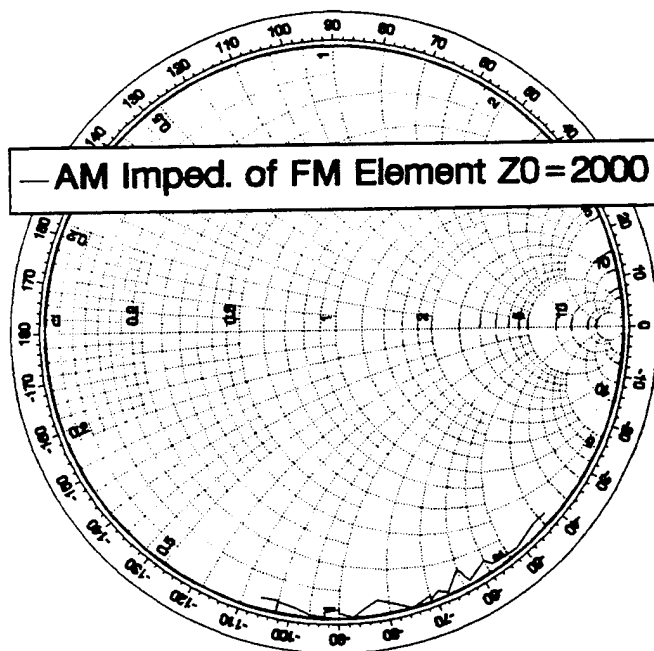
Figure 11. AM impedance of the FM element normalized to 2000 ohms.

55
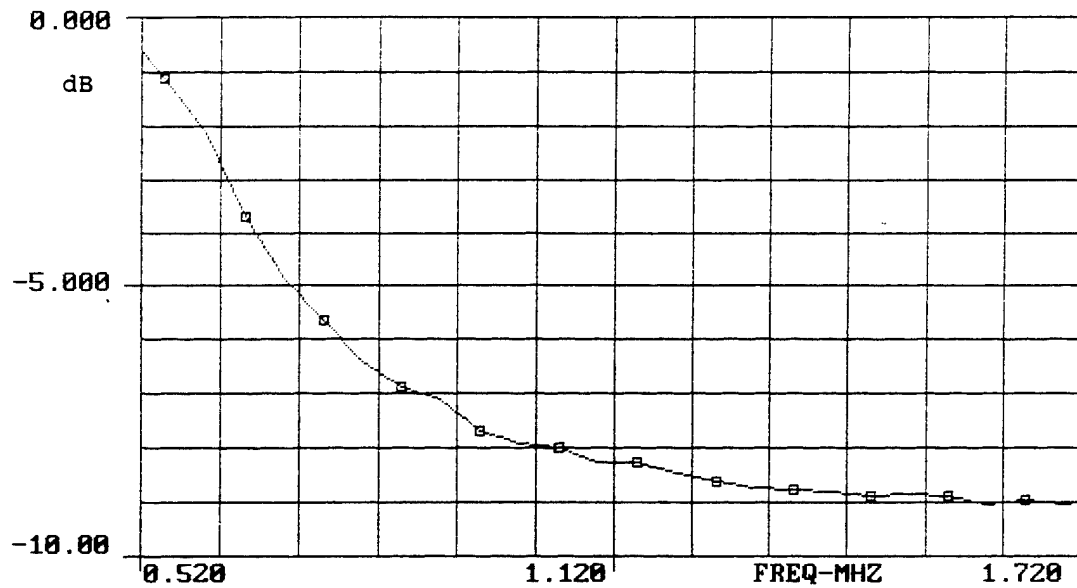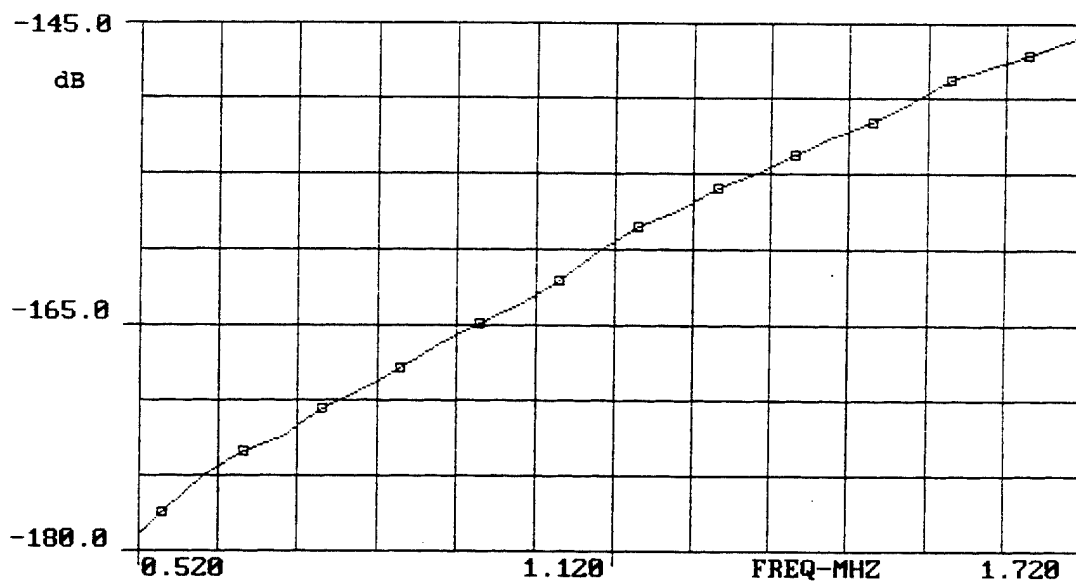
Figure 12. (a) Calculated AM voltage gain from the heater grid to the radio receiver. (b) Calculated AM voltage gain from the FM element to the radio receiver.
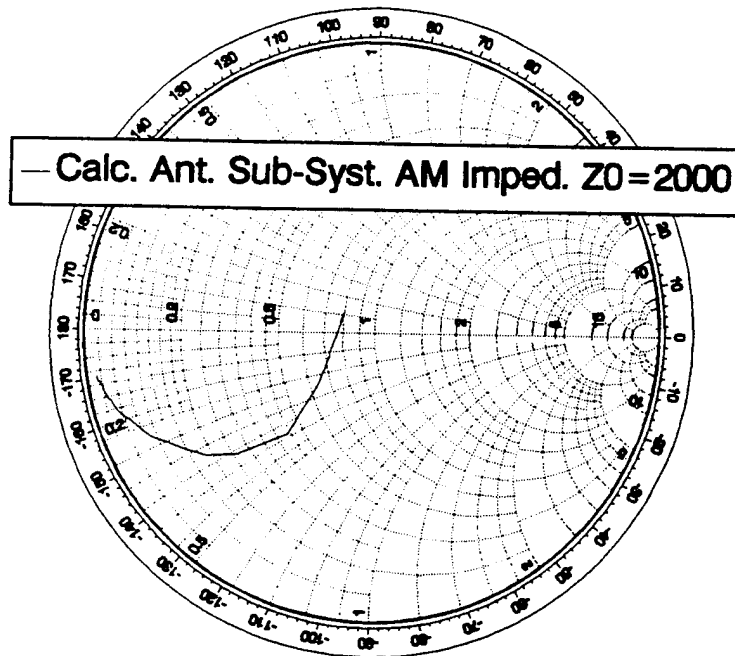
Figure 13. Calculated AM impedance of the concealed antenna sub-system.
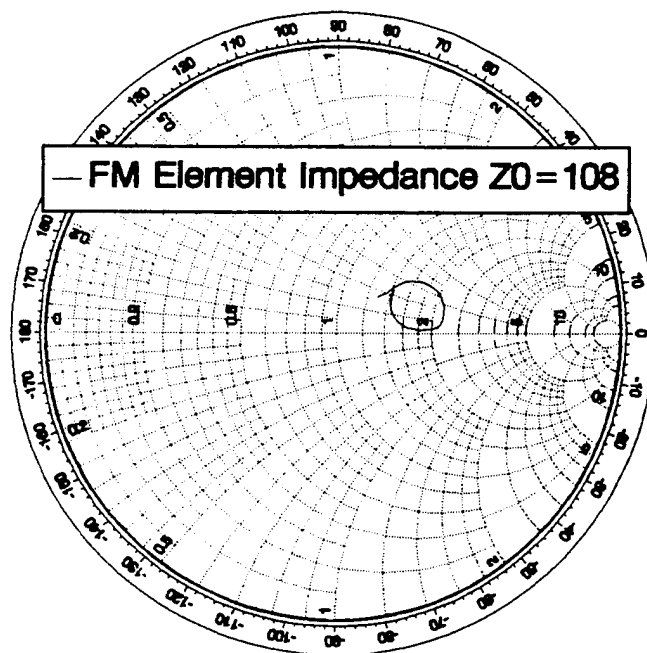
Figure 14. FM impedance of the FM element normalized to 108 ohms.
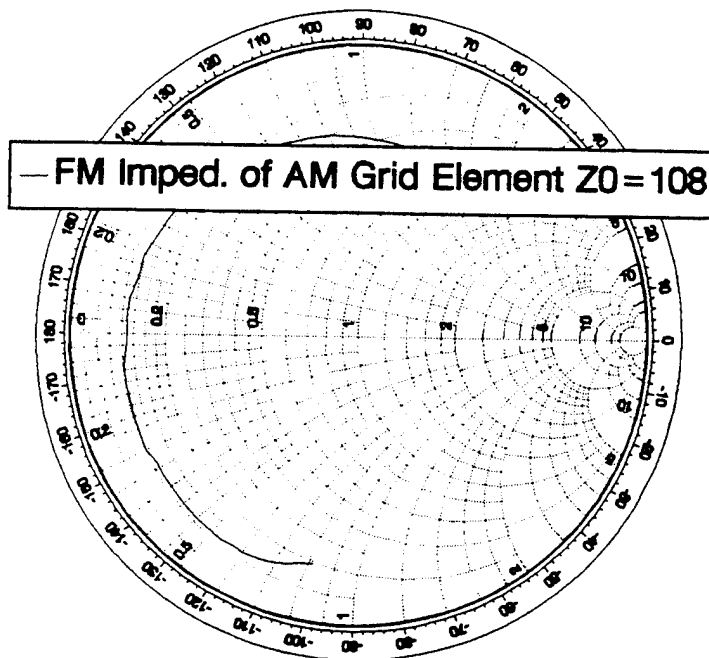
Figure 15. FM impedance of the heater grid normalized to 108 ohms.
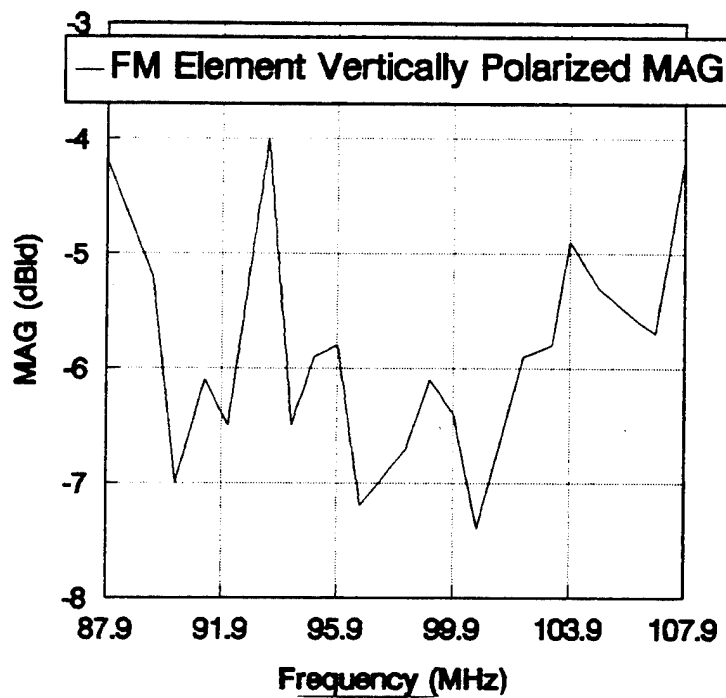
Figure 16. FM MAG of the FM element in the vertical polarization.

58
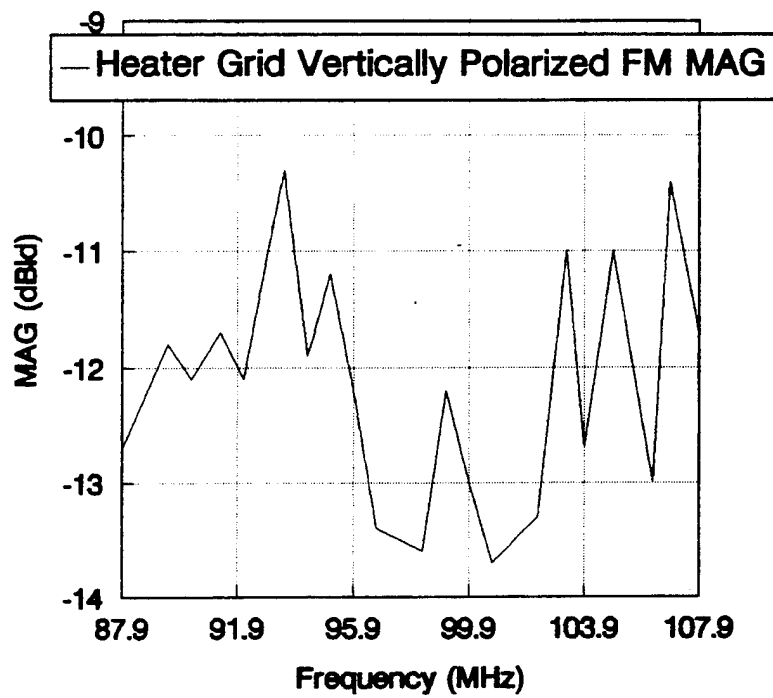
Figure 17. FM MAG of the heater grid in the vertical polarization.

59
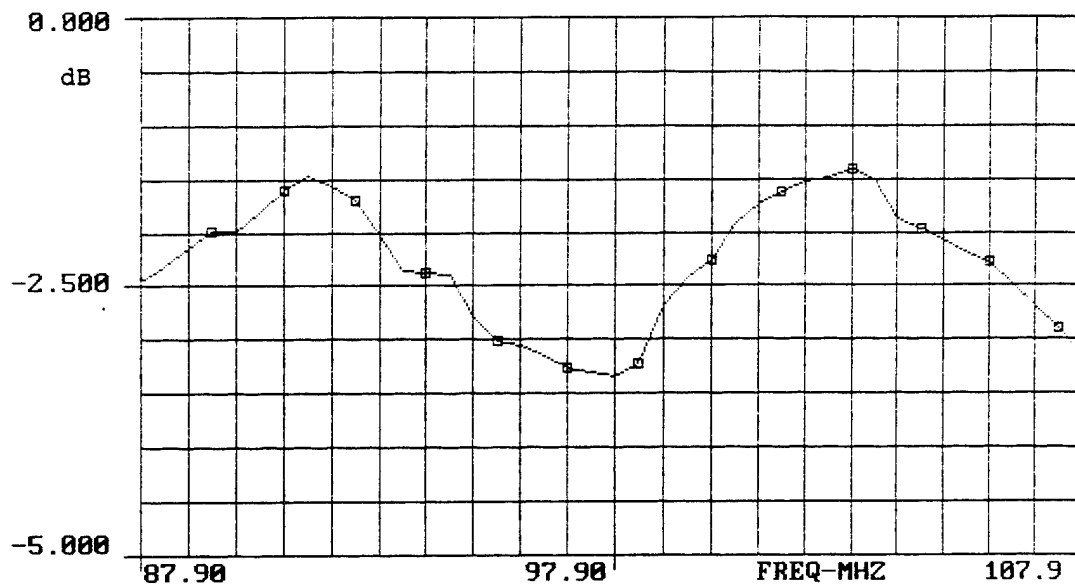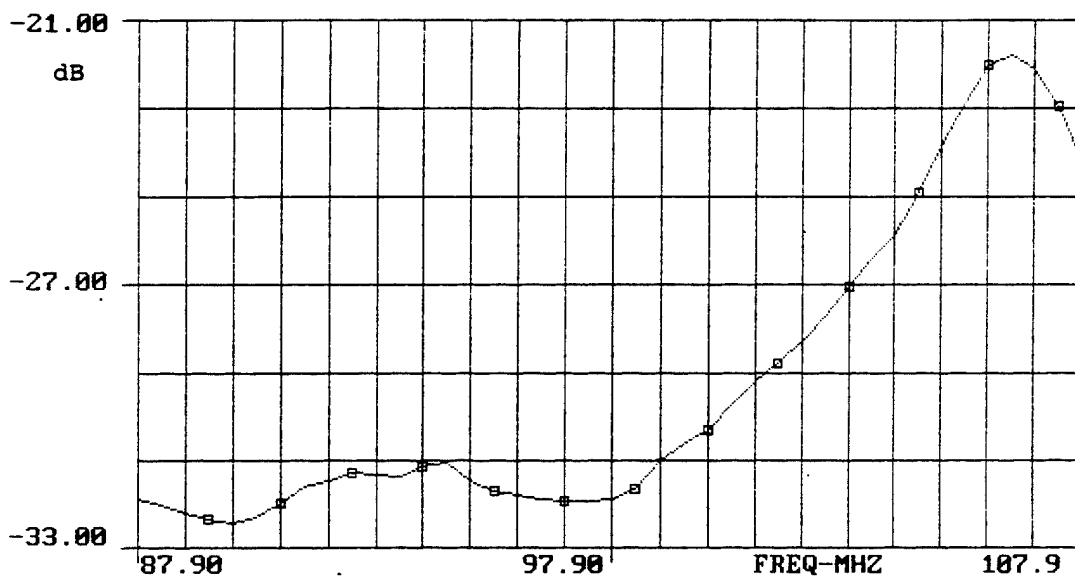
Figure 18. (a) Calculated FM power gain from the FM element to the radio receiver. (b) Calculated FM power gain from the heater grid to the radio receiver.
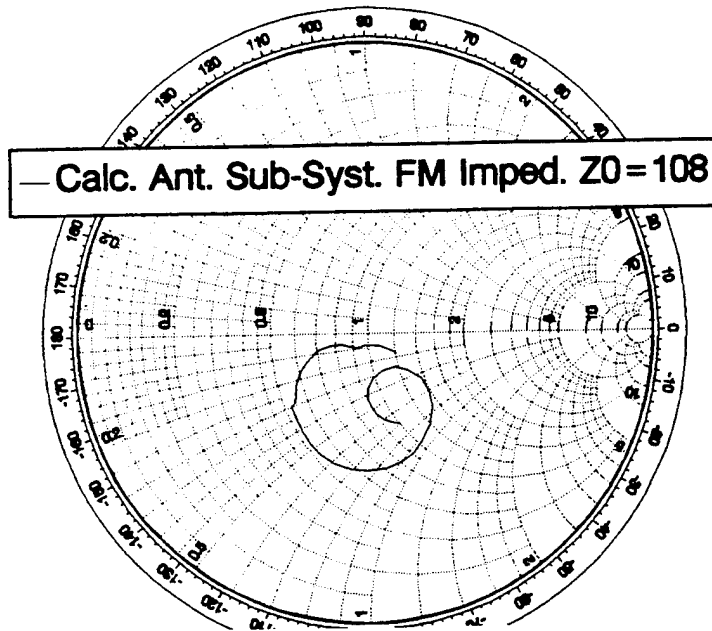
Figure 19. Calculated FM impedance of the concealed antenna sub-system.
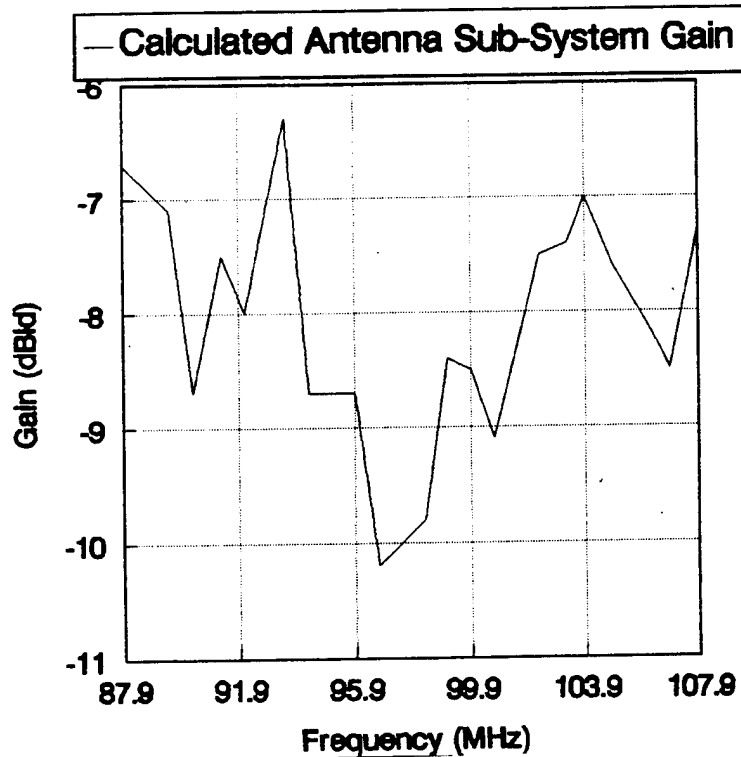
Figure 20. Calculated FM average gain, G_{aREC}, of the concealed antenna sub-system with the radio receiver load.

61
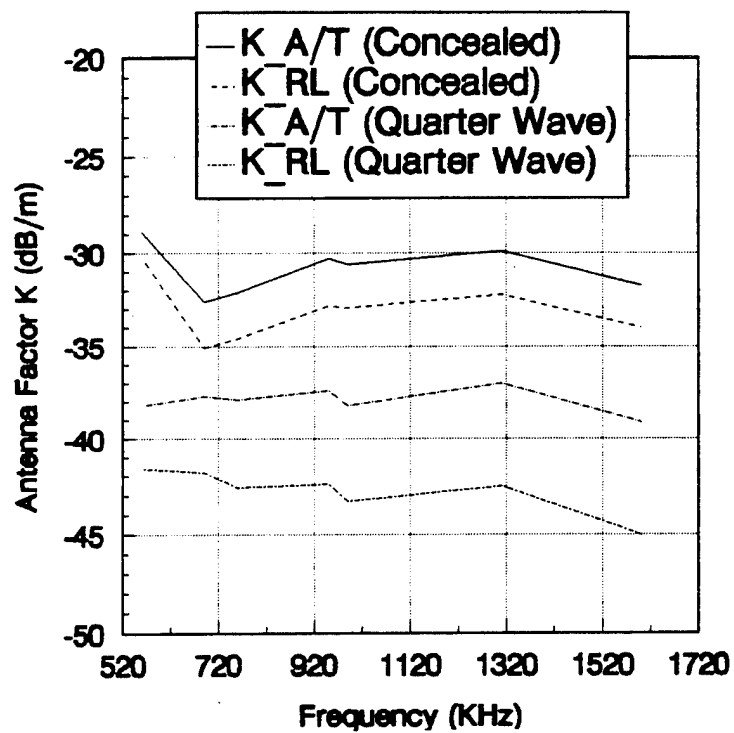
Figure 21. $K_{A/T}$ and K_{RL} for the concealed and quarter wave mast antenna sub-systems.
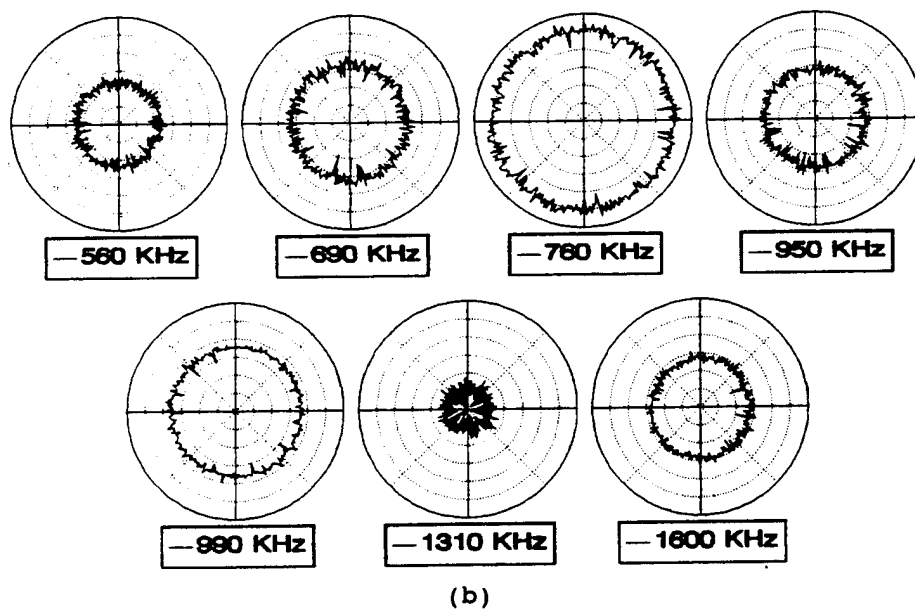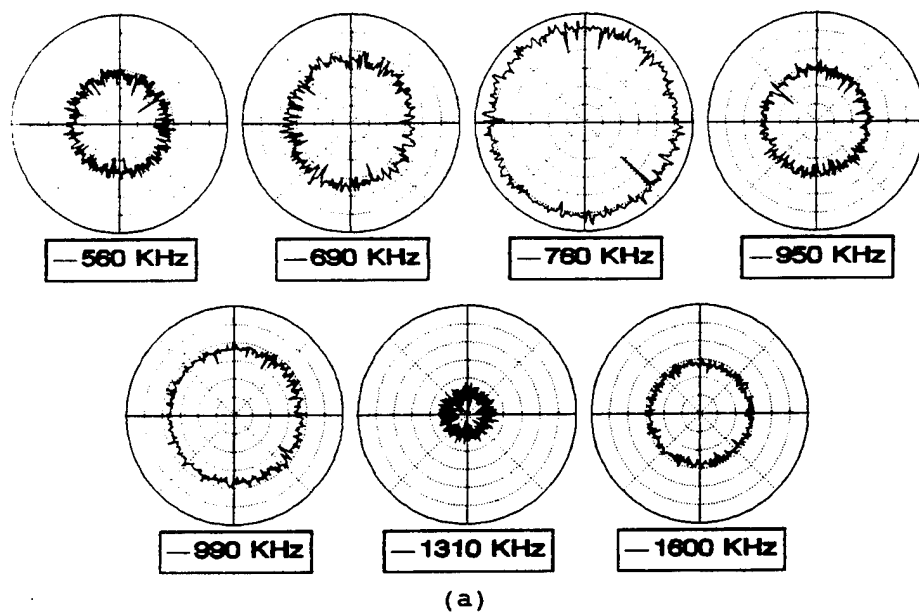
Figure 22. (a) Vertically polarized AM antenna patterns for the concealed antenna sub-system. (b) Vertically polarized AM antenna patterns for the quarter wave mast antenna sub-system. (10dB per division)
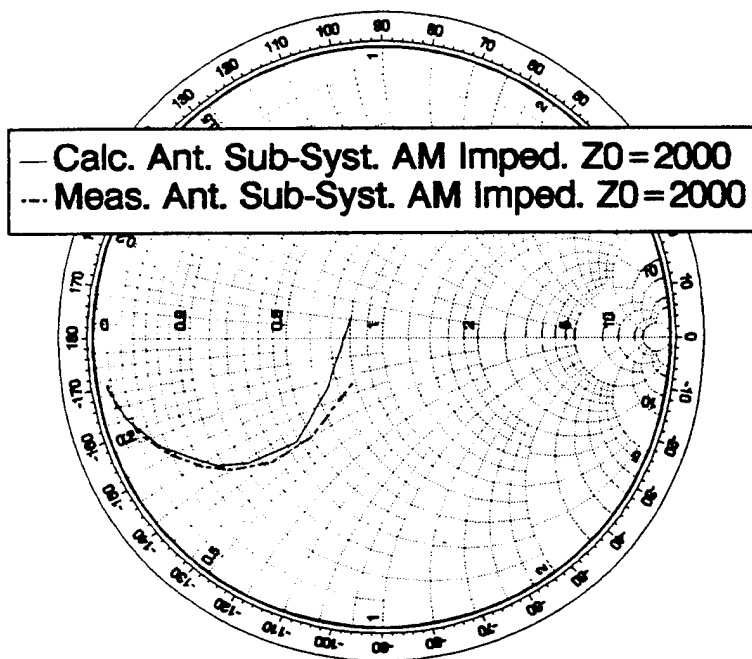
Figure 23. Calculated and measured AM impedance of the concealed antenna sub-system normalized to 2000 ohms.

(a)

(b)
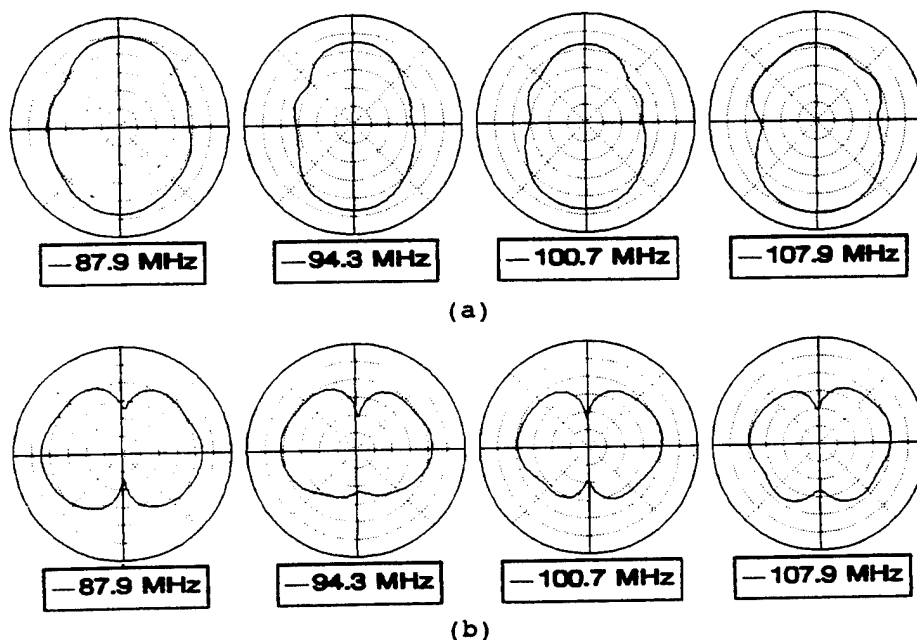
Figure 24. (a) Vertically polarized FM antenna patterns of the concealed antenna sub-system. (b) Horizontally polarized FM antenna patterns of the concealed antenna sub-system. (10dB per division)
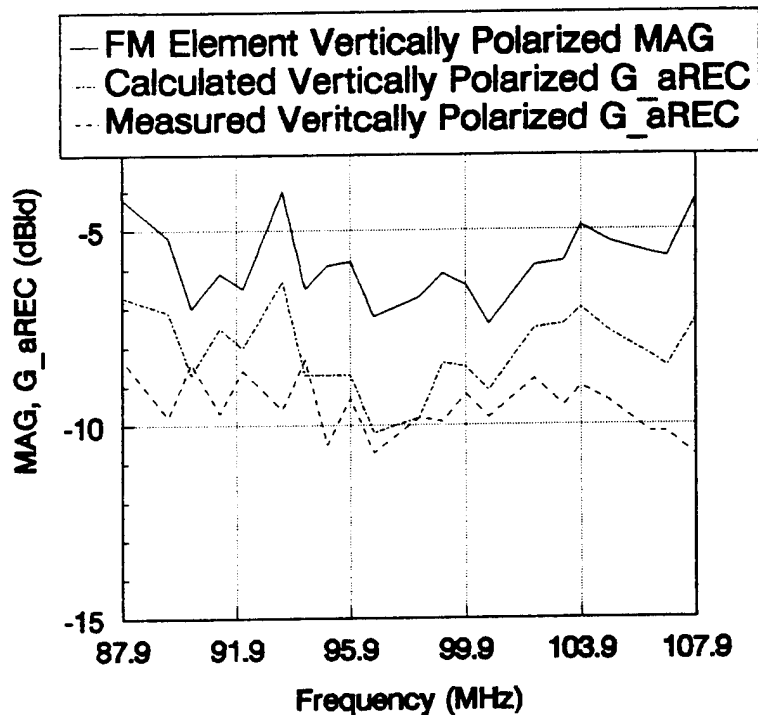
Figure 25. FM MAG of the FM element, calculated FM average gain, G_{aREC}, of the concealed antenna sub-system with the radio receiver load, and the measured average gain, G_{aREC}, of the concealed antenna sub-system with the radio receiver load, all for the vertical polarization.
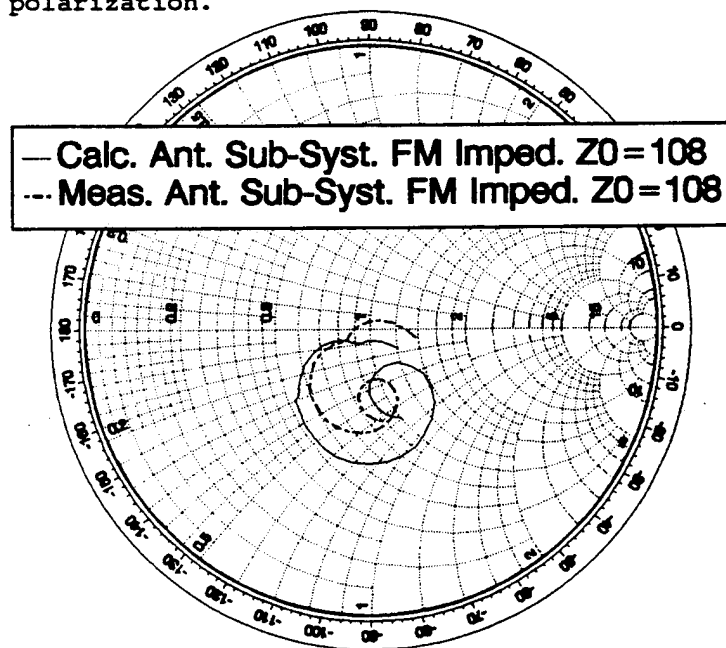
Figure 26. Calculated and measured FM impedance of the concealed antenna sub-system.

A CROSSED-SLOT ANTENNA WITH AN INFINITE BALUN FEED

Dean A. Paschen, Steven C. Olson
Ball Telecommunication Products Division
Broomfield, CO 80038
and
Michel W. Schnetzer
Qualcomm, Inc.
San Diego, CA 92121

ABSTRACT

Microstrip patches have been arrayed in configurations that provide the RF characteristics of a crossed-slot antenna. By driving the patches in full phase quadrature (0, 90, 180, and 270 degrees) a circular polarized (CP) antenna pattern is generated. This concept has been known and implemented for several years. However, with the ever increasing costs of materials, labor and processes it is important to minimize costs to compete effectively in the military and commercial market place. One way to help minimize costs is to simplify the design by reducing the number of components and subassemblies and still maintain the required performance.

This paper presents a novel approach in simplifying the design of a CP microstrip crossed-slot antenna by exciting it in phase quadrature using an infinite balun feed approach. CP performance that has been accomplished in the past with bulky, lossy and often expensive feed networks can now be achieved using a simple infinite balun feed. This antenna design enhances the frequency bandwidth of low profile crossed-slot microstrip elements and competes with the low angle field-of-view of higher, more protrusive antenna designs.

1. INTRODUCTION

Modern communication methods have placed special demands on antenna performance. Satellite communications in particular require antennas with reasonably high gain over hemispherical regions. When placed on a mobile platform, these antennas must employ beam steering, either mechanical or electronic, to maintain the satellite link. Such beam steering is quite expensive to implement. If data rates are allowed to decrease, a broad beam antenna element can be employed. This eliminates the need for beam steering, thus reducing the user terminal cost. This antenna development stemmed from just such a requirement. This paper will cover prior art, improvements allowed by the featured design, and measured data from production units.

2. BROAD COVERAGE CIRCULAR POLARIZATION ANTENNAS

Roughly 30 years ago at the start of the satellite communications era, requirements for wide beam antennas became increasingly apparent. Early satellites were low-earth-orbiters (LEO's), and tracking of the satellite path as it traced the sky proved difficult for many users. Mobile platforms further complicated the problem. By employing broad beam antennas, the communication link could be maintained as the satellite flew overhead, without knowledge of the satellite position or the user's orientation. Geosynchronous earth orbit (GEO's) satellites eliminated the need for

broad beams for fixed installations, but such antennas were still required for mobile users.

Broad beam antennas for satellite communications are typically circularly polarized. At VHF/UHF frequencies, Faraday rotation creates alignment problems when linear polarization is used. Additionally, geometric transformation creates problems for LEO systems or GEO users near the equator. Some of the circularly polarized antennas used include the quadrifilar helix [1], crossed drooping dipoles [1], and crossed slots [2,3,4]. One original feed mechanism for the crossed slot is shown in Figure 1. Impedance matching requirements led to greater use of the feed arrangement shown in Figure 2.

3. MICROSTRIP CROSSED SLOT ANTENNAS

Crossed-slot antennas provide excellent wide angle circular polarization. Low profile crossed-slot antennas can be much thinner than either the quadrifilar helix or the crossed drooping dipole antennas, which is valuable on airframes or other installations where the benefits of reduced volume are typically desired. Conventional crossed-slot antennas used a conductive cavity to contain the parallel-plate modes used to excite the slot radiation. Several drawbacks presented themselves with this type of construction. In order to achieve resonance, the slot

length is required to be half-wavelength in the dielectric. This placed a minimum on the size of the radiating element, and as a result, the beamwidth of the pattern. The beamwidth could be broadened by increasing the dielectric constant, but this increased the Q of the cavity, reducing the impedance bandwidth. Also, dielectric loading increased the cost of the element due to the use of more expensive materials. Construction of the conductive cavity also proved costly. Stripline implementations using mode suppression screws, eyelets, or vias to form the conductive cavity were employed to improve construction yield.

In an effort to eliminate many of the inherent disadvantages of the conventional crossed-slot implementations, work began on microstrip versions of widebeam circular polarization antennas. One of the first microstrip crossed-slot antennas is shown in Figure 3 [5]. The antenna consists of four quarter-wave microstrip patches arrayed in a turnstile fashion. The patches are then fed in phase quadrature. This antenna used the more complex arrangement of Figure 2 to feed the patches in a very conventional manner for microstrip elements.

4. IMPROVED MICROSTRIP CROSSED-SLOT WITH INFINITE BALUN FEED

Evaluation of the microstrip crossed-slot showed that an infinite balun could be used to reduce the complexity of the feed network. The concept of the infinite balun is not new, having been used for spiral antennas [6], but this is the first known application to the microstrip crossed-slot. A microstrip line implementation of the infinite balun for single linear polarization is shown in Figure 4. The transition from the unbalanced line to the balanced patch configuration excites the 'patch pair' 180 degrees out of phase. The orientation of the patches results in constructive combination of a hemispherical pattern broadside to the element. This feed configuration is repeated for the perpendicular 'patch pair', giving dual linear polarization. These two modes can then be fed with a simple 90 degree hybrid to achieve circular polarization. Feeding the element in this manner results in fewer components, lower parts count, and lower cost. Measured port-to-port isolation for the two linear modes was in excess of 20 dB. A typical input impedance plot of a linear port before the hybrid is shown in Figure 5 and Figure 6 shows the match into the hybrid for the CP mode. Figure 7 shows a typical radiation pattern for the circularly polarized configuration. Note the broad beamwidth and low cross-polarization performance of this antenna. The overall dimensions of this antenna configuration measures 24 x 24 x 2.5 inches.

The microstrip implementation of the infinite balun has the further advantage that broadbanding methods can be incorporated directly into the feed circuit. By controlling the width of the feeding line a second order resonance was achieved, increasing the impedance bandwidth. For an air-loaded element .05λ thick, a bandwidth of 30% was achieved (2:1 VSWR). This was measured for both the dual linear mode and the CP mode.

As stated previously, one disadvantage of the conventional crossed-slot is the need for the λ/2 slot length. By reducing the width of the quarter-wave patches they can be placed closer together resulting in a much smaller package. This configuration is illustrated in Figure 8. The loss in bandwidth as a result of decreased patch width can be recovered by increasing the thickness of the patches. Radiation patterns of this reduced size element are given in Figure 9. The patterns are of an isolated element, without any additional ground plane. The axial ratio was less than 2 dB across the UHF SATCOM band.

5. CONCLUSION

This paper has presented a new implementation of a microstrip crossed-slot antenna that results in lower overall costs. The integration of broadbanding

techniques results in performance exceeding that of other similar function antennas including drooping dipoles, cavity-backed slots, and spirals. The antenna has been applied to many applications, including vehicular, aircraft, and manpack versions. The cost savings realized through the new feed method has allowed the design to penetrate new markets quickly and effectively.

REFERENCES

[1] H. A. Haddad, D. A. Paschen, and B. V. Pieper, "Land Vehicle Antennas for Satellite Mobile Communications", IEEE Global Telecommunications Conference, GLOBECOM '85, New Orleans, pp. 1172-1175, 1985.

[2] C. A. Lindberg, "A Shallow-Cavity UHF Crossed-Slot Antenna", *IEEE Transactions on Antennas and Propagation*, vol. AP-17, no. 5, pp. 558-563, 1969.

[3] H. E. King and J. L. Wong, "A Shallow Ridged-Cavity Crossed-Slot Antenna for the 240-400 MHz Frequency Range", *IEEE Transactions on Antennas and Propagation*, vol. AP-23, no. 5, pp. 687-689, 1975.

[4] R. C. Johnson, *Antenna Engineering Handbook*, 3rd Edition, pp. 8.9-8.10, McGraw Hill, 1993.

[5] G. G. Sanford and L. Klein, "Recent developments in the design of conformal microstrip phased arrays", *IEE Conference on Maritime and Aeronautical Satellites for Communication and Navigation*, IEE Conf. Publ pp. 126-129, 1979.

[6] R. C. Johnson and H. Jasik, *Antenna Engineering Handbook*, 2nd Edition, p. 14-9, McGraw-Hill, 1984.
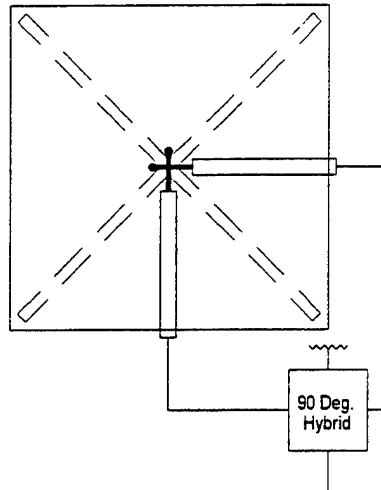
Figure 1. Early low profile crossed-slot antenna uses crossed coax feed arrangement.
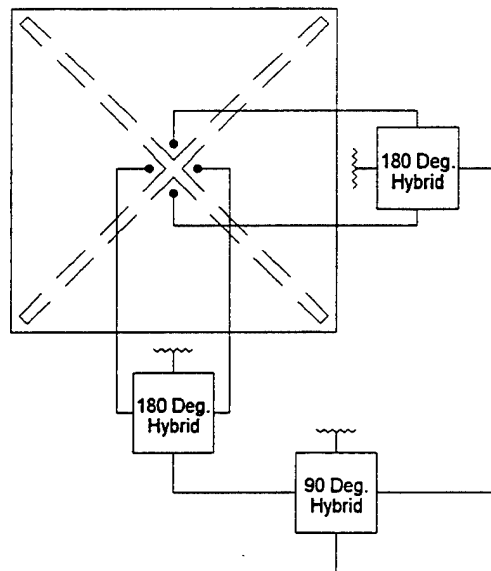
Figure 2. Feed complexity is increased to allow for integration of matching networks.
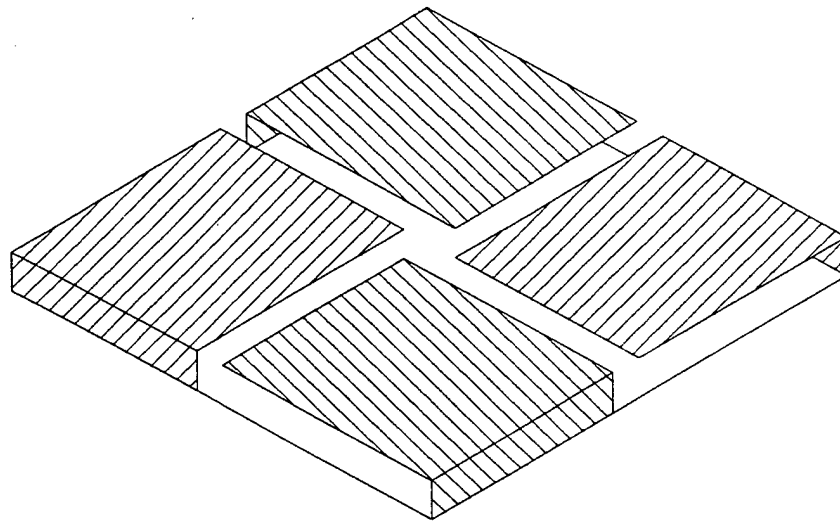
Figure 3. Microstrip crossed-slot antenna uses four quarter-wave elements.

Feed for single linear polarization
Groundplane
Infinite balun
Quarter-wave 'patch pair'
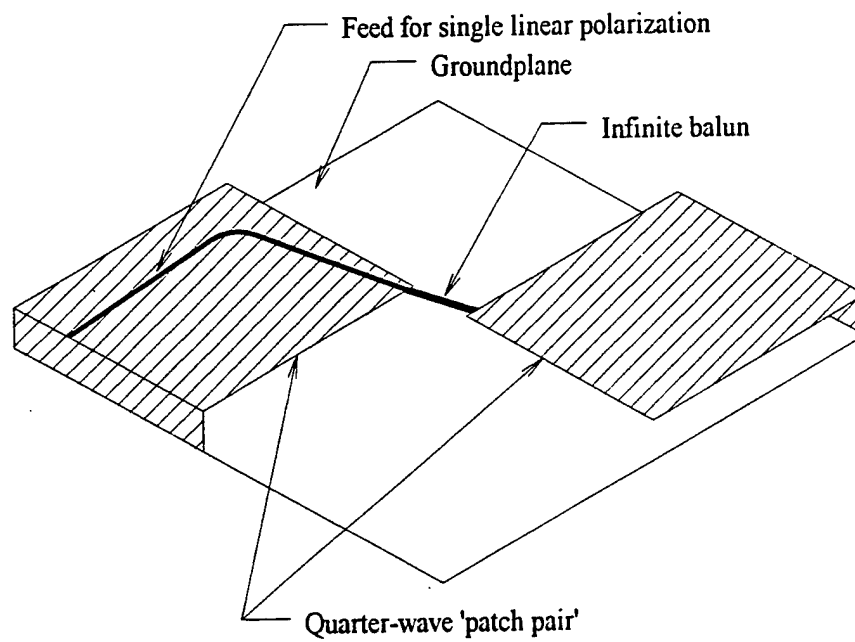
Figure 4. Balun feed is shown for single linear polarization of 'patch pair'.
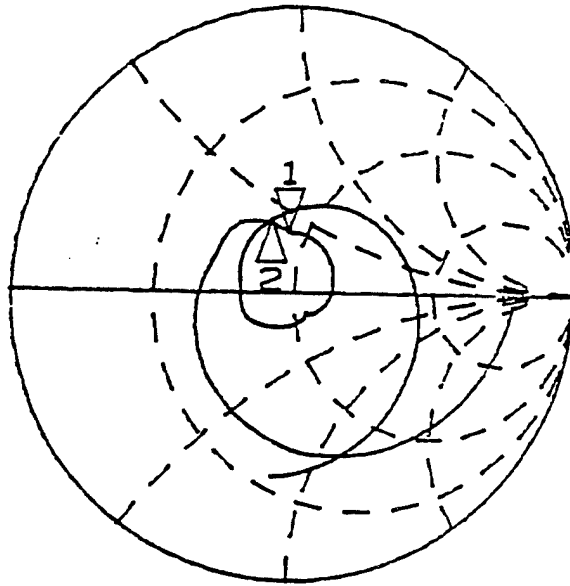
Figure 5. Typical input impedance of linear polarized 'patch pair'.
(Markers 1 and 2 are 240 and 318 MHz, respectively)
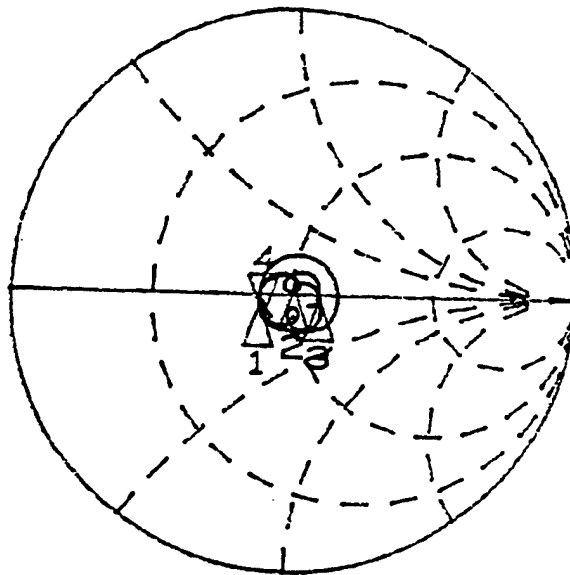
Figure 6. Typical input impedance of CP mode through 90 degree hybrid.
(Markers 1 and 4 are 240 and 318 MHz, respectively)
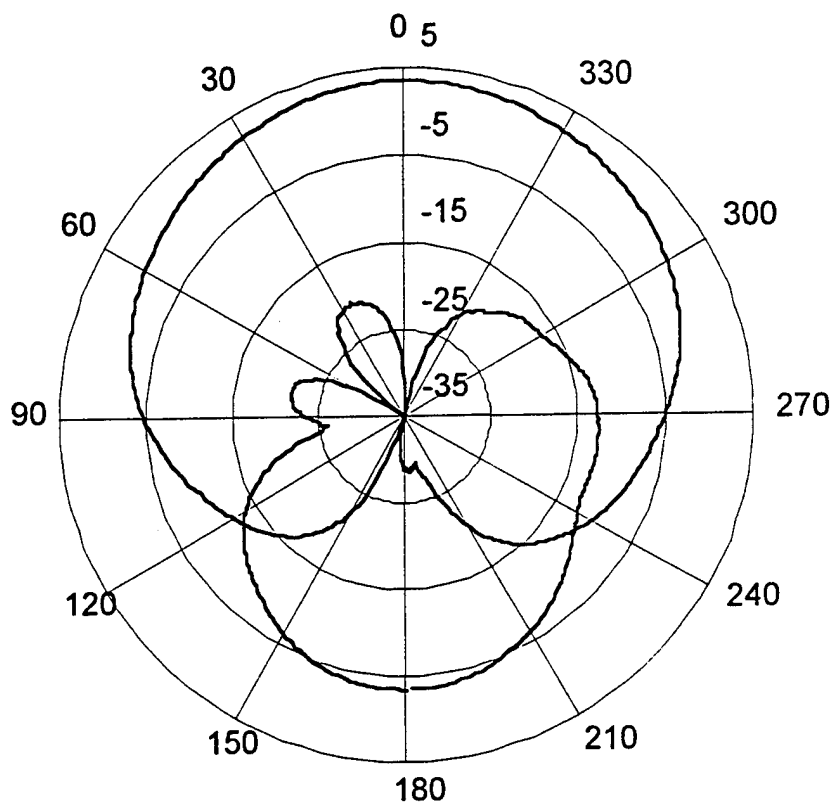
Figure 7. Typical radiation pattern of 24 x 24 x 2.5 inch μ-strip cross-slot element shows broad beamwidth (260 MHz).
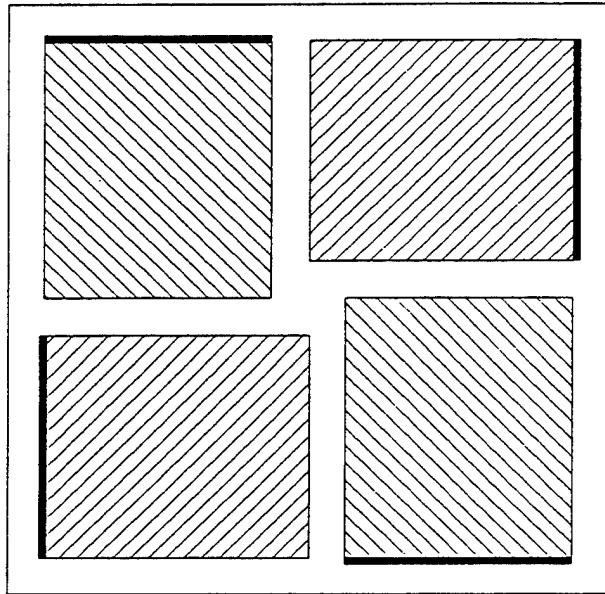
(24 x 24 x 2.5 inch configuration)
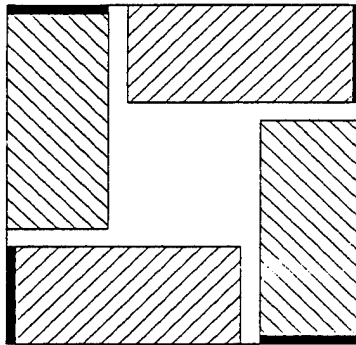
(14 x 14 x 3.25 inch configuration)

Figure 8. Sketches show comparison of 24 and 14 inch configurations for same frequency of operation.
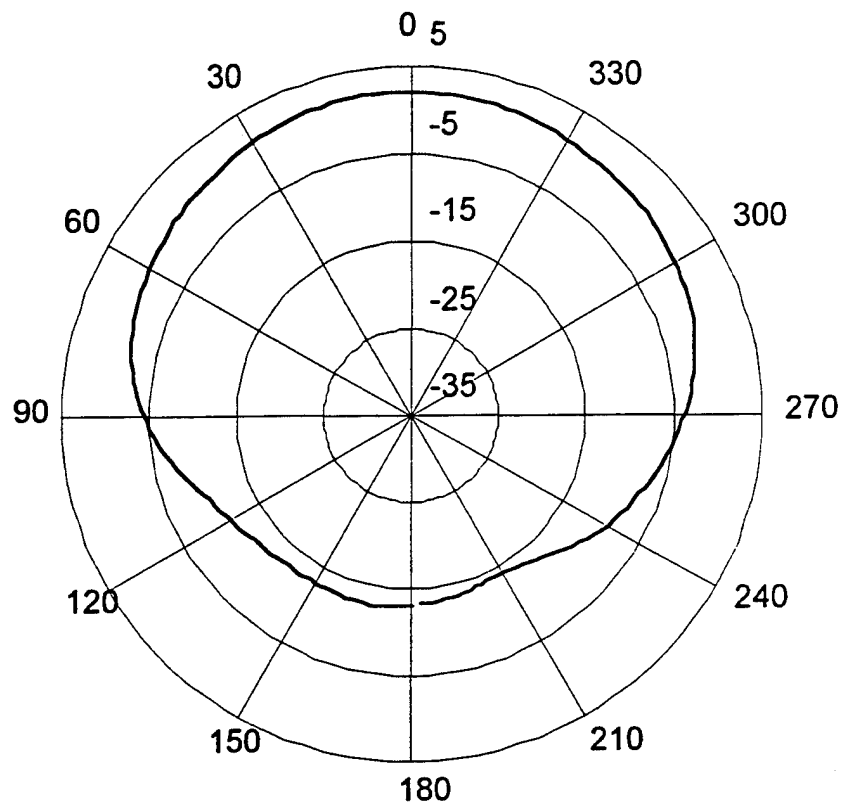
Figure 9. Typical radiation pattern of 14 x 14 x 3.25 inch μ-strip cross-slot element shows broad beamwidth performance (270 MHz).

DUAL BAND TWIST REFLECTOR SEEKER ANTENNA

J. Lane and R. Kliger
Raytheon Electronic Systems
50 Apple Hill Drive
Tewksbury, Massachusetts 01876

Abstract: A prototype monopulse antenna has been developed for a missile seeker application. The design uses a prime focus parabolic reflector with a dual band twist reflector. The antenna operates at both X- and Ka-Band.

The twist reflector seeker antenna concept has some attractive features as compared with other seeker antenna concepts. It has a fixed feed which eliminates the cost and complexity of a rotary joint in an active seeker, the parabolic reflector and all receiver and monopulse circuitry is mounted off gimbal resulting in a low inertia light gimbaled mass. The antenna beam scans at twice the mechanical scan rate of the gimbal. This provides 55 degrees of conical scan coverage for only 27.5 degrees of movement. The concept developed also provides a means to combat the cross polarization jammer using body fixed cross polarized interferometer elements at Ka-band.

1. Introduction

A missile seeker antenna is typically located behind the nose cone, or radome, in the front end of a guided missile. Using monopulse, or some other lobing, the seeker antenna is used to track a given target in angle. The seeker antenna is usually mounted on a two axis "pedestal and gimbal" assembly for mechanical steering. An electromechanical closed loop system drives the antenna to maintain mechanical alignment with the target in two axes, azimuth and elevation.

A prototype monopulse antenna has been developed for a missile seeker application. The design uses a prime focus parabolic reflector with a dual band twist reflector. The antenna operates at both X- and Ka-band.

The twist reflector seeker antenna concept has some attractive features as compared with other seeker antenna concepts. It has a fixed feed which eliminates the cost and complexity of a rotary joint in an active seeker, the parabolic reflector and all receiver and monopulse circuitry is mounted off gimbal resulting in a low inertia light gimbaled mass. The antenna beam scans at twice the mechanical scan rate of the gimbal. This provides 55 degrees of conical scan coverage for only 27.5 degrees of movement. The concept developed also provides a means to combat the cross polarization jammer using body fixed cross polarized interferometer elements at Ka-band.

At X-band the antenna is used in the semi-active (receive only) mode, meaning the target is illuminated by a source other than the missile. At Ka-band the antenna operates in the active (transmit and receive) mode, meaning the target is illuminated by an transmitter within the missile itself. There is also a passive interferometer mode at Ka-band which is polarized orthogonal to the primary mode for tracking radiating targets.

The antenna as constituted for this program consists of four main components; a dual band feed / monopulse, a special parabolic reflector called a transreflector, a dual band twist reflector and the interferometer antenna elements. The twist reflector is the only component mounted on gimbal. A block diagram is given in figure 1.

2. Functional Description

A diagram illustrating how the antenna works is shown in figure 2. Described in transmit mode, the antenna functions as follows. The parabolic transreflector is illuminated by a linearly polarized wave front emanating from the dual band feed aperture located at the transreflector focus. Parallel grid lines etched on the transreflector surface are properly spaced to appear opaque to the feed polarization and transparent to the orthogonal polarization. Thus, incident energy from the feed is collimated and reflected back towards the twist reflector. The twist reflector, mounted on a gimbal, reflects the incident wave front with a 90 degree polarization rotation in a desired direction. The energy then passes through the transreflector unimpeded. Note that the direction of reflected energy is at twice the angle of the twist reflector off the forward axis. Tracking is performed using conventional monopulse tracking techniques.

Three interferometer antenna elements and a guard element are positioned at 90 degree intervals around the forward perimeter of the transreflector. The interferometer elements are polarized orthogonal to the main antenna. They are used to track potential cross polarization jammer targets. The guard element, located at missile 0 degrees, is polarized co-linear to the main antenna. It is used to discriminate between targets in the main beam of the antenna versus targets off the main beam.

3. Component Design Summary

The prototype seeker antenna was form factored and packaged to fit within the missile envelope. A summary of the mechanical design and electrical performance of each component in the antenna is given below.

3.1. Antenna & Test Fixture

A photograph of the antenna mounted on the test fixture with the transreflector removed is shown in figure 3. The twist reflector is shown with the feed protruding through its center. The test fixture was a key design tool during the breadboard stage of the antenna development. It simulates the gimbal by providing two axis, azimuth and elevation, motion with a pivot point centered on the twist reflector. This pivot point was specifically chosen to minimize the size of the clearance hole for the feed.

The test fixture provides an axial adjustment for focusing the transreflector relative to the feed. This is achieved with mechanical slides and a micrometer adjustment. The micrometer makes it possible to measure small differences between the X- and Ka-band feed aperture focal points. The feed focus can then be trimmed accordingly. There is also an axial adjustment for positioning the twist reflector relative to the feed. It was confirmed that the position of the twist reflector has only second order effects on the gain and sidelobe performance of the antenna. A position was selected approximately 0.5 inches behind the feed aperture so that no shadowing occurs when gimbaling.

A photograph of the test fixture with the transreflector attached is shown in figure 4. The interferometer and guard antenna elements can been seen mounted on top. A focal ratio was selected to maximize the size of the antenna aperture and to minimize the size of the feed blockage. This design has a 7.384 inch diameter parabola with a 3.0 inch focal point giving an F/D ratio of 0.4.

3.2. Dual Band Feed / Monopulse

The dual band feed / Ka-band monopulse is an integrated waveguide package. It was designed and manufactured by M/A-COM, Inc. of Burlington, MA. A photograph of the unit is shown attached to a test adapter (figure 5).

One of the main goals of the design was to keep the aperture as small as possible. This minimizes the size of the twist reflector cutout required and subsequent blockage effects. The feed shown has four X-Band apertures and four Ka-Band apertures in a 1.0 inch diameter. The Ka-band feed aperture shown, (center portion 'of feed), is fed by four WR-22 rectangular waveguides. The Teflon dielectric window over the feed aperture serves to allow pressurization of the feed for high power transmission at altitude. The X-band aperture consists of four tapered ridged waveguides. Each ridged waveguide "quadrant" is fed by an end launched coaxial to waveguide transition.

The X-band monopulse comparator is built in stripline using four quadrature hybrids. Two layers of 0.031 in. thick Duriod 5880 was used. The unit fits flush against the Ka-band output flange and feeds the four X-band waveguide quadrants

using surface launch connectors and short sections of coaxial line . A cutaway of a portion of the artwork against the Ka-band output flange is shown in figure 6. A calibration port, not shown, provides -30.0 dB of coupling to the four outputs.

The input return loss of the eight ports of the X-band comparator is better than -15.0 dB over the frequency band. The amplitude balance of the four quadrant outputs when feeding the sum or difference output is within 0.5 dB. The insertion loss of the comparator is approximately 0.9 dB. The phase balance of the unit is within 8 degrees. Further fine tuning of the phase and amplitude can be made on a future unit.

3.3. Transreflector

The transreflector is designed to totally reflect the incident feed polarization while passing, with minimal loss, the orthogonal polarization. It must do this equally well at both X- and Ka-band. Total reflection is achieved by a series of closely spaced grid lines placed on the parabolic portion of the transreflector. Energy from the feed polarized parallel to the grid lines is reflected while energy off the transreflector polarized perpendicular to the grid lines is passed with minimal loss. A tradeoff was performed to determine the optimum line width and spacing. Typically a line width to line spacing of 0.5, with the line width being much less than the shortest wavelength, provides very high reflection for parallel incidence and very low loss for perpendicular incidence. A line width of 0.010 inches was used here.

The support for the grid lines must have both very low loss at X- and Ka-band as well as be mechanically sound for a missile environment. This was achieved by using a three layer cross section. The three layers provide the degrees of freedom required to tune the transmission loss at the two operating frequency bands. The core material is a glass reinforced phenolic honeycomb. The laminate skin on each side of the core is composed of two layers of quartz fabric bonded with an epoxy resin. The cross section, shown in figure 7, is both lightweight and very strong. The measured transmission loss of the transreflector at both bands is at or below 0.25 dB. The reflection loss for a co-polarized wave incident on the grid is negligible. Measurements were made on flat test panels using waveguide simulators.

The forward portion of the transreflector is parabolic just as with a conventional reflector antenna. The side walls serve as the support structure for the parabolic portion and for the interferometer cables laminated between the transreflector walls. The side walls are of the same cross section as the parabolic surface. This minimizes amplitude and phase distortion when scanning the antenna. A boresight error (BSE) analysis was done to select the optimum corner radius between the parabolic portion of the transreflector and the side walls for minimizing its effect on electrical performance. A radius which is too large consumes too much of the aperture, a radius which is too small could have an adverse effect on the BSE or sidelobes. Laser etching technology was used to accurately apply the grid pattern to the inside surface of the transreflector.

3.4. Twist reflector

The design goals for the twist reflector were as follows: 1) Minimize the undesired polarization magnitude . This is a measure of how well the twist reflector converts the incident polarization to the orthogonal polarization. This was optimized over both frequency bands and 0 to 27.5 degrees incidence angels. 2) Minimize the dielectric and conductor losses. 3) Minimize the weight (a critical gimbal requirement). 4) Select materials which meet the environmental requirements.

The design is based on a theoretical model developed by Howard and Cross[1]. The theory was modified for modeling flat metallic strips rather than round conductors which make its fabrication amenable to standard etching techniques. Susceptance equations for round wires were replaced with those for flat strips given in Marcuvitz[2]. The theoretical model was quite accurate, however, empirical design methods had to be used to optimize the twist reflector performance. Measurements were made at both frequency bands on test panels using waveguide simulators.

The design is composed of two layers of parallel grid lines each printed on a 0.001 inch thick layer of Kapton substrate material. The grid lines are oriented at 45 degrees to the feed polarization. Each layer is then bonded to a spacer layer of low loss, low dielectric closed cell Rohacell foam. The bond film, KEENE 6250, was chosen for it's excellent electrical properties and because the required bonding temperature is compatible with the Rohacell. A cross section of the design is shown in figure 8. It weighs only 3 ounces. The entire structure is then bonded to a light weight metal support plate.

The measured reflection loss of the twist reflector at both bands is below 0.25 dB. The twist reflector provides a 90 degree polarization rotation with a resultant axial ratio of better than 20.0 db over most of the operating band and incidence angles. The diameter of the twist reflector is 7.7 inches. A 1.54 inch diameter hole is cut in the center to accept the feed and to allow clearance for gimbaling.

3.5. Interferometer and Guard Elements

The AAAM antenna also includes Ka-Band body fixed antenna elements for the interferometer mode and guard channel. The elements are linearly polarized and provide reasonable gain coverage over a full 0 to 55 degree cone centered on missile boresight.

The interferometer and guard antenna elements consist of a rectangular microstrip patch element soldered to a "direct cable attach" connector. This provides an extremely light weight and compact design for mounting on the transreflector. The patch element was etched on 0.020 inch thick Duriod 5880. A feed pin is inserted through the top surface of the patch making contact with spring fingers inside the connector. The polarization of the patch is determined by the feed probe location. The coaxial cables are imbedded between the side walls of the transreflector and the patch elements are held in place with small dielectric supports bonded to the surface of the transreflector (see figure 4).

Antenna pattern measurements versus scan have shown that the interferometers have negligible effect on the main antenna pattern performance.

4. Discussion of Results

The measured pattern performance of the antenna at X- and Ka-band respectively is shown in figures 9 and 10. The efficiency of the antenna including the monopulse comparators is approximately 35% at X-Band and 40% at Ka-Band. There is a further gain reduction of 0.5 dB over the 55.0 degrees of scan. The sum side lobe level varies between 13 and 18 dB depending on the frequency, cut plane and scan angle. The difference sidelobe level varies between 14 and 22 dB.

Several problems were identified with the prototype dual band feed / Ka-Band monopulse unit. At Ka-band the iris used to tune the magic-T junction between the H-plane delta and the delta-delta channel was off. The isolation between these ports is low resulting in a low H-plane difference channel gain as seen in figure 10.

At X-band, the low gain in the H-plane delta pattern can be attributed to mutual coupling between the X-band feed quadrants. The isolation between adjacent co-polarized ports is only 10.0 dB, between diagonal ports it is only 14.0 dB. Between opposite ports the isolation is 20.0 dB. The active VSWR (S11+S12+S13+S14) for the sum and difference channels was calculated for one quadrant of the X-band feed aperture at the low, middle and high end of the frequency band. All four quadrants are approximately equal. The results are summarized in Table I.

TABLE I: ACTIVE VSWR VERSUS FREQUENCY AND CHANNEL OF THE X-BAND FEED APERTURE			
	Low	Middle	High
Sum	1.8:1	1.4:1	2.2:1
E-Plane Delta	1.5:1	2.0:1	1.5:1
H-Plane Delta	5.2:1	3.8:1	4.8:1

Although the input match of the individual ports with the others terminated in 50 ohm loads is quite good (1.2:1 or better) the active impedance as seen by the H-plane difference channel of the X-Band comparator is not good causing the low gain.

The cross polarization of the antenna is generally better than 25 dB over all frequencies and scan angles. The null depth is also generally better than 25 dB.

5. Recommendations for Improvement

Eliminate the mutual coupling problem of the X-band feed aperture. A second source for the breadboard feed used dielectric loading in place of ridge loaded guide. That feed, which had a slightly larger aperture, did not have the problem with mutual coupling.

Correct the isolation problem in the Ka-band magic-T junction.

Investigate alternate feed apertures for improving feed illumination efficiency.

Use suspended stripline for the X-Band comparator to reduce the insertion loss.

6. Summary

A prototype dual band twist reflector seeker antenna with body fixed interferometer elements was successfully built and tested. The gain and pattern performance of the antenna at each frequency band is comparable to a conventional prime focus reflector of similar aperture size. The performance versus scan of the antenna and the polarization purity, both concerns early in the program, has been shown to be excellent.

In summary, the twist reflector antenna concept demonstrated can provide an effective approach to the multi-mode monopulse seeker.

7. Acknowledgments

8. References

[1] D. Howard and D. Cross, "Mirror Antenna Dual Band Lightweight Mirror Design," IEEE Transactions on A and P, vol. AP-33, N0. 3, March 1985.

Correction to reference. Equation 17 should read:

$$P = 1 + \frac{Y - Y}{1 - Y\,Y}$$

[2] N. Marcuvitz, "Waveguide Handbook," McGraw Hill Book Company, Inc. 1951. Section 5-19, page 284.
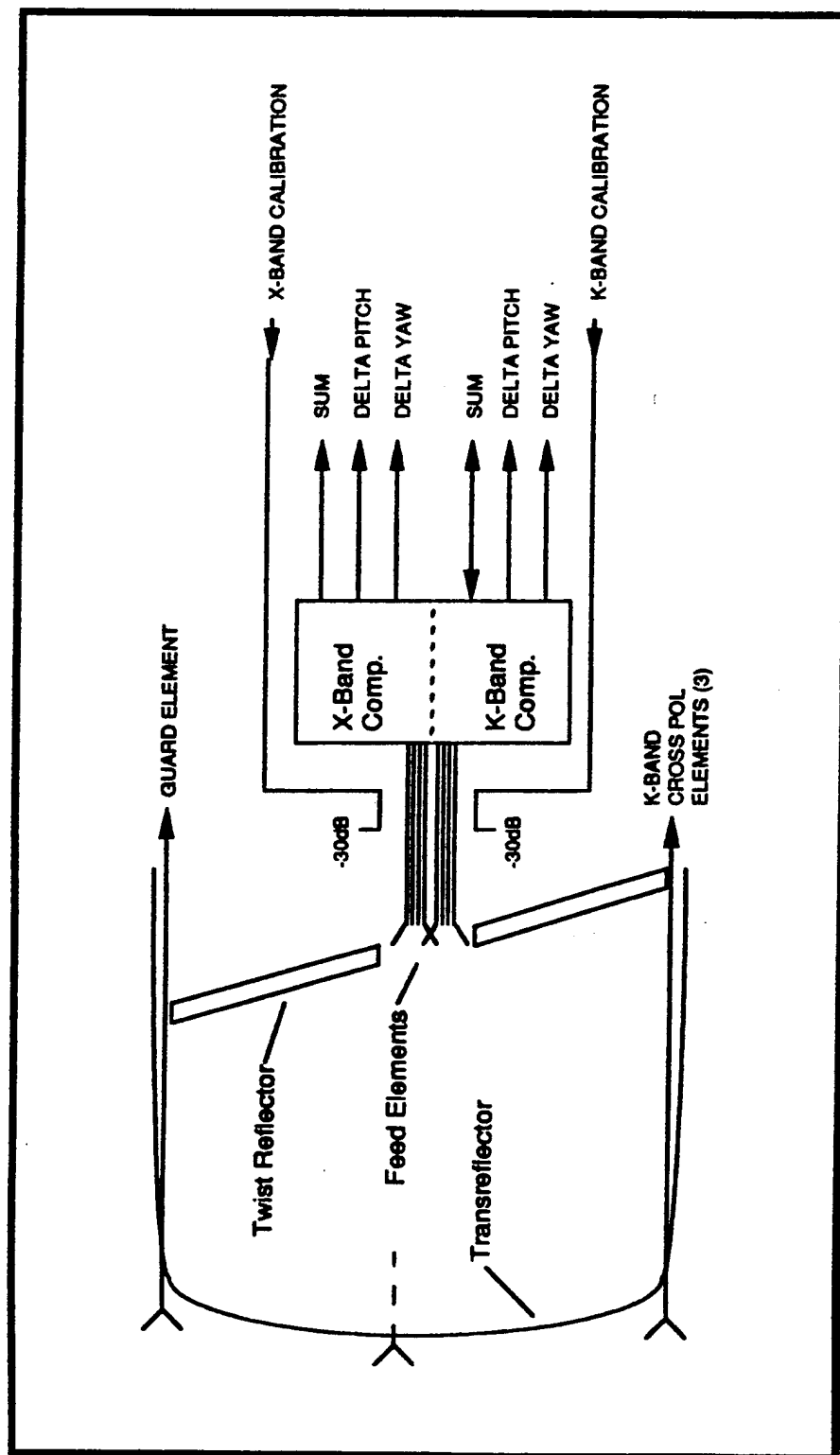
Figure 1 Twist Reflector Antenna Concept
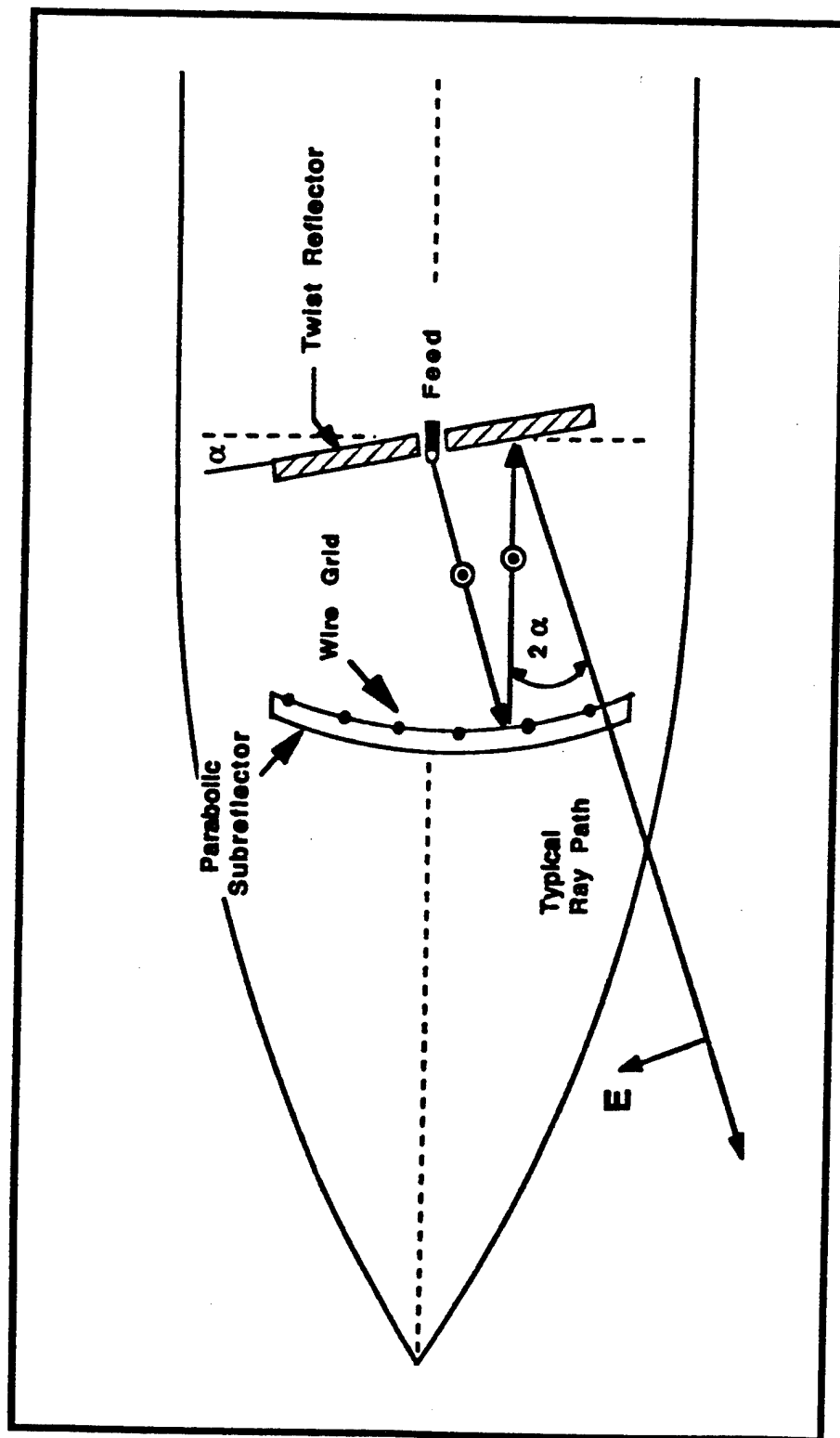
Figure 2 Twist Reflector Seeker Antenna
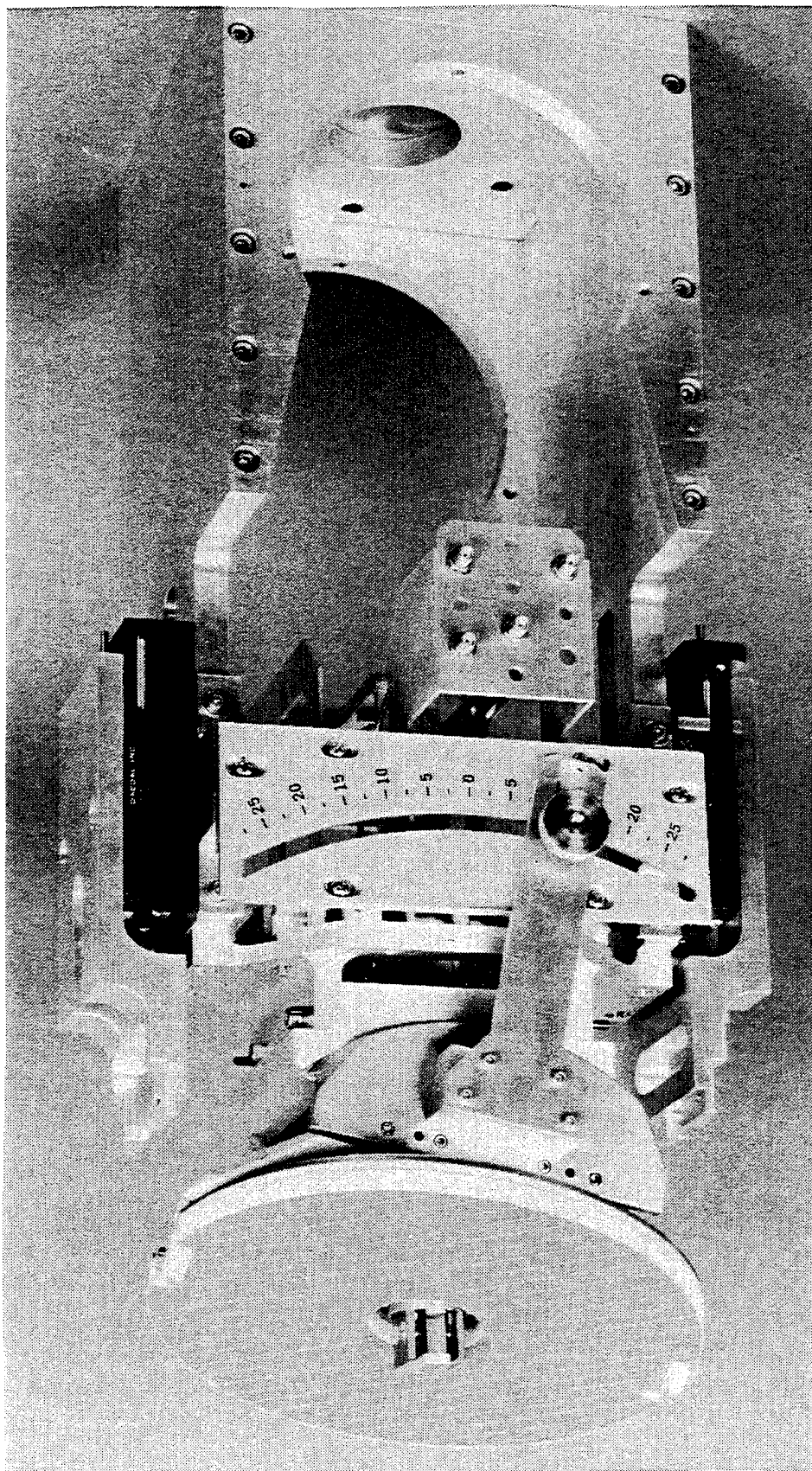
Figure 3 Feed and Twist Reflector Subassembly

95
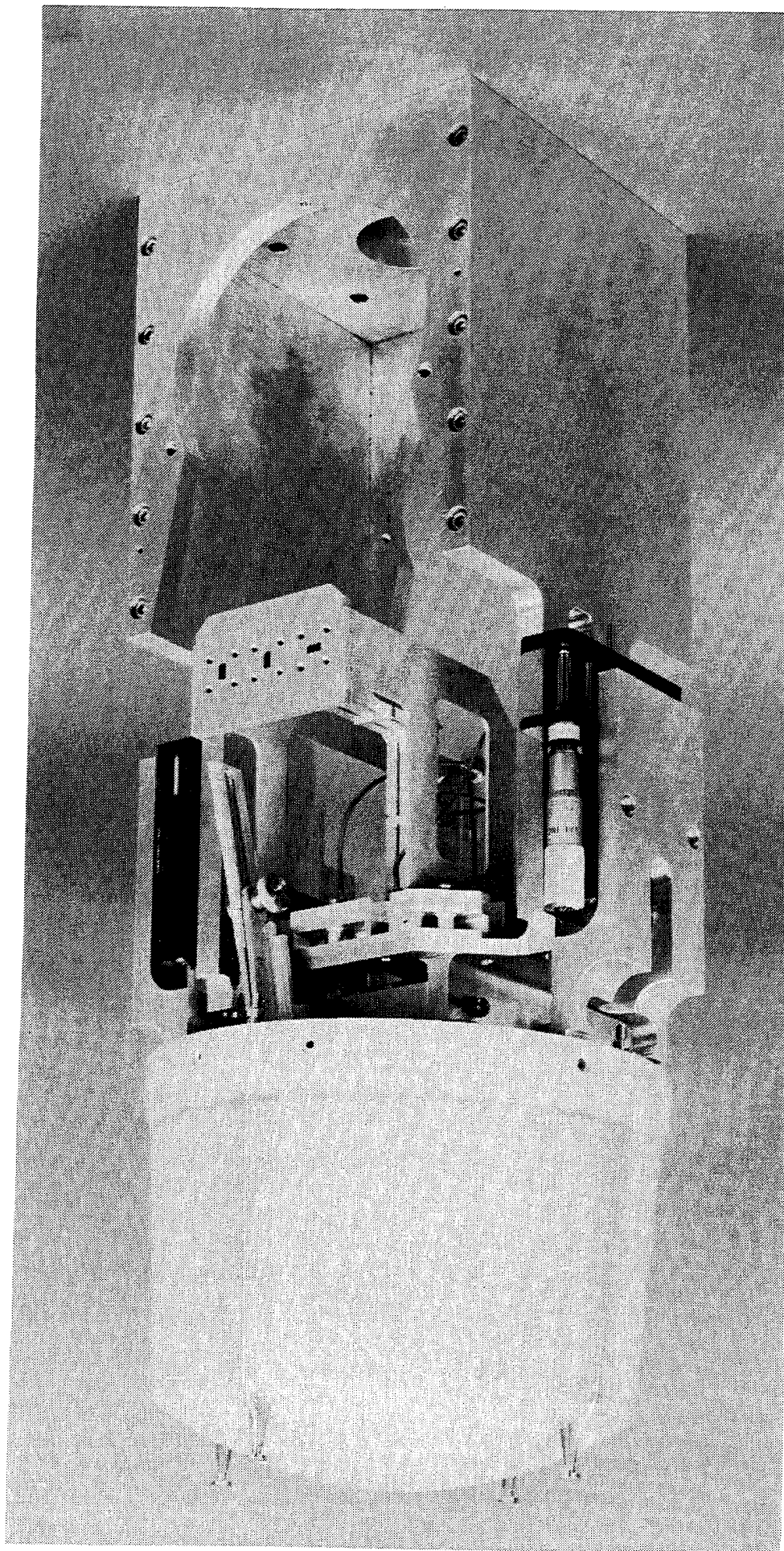
Figure 4 Antenna and Two-axis Test Positioner
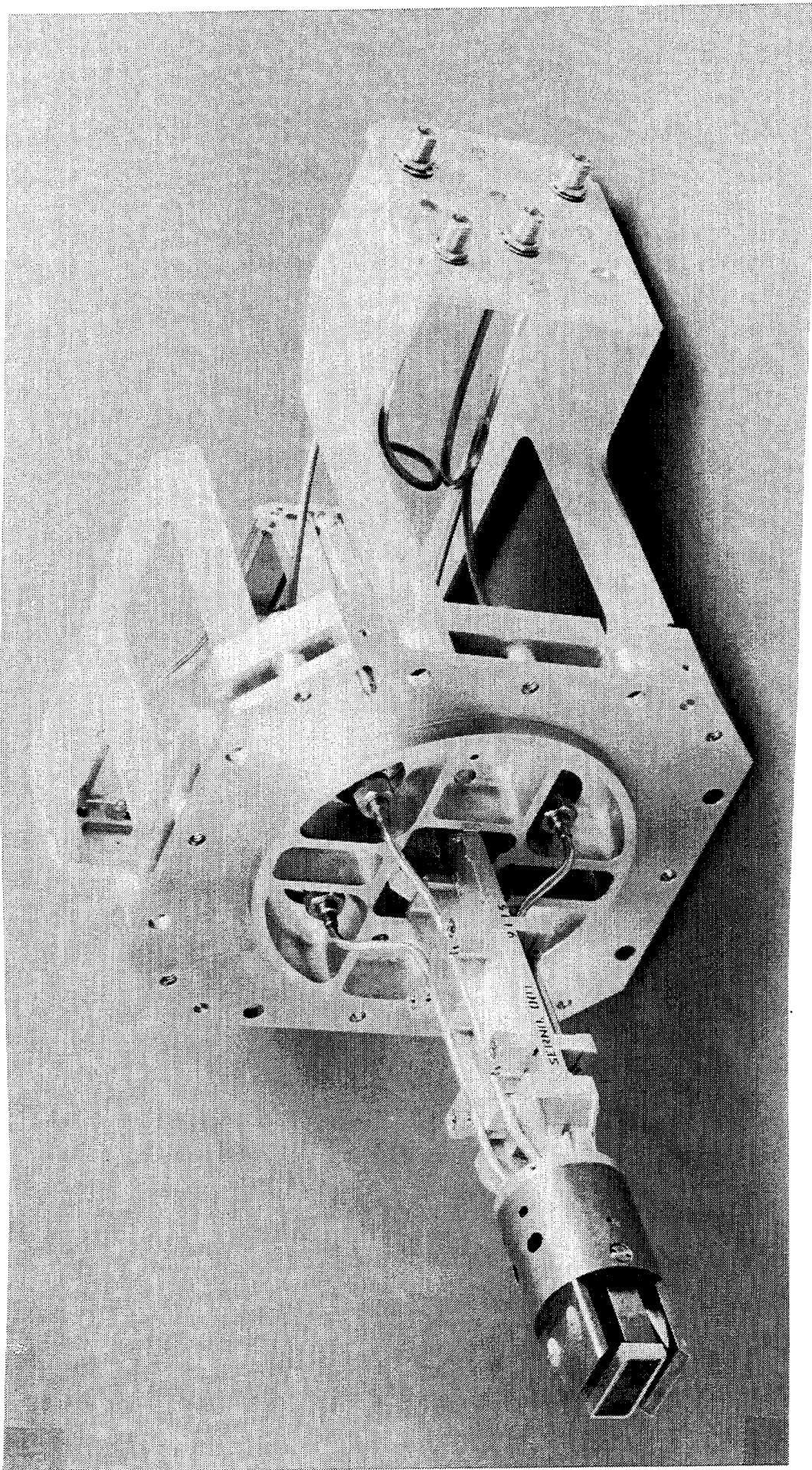
Figure 5 Feed and Monopulse Detail

97
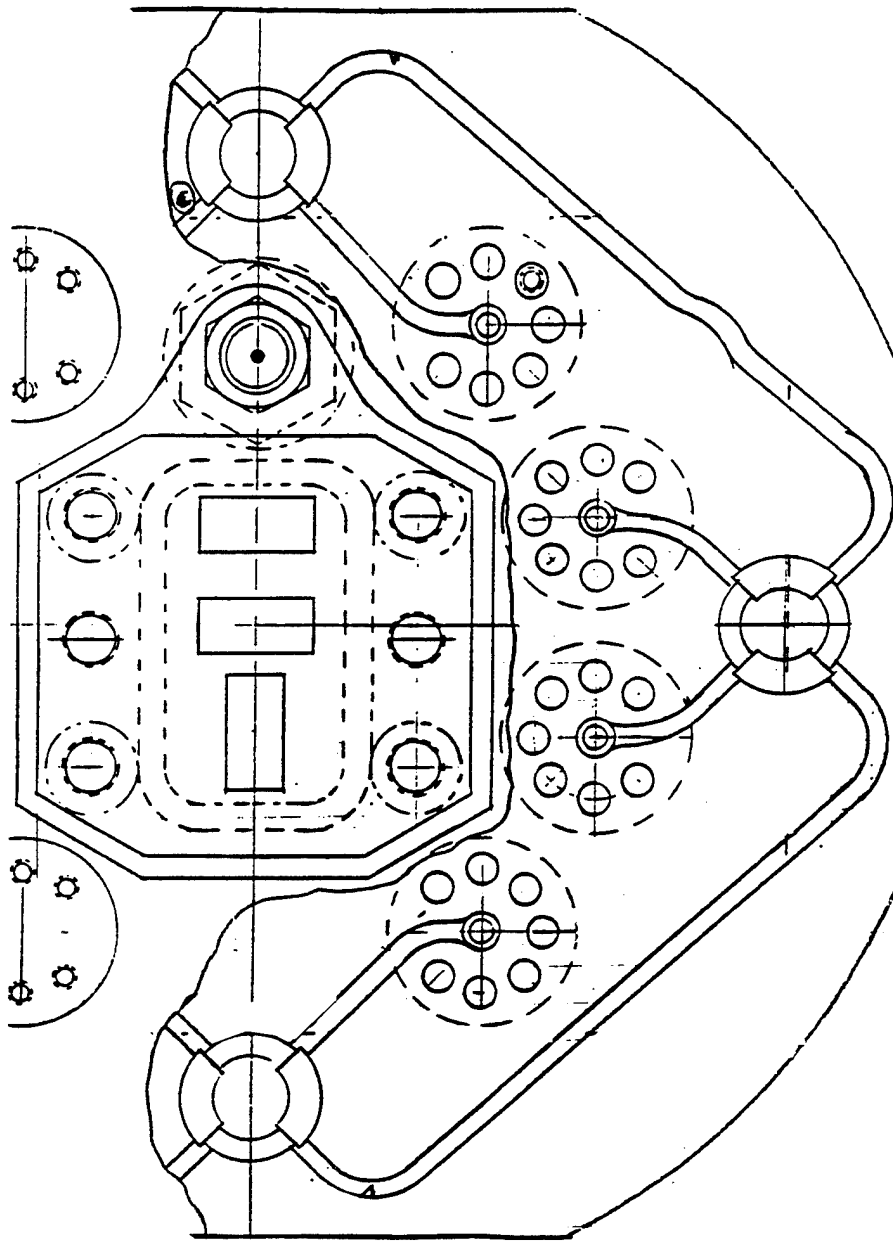
Figure 6 X-Band Monopulse Comparator

"A-Sandwich" Construction

Conducting Grid — 1 Mil
0.010 In.
Quartz Fiber Epoxy Resin — Thin Layer
Adhesive
Phenolic Honeycomb — 0.070 In.
Thin Layer
Quartz Fiber Epoxy Resin — 0.010 In
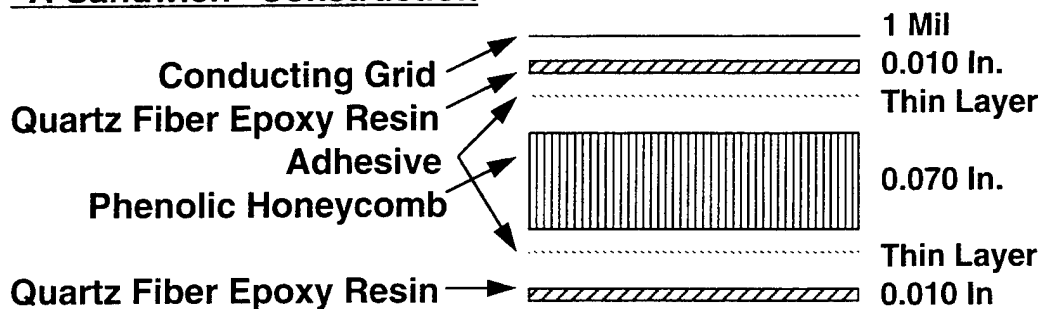
Figure 7 Transreflector Cross Section

Two Layer Grid Structure

Conducting Grid on Kapton — 2 Mil
1 Mil
Adhesive
Closed Cell Rohacell Foam — 0.032 In.
Adhesive
Conducting Grid on Kapton — 1 Mil
2 Mil
Adhesive — 1 Mil
Closed Cell Rohacell Foam — 0.112 In.
Adhesive — 1 Mil
Conductive Support Disk — 0.080 In.
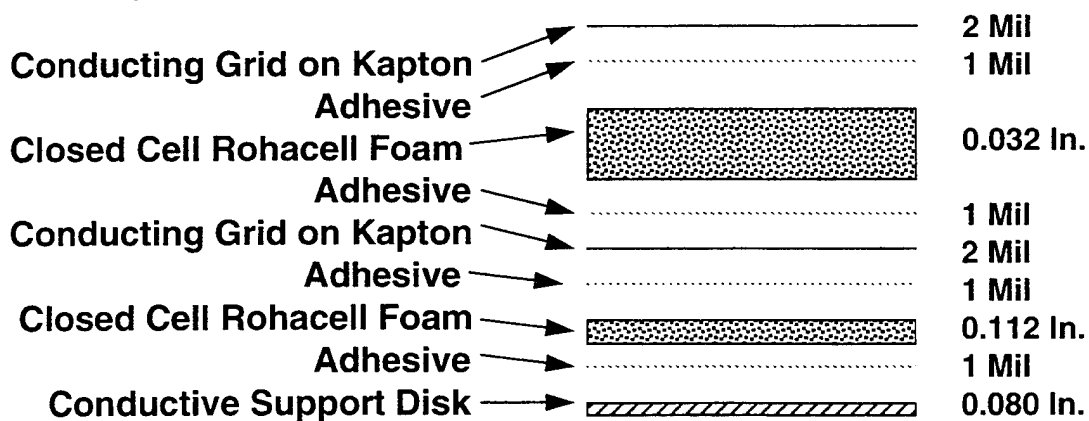
Figure 8 Twist Reflector Cross Section

99
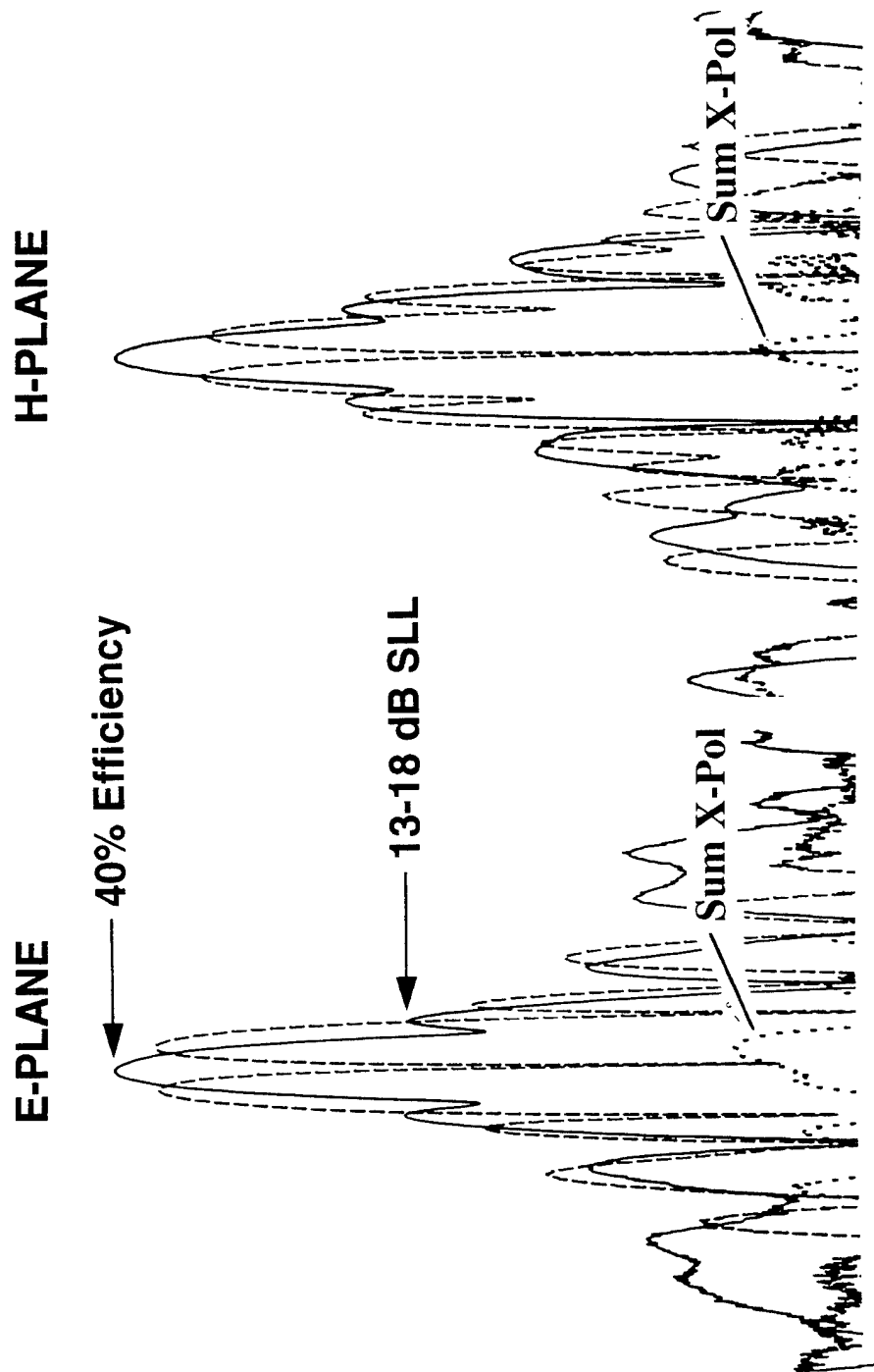
Figure 9 X-Band Pattern Performance
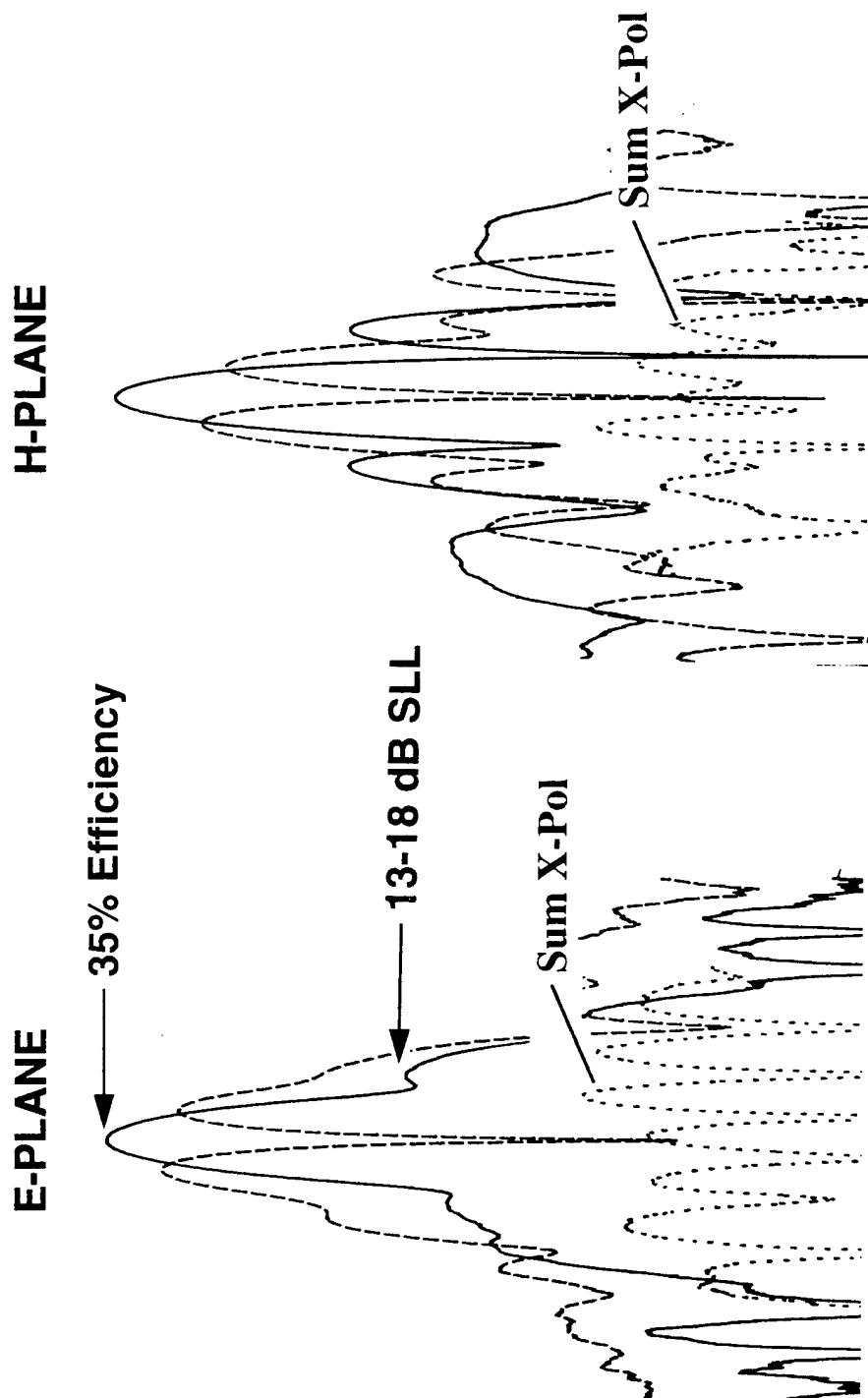
Figure 10 Ka-Band Pattern Performance

Ka-Band Five Horn Feed

Michael Del Checcolo
Jeff Lane
Raytheon Electronic Systems
50 Apple Hill Rd
Tewksbury Ma, 01876

Abstract: A prototype Ka-band Five horn monopulse feed has been developed. It is intended to be used as a prime focus reflector feed in a missile seeker. The feed is composed of two main waveguide components, two magic tees that produce the two difference channels, and an Ortho Mode Transducer (OMT) which generates the two orthogonal sum polarization's necessary for this dual polarized antenna.

The five horn feed has several advantages over the more common 4 horn feed approach. For example, the sum and two difference channels are independent and therefore each channels radiation pattern can be independently tailored without degrading the other's performance.

The design approach as well as tradeoffs that were made during this prototyping effort will be presented and explained. Finally, the measured and predicted performance of the five horn feed illuminating a reflector antenna will also be presented.

1.0 Introduction

A new feed and reflector approach has been conceived which has the potential for no less than 36 dB gain in the Ka-band frequency range. The approach consists of a five horn feed and a dichroic parabolic reflector. A breadboard feed has been designed, fabricated and tested. This paper will concentrate on the feed design and measured results from the breadboard fabrication. These measurements include return loss, isolation, primary feed patterns, secondary reflector patterns and gain. Finally, ways of improving the feed performance will be discussed as future work.

2.0 Design

The design of this five horn feed, which will be here after referred to as the feed, was a collaborate effort between Raytheon and Microwave Development Laboratories (MDL). MDL supplied the waveguide manufacturing capability as well as expertise in waveguide component design. To minimize cost, "Off the shelf" components were used wherever possible.

The feed is made up of two main waveguide components; the Ortho Mode Transducer (OMT) and the Magic Tee. A single OMT is used to transmit the two polarization's of the sum pattern. An OMT is a three port device with two inputs and one output. Each of the input ports transmits one of two orthogonal polarization's through the output port. This is an off-the-shelf item that was developed by MDL.

The two delta channels are transmitted through two identical Magic Tee's. Only the difference port, of the magic tee, which causes equal amplitude and a 180° phase difference at the two outputs is used. The sum port of each Magic-T is terminated. A Ka-Band Magic Tee component was not an "off the shelf" item. It was designed with the aid of Hewlett Packards High Frequency Structure Simulator (HFSS). This software package was used to optimize tuning structures inside the waveguide Magic Tee in order to maximize both input return loss and the isolation between ports. An equal power split between output aperture ports was also optimized with the help of HFSS. The final HFSS model predicted a input VSWR of less than 1.1:1 and this was later confirmed with measurements made by MDL.

The E and H plane bends used to correctly orient the feed apertures from the magic tees and OMT were off the shelf components provided by MDL. With all of the components which make up the feed designed, the next design task was to correctly orient the apertures for optimum reflector performance. Figure 1 contains a schematic of the feed.
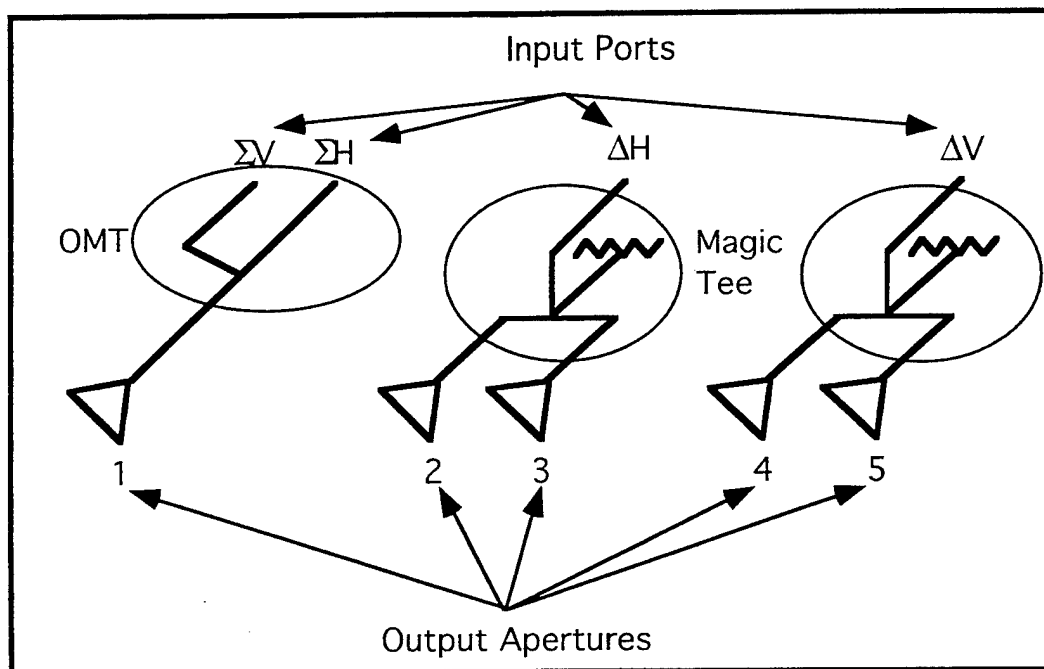
Figure 1: Five Horn Feed Schematic

The following range of parameters (see Figure 2) have been shown to yield near optimum gain performance for a five horn feed illuminating a parabolic reflector within the required seeker volume. These values were optimized using the "Refl" program written by Dr. Yueh-Chi Chang of Raytheon Co. This program models reflector gain and pattern performance for various feed input data.

Diameter (D) = 11.0 in.
F/D = 0.35
    A = 0.551 to 0.61
    B = 0.91
    C = 0.91
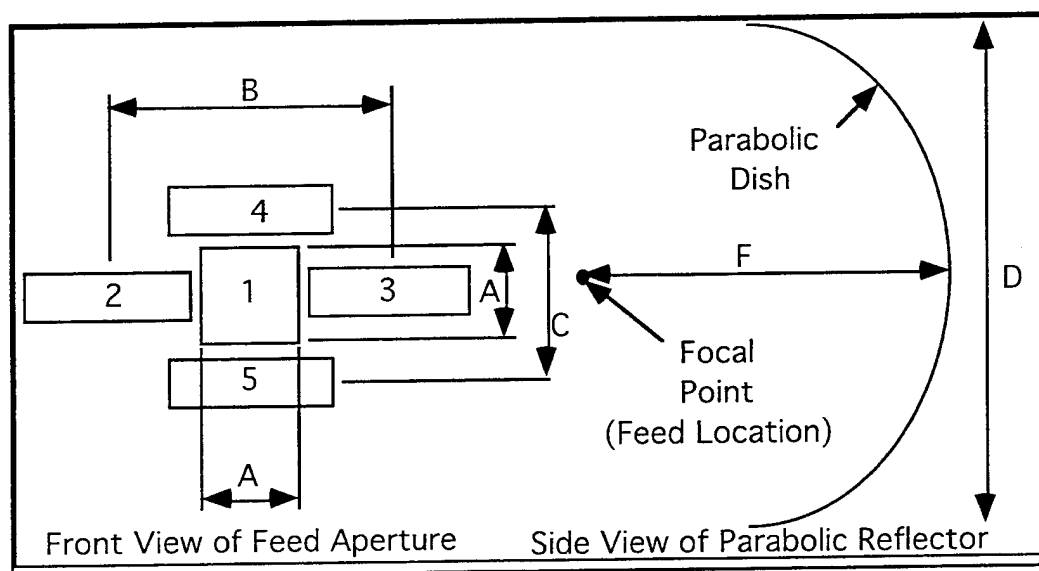
Figure 2: Reflector Antenna Dimensions

The numbers seen in Figure 2 correspond to the output aperture numbers seen in Figure 1. The OMT output port inner wall dimension (A) is 0.57λ square. As can be seen in the front view of the feed aperture in Figure 2, the Azimuth and Elevation channels phase center aperture spacing (B) and (C) are limited by the sum channel aperture size (A), the finite thickness of the waveguide walls and the orientation of the WR-28 waveguide opening which are serving as the delta channel apertures. With these limitations, the Elevation channel phase center spacing (C) is limited to 1.4λ. Because of the orientation of the broad wall of the WR-28 waveguide for the Azimuth channel, the phase center spacing (B) is limited to 1.8l. This waveguide

orientation is necessary in order to correctly orient the electric field polarization. The electric field polarization for each of the five apertures which make up the feed can be seen in Figure 3.
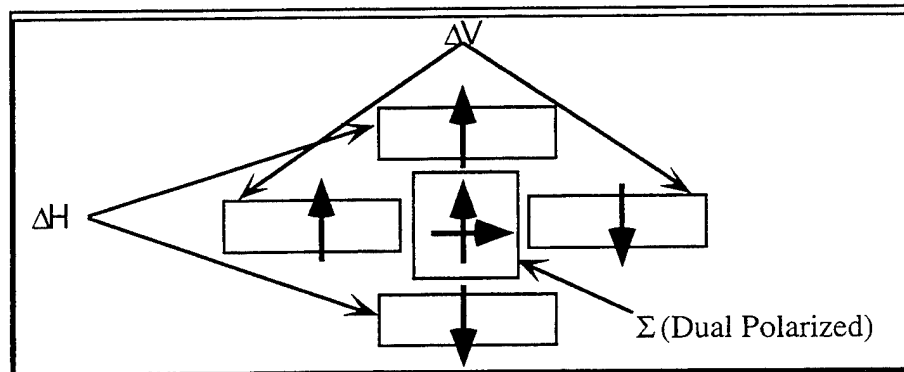
Figure 3: Polarization Diagram of Feed

In order to reduce these spacings (B and C) several things were done. Figure 4 illustrates the changes that were made in order to reduce these spacings to there optimum spacing.
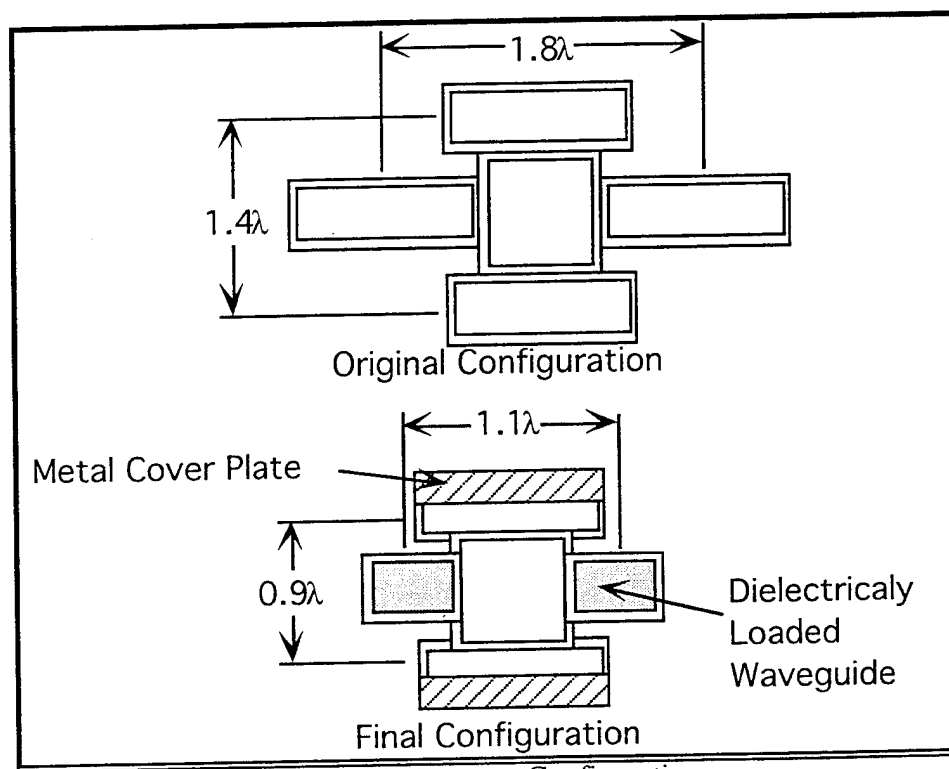
Figure 4: Aperture Configuration

As can be seen in Figure 4 the phase center aperture spacing for the Elevation channel was reduced to the optimum value of 0.9λ. This was accomplished by sharing the common walls between the OMT output and the broad wall of the waveguide which make up the Elevation channels apertures. In order to further reduce this spacing a metal cover plate is placed over half of each of the waveguide apertures. This effectively moves the waveguide phase centers closer to the common wall between the OMT and the WR-28. This approach also improves the feeds input match.

The common wall approach was again used to reduce the spacing between the Azimuth channel apertures. To further reduce this spacing the waveguide has been tapered and dielectrically loaded so that the waveguide would not be cut off at the design frequency Fo (Figure 5). Emerson and Cummings Stycast High K was used as the loading material. This material has a dielectric constant (ϵ_r) of 3.8. Using this approach a spacing of 1.1λ was achieved. The optimum 0.9λ could be achieved by using a higher dielectric loading material which would allow the aperture size to be reduced even further. This was not done because a higher ϵ_r degrades the waveguide's match to free space. This compromise in aperture spacing results in a loss of delta azimuth peak gain of less than 0.1 dB.

3.0 Modeling

HFSS was found to be an invaluable tool in optimizing the tuning structures inside the magic tee. These tuning structures were used to optimize input and output return loss, insertion loss and isolation. Table 1 outlines the final results predicted by HFSS for the optimized magic tee model. While this data was taken at the design center frequency Fo, the HFSS magic tee model was swept over frequency and found to have more than enough bandwidth for this application

Table 1: HFSS Model Data for Magic Tee

Measurement	Measured Results At Fo
input Return Loss	25 dB
output Return Loss	30 dB, 32 dB
Isolated Return Loss	23 dB
Power Split	3.0 dB
Isolation	49 dB
output Delta Phase	180 .0°

From this HFSS magic tee model the feeds two delta channels were modeled by adding the appropriate E and H plane waveguide bend along with straight sections of WR-28 to correctly orient the feed apertures. A separate HFSS model was also used in order to optimize the loaded waveguide apertures match to free space by placing a 377 Ω impedance dome over the aperture. Figure 5 illustrates a sketch of the final model. This loaded waveguide model was added to the Azimuth channel model in order to fully analyze both channels.
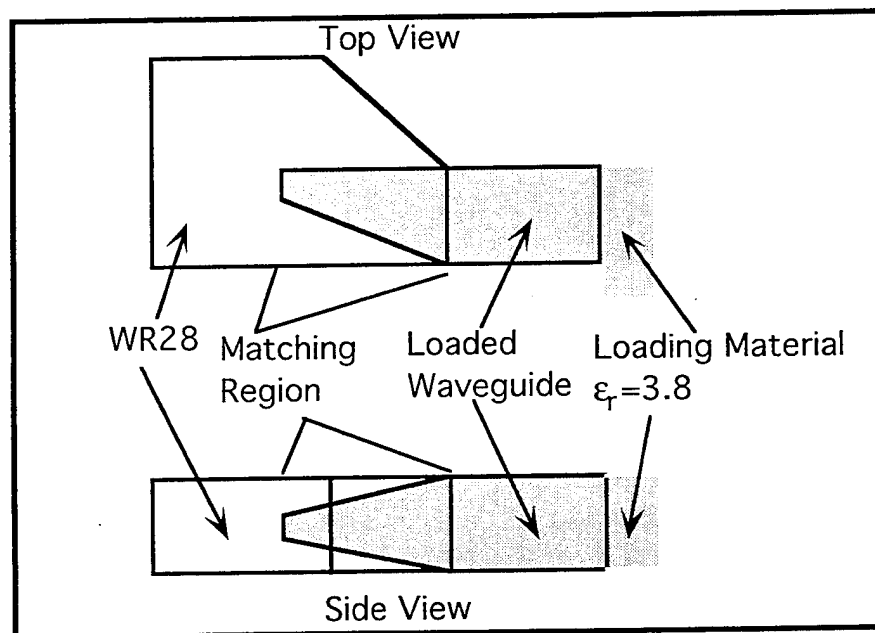
Figure 5: Loaded Waveguide Sketch

The predicted data from these models can be seen in Table 2. This data was also taken at the design center frequency Fo but again a frequency sweep revealed that the addition of this waveguide hardware did not dramatically affect the magic tee's bandwidth performance.

Table 2: HFSS Model Data for Delta channels

	Return Loss	Insertion Loss	Isolation	Output Δ Phase
Azimuth channel	-17 dB	3.0 dB	-49 dB	180.06°
Elivation channel	-23 dB	3.0 dB	-53 dB	179.94°

The slight degradation in the Azimuth channels return loss can be attributed to the dielectric loading of the output ports.

The OMT was not modeled because measured data was available for this component. The input return loss radiating into free space was measured to be better than 15 dB for each of the input ports across the entire frequency of interest. The isolation between input ports was measured to be better than 30 dB across the same bandwidth. These results were acceptable for this application.

Using the "REF1" program the feed in its final configuration, seen in figure 4, was analyzed illuminating an eleven inch parabolic dish. An F/D ratio of 0.35 was used. The predicted H-plane pattern is presented in Figure 6. This pattern shows a gain of 36.4 dB and a sidelobe level of -22.0 dB. The 3 dB beam width was also predicted to be 2.2°. With the feed and the seeker antenna fully modeled and optimized the feed design was sent for fabrication of the first engineering model.

4.0 Fabrication

The feed was fabricated by MDL. The individual components were made of Aluminum and a brazing process was used for their assembly. The dielectric inserts were machined for the breadboard design but will ultimately be cast. The

fabrication of the feed, which is very tightly packaged, was a success; however, an error was made in the layout of the feed. The input difference port of the delta elevation channel was mistakenly terminated while the sum port was fitted with an input waveguide flange. This means instead of producing an elevation response this port produces a sum pattern which is not usable. While the delta elevation channel could not be evaluated the two sum channel responses as well as the delta azimuth channel could. The delta azimuth channel is considered more crucial to the design than the delta elevation channel. This is because dielectric loading is used in the azimuth channel and the phase center is not entirely optimized as discussed previously.
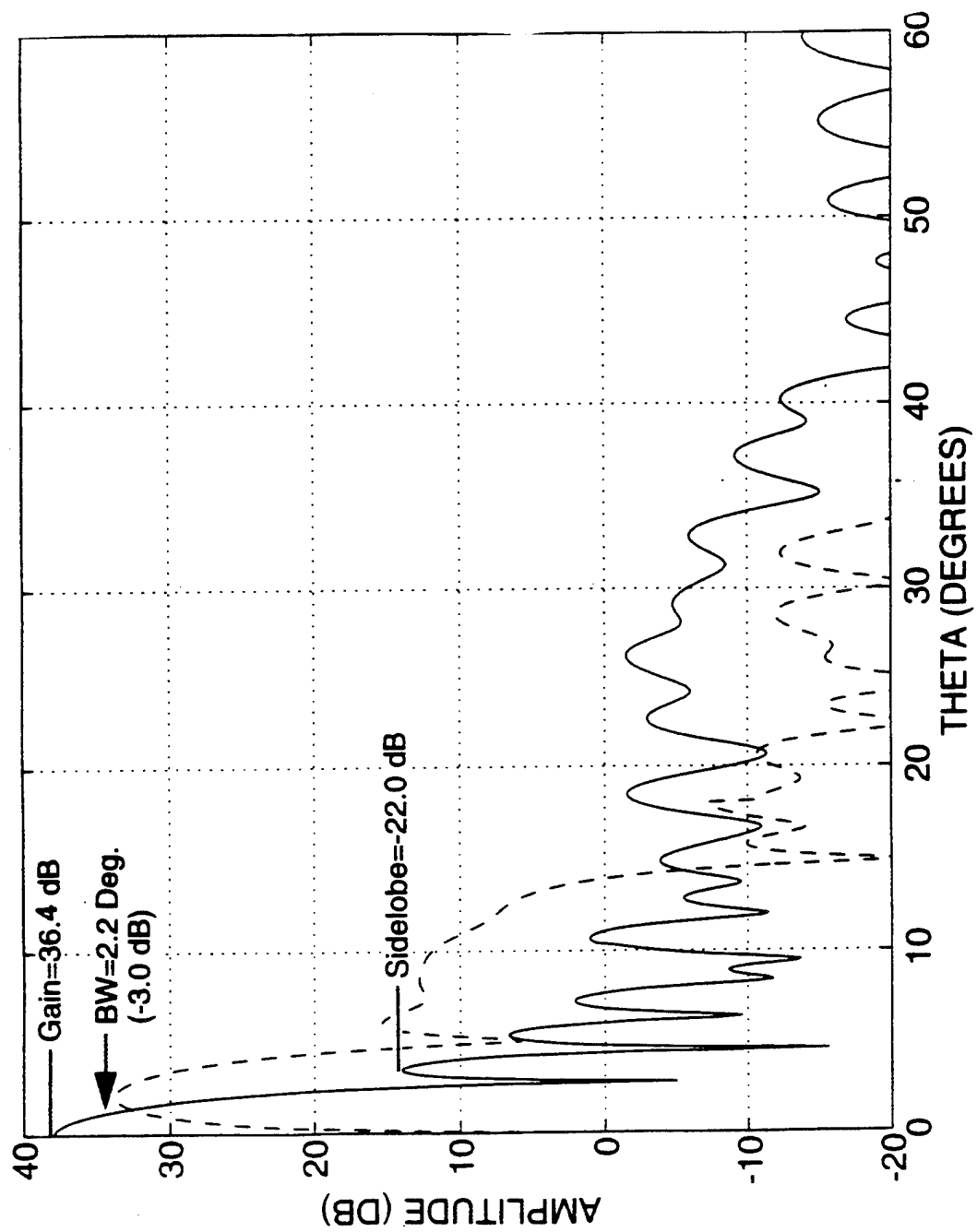
Figure 6: Predicted H-Plane Pattern of 11 inch Parabolic Dish With 5 Horn Feed
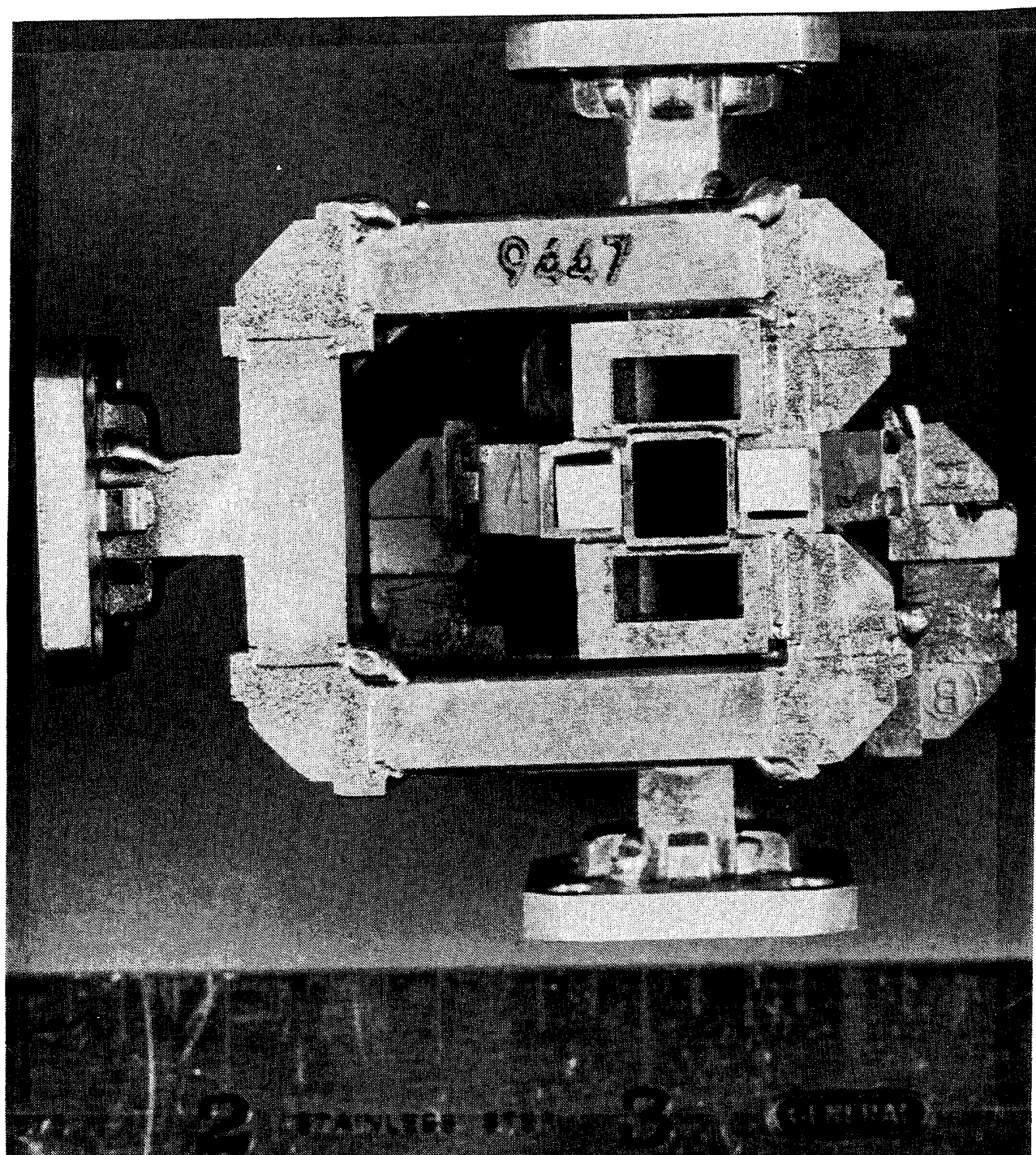
Figure 7: Photo of First Breadboard Five Horn Feed

113

A photograph of the final feed assembly can be seen in Figure 7. This photo is a view of the feed facing the output apertures. A scale has been included so that the small size of the feed can be appreciated. Please note that WR-28 waveguide flanges have been attached to each of the input ports for testing purposes. In the final form factored design these will be replaced with waveguide struts.

5.0 Measurement Results

Return loss and isolation measurements were made on the Hewlett Packard 8510C Network Analyzer with all feed apertures radiating into "free space" and WR-28 waveguide loads terminating all unused ports. The return loss measurement results can be seen in Figure 8.
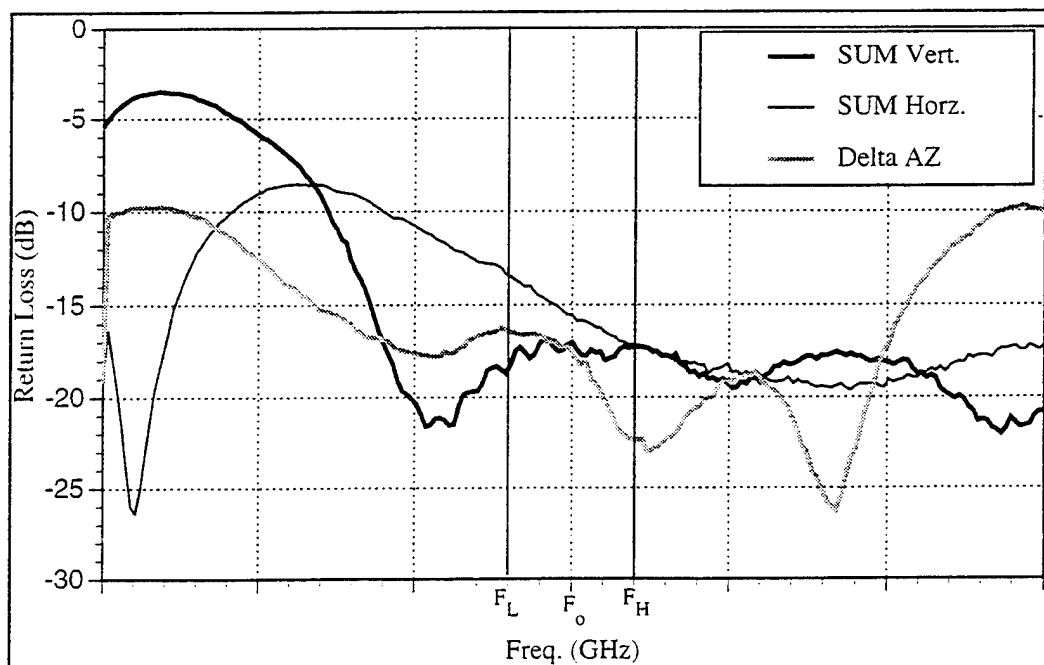
Figure 8: Feed Return Loss

114

The low and high frequency band edges for the seeker requirement are labeled as F_L and F_H in Figure 8. All three measured channels have better than 15 dB return loss at the center frequency (F_o). The Sum Vertical and Delta Azimuth channels sustain a 17 dB return loss across the entire bandwidth while the Sum Horizontal channel degrades slightly at the low end of the frequency band to approximately 13 dB. Figure 8 was plotted over such a broad frequency range to indicate the large potential bandwidth achievable with this feed design. Secondary pattern and gain measurements taken at 2 GHz above F_o show excellent performance.

The isolation measurement results are presented in Figure 9.
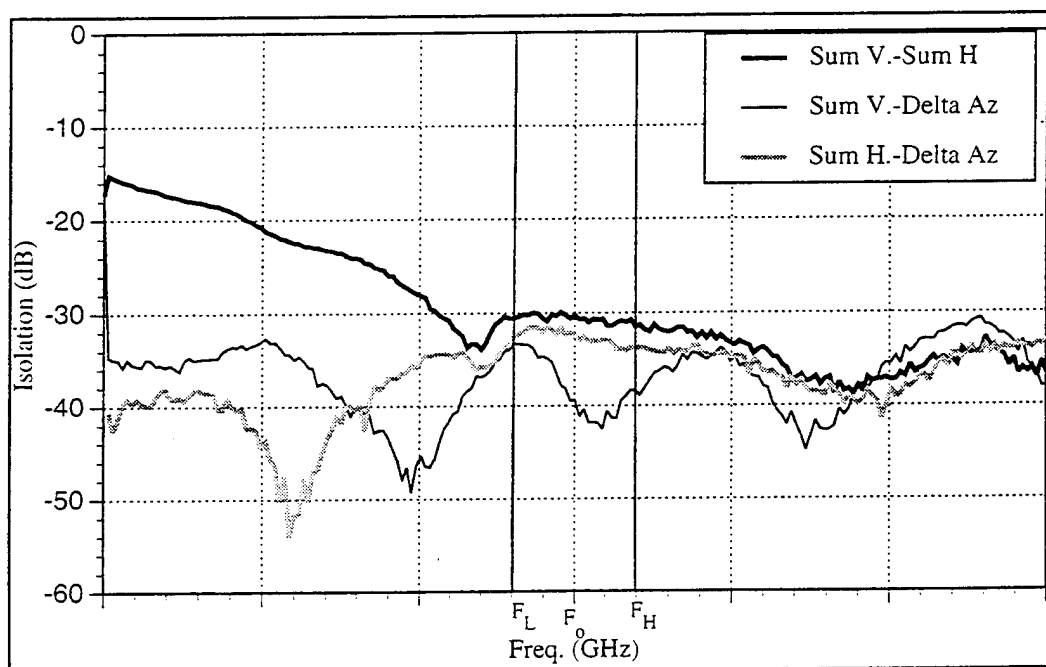
Figure 9: Isolation Measurement

All ports are isolated by better than 30 dB across the frequency band of interest. Again this feed design shows a much broader frequency response. Note that even the two sum channels, which utilize the same output aperture are isolated by better than 30 dB.

Next, the primary principle plane feed patterns were taken. All primary feed pattern data was measured in an Anechoic Chamber. All primary feed pattern data was taken at the center design frequency Fo, and was measured in dBi. Figures 10 and 11 show the Sum Vertical (E-plane cut) and the Sum Horizontal (H-plane cut) with the Delta Azimuth pattern overlaid respectively.
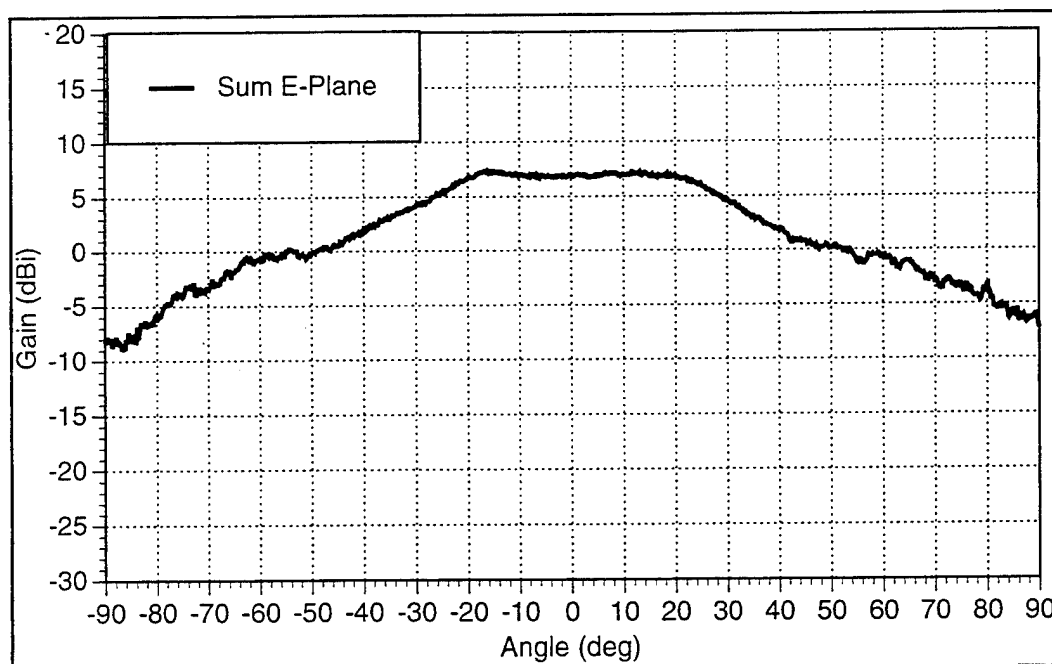
Figure 10: Primary Feed Pattern Sum Horizontal E-Plane Cut
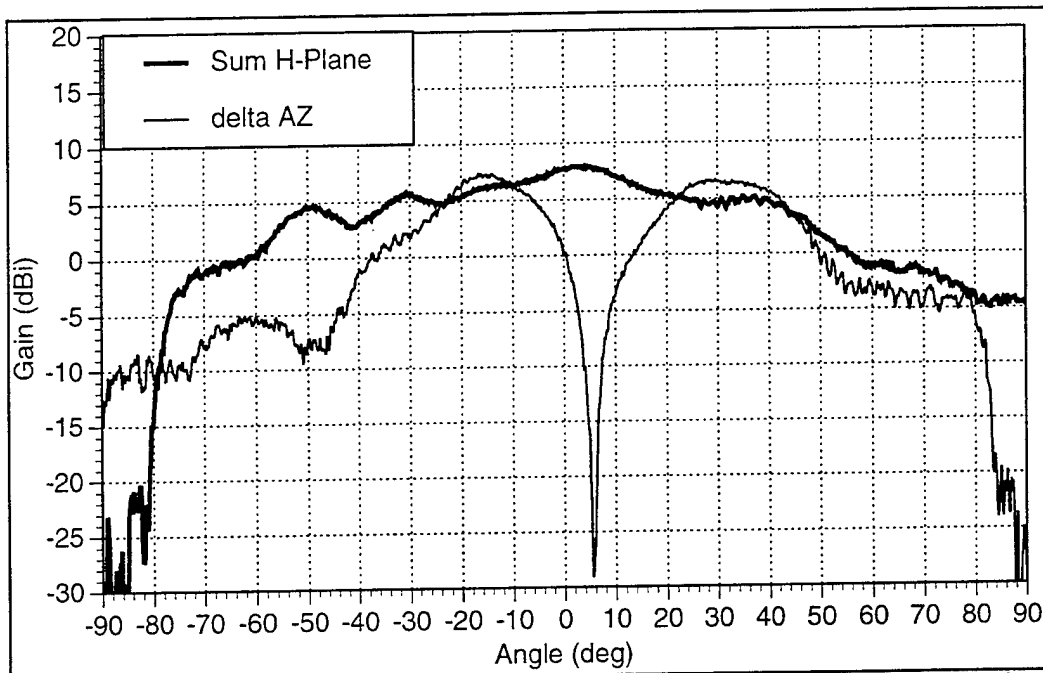
Figure 11: Primary Feed Pattern Sum Horizontal and Delta Azimuth H-Plane Cut

From the above figures it can be seen that the gain of the feed Sum E and H channels is 7.5 dBi. The edge tapers of the Sum E and H polarizations at 72° are 10 dB. The edge taper of the Delta Azimuth channel at 72° is 15 dB. This is slightly lower than the ideal value calculated by the Chang program because the aperture spacing was larger than the optimum. Recall that the Delta Azimuth channel utilizes the dielectrically loaded waveguide and a compromise was made between impedance match and aperture spacing. The offset of the Delta Azimuth channel null is caused by the crude fixturing used to make the breadboard measurement.

The feed was next attached to a reflector antenna in order to measure the antenna's secondary pattern and gain performance. The feed was designed to illuminate an 11

inch parabolic dish but because this reflector was not readily available, a 13 inch flat reflector, designed by Dan Fontaine of Raytheon Co., which operates at the desired frequency (f_o) was used for these measurements. This flat reflector uses printed crossed dipoles which are phased to emulate a parabolic reflector. While this replacement will not yield the optimum performance it will allow a figure of merit to be placed on the feed design. The anechoic chamber receiver was calibrated to dBi with a standard gain horn so that all measurements would be referenced to actual gain. The feed was also attached to the reflector using a micrometer so that it could be moved in order to find the optimum focal point of the flat reflector. This distance was found to be 4.9375 inches.

First, the feed/reflector antenna assembly was measured at 11 discrete frequencies between $F_o-.5$ GHz and $F_o+.5$ GHz in order to find the maximum gain point. A maximum gain of 36.9 dBi was measured at $F_o-.1$ GHz. This data can be seen in Figure 12.
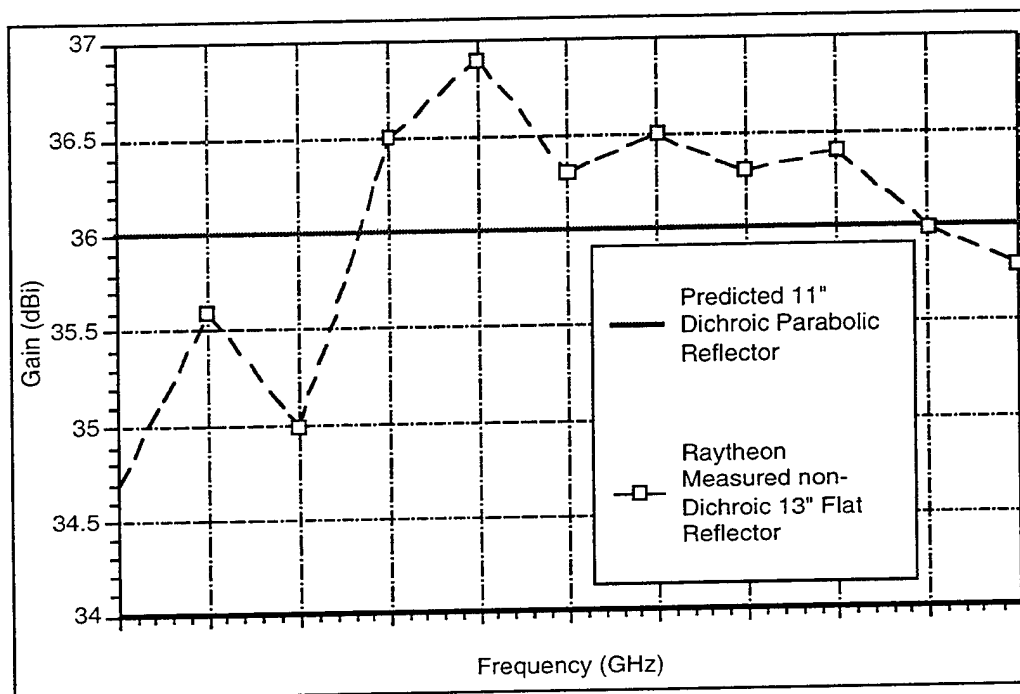
Figure 12: Gain Versus Frequency

The degradation of the gain performance at the high and low frequencies is primarily caused by the bandwidth limitations of the flat reflector. A gain of 36 dB across the entire 1 GHz span has been predicted for the 11 inch diechroic parabolic reflector antenna.

Next, pattern data was taken at F_o-.1 GHz. The Sum and Delta Azimuth channel patterns were measured (figure 13).
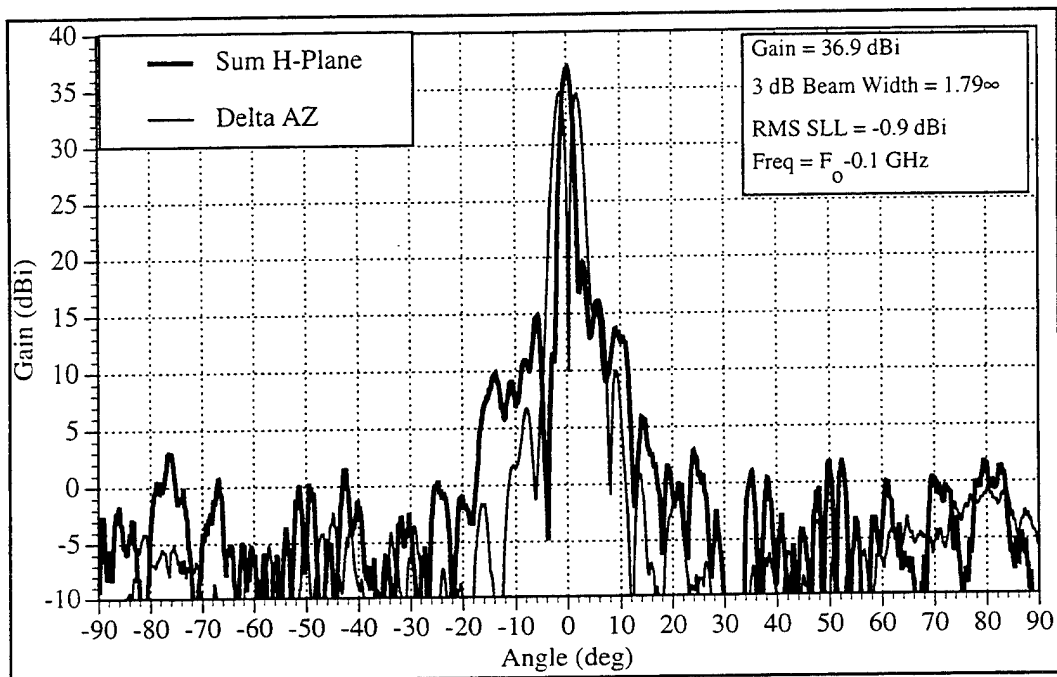
Figure 13: H-Plane Sum and Delta Azimuth Reflector Antenna Patterns

The sum Channel gain was measured to be 36.9 dBi. The sum 3 dB beam width is 1.79° and the RMS Side Lobe Level (SLL) is -0.9 dBi. The pattern is also shown on an expanded scale in Figure 14.
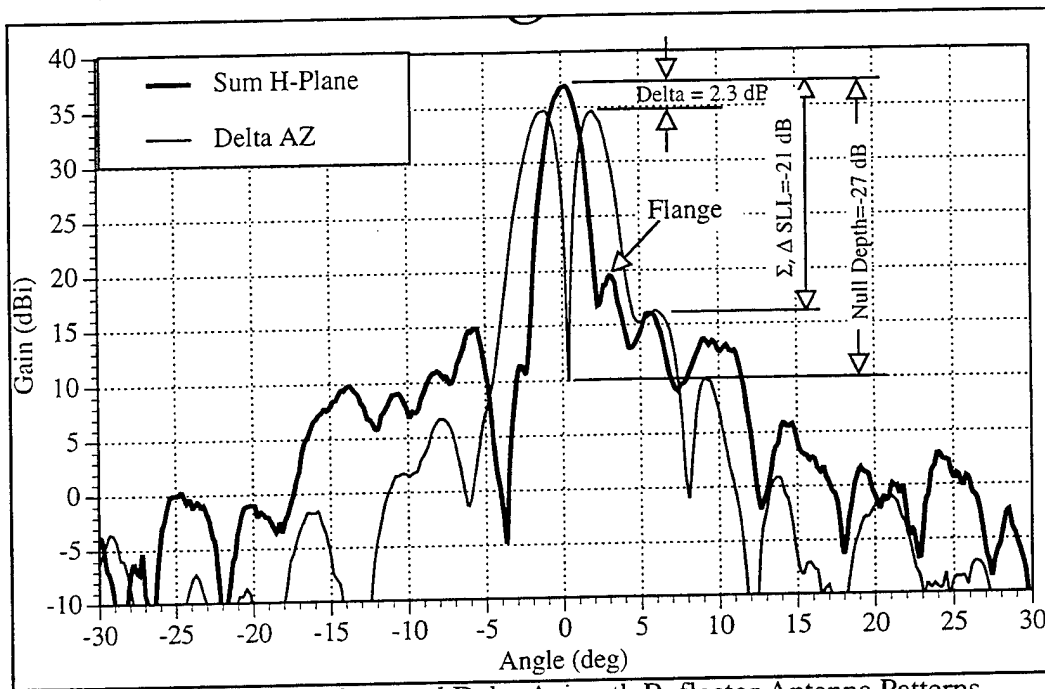
Figure 14: H-Plane Sum and Delta Azimuth Reflector Antenna Patterns

The highest sidelobe, at +3° in the sum pattern, was found to be caused by the Delta Elevation channel's input flange This was verified by rotating the feed antenna by 180° and re-measuring the pattern. This sidelobe may be reduced when the flange is eliminated in the final design. The next highest SLL of the Sum and Delta Azimuth channels is 21 dB at 6° scan angle. The difference in gain between the Sum and Delta Azimuth is 2.3 dB. The Delta Azimuth null depth with respect to the Sum beam peak is 27 dB. The delta null is offset from the sum peak slightly since the sum and difference measurements had to be fixtured and measured individually.

The E-plane cut is shown plotted in Figure 15.
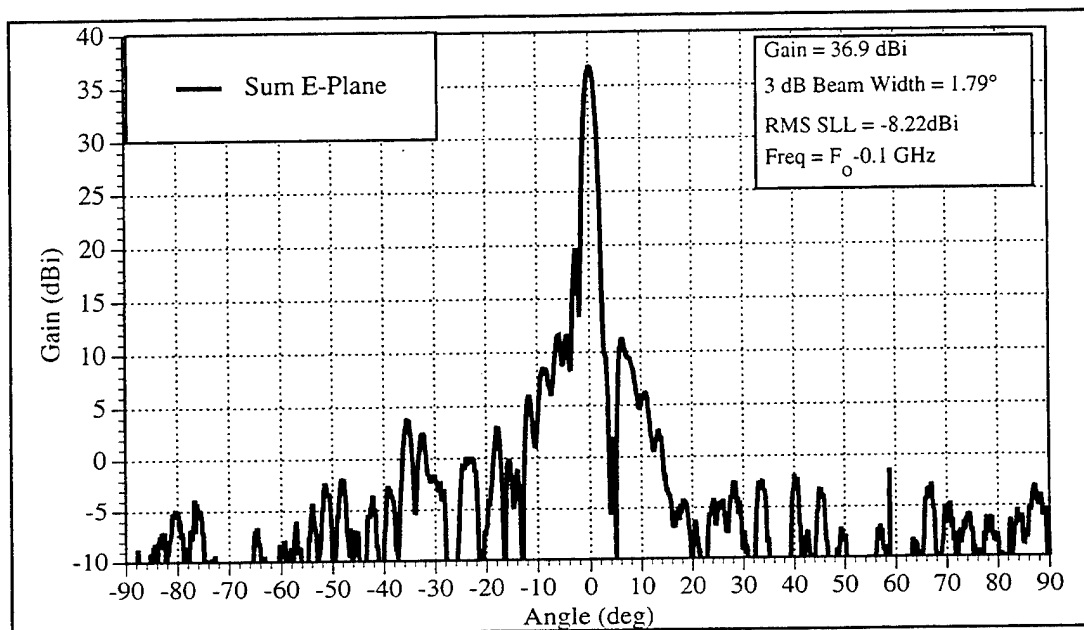
Figure 15: E-Plane Sum Reflector Antenna Patterns

In this plane the Sum 3 dB Beamwidth is also 1.79° showing excellent symmetry and the RMS SLL is -5.1 dBi. The expanded view of this data is shown in Figure 16.
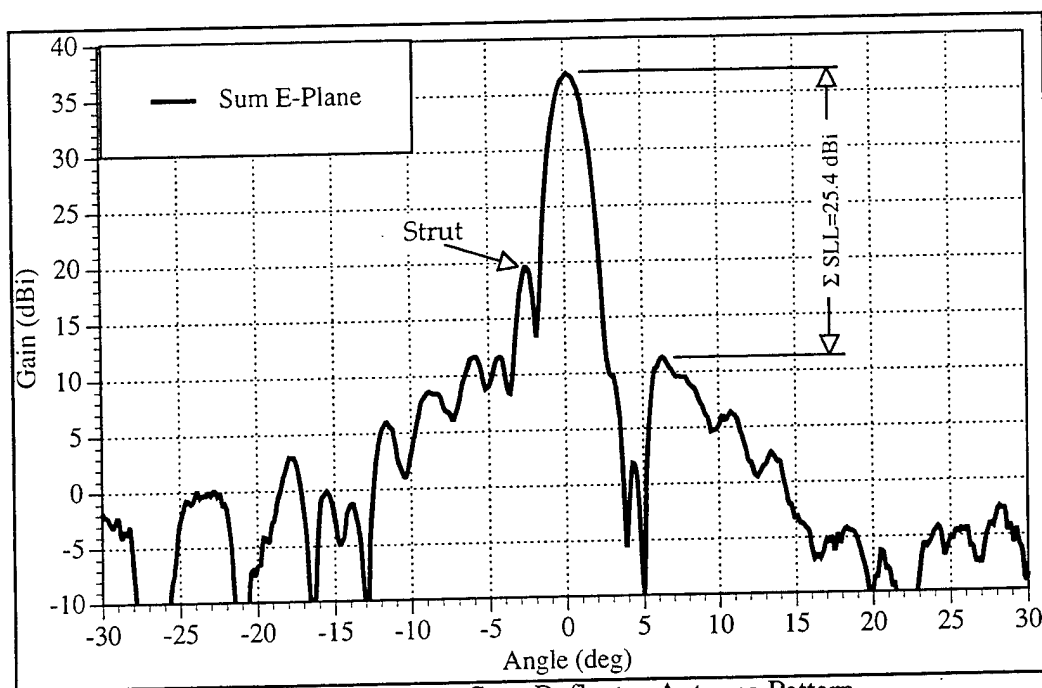
Figure 16: E-Plane Sum Reflector Antenna Pattern

The Sum first SLL in the E-plane pattern is approximately 17.0 dB. This is caused by the presence of the broad wall of the WR-28 waveguide which is used in the breadboard setup to feed the sum input flange. The next higher sidelobe is at -25.4 dBi. The final sidelobe structure will be determined when the next iteration of feed with waveguide struts and a parabolic reflector is measured.

6.0 Conclusions

The measured results obtained from the first engineering model of the Ka-band five horn feed are very promising. A sound design procedure and accurate modeling tools have been found for the design of this five horn feed. The data compiled from this first engineering model has proven that a five horn feed can produce reflector antenna patterns which are desirable in a seeker system.

The following has been identified as future work. First, the correct elevation port will be terminated so that the elevation channel can be evaluated. Next, the long straight waveguide sections in the delta elevation channel (labeled 9447 in Figure 7) will be shortened in order to further reduce feed blockage. A 1.5 inch diameter metal plate will be placed over the front of the feed with cut outs for the five apertures. This is expected to make the reflector patterns more symmetric. Finally, a form factored feed with struts will be integrated with an 11 inch parabolic reflector so that more accurate measurements can be made.

6.0 Acknowledgments

7.0 References

[1] A. F. Sciambi, Jr., "Five-Horn Feed Improves Monopulse Performance" Microwaves, p56-58, June 1972.

[2] C. A. Balanis, "Antenna Theory Analysis and Design" John Wiley and Sons, Inc. 1982., p 593-635.

A rigorous technique for synthesis of offset three-reflector antennas

Vladimir Oliker

Emory U., Atlanta, GA 30322 and Matis, Inc., Atlanta, GA 30329

1 Introduction

The problem of synthesis of offset single and dual reflector antennas has been studied by many authors [1], [2], [3], [4], [5], [6], [7], [8], [9]. The objectives of design are to synthesize high efficiency antennas with capabilities to produce prespecified field amplitude and/or phase on the output aperture, and, at the same time, minimize energy losses due to spillovers, reduce blockage, achieve low sidelobes, etc.; see [10]. The geometric optics approximation is usually used for deriving the corresponding ray-tracing and energy conservation equations. Most of the known results rely on heuristic arguments and use numerical calculations in special model cases to justify the utilized approaches.

In our recent paper [11] we described an approach that allows to synthesize a system with two reflectors satisfying most of the above requirements provided that the input and output beams are plane wave fronts propagating in the same

126

direction. The approach is based on a study of a certain second order partial differential equation of Monge-Ampère type for which a rigorous solvability theory is available. However, the requirement in [11] that the input beam should be a plane wave does not allow to apply this approach in cases where the input is a spherical wave front. For instance, in applications involving reflector antennas it is important to be able to convert a spherical wave front from a point source into an output plane front and at the same time control the output energy pattern. In this note we outline an approach for designing a system with three reflectors that has such capabilities. The basic idea is to introduce into the system described in [11] a parabolic reflector with the focus at the source. This will produce a parallel wave front that is required for the system designed in [11]. In such circumstances one can apply the technique described in [11] and determine all three reflectors. The approach presented here allows substantial flexibility in the choice of the parabolic mirror and of the second mirror. This flexibility is essential for optimizing various design parameters in addition to producing on the output aperture the required energy pattern. For example, in such system blockage can be completely avoided. At least theoretically, spillovers are reduced to zero. Furthermore, the numerical algorithm REFSYS developed by us earlier for synthesis of dual systems with plane input and output wave fronts is adaptable to the situation described here with only minor modifications.

The paper is organized as follows. First we describe the configuration of the three-reflector system. Then we derive the main partial differential equation and show how the results in [11] can be applied in this case as well.

Inquiries regarding synthesis of concrete reflector systems are welcome.

2 Configuration of the system
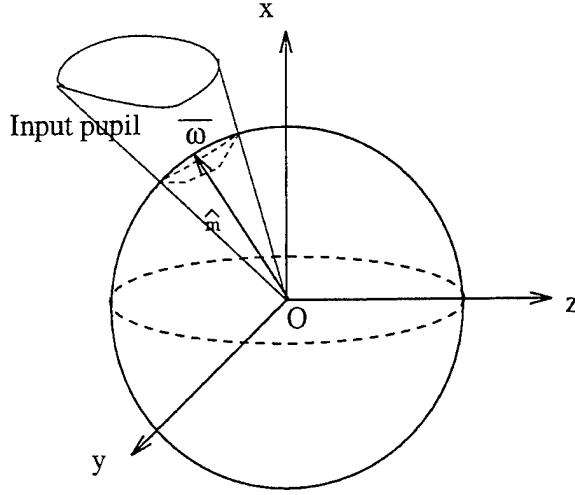
Figure 1:

On figures 1 and 2 below we show an offset antenna system with three reflectors. The input pupil $\bar{\omega}$ is described by a vector function $\hat{m}(u^1, u^2)$ in some coordinates u^1 and u^2 on the unit sphere S. Usually, $u^1 = \theta$, $u^2 = \phi$ are the spherical coordinates on S, and in these coordinates $\hat{m}(\theta, \phi) = (\sin\theta\cos\phi, \sin\theta\sin\phi, \cos\theta)$. The bar over ω indicates that the boundary $\partial\omega$ of ω is included; thus, $\bar{\omega} = \omega \bigcup \partial\omega$.

The following data is assumed to be available to the design engineer.

- The position of the point source;

- The shape, position, and output energy pattern $L(p, q)$;

- It is required that the output front be a plane wave; on figure 1 and in our description below it is assumed that the output front propagates in the direction $\hat{k}$.
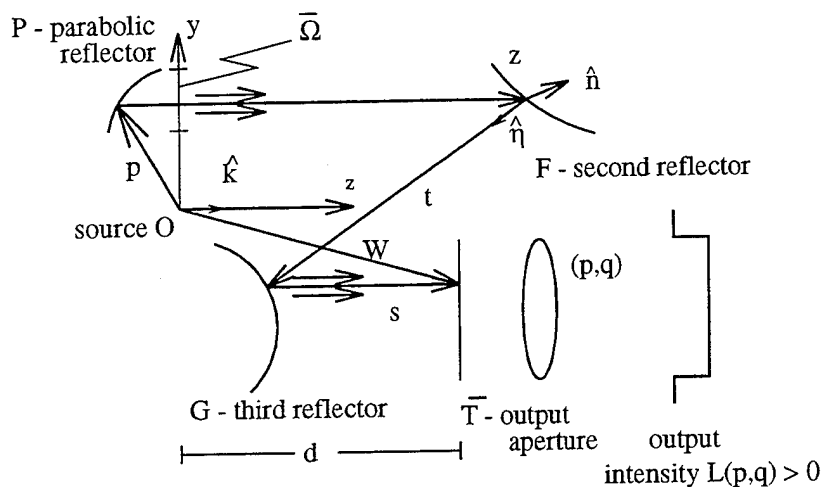
Figure 2:

The first reflector P is always a rotationally symmetric paraboloid with axis of the same direction as that of the output front anf focus at O. The position of the input pupil is chosen by the designer so that the rays reflected off P do not overlap with the input horn. These are the only restrictions on the reflector P. This leaves substantial flexibility to the designer in choosing the input pupil, in particular, its size, direction, etc. One should only remember that the second mirror will be positioned so as to intercept the plane wave produced by P. The radiation pattern I of the source is subject only to the energy balance requirement (see eq. (13) below).

The system that we want to synthesize is required to convert the spherical wave front from O with input energy pattern I into a plane wave front passing through a prespecified output aperture $\bar{T}$ with output intensity pattern $L(p,q)$, where p,q are the coordinates on the output plane front propagating in direction of the vector kh. On the figure 1 the output energy pattern is shown to be uniform. In addition, the shape of the output aperture is also

prespecified; for example, on figure 1 it is shown to be elliptic.

The input power pattern $I(\hat{m})$ is specified for the point source O as a function of the input direction $\hat{m} \in \omega$. The vector function describing the reflector P is denoted by $\mathbf{p}(\hat{m}) = \rho(\hat{m})\hat{m}$, $\hat{m} \in \bar{\omega}$, where ρ is the polar radius of P.

Denote by $\bar{\Omega}$ the region on the $z = 0$ plane onto which the reflector P can be projected. Since P transforms the spherical wave into a plane wave propagating in direction $\hat{k}$ the region $\bar{\Omega}$ is well defined. Each point $(x, y) \in \bar{\Omega}$ can be written now as $x = x(\hat{m}), y = y(\hat{m})$ with $\hat{m} \in \bar{\omega}$.

Consider now the second and third reflectors. We treat $(x, y) \in \bar{\Omega}$ as independent variables and follow the development in [11]. A ray from the source O is reflected off P, passes through a point x, y propagating in the direction of the unit vector $\hat{k} = (0, 0, 1)$, strikes the second reflector F, reflects off F in the direction of the unit vector $\hat{\eta}(x, y)$, strikes the third reflector G, and reflects off it, again, in the direction $\hat{k}$. The reflector F we describe by a function $z(x, y), (x, y) \in \bar{\Omega}$. For simplicity, we assume that $z \geq 0$ in $\bar{\Omega}$. By adding a suitable constant to z this assumption can be always satisfied. In vector form F is given by the vector function $\mathbf{r}(x, y) = (x, y, z(x, y)), (x, y) \in \bar{\Omega}$. Denote by $\hat{n}$ the unit normal vector on F. Put $z_x = \frac{\partial z}{\partial x}, z_y = \frac{\partial z}{\partial y}$. Then

$$\hat{n} = \frac{(-Dz, 1)}{\sqrt{1 + |Dz|^2}}, \quad Dz = (z_x, z_y). \tag{1}$$

The unit vector $\hat{\eta}(x, y)$ in the direction of the ray reflected off F can be found by applying Snell's law,

$$\hat{\eta} = \hat{k} - 2(\hat{k} \cdot \hat{n})\hat{n}. \tag{2}$$

Denote by $t(x, y)$ the distance from reflector F to reflector G along the ray

reflected in the direction $\hat{\eta}(x,y)$ and let $s(x,y)$ be the distance from G to the output aperture $\bar{T}$ along the corresponding ray reflected off G.

The optical path length from the plane $z = 0$ to the output aperture $\bar{T}$ corresponding to the ray associated with the point (x,y) is denoted by $l'(x,y)$ and it is given by

$$l'(x,y) = z(x,y) + t(x,y) + s(x,y). \tag{3}$$

Because $l'(x,y)$ is the distance between input and output fronts, we have (see [12]):

$$l'(x,y) = const. \tag{4}$$

Similarly, let $q(\hat{m}) = -\mathbf{p}(\hat{m}) \cdot \hat{k}$. Then $|q|$ is the distance from the point $\rho(\hat{m})\hat{m}$ on the reflector P to the plane $z = 0$. The optical path length $l'' = \rho(\hat{m}) + |q(\hat{m})|$ is also constant for all $\hat{m} \in \bar{\omega}$. The total optical path length (OPL) for the entire system is given by

$$l = \rho(\hat{m}) + q(\hat{m}) + l'(x(\hat{m}), y(\hat{m})) = const. \tag{5}$$

It is convenient to introduce vector notation for the surface G and the output aperture $\bar{T}$. Respectively, we put

$$G: \quad \mathbf{R}(x,y) = \mathbf{r}(x,y) + t(x,y)\hat{\eta}(x,y), \quad (x,y) \in \bar{\Omega}, \tag{6}$$

$$\bar{T}: \quad \mathbf{V}(x,y) = \mathbf{R}(x,y) + s(x,y)\hat{k}, \quad (x,y) \in \bar{\Omega}. \tag{7}$$

The complete ray tracing map is given by

$$\bar{T}: \quad \mathbf{W}(\hat{m}) = \mathbf{p}(\hat{m}) + (q(\hat{m}) + z(x(\hat{m}), y(\hat{m}))$$

$$+ s(x(\hat{m}), y(\hat{m})))\hat{k} + t(x(\hat{m}), y(\hat{m}))\hat{\eta}(x(\hat{m}), y(\hat{m})), \quad \hat{m} \in \bar{\omega}. \tag{8}$$

131

Thus, a point $(p, q, d) \in \bar{T}$ is the image of some $\hat{m} \in \bar{\omega}$ under the ray tracing map $\mathbf{W}$, that is,

$$(p, q, d) = \mathbf{W}(\hat{m}), \quad \hat{m} \in \bar{\omega}. \tag{9}$$

Next, we relate the radiation pattern $I(\hat{m})$ of the input beam to the output radiation pattern $L(\mathbf{W}(\hat{m}))$ on T. This relation is based on the energy conservation law for the energy flow along differential tubes of rays. It will be convenient to obtain this relation in two steps.

Denote by $dxdy$ the area element in Ω. Let

$$Q(\hat{m}) = \mathbf{p}(\hat{m}) + q(\hat{m})\hat{k}.$$

Thus, Q maps $\bar{\omega}$ onto $\bar{\omega}$. The input radiation pattern I and the radiation pattern $\tilde{I}$ produced by P in Ω are related as follows:

$$\tilde{I}dxdy = \tilde{I}|J(Q)|d\sigma = Id\sigma, \tag{10}$$

where $J(Q)$ is the Jacobian determinant of the map Q and $d\sigma$ is the area element on the sphere S.

Let $dpdq$ denote the area element in T. Since $\bar{T}$ is the image of $\bar{\Omega}$ under the ray tracing map $\mathbf{V}$, we have the relation

$$dpdq = |J(\mathbf{V})|dxdy,$$

where J is the Jacobian determinant of the map $\mathbf{V}$.

According to the differential form of the energy conservation law [12], p. 115,

$$L(\mathbf{V}(x, y))J(\mathbf{V}(x, y))dxdy = \pm\tilde{I}(x, y)dxdy. \tag{11}$$

132

We assign a ± sign to the Jacobian according to whether **V** preserves the orientation of Ω or reverses it.

Combining equations (11) with (10) and using (9), we obtain

$$L(\mathbf{W}(\hat{m}))J(\mathbf{V}(x(\hat{m}), y(\hat{m})))J(Q(\hat{m})) = \pm I(\hat{m}). \tag{12}$$

This is the required relation between input and output radiation patterns.

The total energy conservation equation is given by

$$\int_T L(p, q)dpdq = \int_\omega I(\hat{m})d\sigma. \tag{13}$$

It follows from (12) that

$$\int_T L(p, q)dpdq = \int_\omega L(\mathbf{W}(\hat{m}))|J(\mathbf{V}(x(\hat{m}), y(\hat{m})))||J(Q(\hat{m})|d\sigma = \int_\omega I(\hat{m})d\sigma. \tag{14}$$

3 The PDE associated with the equation (12)

It will be convenient to assume that the paraboloid P is parametrized by the x, y variables in the domain $\bar{\Omega}$. This can be easily done and we omit the details. Since

$$\tilde{I}(x, y) = I(x, y)|J(Q^{-1}|, \tag{15}$$

where Q^{-1} is the map inverse to Q, and it is well known that $J(Q) = \rho^2$ we can rewrite the equation (12) in the form

$$L(\mathbf{V}(x, y))J(\mathbf{V}(x, y)) = \pm I(x, y)/\rho^2(x, y). \tag{16}$$

If condition (13) is satisfied then it follows from (14) and (15) that

$$\int_T L(\mathbf{V}(x,y))dxdy = \int_{\bar{\Omega}} \frac{I(x,y)}{\rho^2(x,y)}dxdy. \qquad (17)$$

In the following we restrict our discussion to the case where the "+" is taken in 16. It is shown in [11], formula (14) that under such circumstances the equation (16) implies that the function z describing the first reflector must satisfy the equation

$$L(x + \lambda z_x, y + \lambda z_y)[(1 + \lambda z_{xx})(1 + \lambda z_{yy}) - (\lambda z_{xy})^2] = I\rho^{-2}, \qquad (18)$$

where $\lambda = l' - d$. It is also shown in [11] that the vector function V is given by

$$V(x,y) = (x,y,0) + \lambda(z_x, z_y, 0) + d\hat{k}. \qquad (19)$$

Thus analytically the problem is reduced to finding a function z such that the map (19) maps $\bar{\Omega}$ onto $\bar{T}$ and the equation (18) is satisfied. The theretical results will be presented elsewhere. The main conclusion is that if domains $\bar{\Omega}$ and $\bar{T}$ are convex and the energy balance equation (17) is satisfied the there always exist two (generalized) solutions. One of them is a convex function and this is the one that is of interest.

Once the function z is constructed, one recovers in a unique fashion the second mirror. The corresponding formulas are presented in [11]. The reader will also find in [11] several examples illustrating the technique.

134

4 Conclusions

In this paper we consider the problem of synthesizing a three-reflector system which transforms a given input power pattern into a plane wave with prespecified power pattern on the output aperture. We outline here a new apporach to formulating the problem analytically and use our previous work to analyze the system. The proposed approach allows substantial control over many design parameters. In particular, blockage can be completely avoided.

References

[1] B. E. Kinber. On two reflector antennas. *Radio Eng. Electron. Phys.*, 7(6):973–979, 1962.

[2] B. E. Kinber. Inverse problems of the reflector antennas theory - geometric optics approximation. *preprint No. 38*, pages 1–48, 1984. in Russian.

[3] V. Galindo-Israel, R. Mittra, and A. G. Cha. Aperture amplitude and phase control on offset dual reflectors. *IEEE Transactions on Antennas and Propagation*, AP-27:154–164, 1979.

[4] V. Galindo-Israel, W. A. Imbriale, and R. Mittra. On the theory of the synthesis of single and dual offset shaped reflector antennas. *IEEE Transactions on Antennas and Propagation*, AP-35(8):887–896, 1987.

[5] V. Galindo Israel, W. A. Imbriale, R. Mittra, and K. Shogen. On the theory of the synthesis of offset dual-shpaed reflectors – case examples. *IEEE Transactions on Antennas and Propagation*, 39(5):620–626, May 1991.

[6] B. S. Westcott, F. A. Stevens, and F. Brickell. Go synthesis of offset dual reflectors. *IEE Proceedings : H*, 128(1):11–18, February 1981.

[7] B. S. Westcott. *Shaped Reflector Antenna Design*. Research Studies Press, Letchworth, UK, 1983.

[8] B.S. Westcott, R. K. Graham, and I. C. Wolton. Synthsis of dual-offset shaped reflectors for arbitrary aperture shapes using continuous domain deformation. *IEE Proceedings:H*, 133(1):57–64, February 1986.

[9] C. J. Sletten. Reflector antennas and surface shaping techniques. In C. J. Sletten, editor, *Reflector and Lens Antennas*. Artech House, Norwood, MA, 1988.

[10] W. V. T. Rusch. Quasioptical antenna design (section 3.4). In A. W. Rudge, K. Milne, A. D. Olver, and P. Knight, editors, *The handbook of antenna design, Volumes 1 and 2*. Peter Peregrims Ltd., London, UK, 1986.

[11] V. Oliker and L. Prussner. A new technique for synthesis of ofset dual reflector systems. In *10-th Annual Review of Progress in Applied Computational Electromagnetics*, pages 45–52. A.C.E.S., Monterey, 1994.

[12] M. Born and E. Wolf. *Principles of Optics*. Pergamon Press, 4 edition, 1970.

MONOPULSE STICK PHASED ARRAY

Richard Kinsey

Sensis Corporation

5793 Widewaters Parkway

DeWitt, NY 13214

Abstract: Planar array antennas have often been formed by stacking edge-slotted waveguides (sticks) to obtain low sidelobes, light weight and low cost. A beamforming network with a phase shifter at each stick port, may provide one-dimensional monopulse and one-dimensional phase scanning in the plane orthogonal to the sticks. Previous attempts to add monopulse in the plane of the sticks have been made, but without much success. This has usually involved forming a pair of overlapped pencil beams which are combined in a hybrid to form Σ and Δ patterns. However, monopulse tracking performance using this approach is rather poor ($\approx$-5 dB) compared to Taylor/Bayliss patterns with similar sidelobe levels. A superior configuration involves interleaving a Σ array and a Δ array which are independent of one another by virtue of their orthogonal excitations. However, as only the sum array is used for transmit, the maximum RF power is limited to the combined power handling of one-half the array phase shifters including the effects of amplitude taper. A new Monopulse Stick Phased Array (MSPA) configuration has been developed that provides dual-plane monopulse, one-dimensional phase scanning, and uses all array phase shifters on transmit thereby doubling RF power capability.

1.0 Introduction

Situated between the surveillance capabilities of reflector type antennas and fully phased arrays are rotating planar arrays with electronic scanning in elevation. Antenna apertures formed by stacking edge-slotted row waveguides offer attractive advantages in terms of weight and cost but have a significant shortcoming with monopulse only in the plane orthogonal to the sticks. In such a case, target location in azimuth relies on run length estimation (beam splitting using the sequence of radar returns as the antenna beam rotates through the target

138

position). This "track-while-scan" technique is less accurate than monopulse, more susceptible to ECM, and not well suited to a dense target environment. An attractive improvement would be an antenna that retains the weight and cost advantages of an edge-slotted waveguide planar array while also providing dual-plane monopulse, wide frequency bandwidth, and one-axis phase scanning.

A number of prior attempts to obtain monopulse from traveling wave linear arrays have usually involved a pair of overlapped pencil beams which are combined in a hybrid to obtain sum and difference outputs. This pair of pencil beams may be obtained from a pair of interleaved arrays [1], or by slotted waveguides that operate in either of two different modes of excitation with separate hybrid ports for each mode [2]. A significant limitation of these overlapped beam techniques has been the relatively poor monopulse performance obtained with these non-ideal array excitations. Additionally, departures from the RF design frequency tend to change the angular overlap between the pair of beams in addition to the nominal change in beam squint (off-broadside pointing angle). This further degrades the sum pattern beamwidth and the difference pattern error slope.

1.1 The Fundamental Approach

It is instructive to consider the aperture field from a uniform incident plane wave. Referring to Fig. 1, the incident wavefront is mathematically described by

$$E^i = e^{jkp} = e^{jk(z \cos \theta + x \sin \theta)} \tag{1}$$

where $k = 2\pi/\lambda$ and the time variation $e^{j\omega t}$ is suppressed.
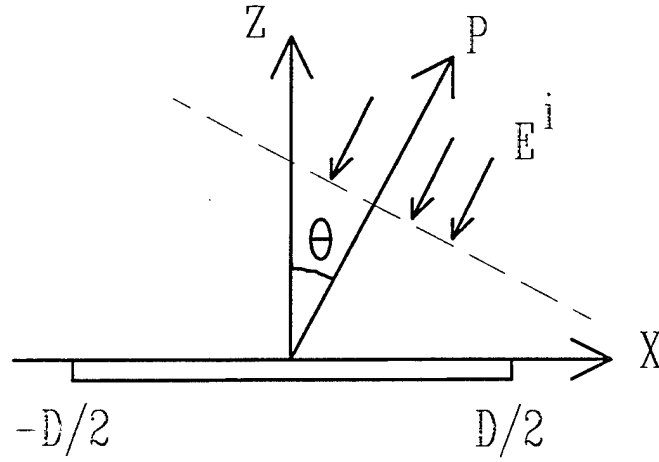
Fig. 1 Incident Uniform Plane Wave

Along the aperture plane (z=0), the incident plane wave is composed of even and odd components in *phase quadrature* as shown by (1) which reduces to

$$E\big|_{z=0} = e^{jk(x \sin \theta)} = E_e + j\, E_o \tag{2}$$

where $E_e = \cos(kx \sin \theta)$ and $E_o = \sin(kx \sin \theta)$

Let $x' = x/D$, so that $-\frac{1}{2} \leq x' \leq \frac{1}{2}$, and let $u = D/\lambda \sin\theta$. Substituting in (2) will give

$$E_e = \cos(2\pi u x') \tag{3}$$

$$E_o = \sin(2\pi u x') \tag{4}$$

Ideal monopulse sum and difference aperture tapers can also be expressed in terms of even and odd components. For example, if f(x') is the aperture excitation, expressions for Taylor [3] and Bayliss [4] amplitude tapers can be written in the same functional form as the even and odd aperture field components in (3) and (4), where the integer $\bar{n}$ defines the region of controlled pattern sidelobes. The 35 dB, $\bar{n}=5$ amplitude tapers illustrated in Fig. 2 will be the basis for the concept descriptions that follow later in this section.
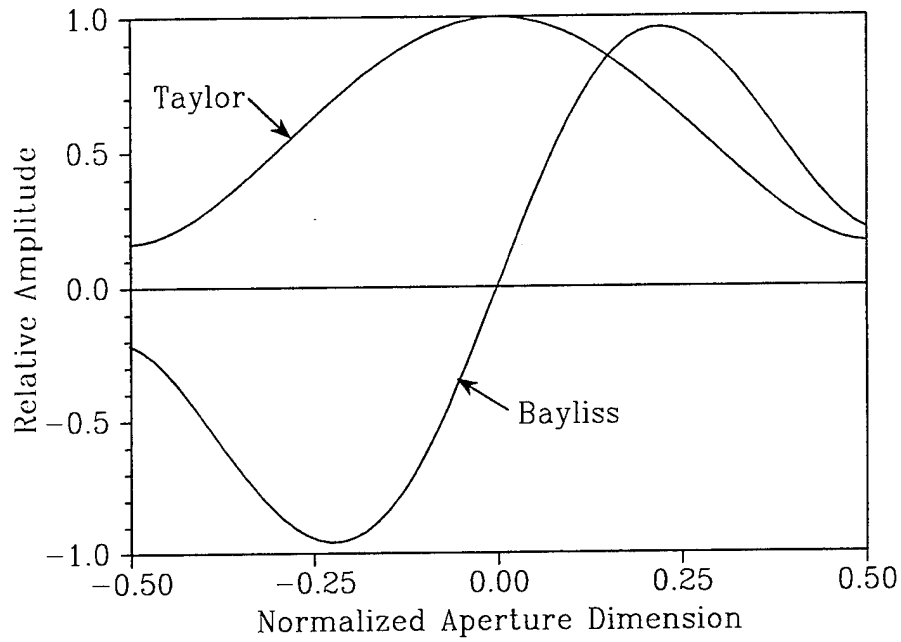
Fig. 2 Independent Sum (Taylor) and Difference (Bayliss) Amplitude Tapers

Taylor

$$f_\Sigma(x') = \sum_{i=1}^{\bar{n}} A_i \cos[2\pi(i-1)x']$$ (5)

Bayliss

$$f_\Delta(x') = \sum_{i=1}^{\bar{n}} B_i \sin[2\pi(i-\frac{1}{2})x']$$ (6)

The field component E_e in (3) couples only with $f_\Sigma(x')$ in (5) and the field component E_o in (4) couples only with $f_\Delta(x')$ in (6). Note that if the antenna implementation is such that $f_\Delta(x')$ is in phase quadrature with $f_\Sigma(x')$, the array sum and difference outputs will be co-phasal or anti-phasal with respect to one another because of the quadrature relation of the odd and even field components they couple to as shown by (2). Similarly, if $f_\Delta(x')$ and $f_\Sigma(x')$ are both real (co-phasal

141

and anti-phasal), they will have array outputs in phase quadrature for the same reason. Historically, the first case has been referred to as "amplitude monopulse" while the second case has been termed "phase monopulse". For an array antenna with independent sum and difference excitations, the distinction is meaningless since the array monopulse gain and error slope are the same for either case.

By interleaving two arrays of slotted waveguides, one providing an even (sum) excitation and the other providing an odd (difference) excitation, the field components contributing to the monopulse sum and difference signals may be separated in the array aperture itself rather than in separate beamforming networks located behind the array elements [5]. In theory, the sum beam gain and the difference pattern error slope are each realized without any additional loss due to the presence of the other interleaved array. It should be noted that the spacing of adjacent sticks in an interleaved array must be one-half the spacing of a conventional array for a given beam scan requirement in order that no undesired grating lobes shall appear in visible space. In contrast to the technique of forming monopulse from a pair of overlapped beams, the beam squint for sum and difference interleaved arrays is designed to be the same for both. This has the advantage that the waveguide propagation velocity and slot spacing for both arrays may also be the same with the result that sum and difference patterns remain coincident with changes in RF frequency.

In spite of these advantages, one shortcoming of this approach is the fact that only *one* of the interleaved arrays (the sum) is used on transmit for target illumination.

Although phase shifters are required at the input to each slotted waveguide, for beam steering in the orthogonal plane, the maximum array RF power is limited by the combined power handling capability of only one-half these phase shifters. This may impose an undesired limit on transmitter power, especially at high RF frequencies, or else unnecessarily increase phase shifter costs.

2.0 The MSPA Concept

The MSPA planar array aperture is formed by stacking traveling-wave type linear arrays (sticks). The odd-numbered sticks have an excitation different from the even-numbered sticks. These two excitations are derived from a combination of independent sum and difference amplitude tapers. Maximizing the RF power capability of the antenna, by utilizing phase shifters for both interleaved arrays, means that *all* sticks must couple to the even field components as well as the odd. If $f_o(x')$ is the excitation for the array of odd numbered sticks and $f_e(x')$ is the excitation for the array of even numbered sticks, then two candidate excitations that fulfill this objective can be expressed in canonical form as follows.

Complex Excitations

$$f_o(x') = f_\Sigma(x') - jf_\Delta(x') \tag{7}$$

$$f_e(x') = f_\Sigma(x') + jf_\Delta(x') \tag{8}$$

Real Excitations

$$f_o(x') = f_\Sigma(x') - f_\Delta(x') \tag{9}$$

$$f_e(x') = f_\Sigma(x') + f_\Delta(x') \tag{10}$$

If adjacent odd and even sticks are combined in a hybrid, the aperture excitation from the pair will be $f_\Sigma(x')$ for an input at the sum port and $jf_\Delta(x')$ or $f_\Delta(x')$ for the difference port (Complex or Real Excitations respectively).

2.1 Complex Excitations

Consider the Complex excitations first. The $f_0(x')$ and $f_e(x')$ in (7) and (8), obtained by combining (5) and (6) will both have the same amplitude taper but opposite (non-linear) phase characteristics. A -35 dB design SLL was used to compute the graphs in Fig. 3 and Fig. 4. The nominal beam squint was removed so that the phase characteristics are more clearly evident. The resulting far-field patterns from both the odd and even stick excitations are shown in Fig. 5 and can be seen to be mirror images of one another about the vertical reference axis. If the odd and even stick ports are summed in a hybrid comparator, the resulting patterns at the hybrid outputs will be Taylor and Bayliss (Fig. 6).

The non-linear phase characteristics of these Complex Excitations make them unattractive for a practical edge-slotted array. However, it should be evident from these results that the prior monopulse technique of overlapping a pair of pencil beams is actually a crude approximation to the optimum stick patterns. While the sum and difference pattern sidelobes obtained with the overlapped beam technique may be acceptable, the loss in gain and angular sensitivity are substantial (a 1.6 dB gain loss and 3 dB loss in angular sensitivity are typical, giving close to a 5 dB loss in skin tracking performance).
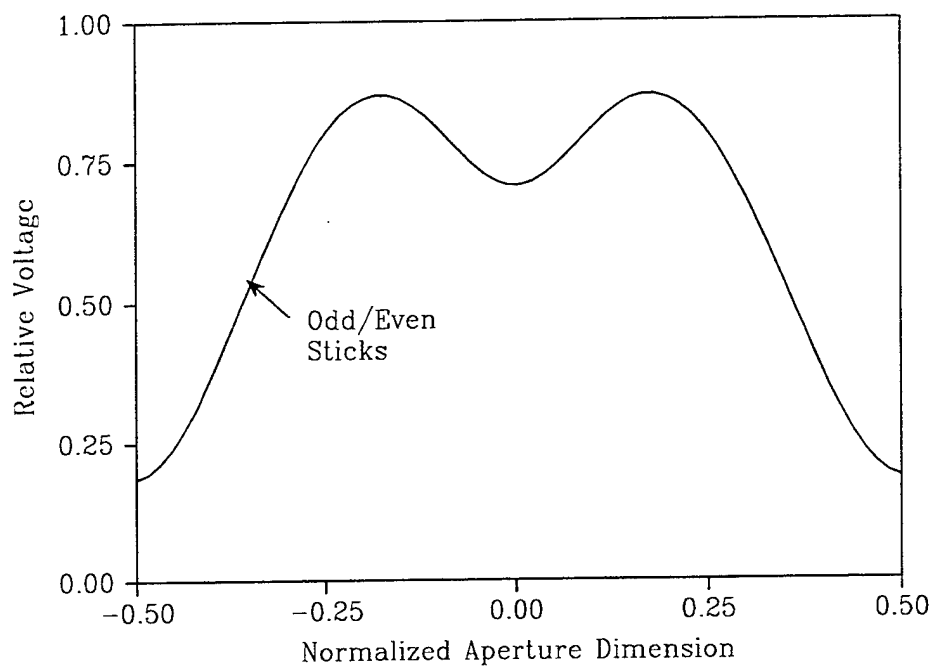
Fig. 3 Complex Excitation Amplitude Taper
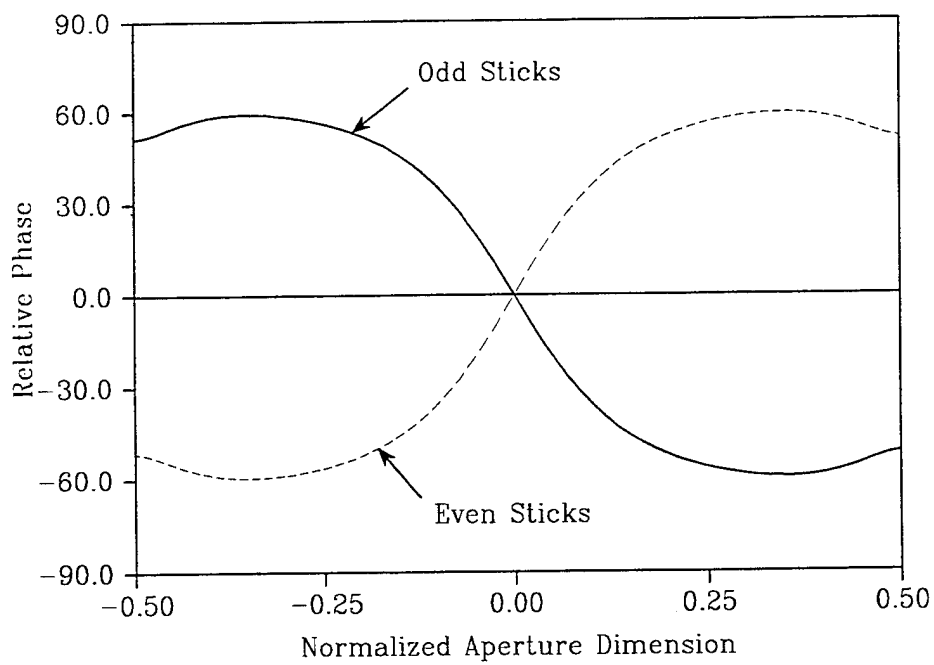
Fig. 4 Complex Excitation Phase Tapers

145
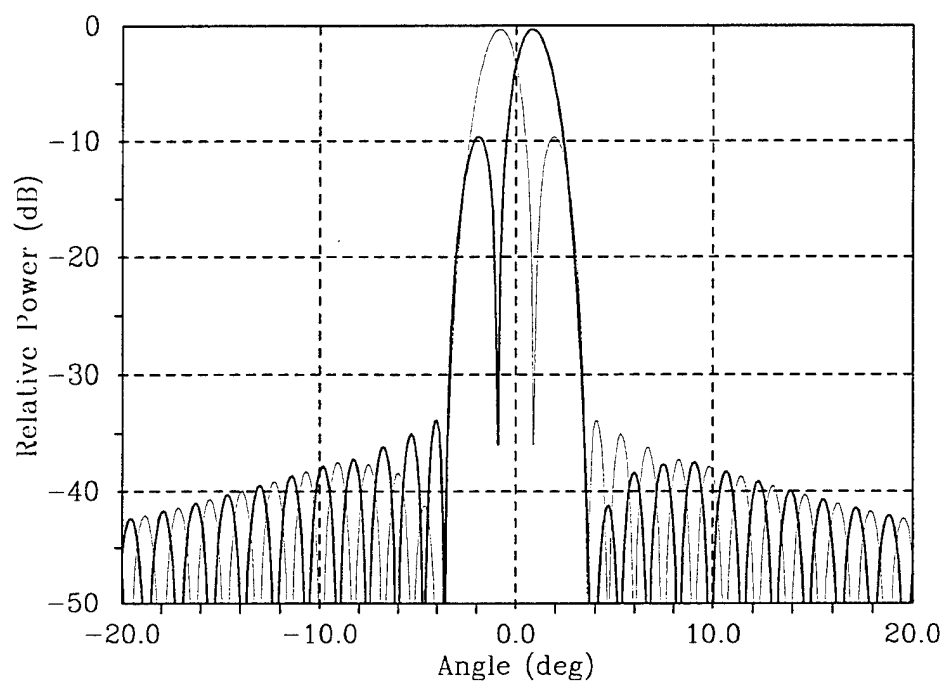
Fig. 5 Far-Field Patterns from Individual Odd and Even Complex Excitations
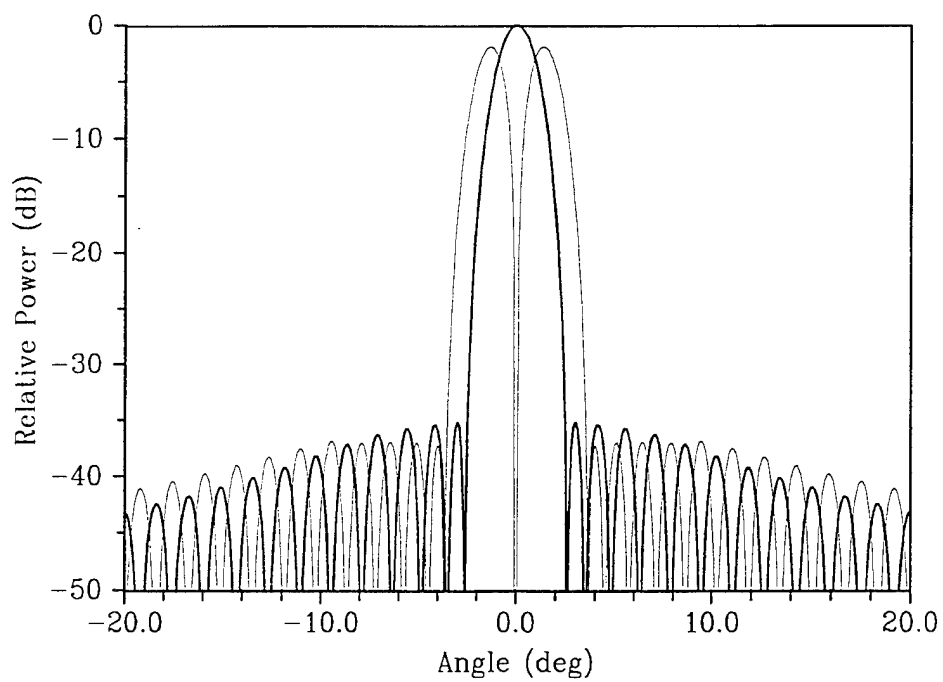
Fig. 6 Theoretical Far-Field Patterns From a Hybrid Combined Row Pair

146
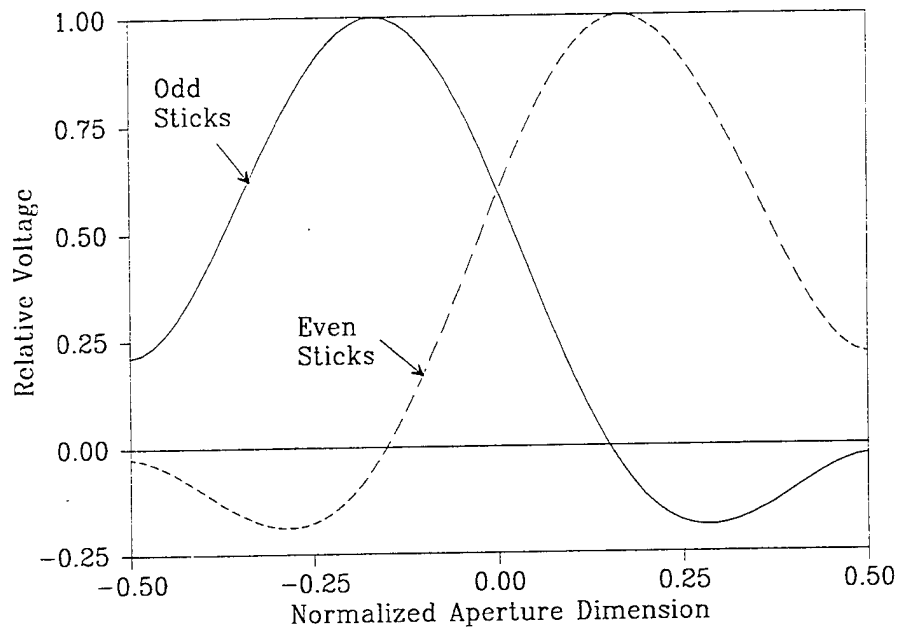
Fig. 7 Odd and Even Stick Excitations

2.2 Real Excitations

The Real Excitations in (9) and (10) have the same theoretical advantages as the Complex Excitations just described but also readily lend themselves to practical stick implementation. Since the $f_o(x')$ and $f_e(x')$ are the arithmetic sum and difference of Taylor and Bayliss amplitude tapers, they yield real rather than complex excitations. These are shown in Fig. 7 for the same 35 dB design sidelobe level as before. Note that the excitation amplitude of a waveguide edge-slot is controlled by the angle of the slot tilt and that changing the tilt from a + angle to a − angle introduces a 180° phase change in this excitation. Since the $f_o(x')$ and $f_e(x')$ excitations both enjoy the same linear beam squint, the slot spacing is uniform and the additional 180° phase change required at the point where an excitation goes negative is simply introduced by changing the direction

147

of the slot tilt. Combining each pair of neighboring sticks (odd and even) in a 3 dB hybrid recovers the row-pair Σ and Δ outputs. However, these row-pair Σ and Δ outputs can instead be formed on the *transmitter* side of the phase shifters by first combining all the odd rows and all the even rows in separate column beamformers (Fig. 8). In this case, *all* phase shifters share the transmit power thereby doubling the array RF power capability. Monopulse in the plane orthogonal to the sticks is obtained in the conventional manner, by combining the individual linear array outputs in beamforming networks that form independent sum and difference patterns. A single pair of hybrid-tees then combine the beamformer ports to obtain the full monopulse set of Σ, Δ_{az} and Δ_{el}.
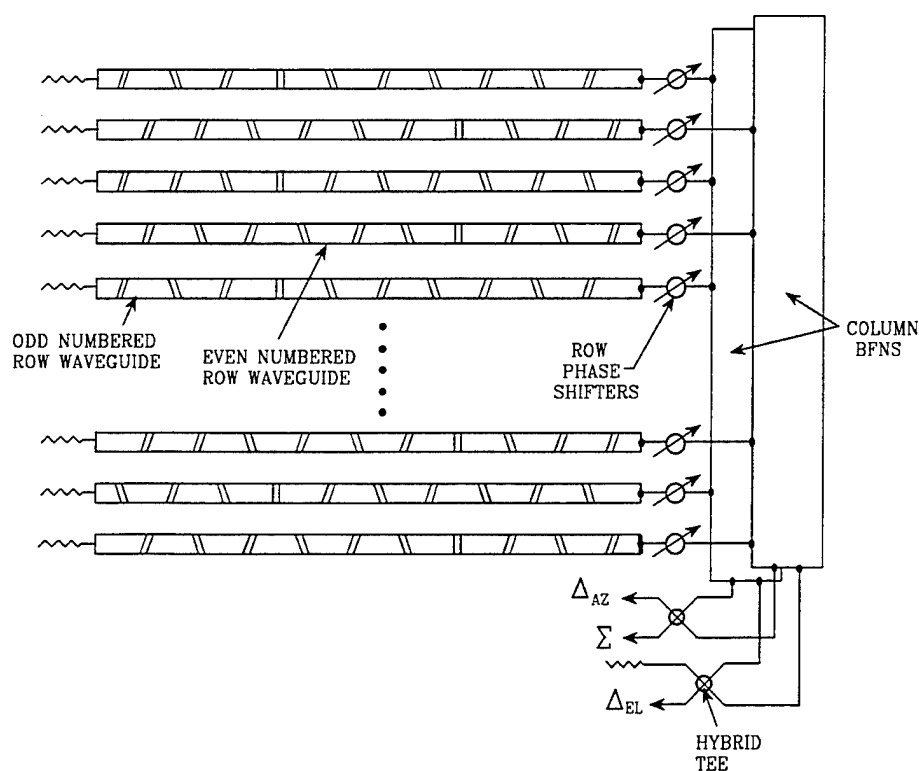
Fig. 8 Block Diagram of Array Architecture

3.0 Demonstration Array

3.1 Architecture

To demonstrate the feasibility of the MSPA design concept, a full scale planar array was developed. The most useful configuration for eventual test and evaluation was one that could utilize the existing Phalanx Radar test facility at Dahlgren, VA. With this in mind, the antenna was to be provided with the means to mount it within a Phalanx Radar Servo Structure in place of the existing track reflector. Design goals were based on improved sidelobe performance while providing electronic scan in azimuth with similar beamwidths and antenna gain.

<u>Table 1 Initial Antenna Design Goals</u>

RF Frequency	Ku-Band
Agile Bandwidth	10%
Monopulse	Az and El
Aperture Size	Maximize
HPBWs (track reflector)	2.6° az. x 1.5° el.
Gain	36.5 dBi
Polarization	Linear Vertical
Az and El SLL	<-30 dB
Azimuth Electronic Scan Sector	70° to 90°
RF Input Power Capability	25 kWp, 1 kWa
Antenna Weight	50 lbs.
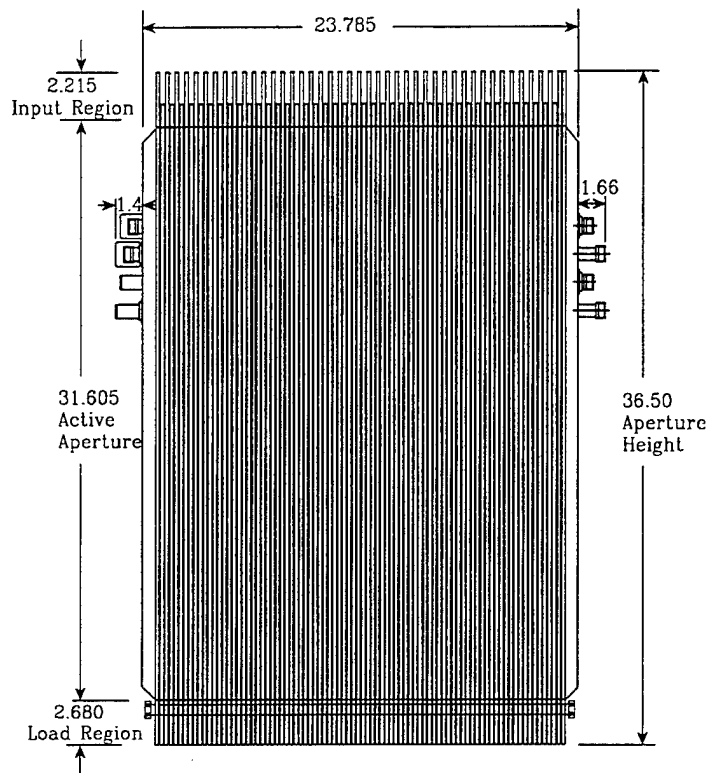
Fig. 9 A Front View of the Array Aperture

The largest array aperture that can fit in place of the reflector, and assure minimum antenna clearances of 0.5 inches under all possible gimbal motions, is 3 ft. by 2 ft. Fig. 9 illustrates the active slotted region, the input region and the load region of the array face. A linear waveguide feed along the bottom of the array permits a signal to be injected into the sticks for test purposes. Two support cradles pick up the array at the rear edges of the aperture backing plate and provide three attachment pads that mate with the bosses previously used to mount the reflector. The phase shifters, monopulse BFNs (Beam Forming Networks), and phase shifter driver box, all mount to the back of the array. The BSC (Beam Steering Controller) and dc power supplies are connected to the array by cables.

150
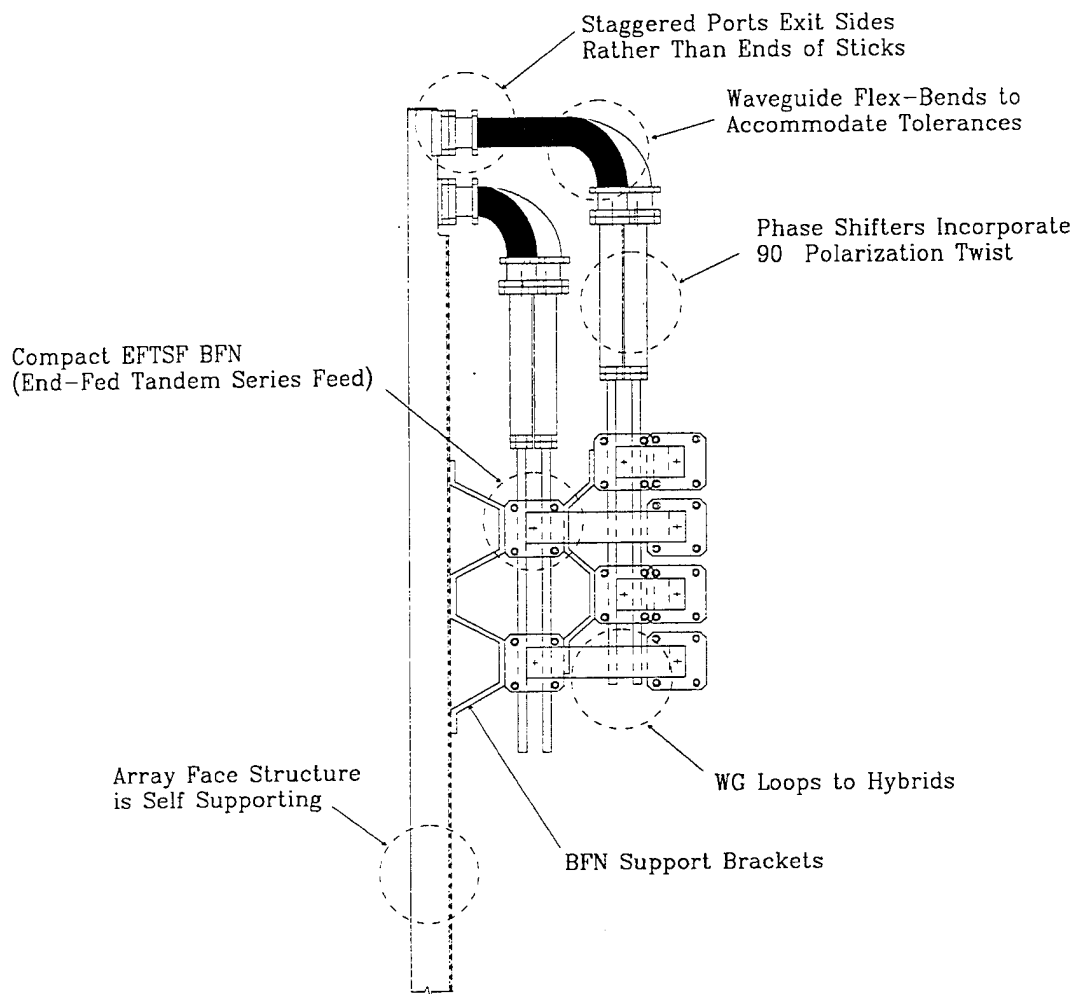
Fig. 10 Side View of Array Component Packaging

Several innovations that make the phasing/beamforming assembly very compact are illustrated in Fig. 10. First, the waveguide sticks incorporate an H-plane bend in the feed end so that the input ports are at the rear of the array rather than the top end of the sticks. This allows the odd and even arrays to have their flanges offset above and below each other permitting the same half-height waveguide flanges to be used throughout the array. The waveguide length differences resulting from the

151

stagger in flange locations and the offset in the BFNs, is equalized by the waveguide loops connecting the feed ports to the 3 dB hybrids.

Second, the flange offset permits two identical BFNs to be used with their corresponding Σ and Δ ports offset the exact amount necessary to mate with a standard hybrid-tee panty adapter. This simplifies the waveguide runs and minimizes the depth of the beamforming assembly. The transmit power is divided equally between the two BFNs which provide a large area heat sink for the phase shifter and feed losses. At the load ends of the BFNs, ambient air-cooled waveguide loads must each handle only 1/2 the total main-line load loss.

Third, the waveguide twist normally required between the stick ports and the BFN ports is incorporated in the phase shifter itself at no additional length. This is possible because dual-mode reciprocal phase shifters have circular polarizers at either end and orientation of the waveguide interface is arbitrary. While the length of the phase shifters is only 3.5 inches, note that they can be either shorter or longer without affecting the basic design layout.

Finally, waveguide phasing loops between the BFNs and the hybrids at the rear can easily be shimmed if necessary to correct errors in electrical path length.

The stick spacing in the array aperture is very tight to permit scanning an azimuth sector of 70° or more. As there is essentially no room between adjacent sticks for mounting hardware, a new approach to the array face construction was employed.

3.2 Array Construction
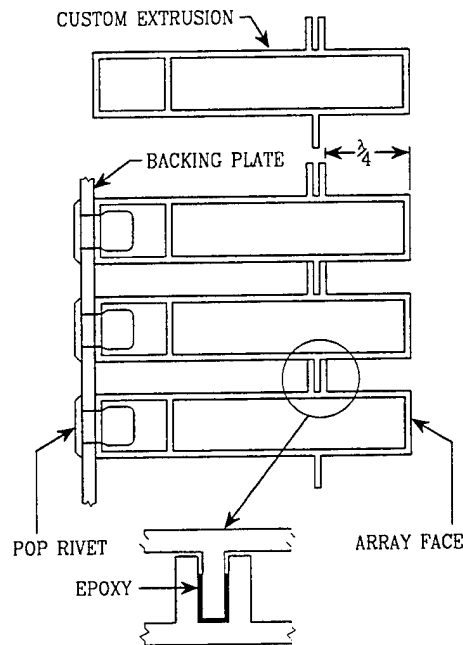
Fig. 11 Array Face Construction Technique

Illustrated by the cross-sectional view in Fig. 11, are custom aluminum extrusions designed with a rivet box at the back of the waveguide and broadwall tabs at the short-circuit position, one-quarter wavelength behind the array face. By pop riveting the waveguides to a backing plate and epoxy bonding the interleaved tabs, the waveguides become part of the array structure and provide a rigid but lightweight aperture. Pre-boring the backing plate and rivet box holes in the waveguides assures precise alignment while retaining a simple assembly procedure. After riveting a waveguide, epoxy is applied to the groove (Fig. 12) after which the next stick is added and riveted to the backing plate. The assembly proceeds by sequentially adding sticks one above the other (Fig. 13).

153
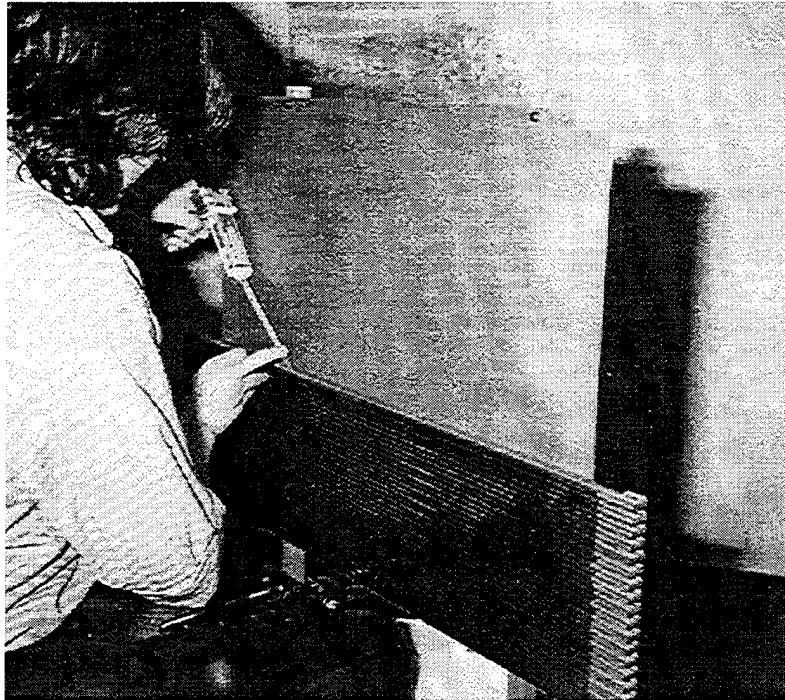
Fig. 12 Applying the Epoxy Adhesive to a Stick
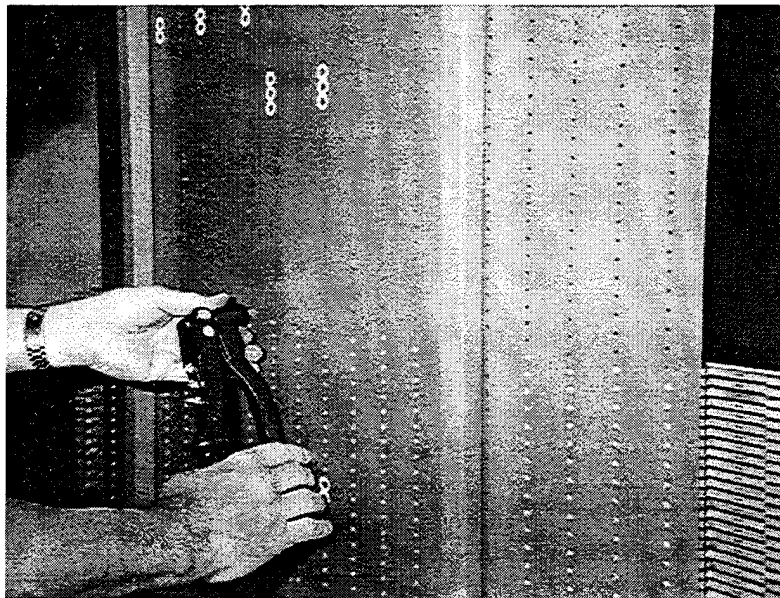
Fig. 13 Riveting the Sticks to the Backing Plate

The phase shifters are reciprocal dual-mode latching ferrite units manufactured by MAG (Microwave Applications Group). Average insertion loss is 0.6 dB and each unit weighs less than 1.5 ozs. Rated RF power level is 650 Wp and 20 Wa. Each driver card accepts 8-bit phase shifter commands and switches 32 phase shifters at 1 kHz maximum. Input and output flanges are oriented at 90° with respect to each other. This eliminates a waveguide twist that would otherwise be required to mate the phase shifters with the cross-guide couplers of the BFN. Fig. 15 illustrates the internal elements of a dual-mode phase shifter.
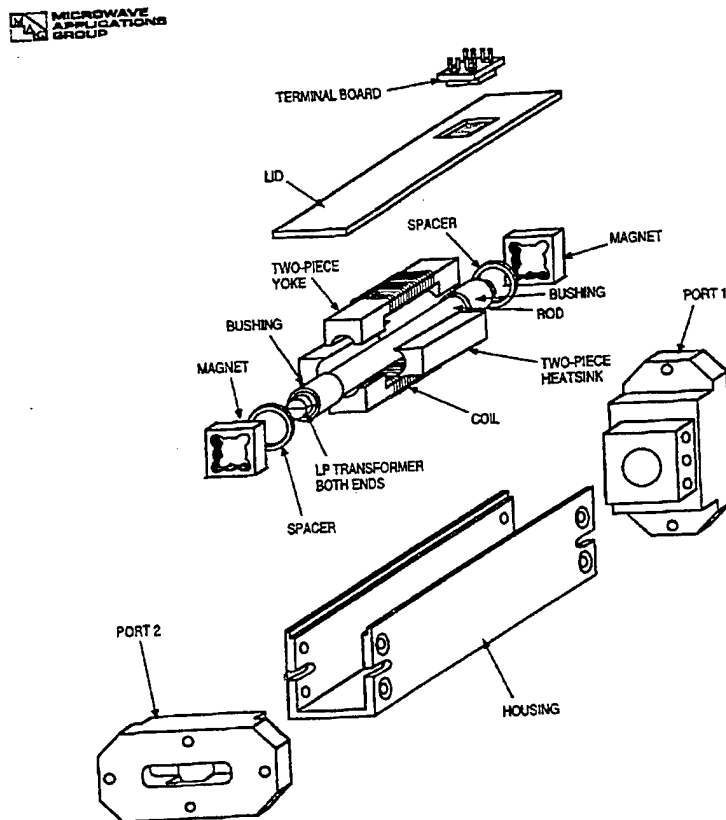
Fig. 14 Exploded View of Ku-Band Dual-Mode Phase Shifter

A schematic diagram for the azimuth BFNs is shown in Fig. 15. Cross-guide couplers in the Σ and Δ feedlines provide independent excitations at the antenna ports. Matched dielectric phase shifters in the cross-guides between the Σ and Δ feedlines compensate for the differences in coupler phase lags.
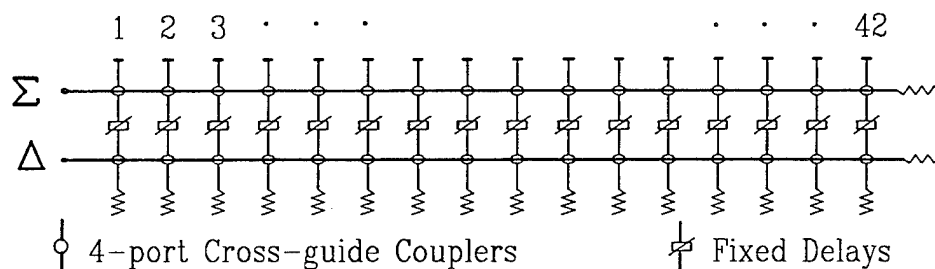
Fig. 15 Schematic Diagram of an End-Fed Tandem Series Feed BFN
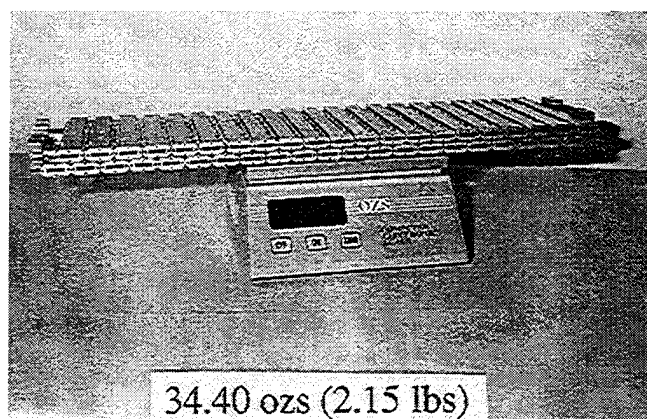
Fig. 16 Completed 42 Port Ku-Band BFN

Fig. 16 shows one of the two identical BFNs. The construction technique for the cross-guide couplers utilize specially extruded thin wall waveguide with broadwalls extended to form longitudinal fins along the sides. The 4 corners of each waveguide coupler, where the fins overlap, may be fastened with screws or rivets (screws in this case). The cross-guides are half-height WR62 while the main guide is full height WR62 to minimize ohmic losses.

156
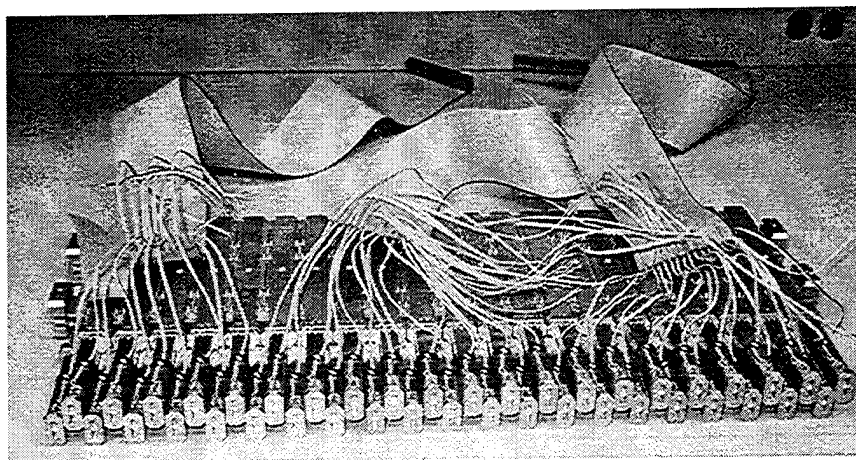
Fig. 17 Phase Shifters Mounted on the BFN

As shown by the photograph in Fig. 17, the phase shifters were mounted on each of the two BFNs and the ribbon cable drive wires connected (3 per shifter) before mounting the assembly on the array. Fig. 18 shows the array face down nearing the final stages of assembly. The two BFNs mount one above the other with the phase shifter drive cables between them. Waveguide runs connecting the hybrids to the BFNs, and the phase shifter driver box mounted below them, are also visible. The completed antenna is shown in the photographs of Figs. 19 and 20.
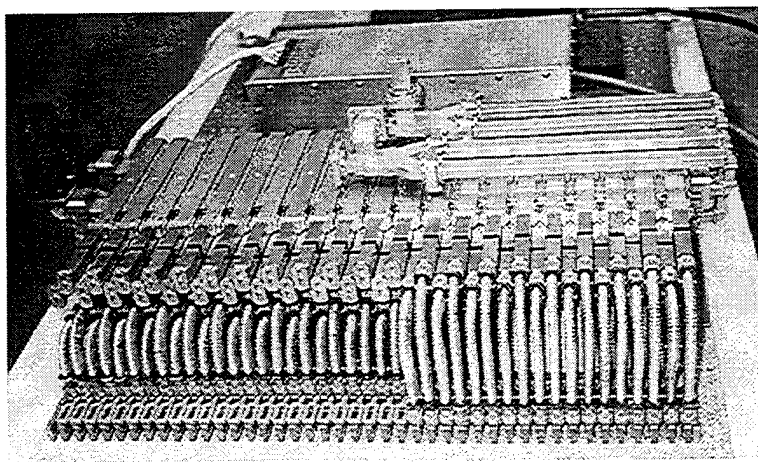
Fig. 18 Adding the Flexible Waveguide Bends
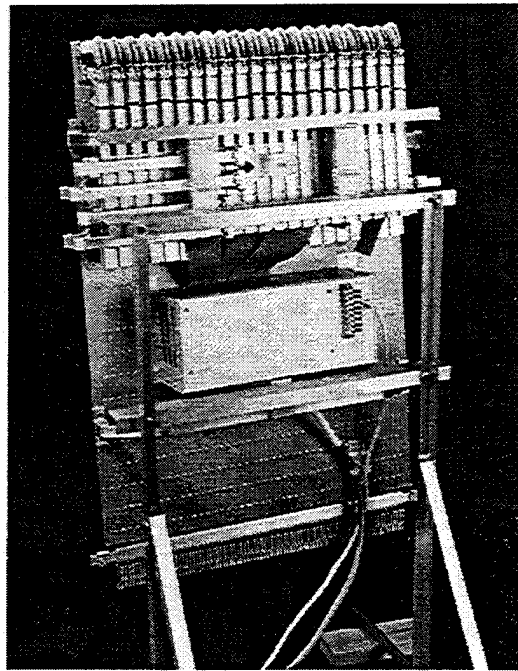
Fig. 19 A Rear View of the Completed Array Antenna

Fig. 20 The Antenna Installed in a Phalanx RSS with the Radome Removed

4.0 Array Performance

A compilation of antenna performance parameters is presented in Table 2. These are either measured or calculated from available experimental data and are believed to fairly represent the performance of the demonstration antenna.

Table 2 Array Performance Characteristics

RF Frequency	Ku-Band
Agile Bandwidth	10%
Monopulse	Az and El
Overall Aperture Size	.93 m vert x .60 m horiz
Active Aperture Size	.80 m vert x .55 m horiz
Polarization	Linear Vertical
Mid-band Gain (Hybrid Σ Port)	36.5 dBi
HPBWs	2.8° az x 2.0° el
Azimuth SLL	<-30 dB
Elevation SLL (after 1st)	<-30 dB
El Beam Squint (midband)	8.4°
Beam Squint Sensitivity	$\frac{2}{3}$°/100 MHz
No. Phase Shifters	84
Azimuth Phase Scan (midband)	±35°
Beam-to-beam Sw Rate	1 kHz
Beam Re-phasing Time	60 µs
Max RF Power:	26 kWp, 800 Wa
Antenna Weight (meas)	49.25 lbs.

Array gain computations are tabulated in Table 3. Taper efficiency at the low-, mid-, and high-band frequencies were computed from measurements of BFN excitations and from near-field probe data for the sticks. Tabulated component ohmic losses are an average of the measurements made at each frequency.

Table 3 Array Gain Computations

	Fmid-5%	Fmid	Fmid+5%
Area Gain	40.19	40.65	41.08
Azimuth Taper Gain Factor	-1.01	-1.16	-1.38
Stick (pair) Taper Gain Factor	-1.10	-1.14	-1.35
Error Effects	-0.10	-0.10	-0.10
Directivity	37.98	38.37	38.25
Ohmic Losses			
Stick WG	0.19	0.18	0.17
Stick load	0.62	0.17	0.34
Flex Bends	0.10	0.10	0.10
Phase Shifter	0.60	0.60	0.60
EFTSF	0.90	0.70	0.70
Hybrid and WG Loops	0.16	0.15	0.14
Total	2.57	1.90	2.05
Array Gain	35.41	36.47	36.20

The original weight goal for the (gimbaled) array was 50 pounds. This included the array face, phasing and beamforming assemblies, phase shifter drivers, and array mounting cradles but excluded d-c power supplies (7 pounds) which are mounted inside the RSS but off the array. A detailed weight budget was carried throughout the course of the contract. Calculated and estimated weights were replaced with measured weights as they became available. A high level summary of the final measured weights is presented in Table 4.

Table 4. Major Component Weight Tabulation

Sticks	13.80
Aperture Backing Plate and Assembly Hardware	4.40
Flex Bends	5.44
Phase Shifters	8.58
Phase Shifter Driver Box	6.42
Azimuth BFN (incl. hybrids)	6.41
Supports and Hardware	4.20
Total Measured Antenna Weight	**49.25 lbs.**

4.1 Stick Measurements

Two neighboring sticks (odd and even), located about one-third of the way across the aperture width, were near-field probed at Fmid. The holographic amplitude and phase for each stick is shown in Figs. 21 and 22 with the ideal design curves dotted. Probe data at other frequencies within the band gave similar plots. Additional stick design iterations should reduce the excitation errors which mainly affect the first one or two sidelobes. Far-field patterns for this stick pair, computed from the near-field probe data, are shown in Figs. 23-27 for 5 frequencies across the 10% band. The goal of sidelobes below 30 dB (after the first) appears quite realistic as there is no averaging effect of uncorrelated errors for a single pair of sticks as there would be for the full array. Program funding was not sufficient to provide for far-field pattern measurements on the full array. However, based on measurements of the edge-slot H-plane pattern in an array environment, and on tests using the calibration feed to inject signals in all the sticks, sidelobes in the scan plane are expected to remain below -30 dB.

161
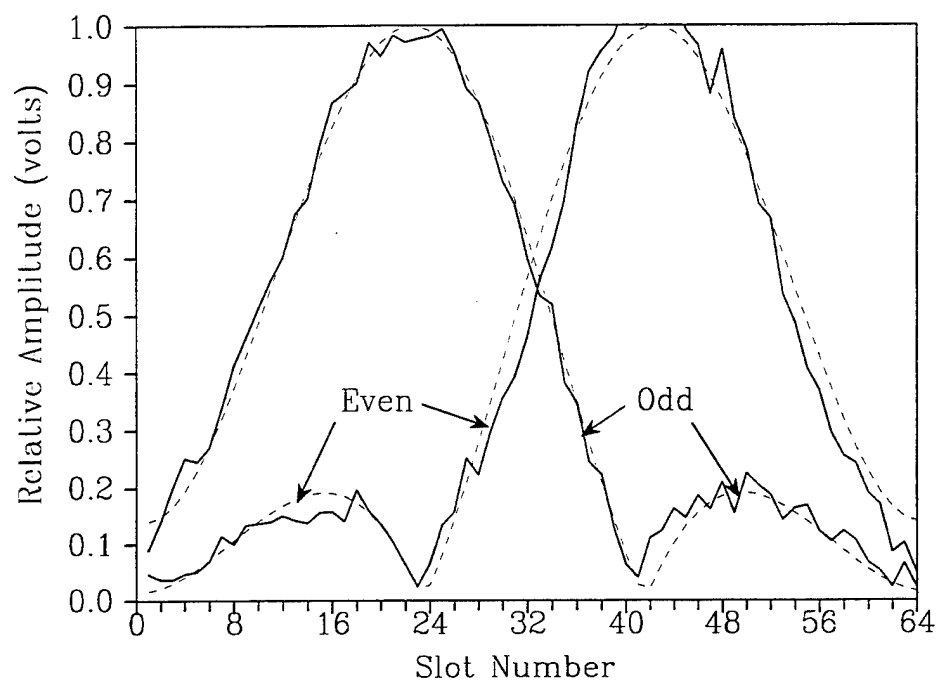
Fig. 21 Odd and Even Stick Probed Excitation Amplitude at Fmid
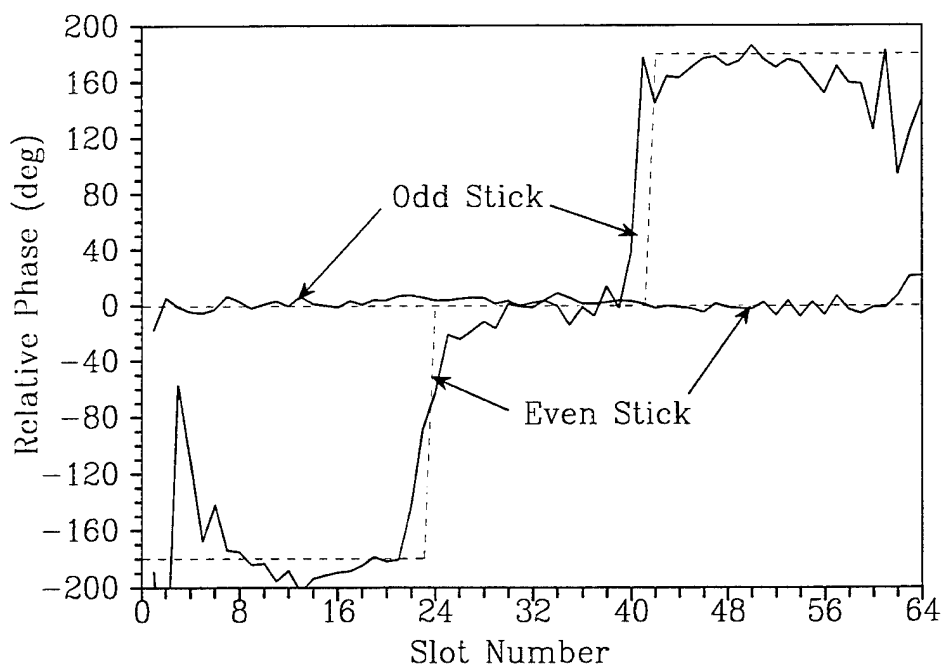
Fig. 22 Odd and Even Stick Probed Excitation Phase at Fmid
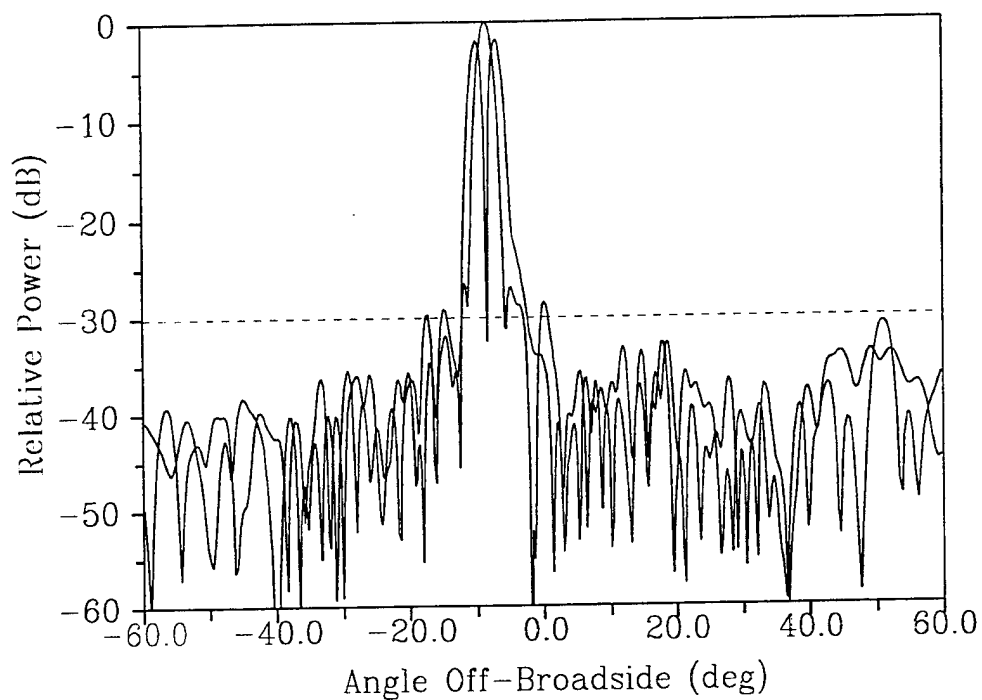
Fig. 23 Stick -Pair Monopulse Patterns at Fmid
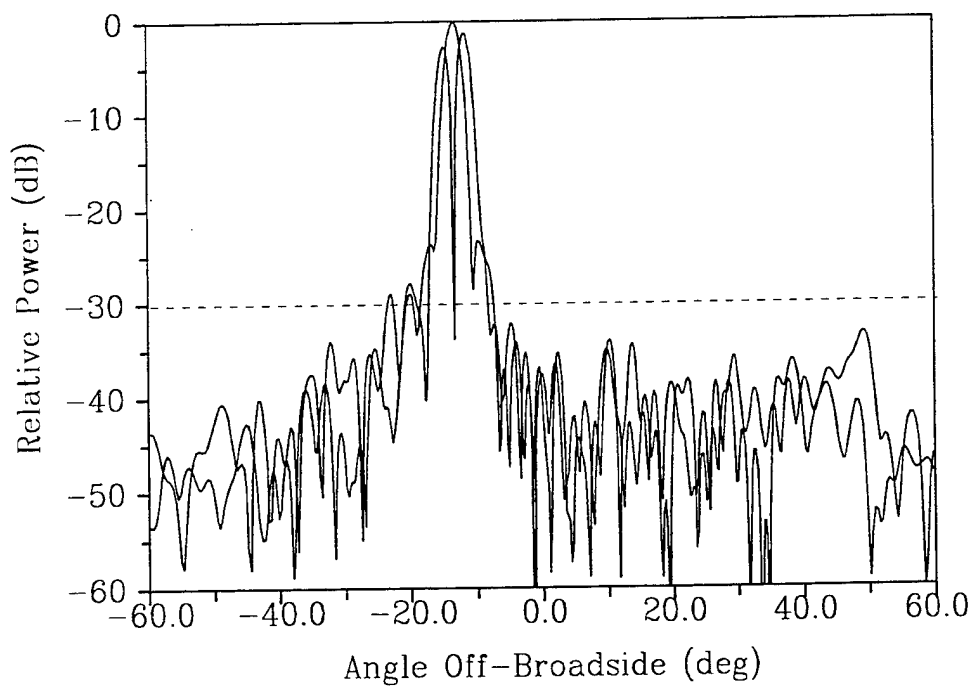
Fig. 24 Stick-Pair Monopulse Patterns at Fmid-5%

163
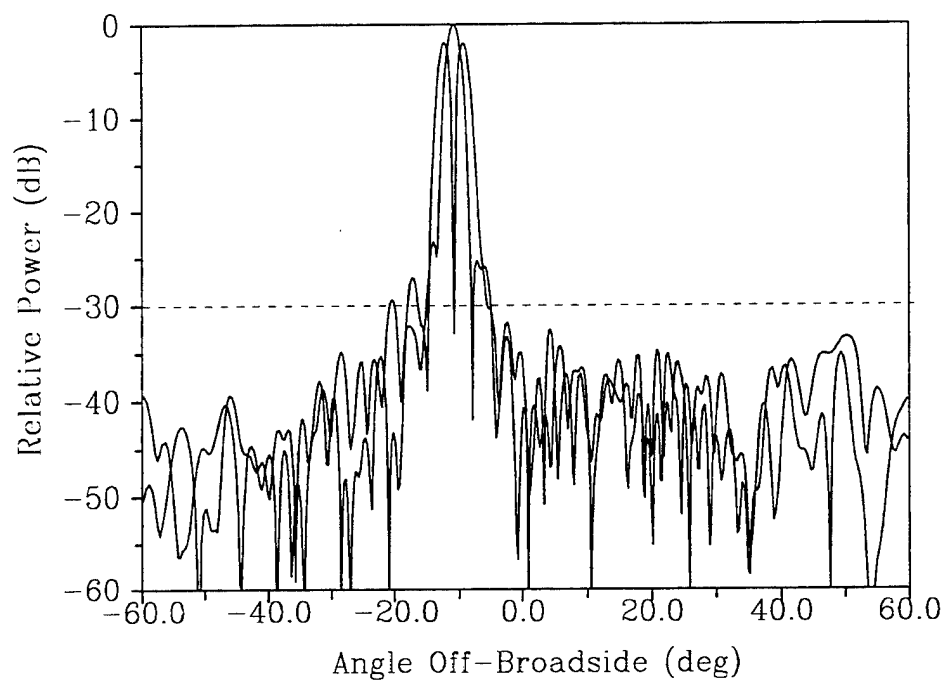
Fig. 25 Stick-Pair Monopulse Patterns at Fmid-2.5%
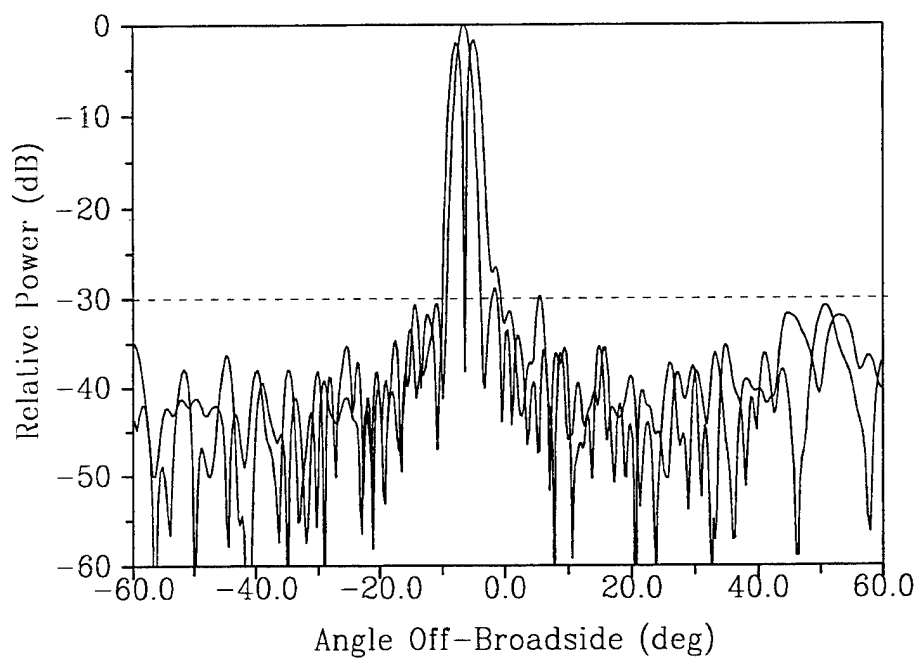
Fig. 26 Stick-Pair Monopulse Patterns at Fmid+2.5%
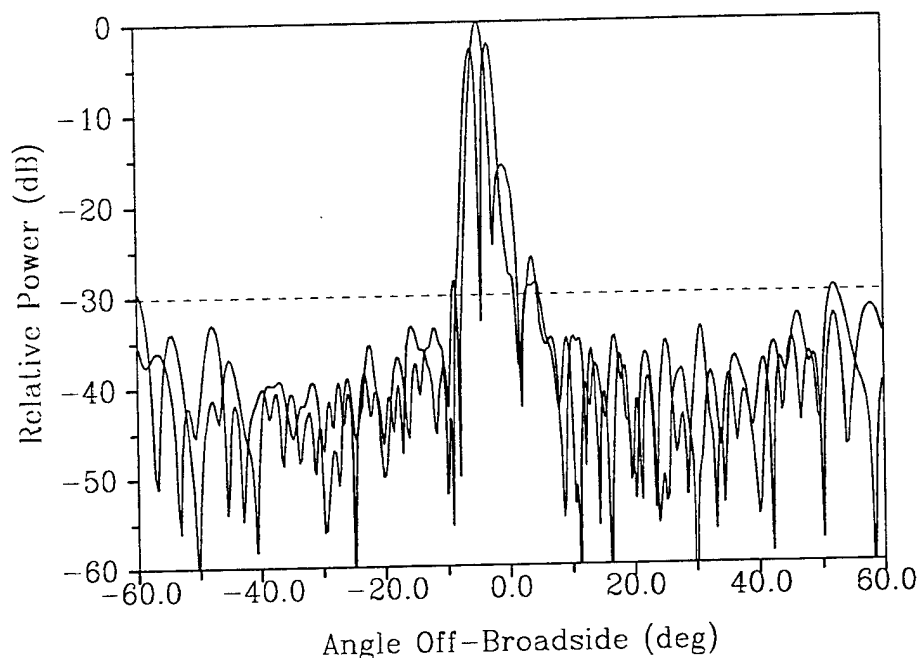
Fig. 27 Stick-Pair Monopulse Patterns at Fmid+5%

The frequency bandwidth for good array performance depends largely on the slot Q. In the case of sticks closely spaced for wide-angle scan capability, mutual coupling effects were found to manifest themselves in two significant ways. On the down side, slot resonant conductance for a given slot tilt dropped by a factor of about 2:1 (on average) compared to an isolated stick. This requires greater slot tilts to obtain the desired stick amplitude taper for a given waster load loss and must be balanced against adverse effects on antenna cross-polarization response. Although slot spacing is greater along the sticks (E-plane) than between sticks (H-plane), mutual coupling effects are much greater. As a result, slot conductance for a given slot tilt also varied by 2:1 or more depending on its particular location in the stick. On the up side, the slot Q also dropped by a factor of about 2:1 (from 14 to about 7 in the full array) resulting in a much improved bandwidth.

The computer code for the mutual coupling analysis of arrays is relatively straightforward in many cases, but not for edge-slot arrays such as this one. Since mutual coupling effects have to be accounted for to achieve the desired aperture tapers, a pragmatic procedure was adopted. A computer program (SAM) was first developed to compute the conductance of each stick slot for a particular excitation taper at the design frequency. This program accounts for slot scattering internal to the sticks (but not for external mutual coupling). SAM initially computes the tilts and cutbacks for all the slots utilizing an experimentally derived data base. The problem is this slot data base was obtained for sticks with all slots the same, whereas in the actual array the conductance of neighboring slots is generally different. Thus, as mutual coupling effects are also different the aperture excitation deviates in amplitude (and or phase) from the design taper. The next step is to use the measured (probed) amplitude taper as an input to the program as if it were the design taper. SAM then dutifully computes the slot conductances that would give this measured excitation. These are the conductances, including mutual coupling effects, that the slots of the existing design actually produced. Knowing the effective conductance at each slot location in the array, as well as the conductance required, provides the basis for an improved stick design.

5.0 Conclusions

Two significant array technology improvements have been described. By interleaving two closely spaced arrays with the proper excitations, it has been shown how dual-plane monopulse with Taylor/Bayliss excitations can be obtained. All array phase shifters are used in forming the sum pattern thereby

maximizing the possible transmit power for a given phase shifter capability. The second improvement is a new construction technique for the array face that provides a lightweight rigid face structure with high precision and ease of assembly.

6.0 Acknowledgment

References

[1] Branigan, et al., US. Patent No. 4,958,166, 9/1990

[2] Nemit, US. Patent No. 4,164,742, 8/1979

[3] T.T. Taylor, "Design of Line-Source Antennas for Narrow Beamwidth and Low Side Lobes," IRE TAP, Jan. 1955, pp. 16-28

[4] E.T. Bayliss, "Monopulse Difference Patterns with Low Sidelobes and Large Angle Sensitivity," BTL Memo MM-66-4131, Dec. 2, 1966

[5] Laverick, et al., US. Patent No. 3,636,563, 1/1972

MONOPULSE DF ANTENNA FOR SUBMARINE ESM APPLICATIONS

Paul Eyring
AIL Systems Inc.
Commack Road
Deer Park, NY 11729

Abstract: A new, small, highly integrated 3:1 bandwidth circular array interferometer (CAI) was developed to provide periscope mounted DF systems with high accuracy (1.5- to 3-degrees rms) angle-of-arrival (AOA) measurement over a full 360-degree instantaneous field of view. The new CAI consists of a metallic biconical aperture fed by eight shaped monopole antenna elements, a four grating polarizer integrated into the bicone, and an eight-input, eight-output high precision (0.5-dB rms amplitude tracking and 3.4-degree rms phase tracking) Butler matrix mode forming network. To meet the stringent size requirements for periscope mounting, the CAI was designed to fit inside a 2.25-inch high, 6.5-inch diameter cylindrical volume. Efficient new packaging techniques were utilized on the Butler matrix to facilitate installation in a 0.8-inch high, 6-inch diameter cylindrical volume. Moreover, the Butler matrix is recessed into the antennas' lower conical ground plane to provide a compact, highly integrated assembly where more than 80% of the overall height is utilized for precious antenna aperture.

1. Introduction

Wide-band, high-accuracy, angle-of-arrival (AOA) measurement over a full 360-degree instantaneous field of view (IFOV) is a required ESM/ELINT capability for submarines. The AOA requirements of future periscope mounted systems can best be met utilizing circular array phase interferometry. A circular array interferometer consists of a circular array aperture connected to a Butler matrix mode forming network as shown in Figure 1. In some cases, low-noise amplifiers are utilized between the aperture and the Butler matrix to mask the insertion loss of the

CIRCULAR ARRAY APERTURE
● PROVIDES 360° IFOV FOR
OMNI DF MODES USING
ONLY 3 RECEIVER
CHANNELS

BUTLER MATRIX MFN
● GENERATES THE
REQUIRED
OUTPUTS USED FOR
THE OMNI MODES

1095-599
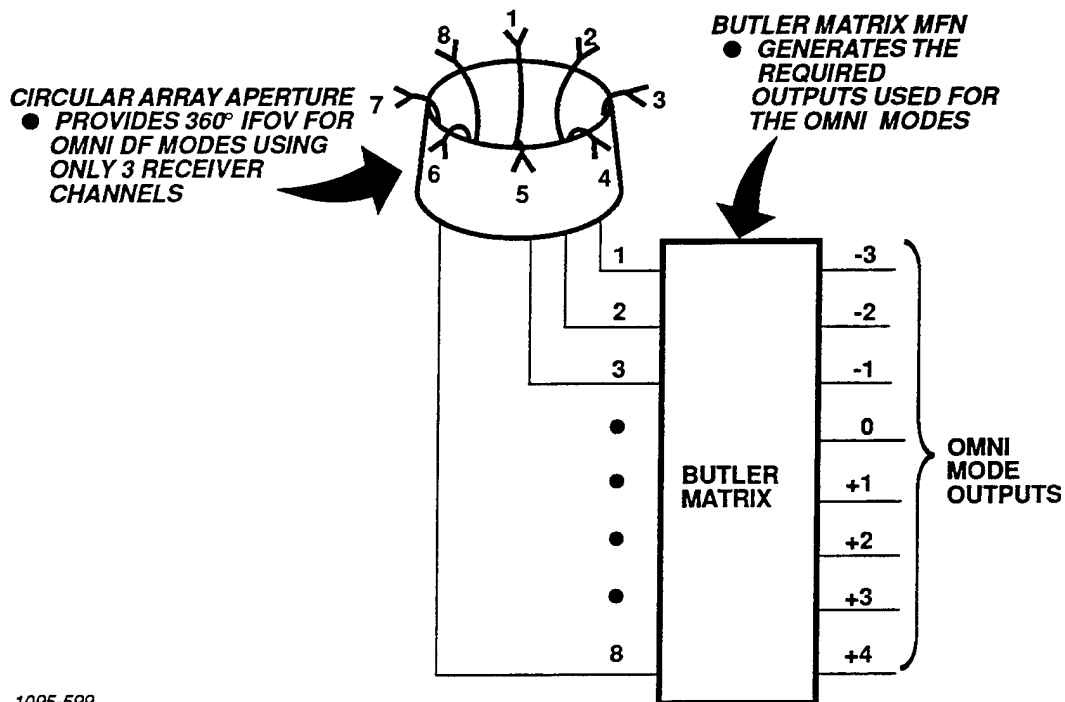
Figure 1. Block Diagram of an Eight-Element CAI

Butler. The outputs of the Butler matrix are the phase modes of the CAI and can be utilized to accurately determine AOA [1].

For some periscope installations, a cylindrical volume approximately 6.5 inches in diameter and 8 to 12 inches in height is allocated for ESM/ELINT antennas. This volume must be shared by a number of CAI's which cover different portions of the required frequency band. A common approach is to locate all of the antenna apertures at the top of the "stack" and all of the Butler matrices at the bottom. This configuration minimizes the effect of the metallic Butler matrix ground planes on the performance of the monopole or dipole elements which are typically

169

utilized. However, the intimate contact between antennas covering adjacent frequency bands results in mutual coupling which degrades AOA accuracy. In addition, a complex "web" of long interconnecting phase matched RF cables is required between the antenna, amplifiers (if utilized), and Butler matrix. This makes system assembly and maintenance very difficult. In particular, if an amplifier in one band fails it is very likely that several bands will have to be partially disassembled to gain access to the failed component.

An improved configuration, which enables each subband to be independently maintained and which eliminates interband mutual coupling, is desired. This can only be achieved by colocating the components in each subband. Therefore, a new aperture design which incorporates upper and lower metallic ground planes extending out to the radome is required to permit the Butler matrices to be intermingled with the circular arrays. Such an aperture design would inherently be imune to interband mutual coupling.

A complete, highly integrated, 3:1 bandwidth circular array monopulse DF antenna system which successfully addresses the key issues discussed has been designed and fabricated. This paper presents the design and performance of the Butler matrix and circular array antenna as well as preliminary data on system performance.

2. Technical Discussion

2.1 System Description

The circular array monopulse DF antenna system, shown in Figure 2, consists of: an eight-element circular array antenna; an eight-input, eight-output Butler matrix; and a polarizer integrated into the antenna aperture.

The circular array utilizes eight shaped, vertically polarized, monopole elements feeding a metallic biconical aperture. The bicone is designed to produce the desired elevation plane beam width. A four grating polarizer is integrated into the biconical aperture to provide slant-45 polarization. A disassembled array is shown in Figure 3. The biconical aperture was realized as a two piece assembly. The outer surface of the top bicone was shaped to provide a recessed mounting location for the Butler matrix. Each monopole antenna element is soldered to the center conductor of a coaxial cable whose opposite end gets directly connected to the Butler matrix. The elimination of a connector at the element interface significantly improves the ability to recess the Butler into the upper bicone. This provides a compact, highly integrated assembly where more than 80% of the required height is utilized for precious antenna aperture.

The four polarizer gratings are each etched on 3-mil thick Kapton and are separated from each other by low dielectric constant foam spaces. Each of the polarizer layers/spacers has been precision machined to fit snugly into the bicone. The integration of the polarizer into the bicone is significant because it facilitates the
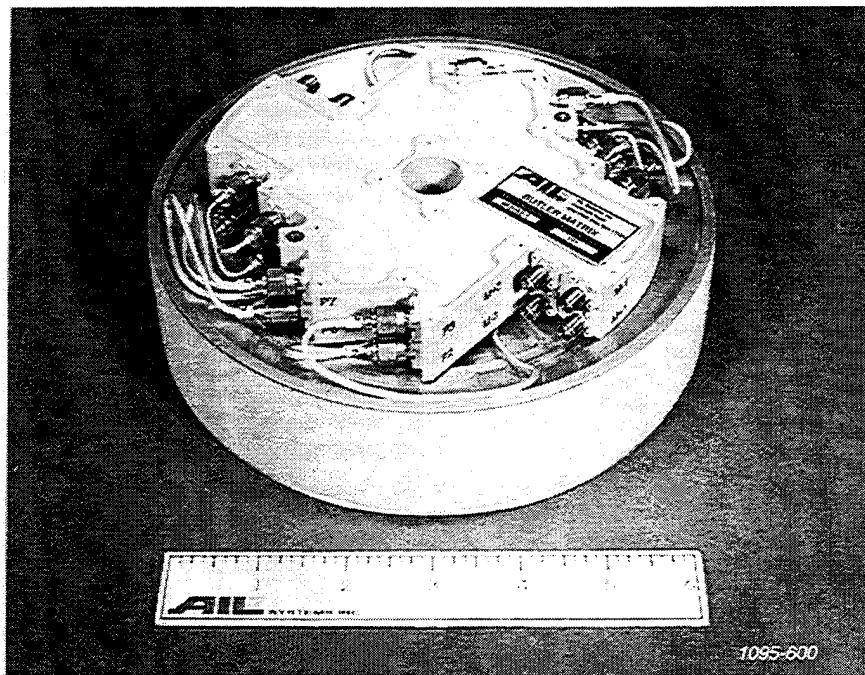
Figure 2. Circular Array Monopulse DF Antenna
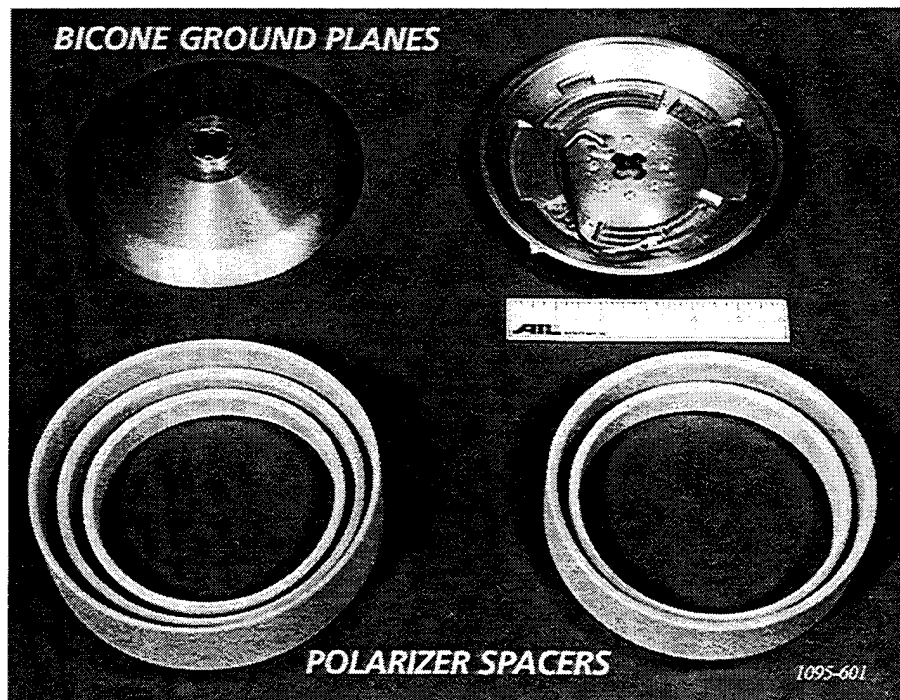
Figure 3. Diassembled Circular Array Aperture

design of separate high performance polarizers for each specific ESM/ELINT antenna system subband. If the polarizer were located outside the bicone, it would have to be designed to cover a much broader frequency range (with degraded performance) due to the presence of antennas covering other system subbands.

When installed, the metallic bicone extends to within 0.05 inches of the inner surface of the radome. The 0.05-inch air gap prevents the antenna from being damaged when the radome compresses due to the extreme hydrostatic pressure when the submarine is submerged. The bicone provides isolation between adjacent ESM/ELINT antennas in the periscope. This results in a significant reduction in mutual coupling, which will translate into a substantial improvement in installed AOA accuracy.

A Butler matrix is a network which performs a discrete Fourier transform on a set of the antenna element signals at its input using analog signal processing in real-time. Its outputs are the omnidirectional phase modes of the CAI. The matrix is implemented via a set of 3-dB quadrature couplers and Shiffman phase shift devices interconnected by a labyrinth of transmission lines. The block diagram of the eight-input, eight-output Butler matrix utilized in this system is given in Figure 4. To eliminate all the transmission line cross-overs and facilitate the fabrication of the matrix in just two stripline circuit layers the block diagram was rearranged as shown
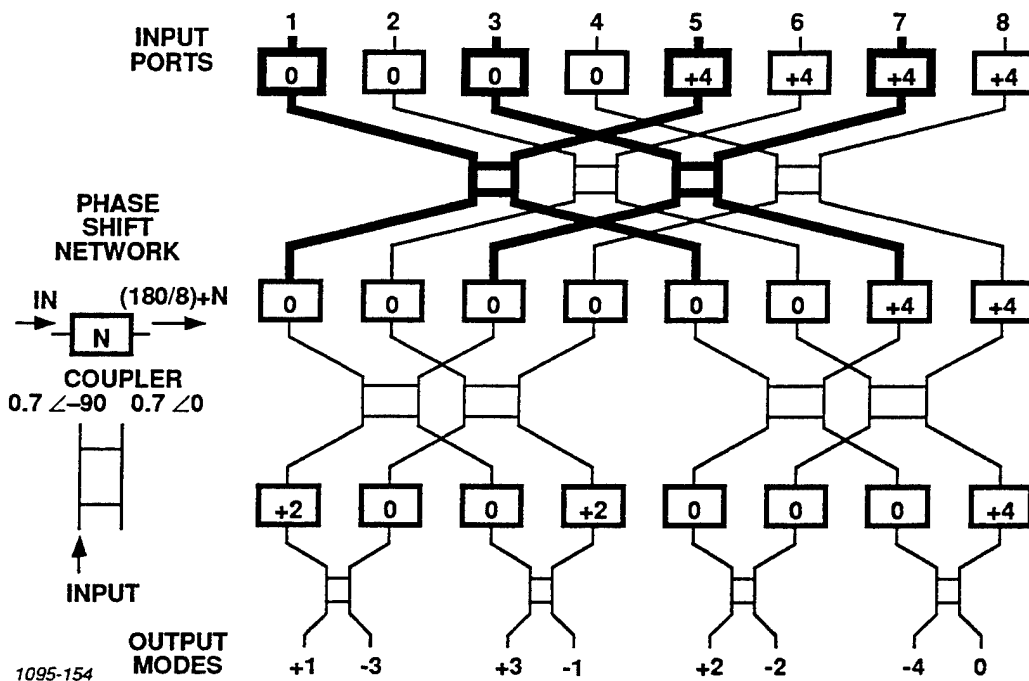
Figure 4. Block Diagram of Eight-Input, Eight-Output Butler Matrix

in Figure 5. A disassembled view of both stripline packages, showing the two pairs of ground planes, the two pairs of duroid cover boards, and both stripline circuits is given in Figure 6.

2.2 Component Design and Electrical Performance

The eight-element circular array antenna and the eight-input, eight-output Butler matrix were individually assembled and tested before being integrated. The antenna element design was accomplished using a combination of computer modeling and experimental optimization. A transmission line model of the monopole element in the bicone environment was approximated using HP/EEsof's Touchstone.
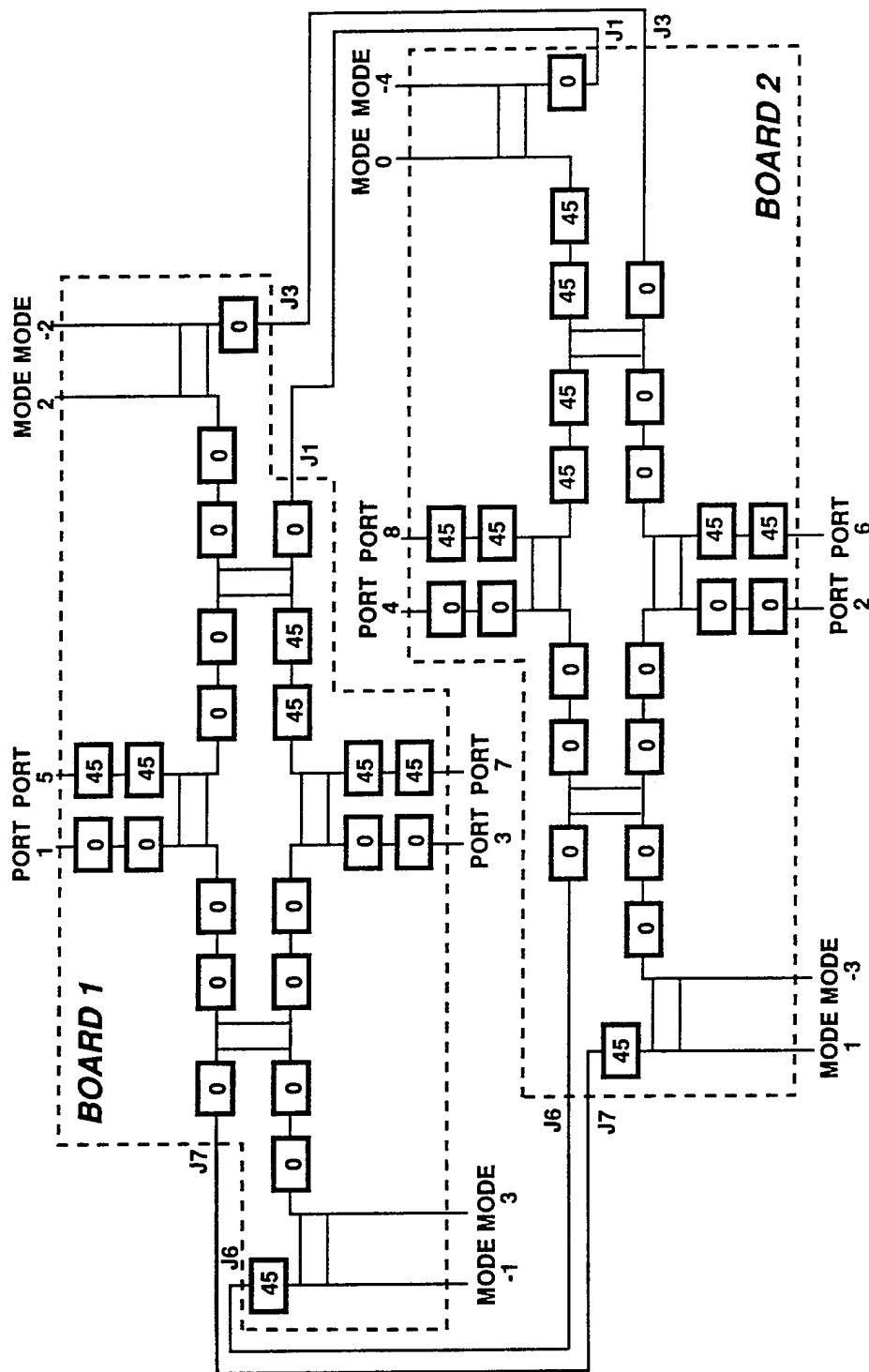
Figure 5. Block Diagram of Butler Matrix for Fabrication in Two Stripline Circuit Layers

1095-602

175
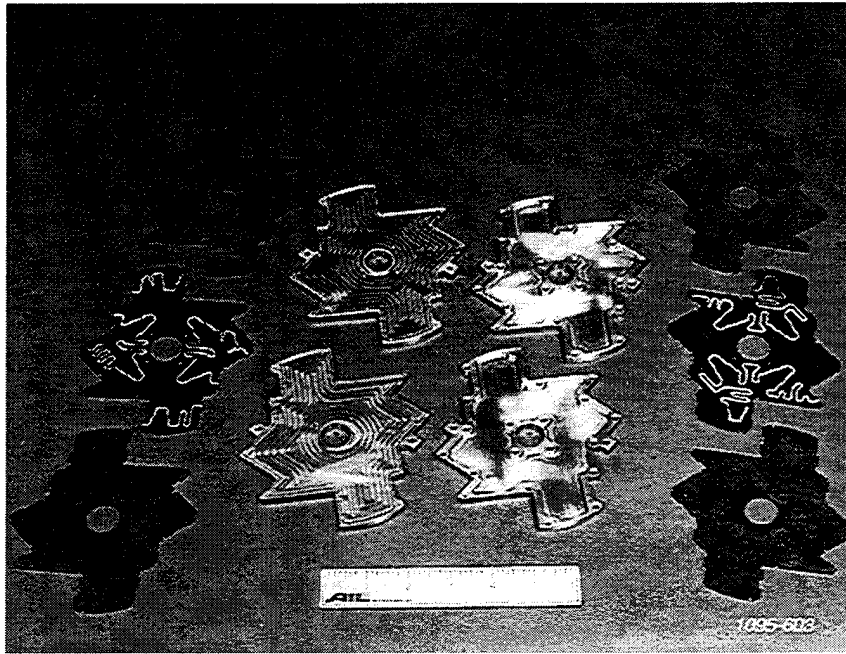
Figure 6. Disassembled View of Butler Matrix

The Touchstone model was utilized to obtain starting points for the experimental design optimization. A complex relationship between element impedance and element spacing to the bicone's back wall, monopole diameter, and monopole spacing above the bottom ground plane was encountered. The optimum selection of the back wall spacing proved to be the driving factor because it also impacts the element's elevation plane pattern at the high end of the band. When the back wall spacing approaches a half wavelength, the reflection causes a radiation pattern null to appear at 0 degrees elevation.

The element design utilized in the array has excellent VSWR, 1.5:1 maximum as shown in Figure 7, over the entire 3:1 frequency band. The pattern null at 0 degrees elevation was pushed to the upper edge of the frequency band, resulting in good element patterns over 75 percent of the band. A sample element pattern at the low end of the band is given in Figure 8.

For circular array applications, the element directivity has a direct impact on the frequency bandwidth of the array. Periodic amplitude nulls appear in the gain response versus frequency of circular array's with omnidirectional elements [2]. The use of directional elements, with at least a 10-dB front-to-back gain ratio, eliminates those periodic amplitude nulls [1]. For the element utilized in this circular array, the worst case front-to-back gain ratio was 12.6 dB (Figure 8) at the low end of the band. The new Butler matrix utilizes previously existing component designs in conjunction with new packaging technology to reduce the matrix height to 0.8 inches. The new Butler matrix and its predecessor are shown in Figure 9. A through hole was designed into the center of the new Butler matrix to provide a path for cables to be fed to the other ESM/ELINT antennas. Input and output connector locations were also rotated to minimize the installed volume (including mating cables) of the Butler matrix.

The artwork for one of the Butler's stripline circuit layers is shown in Figure 10. The 3-dB quadrature couplers are realized as a tandem connection of two 8.34-dB couplers to reduce the coupling sensitivity to stripline center board
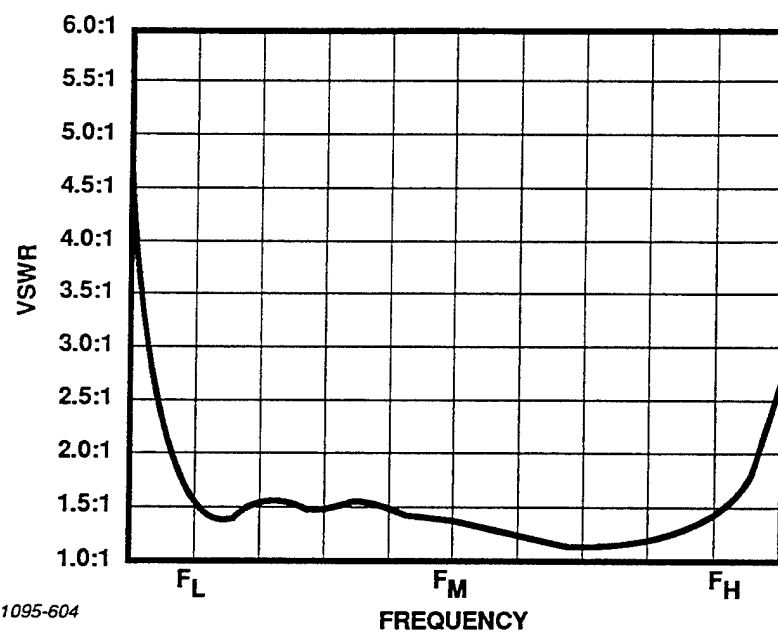
Figure 7. 3:1 Bandwidth Monopole Element VSWR in the Array Environment
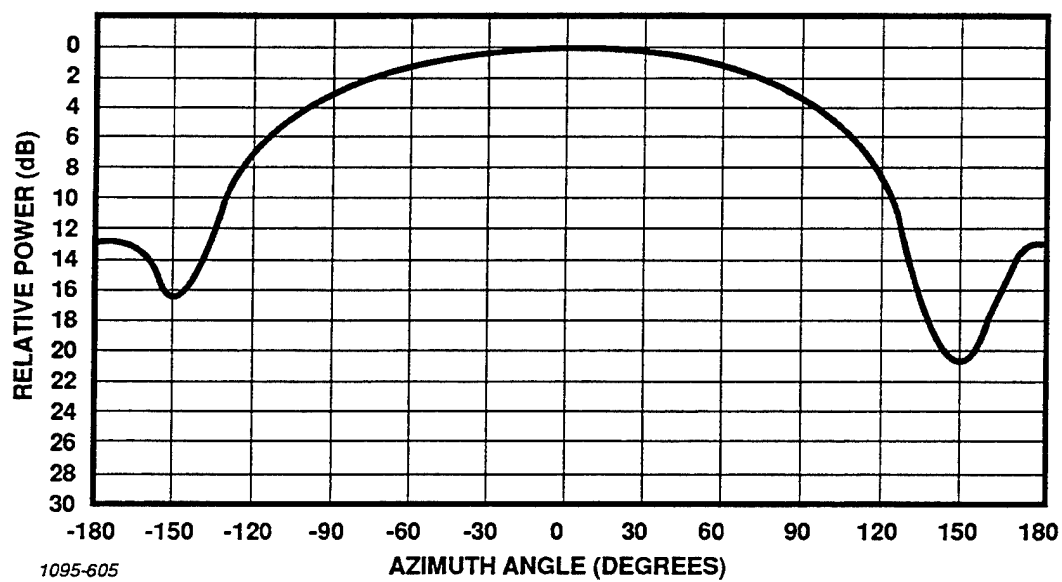
Figure 8. Element Pattern at Low End of Band

178
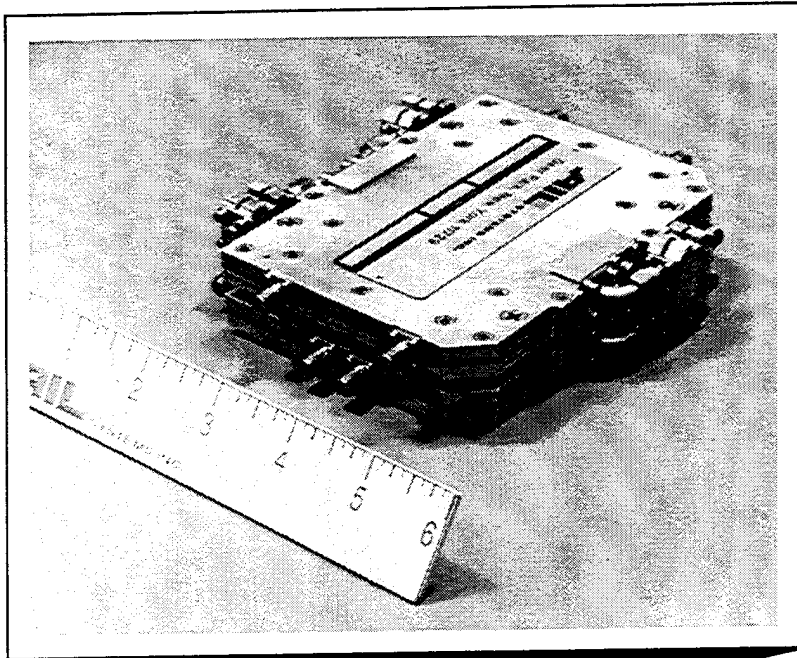
HEIGHT 1.2"
WEIGHT 1.5 LBS
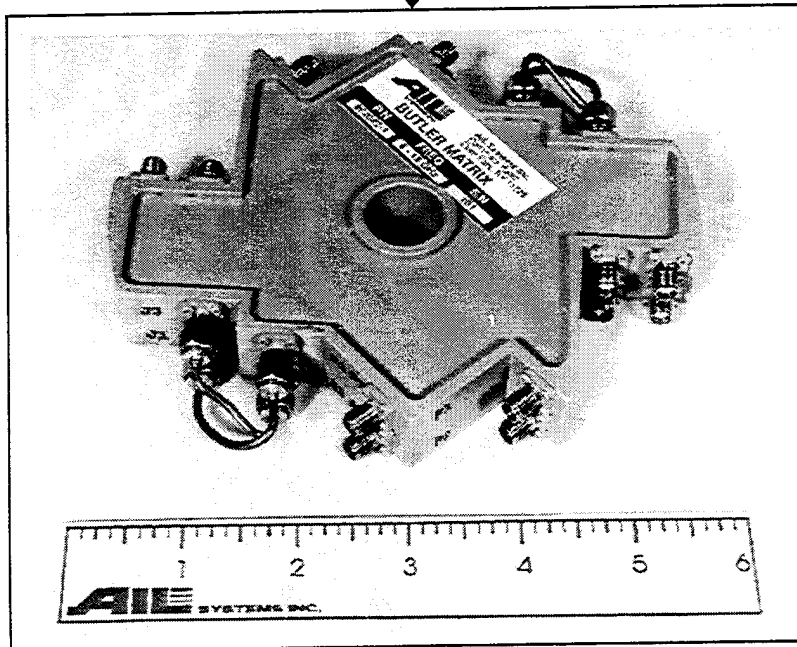
HEIGHT 0.8"
WEIGHT 1.0 LBS

1095-606

Figure 9. Butler Matrix Evotion
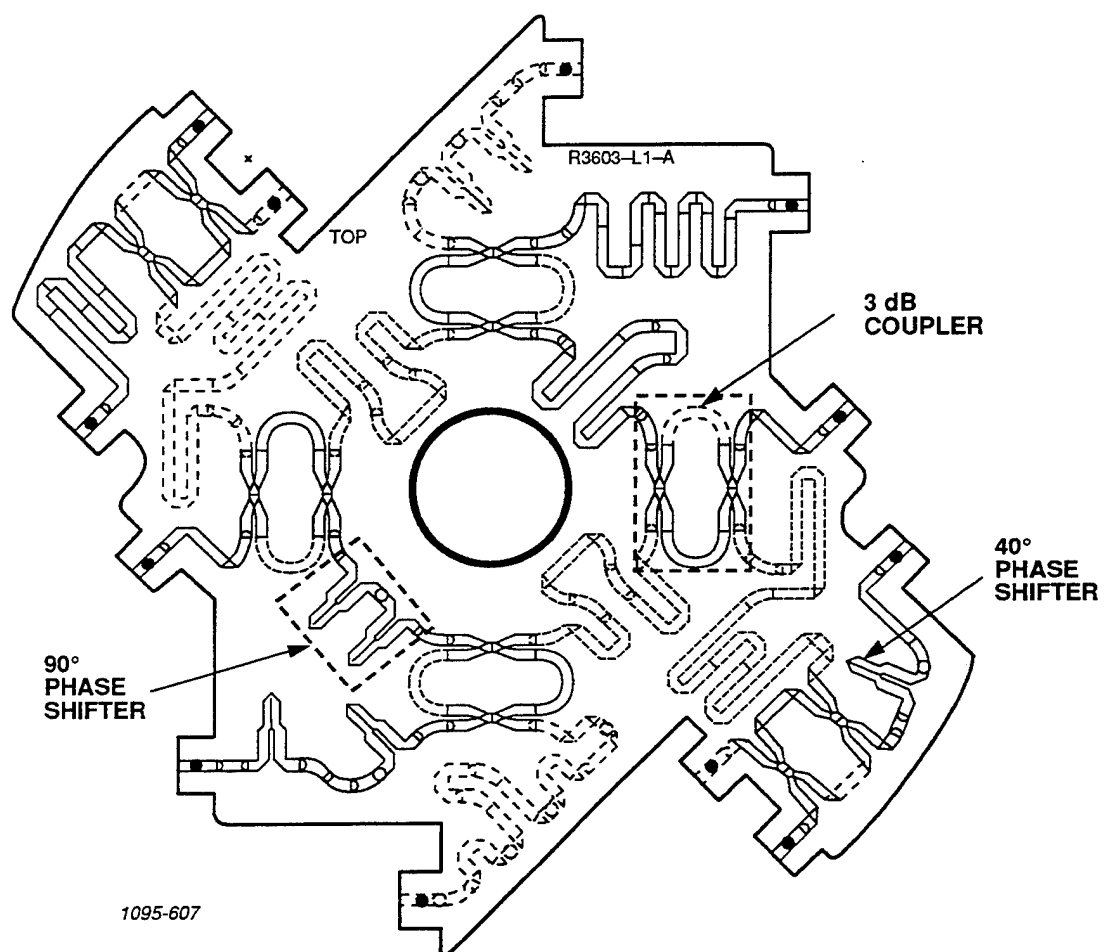
Figure 10. Butler Matrix Stripline Circuit Layout

thickness tolerances and improve production unit performance. The unique "pseudo-continuously" tapered 8.34-dB stripline couplers provide the performance of continuously tapered designs in the same physical length as a discretely stepped coupler; a continuously tapered coupler's overall length is a quarter wave longer. Two 45 degree, two section Schiffman phase shift devices are used to realize the required 90-degree phase shifts. This allows the tightly coupled lines in the phase shift network to be etched on the same side of the stripline center board and eliminates the need for broadside coupled lines which must be connected through the center board.

The performance of the Butler matrix is summarized in Table 1. Typical amplitude and phase tracking performance versus frequency is given in Figure 11. The Butler's 0.5-dB rms amplitude tracking and 3.4-degree rms phase tracking represent state-of-the-art performance.

Table 1. Butler Matrix Performance Summary

Parameter	Performance
Frequency Coverage	3:1 Bandwidth
Phase Tracking	3.4-deg rms
Amplitude Tracking	0.5 dB rms
Dissipative Loss	2 dB at Flow 5 dB at Fhigh
VSWR	90% of Data <1.6:1 2.7:1 Worst Case

A. AMPLITUDE

OUTPUT-PORT VOLTAGE RELATIVE TO THE AVERAGE

STATS FOR F_L TO F_H

MEAN	ST. DEV.	RMS	
0.17	0.41	0.44	M3P5S2 1
0.08	0.44	0.58	M3P6S2 1
-0.07	0.38	0.38	M3P7S2 1
0.05	0.41	0.41	M3P8S2 1

AMPLITUDE (dB)

FREQUENCY

B. PHASE

INSERTION PHASE RELATIVE TO THE MEDIAN

STATS FOR F_L TO F_H

MEAN	ST. DEV.	RMS	REF	
-2.1	2.3	3.2	0	M3P5S2 1
-3.1	2.1	3.7	135	M3P6S2 1
0.3	2.9	2.9	-90	M3P7S2 1
0.0	2.2	2.4	45	M3P8S2 1

PHASE (DEG)

FREQUENCY
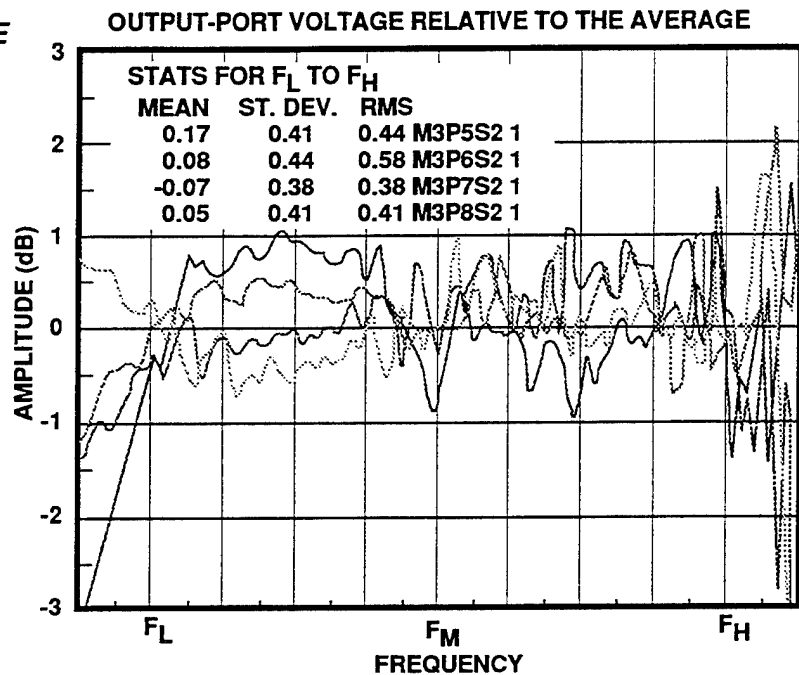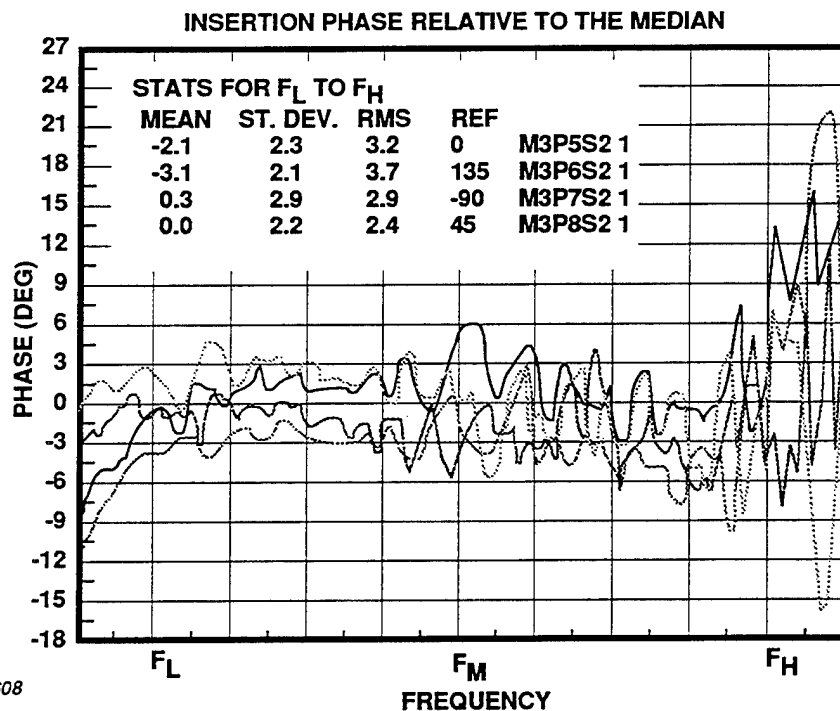
1095-608

Figure 11.   Measured Tracking Performance of 3:1 Bandwith Eight-Input, Eight-Output Butler Matrix Relative to the Median of Error Distribution for Mode-1

182

2.3 System Performance

The performance of the circular array interferometer was only measured over a 2.5:1 frequency band due to the unoptimized monopole element performance at the high end of the band. Mode +2, Mode −1, and Mode −2 were selected for use in determining AOA using the criteria outlined in reference 1. Modes −1 and −2 were compared to obtain nonambiguous coarse AOA information. Typical relative phase versus azimuth angle for this coarse mode pair is shown in Figure 12. Modes +2 and −2 were used to provide high accuracy "fine" AOA information. Widely spaced modes are utilized for fine AOA determination because antenna and receiver phase tracking errors are demagnified by the mode number differential; 4 in this case. Typical relative phase versus azimuth angle for the fine mode pair is shown in Figure 13. Uncalibrated monopulse AOA data is given in Figure 14. The uncalibrated 3-degree monopulse AOA accuracy provided by this antenna is truly noteworthy considering its small size. Improved monopulse AOA accuracy could be obtained from this circular array interferometer using calibration. With a moderate level of calibration, performance on the order of 1.5 to 2 degree monopulse AOA accuracy could be obtained.
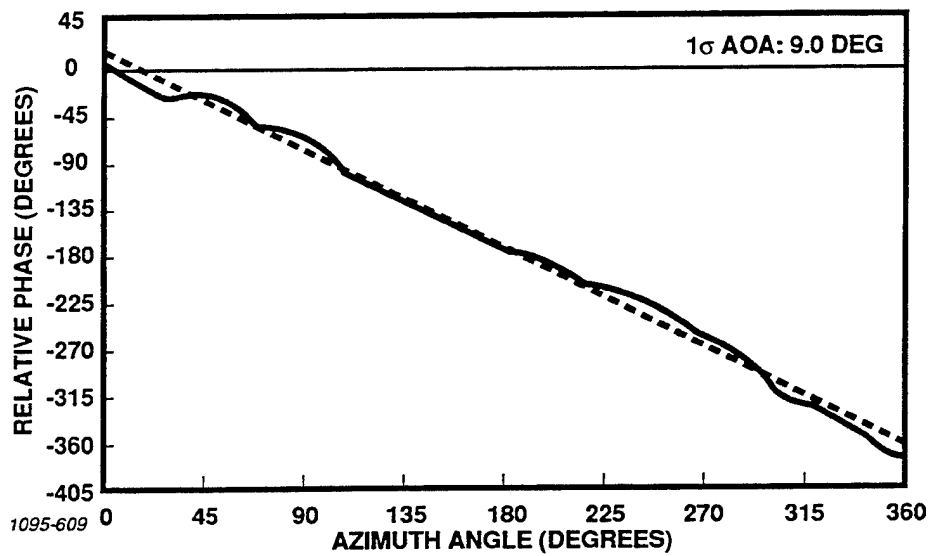
Figure 12. Measured Coarse Mode Pair (Mode-2/Mode-1) Relative Phase
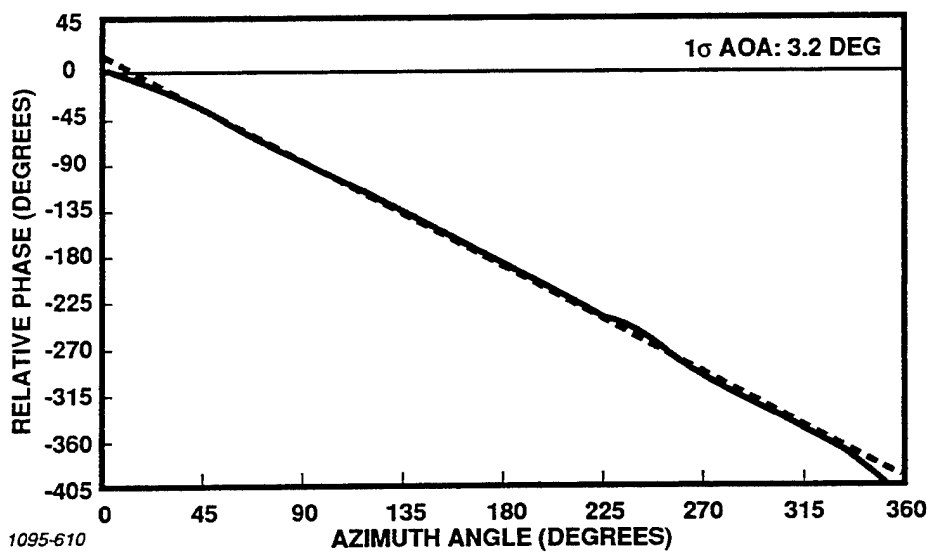
Figure 13. Measured Fine Mode Pair (Mode-2/Mode+2) Relative Phase

184
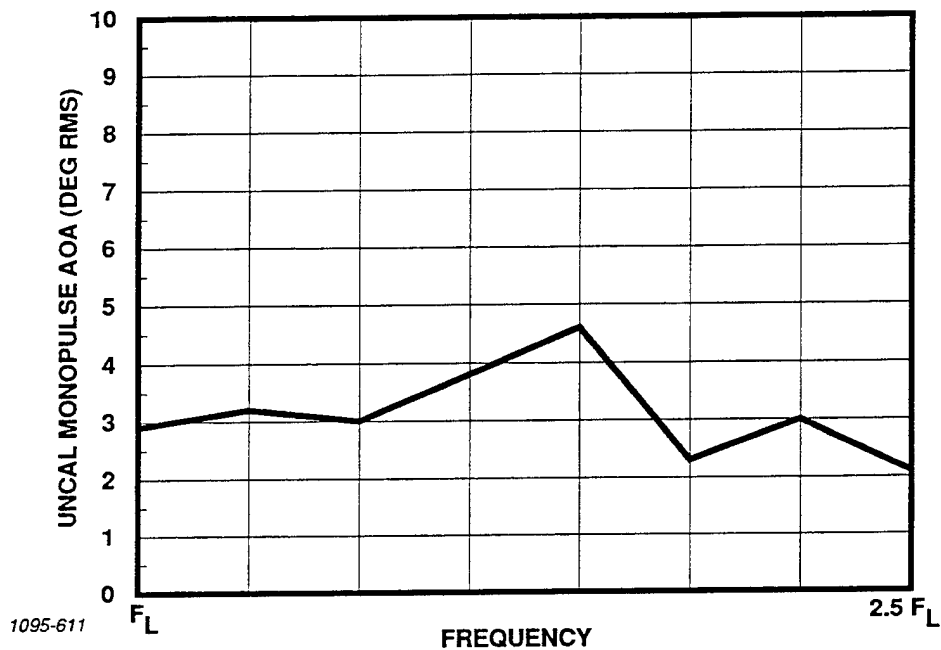
Figure. 14. Measured, Uncalibrated Monopulse RMS AOA Accuracy

3. Conclusions

A new small, highly integrated circular array interferometer capable of providing periscope mounted monopulse DF systems with 3-degrees rms AOA accuracy over a full 360-degree instantaneous field of view was described. The new CAI consists of a metallic biconical aperture fed by eight shaped monopole antenna elements, a four grating polarizer integrated into the bicone, and an eight-input, eight-output state-of-the-art Butler matrix mode forming network. The CAI fits inside a 2.25-inch high, 6.5-inch diameter cylindrical volume. More than 80% of the overall height is utilized for precious antenna aperture.

185

4. Acknowledgments

5. References

[1]   P. Eyring and R. Clapp, "Design and Development of Wide-Band Circular Array Interferometers", Proceedings of the 1994 Antenna Applications Symposium.

[2]   T. Rahim and D.E.N. Davies, "Effect of Directional Elements On The Directional Response Of Circular Antenna Arrays", IEEE Proc., vol. 129, Pt. H, pp. 18 – 22, February 1982.

High Accuracy DF Antenna Using COTS Hardware

T. R. Holzheimer

E-Systems, Inc.

Greenville Division

Greenville, Texas 75403

Abstract:

A high accuracy, quasi flush mount, 360 degree azimuth direction finding (DF) antenna has been designed, built and tested using commercially available off the shelf (COTS) components. The DF antenna was designed to operate over the 2 to 18 GHz frequency range with a goal of 1.0 degree rms angle of arrival (AOA) accuracy. The antenna was built and tested in several configurations, but one in particular will be described which provides for an all polarization detection capability. The beamforming network consists of a Butler matrix where a maximum of five phase channels are used in order to provide the required phase pairs for AOA determinations. The resultant antenna exhibits an rms AOA accuracy of less than 0.6 degrees and typically averages 0.5 degrees of rms AOA accuracy. The antenna has higher element efficiency than a linear multiple element interferometer although it does not have the accuracy potential of the interferometer. Comparisons are drawn between the measured performance of this antenna and the performance of a generic linear multiple element

interferometer. Of the configurations investigated, this antenna lends itself to many installations due to its relatively small height of approximately 8 inches and the maximum diameter of 24 inches. Smaller configurations, on the order of 16 inches in diameter, were investigated with comparable accuracy. The expected relative cost of this antenna is projected to be low due to the use of COTS hardware. Methods of improving system performance of the antenna in combination with the rest of the system are also addressed.

1.0 Introduction:

High accuracy direction finding antennas have been described in many papers and textbooks over the years.[1][2][3] Accuracy for the above antennas is described through various techniques from element switching to processing algorithms that produce the rms angle of arrival (AOA).[4][5] Most DF arrays use omnidirectional, i.e. low gain elements such as spirals in linear interferometers or dipoles in full 360 degree azimuthal field of view applications.[6] Others have gone one step further by using horns as elements.

Linear interferometers of the 4 to 5 element grouping can provide extremely high accuracy AOA of less than 0.1 degree rms. However, these type of arrays exhibit azimuthal field of view on the order of 80 to 120

degrees depending on whether horns or spirals are used as single interferometer elements. Spacing of the interferometer elements is typically optimized to N-multiples of half wavelength at the highest usable frequency. This provides a direct correlation to array size which is typically larger than a lower accuracy circular DF array.

In providing a full 360 degree azimuthal field of view the typical DF array consists of a circular array for which the earliest types were designed using low gain omnidirectional elements. Subsequent investigators then looked at using directional antennas in circular arrays and assessed them for use in DF implementations.[7][8] Many different types of elements and beamformers have been used such as flared notch radiators and N-element Butler matrix.[9][10] Mixed polarizations have also been investigated with varying degrees of success requiring today's easily acquired high speed computers.[11] Derivations of the synthesis used to produce AOA from a circular array has been previously reported and will not be repeated.[7][8][9]

The circular DF arrays investigated in this paper are of the simultaneous modal phase type. Figure 1 illustrates the different phase modes which follow periodic functions of 360 degrees, i.e. N X 360 degrees where N is the modal phase order. They are phase only DF arrays and not amplitude only DF arrays. The phase modes are set up using a modeformer which can be a Butler matrix and/or a circular Rotman lens where the modal phases are all existing simultaneously. The Butler matrix is quasi-frequency independent while the Rotman lens is linearly dependent on frequency. An additional network is required beyond the basic phase modeforming network in order to provide amplitude DF which is illustrated in Figure 2. The rms AOA is derived by differencing the two simultaneous modal phases which results in an azimuthal angle.

2.0 Design of the Circular DF Array

The design of this circular DF antenna has prompted a filing of a patent application. This design uses commercial off the shelf hardware which basically consists of elements and modeformers. The interelement
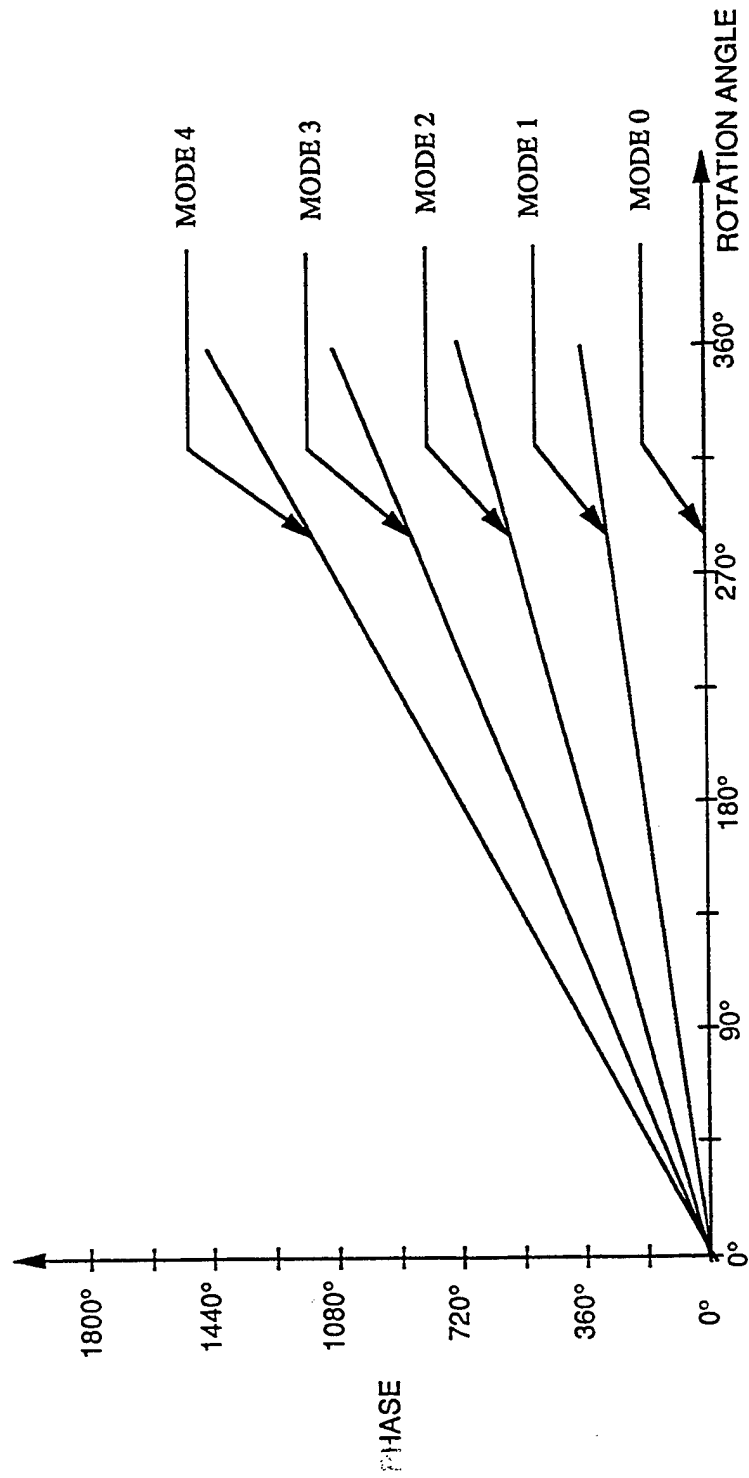
Figure 1.   Modal Phase versus Rotation Angle
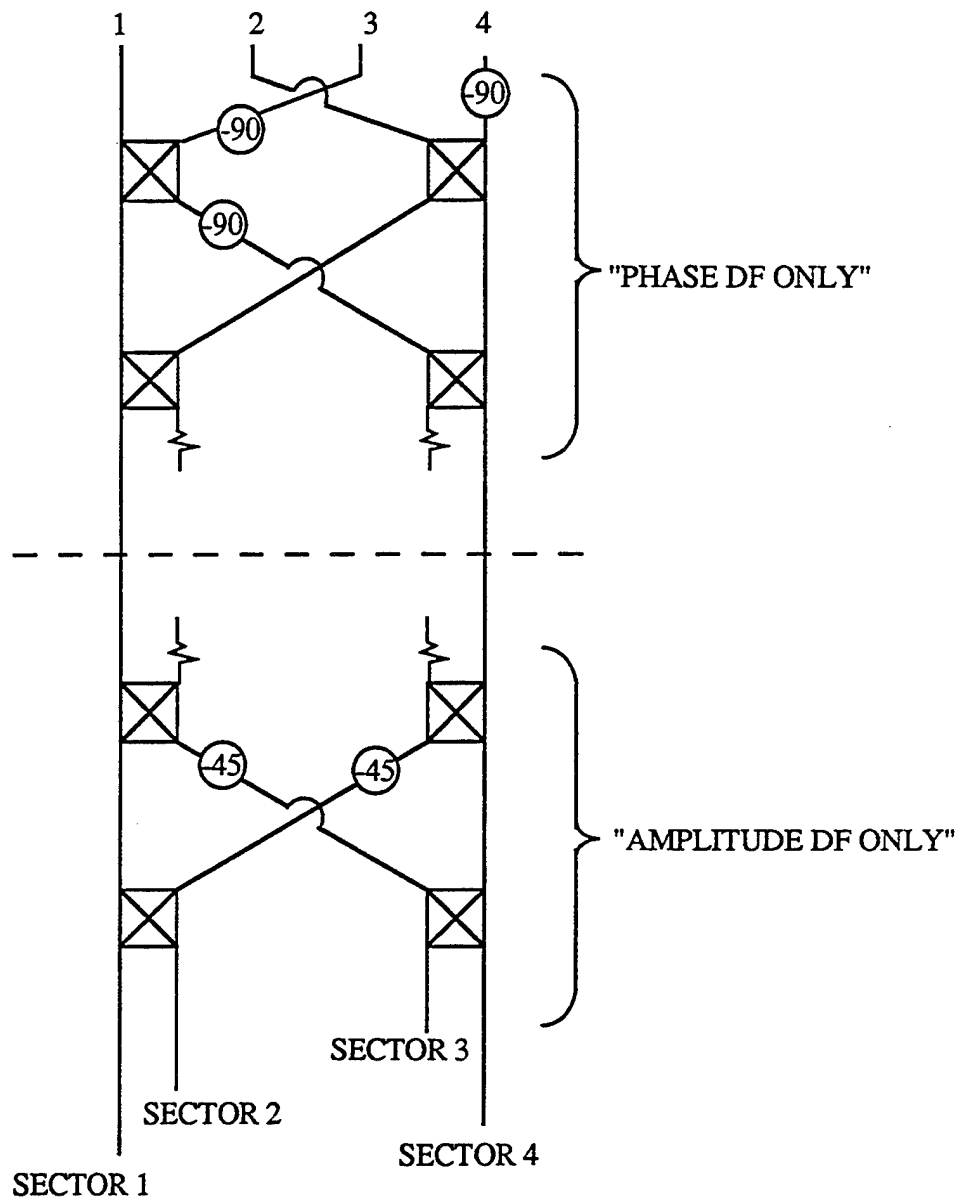
Figure 2.   Phase Only versus Amplitude Only DF

spacing is kept less than a half wavelength in order to minimize higher order mode phase distortion, provide a compact and light weight design, and provide a full 360 degree azimuthal field of view. This concept was arrived at in two steps. The first step was to verify the basic electrical concept with a 4 element circular array. Then with powers of two, for modeformer simplicity, an 8 element array was designed and fabricated in order to meet the less than 1 degree rms AOA goal. Pertinent specifications are listed in Table I.

Table I. Goal Specifications.

Frequency Range: 2 to 18 GHz minimum

Element Gain: 7.5 dBi minimum

Polarization: Dual Linear as minimum

Field of View: Azimuth - 360 degrees
                Elevation - +- 30 degrees minimum

RMS AOA Accuracy: 1 degree maximum

Ambiguity Rate: less than 4%

Unambiguous Data Rate: greater than 90%

Signal to Noise Ratio: 8 dB minimum

The first array designed used four elements to prove
out the basic electrical design. Figure 2 illustrates
the phase only portion of the 4 X 4 Butler matrix used
for the four element antenna. This initial design was
usable over the full 1 to 18 GHz frequency range.
Based on the Figure 2 drawing and a quick analysis it
was discovered that the element spacing drastically
changed as frequency was changed. This was corrected
by turning the elements around providing a constant
element spacing with frequency. The size of this array
was 16 inches in diameter by 8 inches in height.
However, as data of Figure 3 shows, we did not meet the
desired rms AOA accuracy. This implied that we needed
more elements which was implemented in step 2.

Step 2 was implemented with 8 elements in order to meet
the power of two beam forming requirements. The
modeformer used is an 8 X 8 Butler matrix which
provided phase modes 0, +- 1, +- 2, and +- 3. However,
this network limited the frequency range to 2 to 18
GHz. Figure 4 illustrates the 8 element DF array
version of step 2. The actual array that was built and
tested is shown in Figure 5. Data were acquired over
the 2 to 18 GHz frequency range, but for brevity

CIRCULAR DF ANTENNA
RMS ERROR vs. FREQUENCY
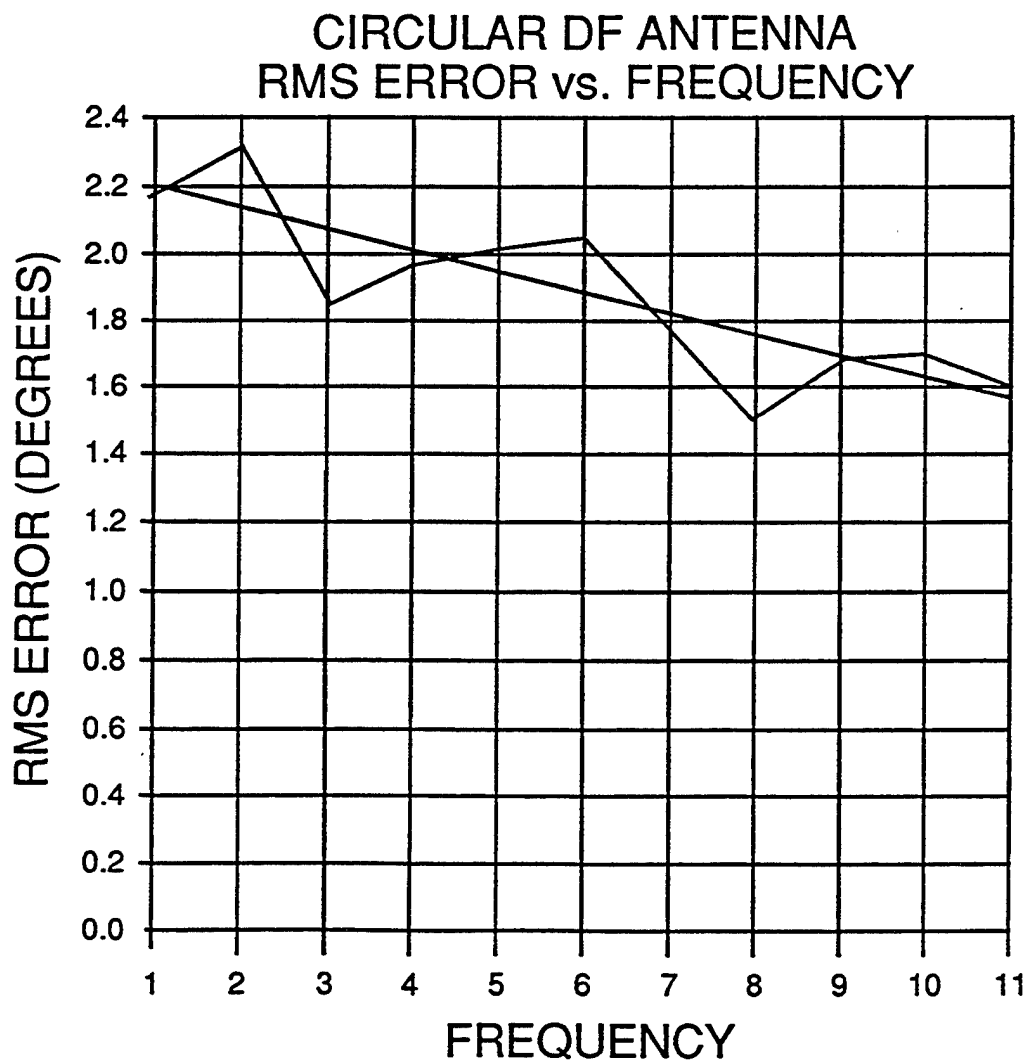
Figure 3.   Four Element RMS AOA Accuracy Versus

Frequency
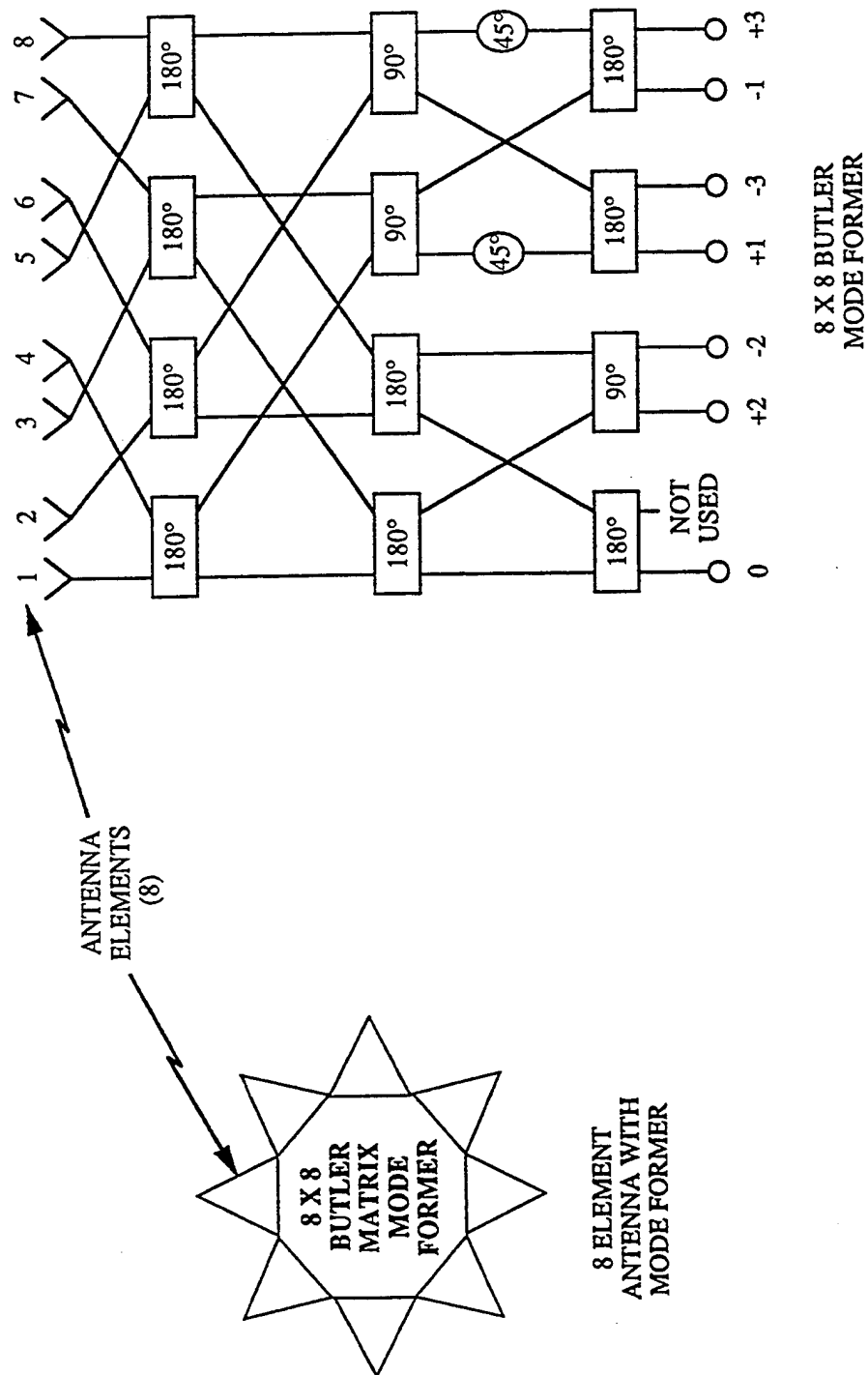
Figure 4.   360 Degree Eight Element DF Antenna

197
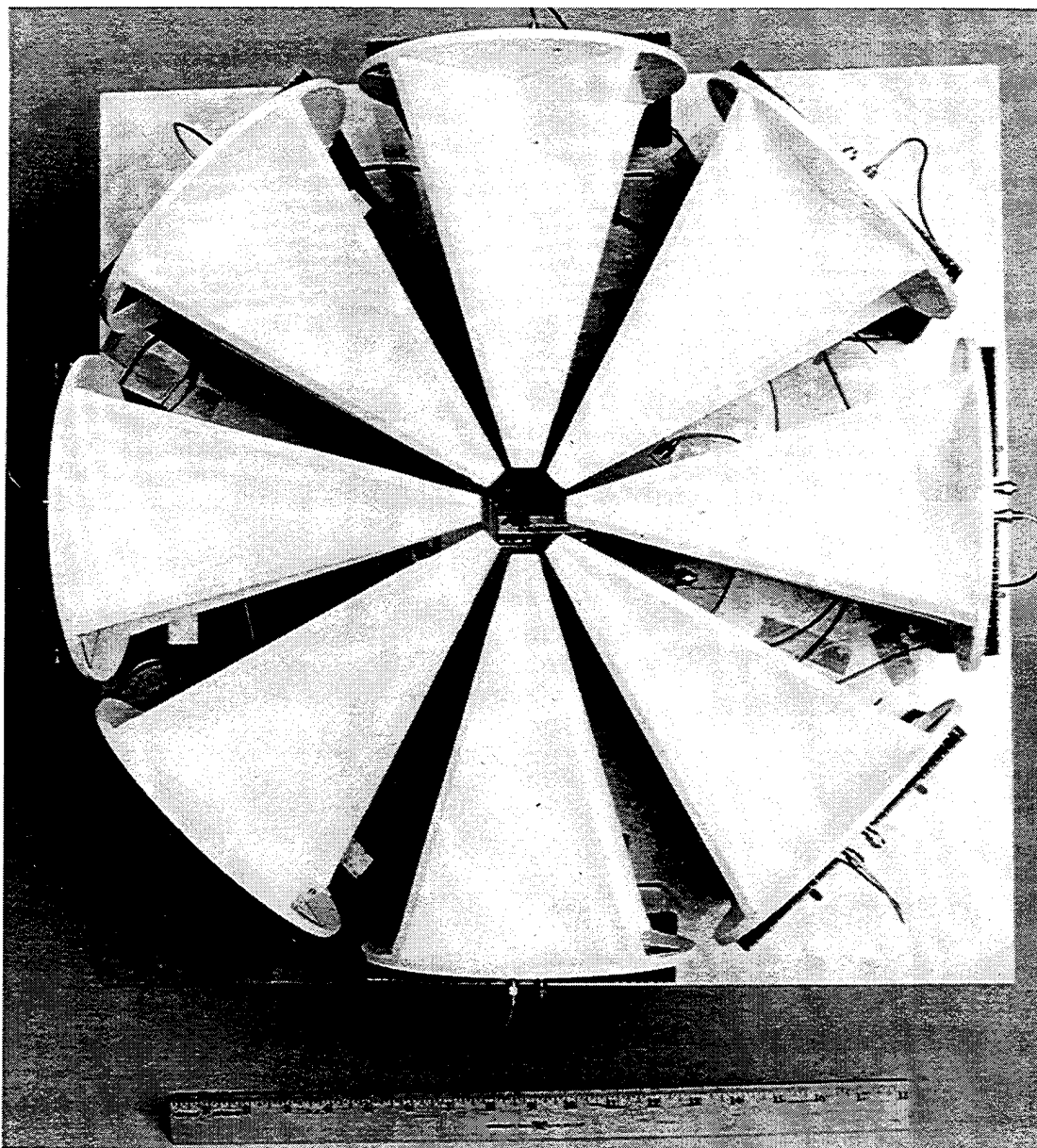
Figure 5. Top View of 360 Degree Eight Element DF

Antenna

only the 8 to 18 GHz data are discussed in the following section.

3.0 Performance of the Circular DF Array

Measured data were collected on every usable phase mode port from 2 to 18 GHz in 100 MHz steps over 360 degrees of azimuthal field of view. However, again for brevity, only the 8 to 18 GHz data will be discussed. Four phase pairs or differential phases were then constructed. A phase calibration table was also constructed. A residual 6.1 degree (one sigma) phase pair tracking error was used as typical for a post calibrated, wide-bandwidth, phase-discriminating receiver. An E-Systems proprietary algorithm was then invoked using a metric in order to determine the rms AOA accuracy.

It was recognized, as has been reported, that a perfect array with no coupling could provide a full unambiguous 360 degree azimuthal field of view. However, it is also recognized that in a realistic situation and installation that ambiguity rate and rms AOA accuracy are driven by element spacing and signal to noise ratio

as in a linear interferometer. The close spacing of
the elements which increases the coupling between
elements and the non-ideal cardioid radiation pattern
of the elements cause the additional error sources and
differences from the perfect array. That is tradeoffs
are made that affect all of the above. Based on the
above, criteria were determined for specifying a DF
system whether it be a circular DF Array or a linear
interferometer. They are listed in Table II.

Table II. Required DF System Specifications.

1. RMS AOA over Frequency.

2. Unambiguous Data Rate over Frequency.

3. Untagged Ambiguity Rate over Frequency.

4. RMS AOA Accuracy over Signal to Noise Ratio.

5. Unambiguous Data Rate over Signal to Noise Ratio.

6. Untagged Ambiguous Data Rate over Signal to Noise
   Ratio.

Good data is labeled as Unambiguous Data Rate, while bad data is Untagged Ambiguity Rate. This says that based on use of proprietary algorithms and calibration, data can be made more accurate and false AOA's can be minimized and identified. Data is shown that sillustrate Table II for the circular DF array and are shown in Figures 6 through 11.

Figures 6 through 11 show both dual linear polarization and dual slant 45 degree polarization. These were both investigated due to potential height and installation constraints that could be imposed. The data show that the RMS AOA Accuracy versus Frequency is less than 0.6 degree and closer to 0.5 degree which is much better than the 1.0 degree goal. The Unambiguous Data Rate versus Frequency is greater than 90% and averages 95%. The Untagged Ambiguity Rate versus Frequency or bad data is less than 3%. The RMS AOA versus Signal to Noise Ratio is less than 0.6 degrees. The Unambiguous Data Rate versus Signal to Noise Ratio rolls off as expected with lower signal to noise ratio and is 70% to 76% at 8 dB. The Untagged Ambiguous Data Rate versus Signal to Noise Ratio increases to as high as 11% at 8
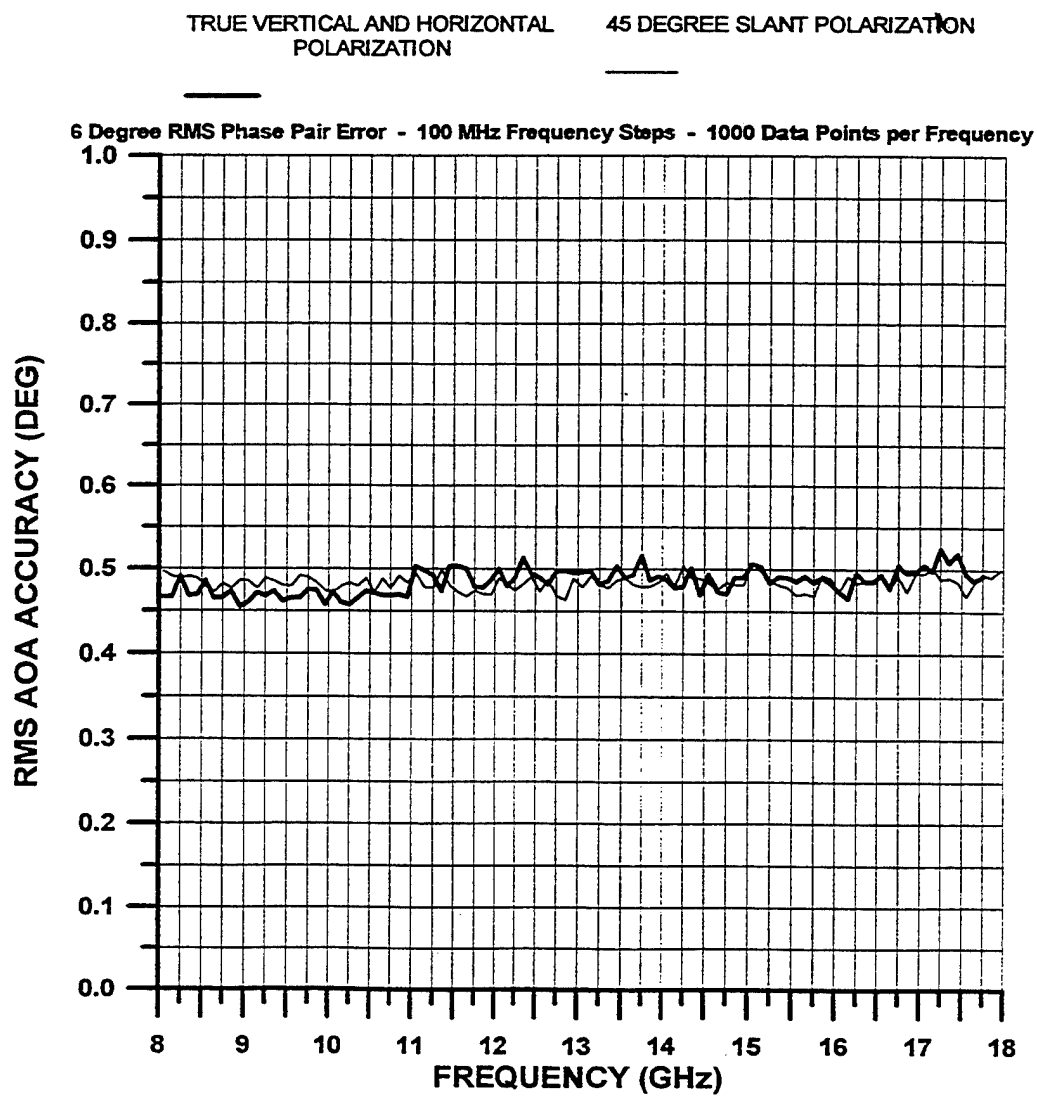
Figure 6. RMS AOA Accuracy Versus Frequency
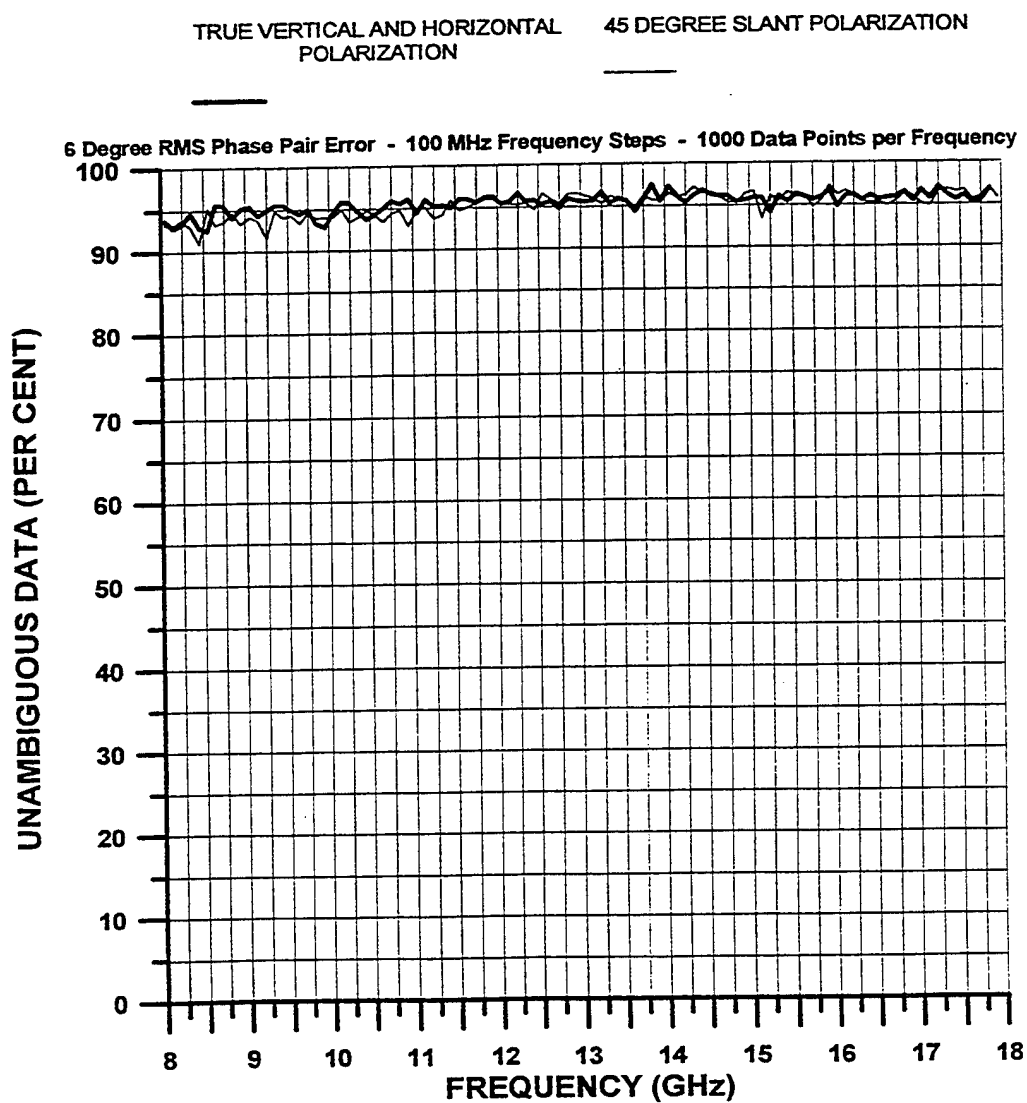
Figure 7.   Unambiguous Data Rate Versus Frequency

TRUE VERTICAL AND HORIZONTAL
POLARIZATION

45 DEGREE SLANT POLARIZATION
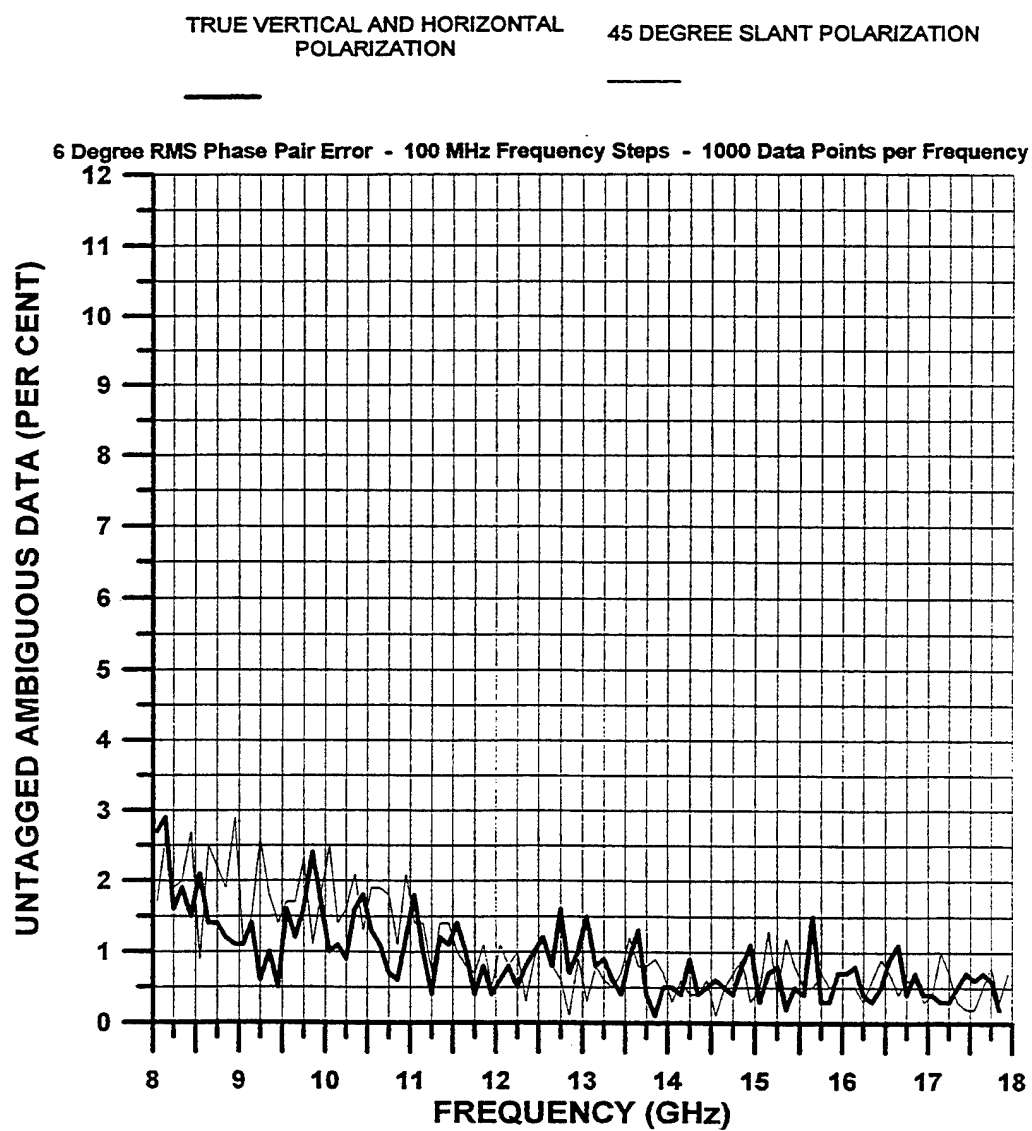
Figure 8. Untagged Ambiguity Rate Versus Frequency

8.05 GHz V+H	8.05 GHz SLANT	13.05 GHz V+H	13.05 GHz SLANT	17.95 GHz V+H	17.95 GHz SLANT

RSS"ED WITH 6 DEGREES RMS PHASE PAIR ERROR - 1000 POINTS PER 100 MHz
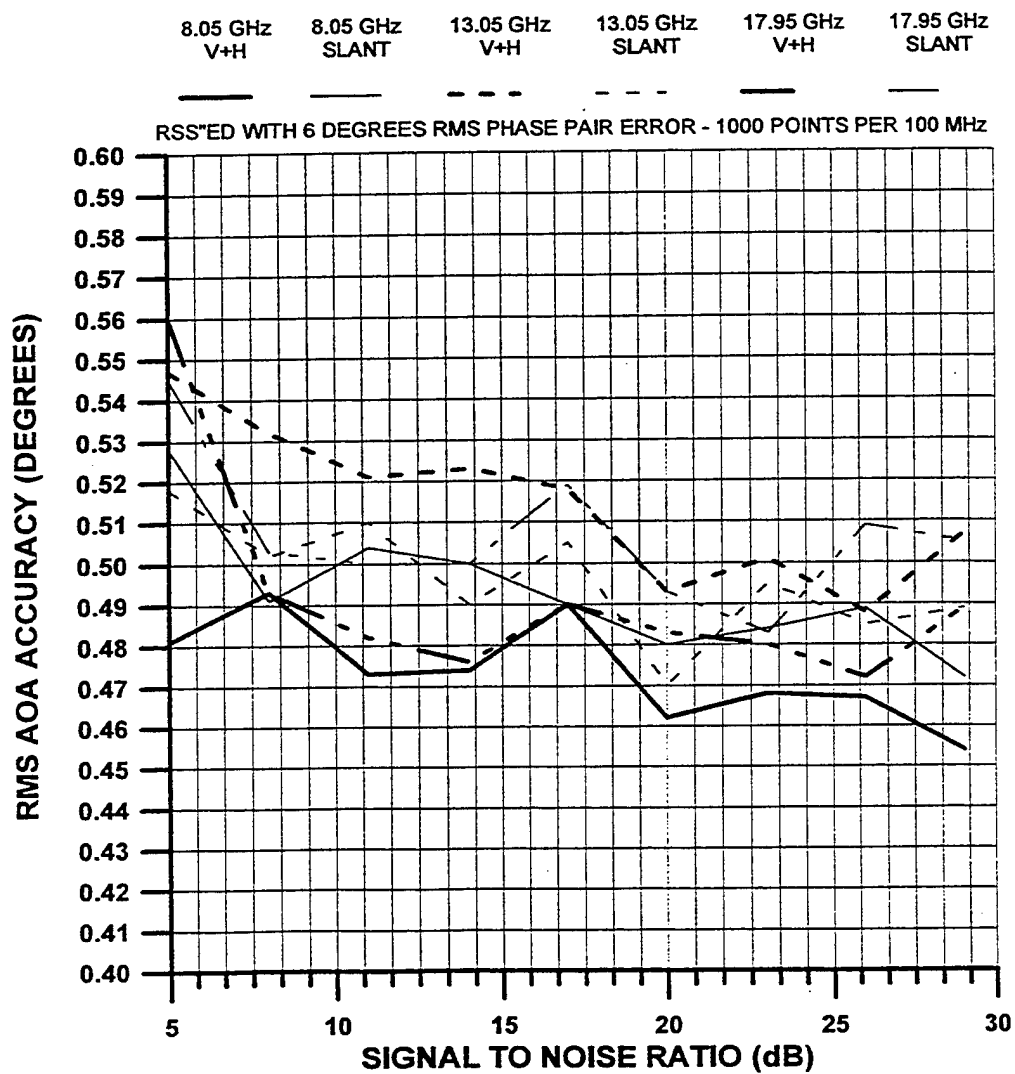
Figure 9.   RMS AOA Accuracy Versus Signal To Noise
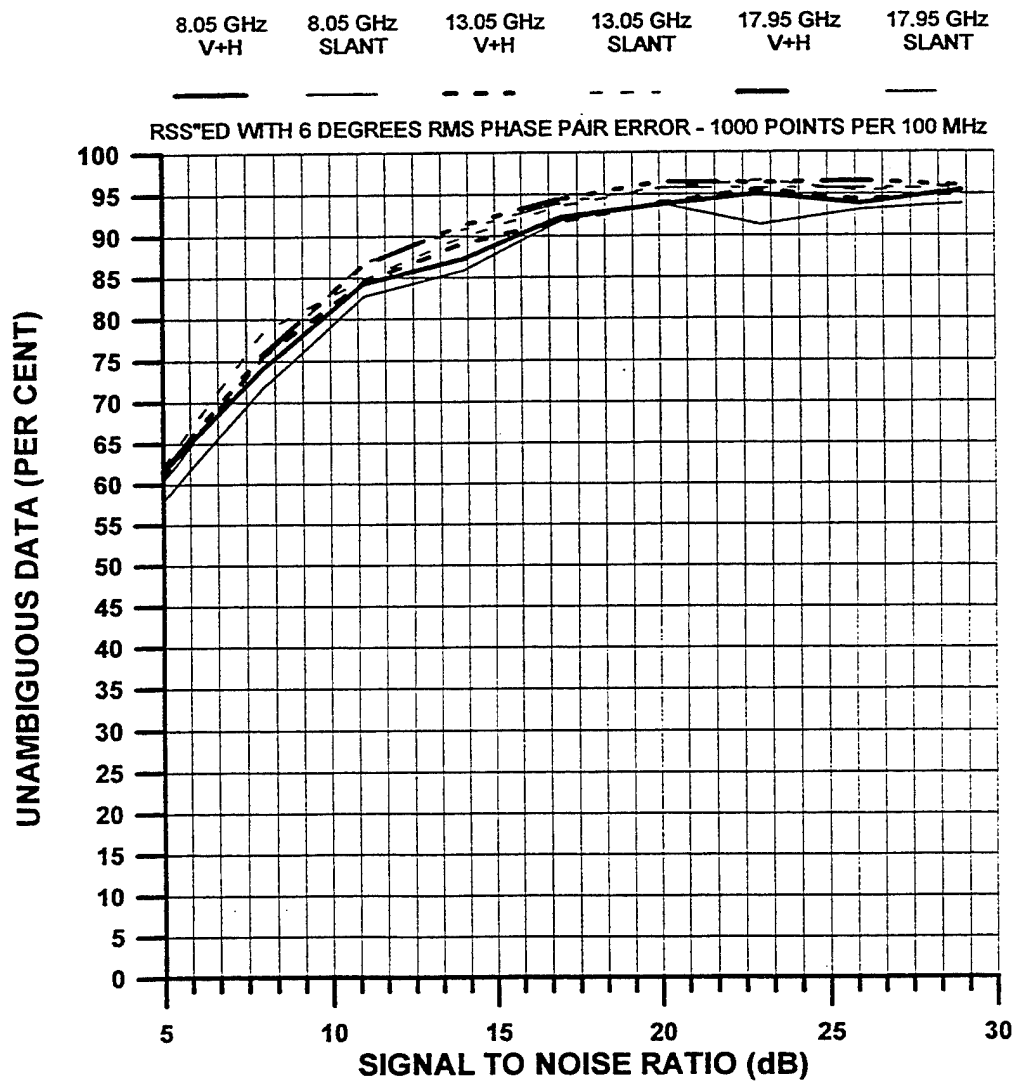
Ratio

Figure 10. Unambiguous Data Rate Versus Signal To
Noise Ratio

| 8.05 GHz | 8.05 GHz | 13.05 GHz | 13.05 GHz | 17.95 GHz | 17.95 GHz |
| V+H | SLANT | V+H | SLANT | V+H | SLANT |

RSS"ED WITH 6 DEGREES RMS PHASE PAIR ERROR - 1000 POINTS PER 100 MHz
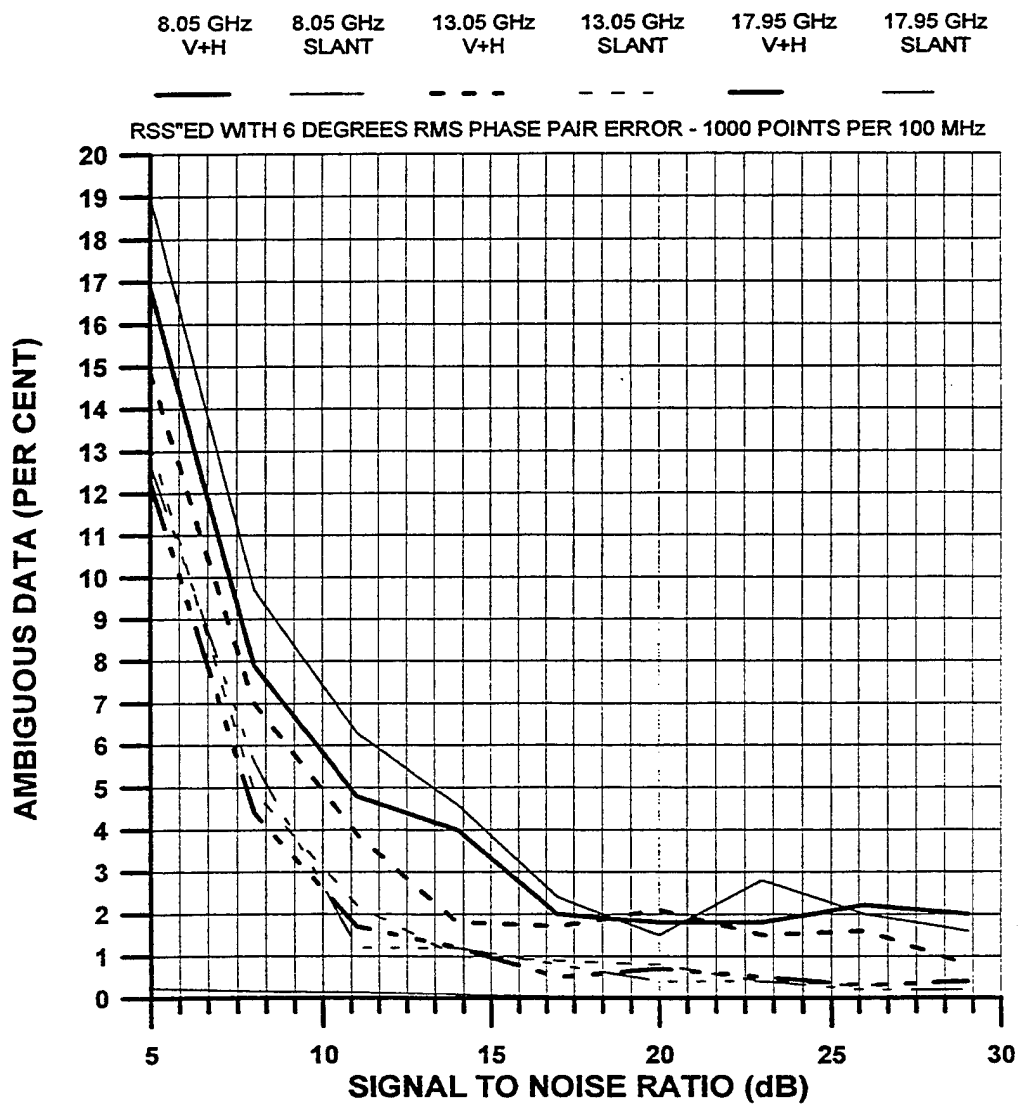
Figure 11. Untagged Ambiguous Data Rate Versus Signal

To Noise Ratio

207

dB and steadily increases as expected when the signal
to noise ratio decreases.

A generic 4 or 5 element linear interferometer would
have the typical specifications illustrated in Table
III. The linear interferometer has the elements spaced
at judiciously selected multiples of half wavelengths.
These are used for comparison to the circular DF array.
The assessment is that the linear interferometer is an
extremely high accuracy AOA antenna over a limited
field of view.

Table III.   Generic Linear Interferometer

specifications.

Frequency Range: 2 to 18 GHz

Element Gain: 0.0 dBi minimum

Polarization: Single

Field of View: Azimuth – 120 to 80 degrees

Elevation – application dependent

RMS AOA Accuracy: 0.1 degrees maximum

Ambiguity Rate: less than 1%

Unambiguous Data Rate: greater than 95%

Signal to Noise Ratio: 8 dB minimum

The real estate required to install an linear
interferometer is greater than that required by the
circular DF array. The size of the high accuracy
Circular DF array was 24 inches in diameter by 8 inches
in height.

4.0 Implementation Issues

In all the configurations of apertures that were looked
at, a Butler beamformer is desired since it is
simultaneous, quasi compact, and already exists. Low
Noise amplifiers should be installed in order to
overcome the insertion loss through the Butler matrix.
Filters can be added to keep out-of-band interference
minimized. Available COTS Butler matrix (beamformer),
switches, LNA's and filters should be used in the
realistic installation. Using COTS available hardware
is the most cost effective method.

The low noise amplifiers used will need to be evaluated
and adjusted in order to optimize and maximize
sensitivity, and 2nd and 3rd order spur free dynamic
ranges based on the requirements of the installation.

Calibration can be extremely important for providing accurate AOA. This needs to be considered in the modal phase data that are measured based on the installation requirements. The calibration data can be used to take out known sources of systematic phase bias errors such as interference from other structure.

With regard to specifications, it is extremely difficult to specify the DF array separately from the DF processor. The reason is that both are intertwined in determining AOA accuracy and sensitivity of the system and highly reliant on the proprietary algorithms used. This is in addition to calibration techniques that are included.

The light weight and simplicity of this design allow for endless installations in ground based, mobile and airborne systems. Different frequency bands of operation are presently being prototyped along with different sizes using a multitude of different dual polarization elements.

5.0 Conclusion

E-Systems, Greenville Division has developed a 360 Degree Azimuth DF antenna using COTS hardware. It was designed to work from 2 to 18 GHz with a goal of 1.0 degree rms AOA accuracy. An antenna prototype has been tested and evaluated using our proprietary algorithms resulting in a 0.6 degree rms AOA accuracy. This antenna is approximately 24 inches in diameter and about 8 inches in height. It is dual linearly polarized with two polarization configurations possible.

Use of this aperture installation is also expected to save weight due to a simplified mounting structure. The antenna aperture has higher gain which translates into larger detection range.

In all the configurations of apertures , a Butler beamformer is recommended since it is simultaneous, quasi compact, and already exists. The performance of the proposed aperture is better than the specified goals.

Implementation issues were addressed with regards to using COTS hardware. Sensitivity improvements to overcome Butler matrix insertion loss was discussed with regards to appropriate situational selection of amplifiers and filters. Calibration was also addressed as a means of increasing accuracy and accounting for known error sources.

A set of criteria was defined for specifying a generic DF antenna with regards to frequency and signal to noise ratio.

The basic circular DF array design can easily be scaled to other frequency bands which are being prototyped. Due to the light weight and simplicity of this antenna, installations are essentially endless for different ground based, mobile, and airborne systems.

6.0 References:

[1] P. J. D. Gething, Radio Direction Finding and The Resolution of Multicomponent Wave-Fields, London, England: Peter Peregrinus Ltd., 1978.

[2] Y. T. Lo and S. W. Lee, editors, Antenna Handbook: Theory, Applications, and Design, pp 25-1 - 25-26, New York: Van Nostrand Reinhold Company, 1988.

[3] J. B-Y. Tsui, Microwave Receivers With Electronic Warfare Applications, pp 92-112, New York: John Wiley & Sons, 1986.

[4] D. E. N. Davies and P. E. K. Chow, "An Experimental Array With Electronic Beam Rotation", Proceedings of the European Microwave Conference, pp 129-132, 1969.

[5] W. M. Sherrill, "Bearing Ambiguity and Resolution in Interference Direction Finders", IEEE Transactions on Aerospace and Electronic Systems, Vol. AE-5, No. 5, pp 959-966, November, 1969.

[6] T. Rahim, J. R. F. Guy and D. E. N. Davies, "A
Wideband UHF Circular Array", Proceedings of the
2nd International Conference on Antennas and
Propagation, pp 447-450, 1981.

[7] D. E. N. Davies, "Circular Arrays: Their
Properties and Potential Applications",
Proceedings of the IEE Conference on Antennas and
Propagation, pp 1-10, York, England, 1981.

[8] T. Rahim and D. E. N. Davies, "Effect of
Directional Elements On The Directional Response
of Circular Antenna Arrays", Proceedings of the
IEE, Vol. 129, Pt. H, No. 1, pp 18-22, February,
1982.

[9] P. Eyring and R. Clapp, "Design and Development of·
Wide-Band Circular Array Interferometers", Antenna
Applications Symposium, Monticello, Illinois, pp
1-35, 21-23 September, 1994.

[10] R. Clapp, "A Resistively Loaded, Printed Circuit,
Electrically Short Dipole Element For Wideband
Array pplications", IEEE Antennas and Propagation

Society International Symposium, pp 478-481, 28
June - 2 July, 1993.

[11] E. R. Ferrara and T. M. Parks, "Direction Finding
With An Array of Antennas Having Diverse
Polarizations", IEEE Transactions on Antennas and
Propagation, Vol. AP-31, No. 2, pp 231-236,
March, 1983.

A Method of System and Sensor Sensitivity Improvement

T. R. Holzheimer

E-Systems, Inc.

Greenville Division

Greenville, Texas   75403

Abstract:

The majority of sensors (i.e. antennas) are
connected to a system whereby the received signal is
amplified at the expense of increased noise (i.e.
decreased sensitivity) and decreased spur free dynamic
range. In practice, the first stage low noise
amplifiers are directly connected to the antenna. The
first stage amplifier typically has the lowest noise
figure possible. Methods to improve overall system
performance require a balancing of tradeoffs against
overall system performance. Typical solutions include
selection of amplifiers with different performance
parameters that have been selected to optimize overall
system sensitivity and spur free dynamic range. It is
also known that temperature of this amplifier can
affect not only its performance but also the overall
system performance. The improvement methods and
implementation described in this report uses
thermoelectric coolers (TEC) applied to off the shelf
low noise amplifiers mounted at the antenna output
connector. Improvements in system sensitivity and spur
free dynamic range *are* investigated over the 2 to 18

GHz frequency range applying this low noise amplifier
technique at the antenna output port. Methods of
implementation and lessons learned are discussed *in*
regard to practical application of this method in real
world environments. Examples of performance
improvement of a low noise amplifier and a generic
system performance improvement are discussed.
Practical limitations and potential limits on
performance improvements are described with regard to
overall system performance as used in this reported
investigation.

1.0 Introduction:

It is well known that amplifiers have better

performance when cold than when they are hot. The cold

amplifier has a lower noise figure (NF), and a higher

gain. These performance improvements can be taken

advantage of with a convenient means of cooling of the

amplifier rather than using liquid nitrogen and/or a

closed cycle stirling cooler which also has liquid

nitrogen in its system. The means of cooling looked at.

here is thermoelectric cooling which uses DC voltage

and current applied across separate "N" and "P" type

doped materials. Depending on how they are hooked up

one can either cool or heat with thermoelectric (TEC)

coolers.

Thermoelectricity was discovered in 1820 by Hans Christian Oersted and by Thomas Johann Seebeck in 1821.[1],[2],[3],[4] Oersted observed a deflection of a magnetic needle when a current flowed through a wire while Seebeck observed the magnetic needle move when two different types of conductors were heated.[5], [6], [7], [8] This is the basis of thermoelectricity today. Unfortunately, the effect was treated as a curiousity until Jean Charles Athanse Peltier observed that the passage of a current through a junction between two different conductors was associated with a thermal effect. This is the Peltier effect which is observed in using the thermoelectric coolers today.

The Seebeck effect, as it is called, converts heat into electrical energy. Heat input into a junction of dissimilar semiconductors ("N" and "P" type materials) causes current to flow from the hot side to the cold side. This in turn causes electric current to flow through the circuit. The Peltier effect is the reverse of the Seebeck effect where electric current is applied by the circuit to the junctions causing the junction to cool or heat. Depending on how the dc voltage is connected heat is absorbed or heat is given up.

When dc current is applied to the TEC, it passes from the "N" type material to the "P" type material causing heat to be absorbed and the common side to become colder. The cooling occurs at the junction due to the "P" type material electrons residing in a low energy state and then moving to the high energy state in the "N" type material. That is by electron transport heat is absorbed from the cold end of the TEC and expended out the hot side of the TEC which are on opposite ends of the TEC.

TECs are not 100% efficient due to joule heating of the junctions and heat generated via thermal conduction from the hot side to the cold side of the TEC. The power required by the TEC to cool is equal to the difference between the disspated heat of the hot side minus the amount of heat that can be absorbed. Temperature differentials are typically increased by stacking of junctions. All factors can be optimized for desired properties of heat dissipated to amount of cooling provided.

2.0 Data Acquired/Measurements for this Study:

Multiple types of thermoelectric coolers were obtained

from Melcor.   True cryogenic amplifiers were acquired

from Miteq for use in the lab testing phase of this

study.   Heat sinks were fabricated which allowed for

installation/removal of the amplifiers and TECs.   Refer

to the photographs of the actual hardware shown in

Figure 1.   Testing occurred in octaves from 2 to 18 GHz

which matched the bandwidths used on the various

platforms whose RF distributions (RFD) are later

analyzed in this report.   The octaves investigated were

2 to 4 GHz, 4 to 8 GHz, 8 to 12 GHz and 12 to 18 GHz.

Both room temperature and cooled down ($-45^{O}F$) data was

recorded as-well-as TEC configuration.   Practical

methods of implementation as-well-as the optimum number

of TECs were incorporated in all measurements.

Amplifiers designed for cryogenic applications were

purchased from Miteq which are actually commercial off

the shelf (COTS) hardware.   These amplifiers are laser

welded internally and not soldered which insures

connection to the GaAs Fets and/or microwave
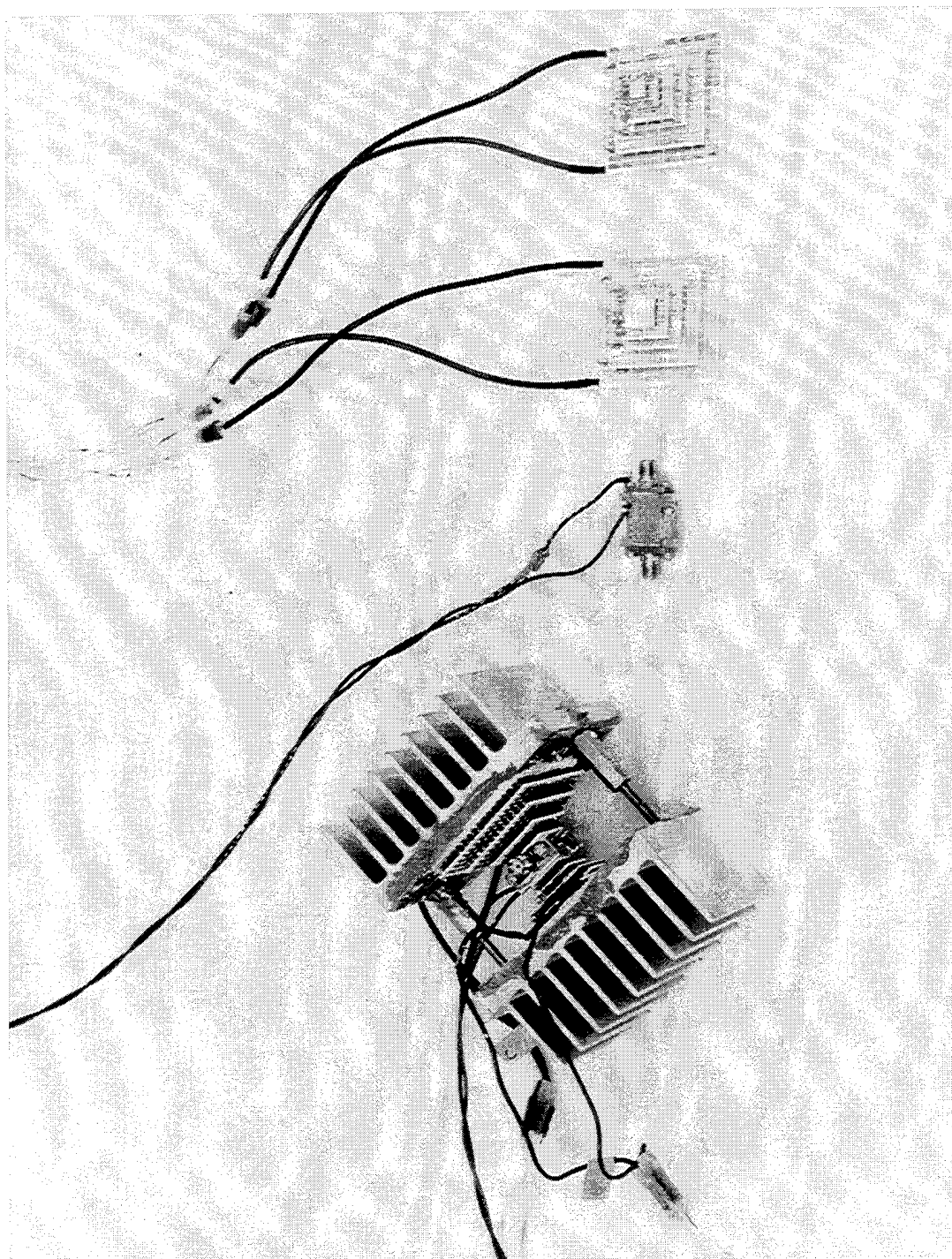
Figure 1. Multistage TEC's With Amplifier Used In Experiments

intergrated circuits (MIC) chips over these large

temperature extremes. Miteq has supplied these type of

amplifiers to Purdue University for use in the VSAT

array outside of Sandia Labs. The amplifiers *were*

literally dropped into liquid nitrogen. After cooling,

they were warmed to room temperature without any

failures occuring over many cycles. Since the

amplifiers regulator is not located inside the

amplifier, the amount of heat generated by the

amplifier is decreased. Therefore, the heat generated

is only due to the GaAs Fets and/or MIC chips alone.

In a practical application, this is by far the best way

to use these amplifiers and derive the maximum

efficiency attainable from the TEC's.

COTS thermoelectric coolers were purchased from Melcor.

The TEC's had almost the identical planform as the

Miteq amplifier. These coolers provided a theoretical

temperature differential (delta-T) of 97 to 131 degrees

Centrigrade (deg. C) which is only obtainable in a

vacuum. The amount of heat absorbed by the TEC varied

from 1.22 to 6.53 Watts.[9] The TEC is approximately

25% to 30% efficient based on test measurements and

specification data sheets. The typical TEC cooler used

required 23.8 Watts of DC power at 7 volts DC for a cooling capability of 6.53 Watts. The amount of heat absorbed is relatively small; therefore, careful attention to layout and incorporation of the amplifier and TEC in the system design under study is critical. The most detremental heat sink is the coaxial cables connecting the input and output connectors of the low noise amplifier (LNA}.[10] In the first test, standard 0.141 inch diameter 50 ohm coaxial cables were tried and then discarded due to the excessive heat loss generated by the cables. To correct this deficiency, two cables were special made by Micro-Coax for use in these test measurements. These coaxial cables are stainless steel with a Berylium (sp) center conductor in a 0.045 inch outside diameter. The new cable design presented almost zero heat load to the TEC's and possessed adequate strength to be easily used for rugged installations.

The measured cable losses of the stainless steel Microcoax cable are 101.6 dB per 100 feet at 5.0 GHz and 146.1 dB per 100 feet at 10.0 GHz which is comparable to the standard 0.85 inch diameter semi-

rigid coaxial cable used by the systems analyzed later in this report.

The test setup used is illustrated in Figure 2. An HP 8970B Noise Figure test setup with downconverter, was used to monitor both noise figure and gain of the TEC cooled amplifier. All supply voltages and currents were monitored via voltmeters. Temperatures were monitored with high sensitivity thermocouples via a Fluke 2280B multichannel temperature meter with printing capability. Additional photographs of the actual test setup are shown in Figure 3. In the actual cool down tests, the TECs, amplifier, coaxial cables and thermocouples for temperature monitoring were located in an accurately controlled temperature and humidity test chamber.

Tests were made both at room temperature (25 degrees C) and at -45 degrees C. The latter temperature represents a realistic thermal environment for a platform at 33,000 feet altitude. The measured test data are summarized in Table I and actual data plots are provided in Figures 4 through 11.
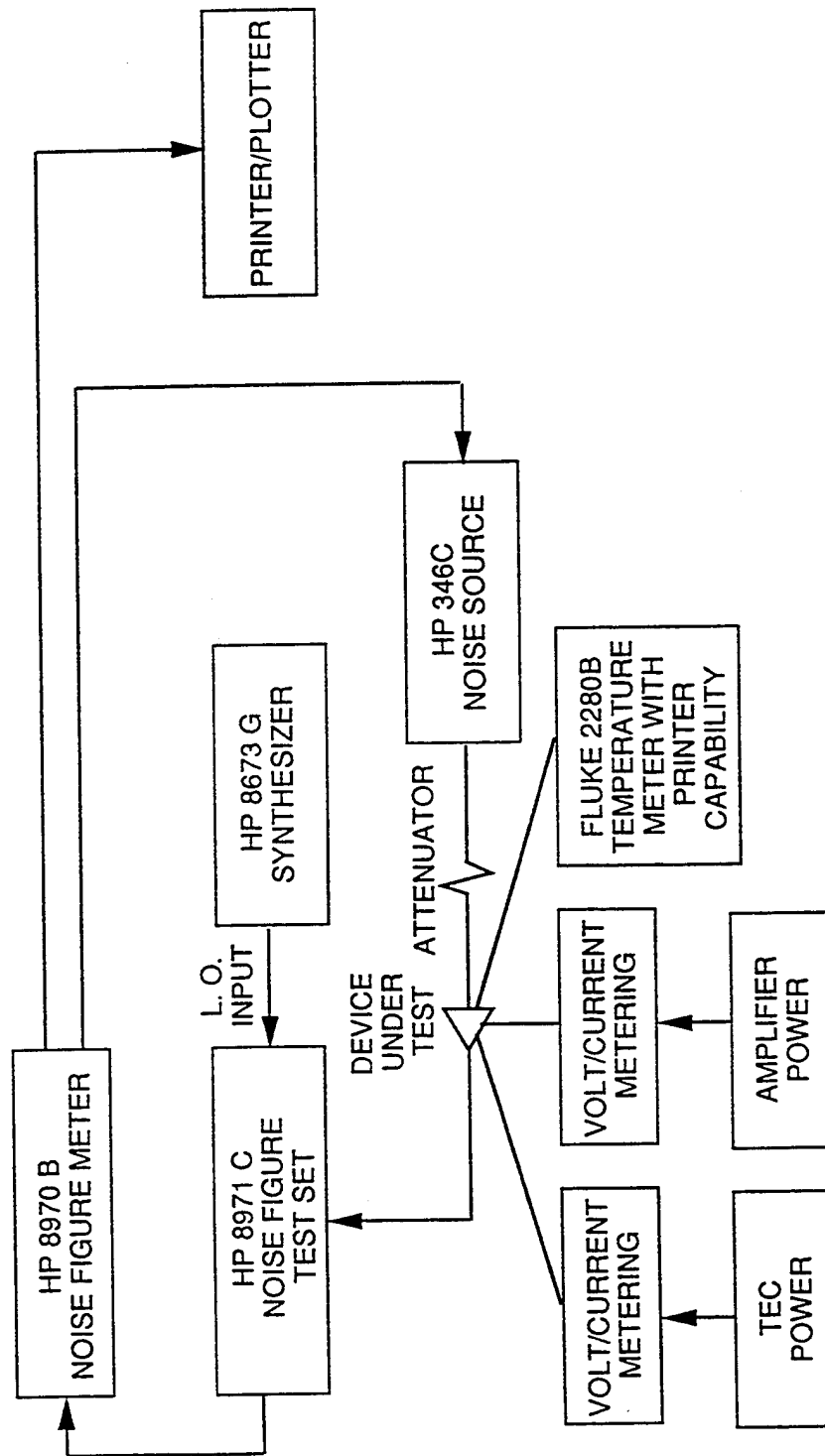
Figure 2.   Block Diagram of Measurement Test Setup
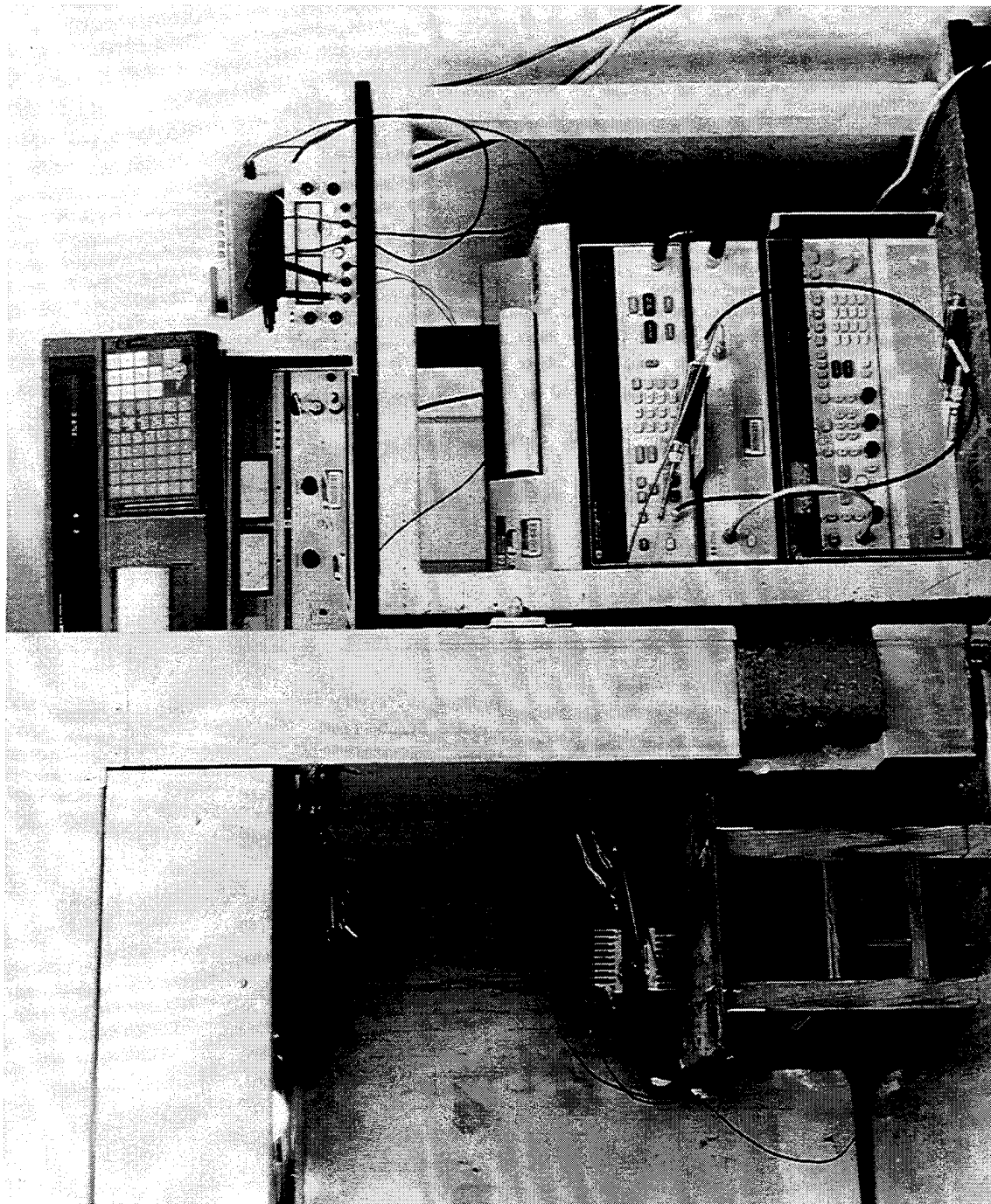
Figure 3.   Actual Measurement Test Setup

Table I. Amplifier Measurement Comparison

Frequency	25 degrees C		-45 degrees C		Delta	Delta
(GHz)	NF	Gain	NF	Gain	NF	Gain
	(dB)	(dB)	(dB)	(dB)	(dB)	(dB)
2	0.74	32.3	0.22	34.5	0.52	2.2
4	0.96	31.77	0.36	33.8	0.6	2.03
4	0.89	31.7	0.20	34.9	0.69	3.2
8	0.77	32.1	0.10	33.8	0.67	1.7
8	0.8	31.7	0.18	34.5	0.62	2.8
10	0.87	32.0	0.10	33.7	0.77	1.7
12	0.88	32.4	0.10	34.2	0.78	1.8
12	1.54	26.98	0.50	29.7	1.04	2.72
15	1.84	25.70	0.68	29.5	1.16	3.8
18	1.87	26.85	0.85	30.6	1.02	3.75
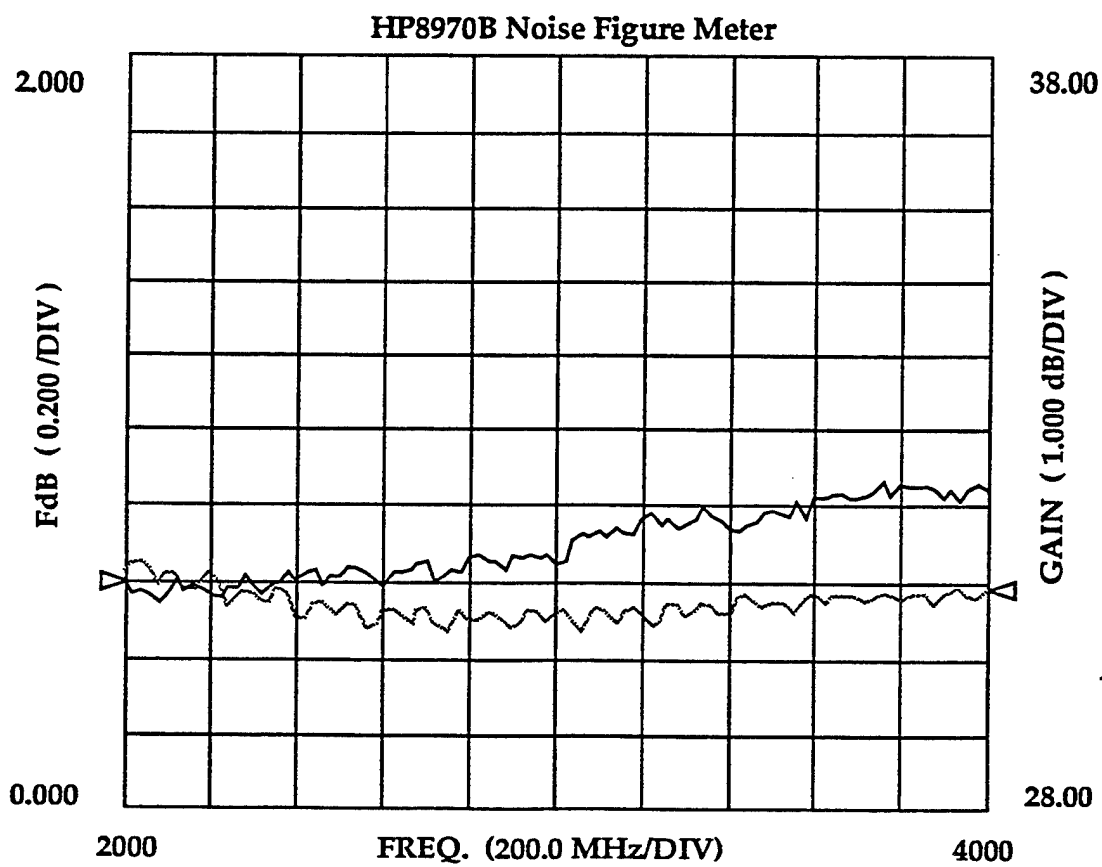
Figure 4. Noise Figure and Gain of Amplifier at 25
Degrees C Operating 2 to 4 GHz
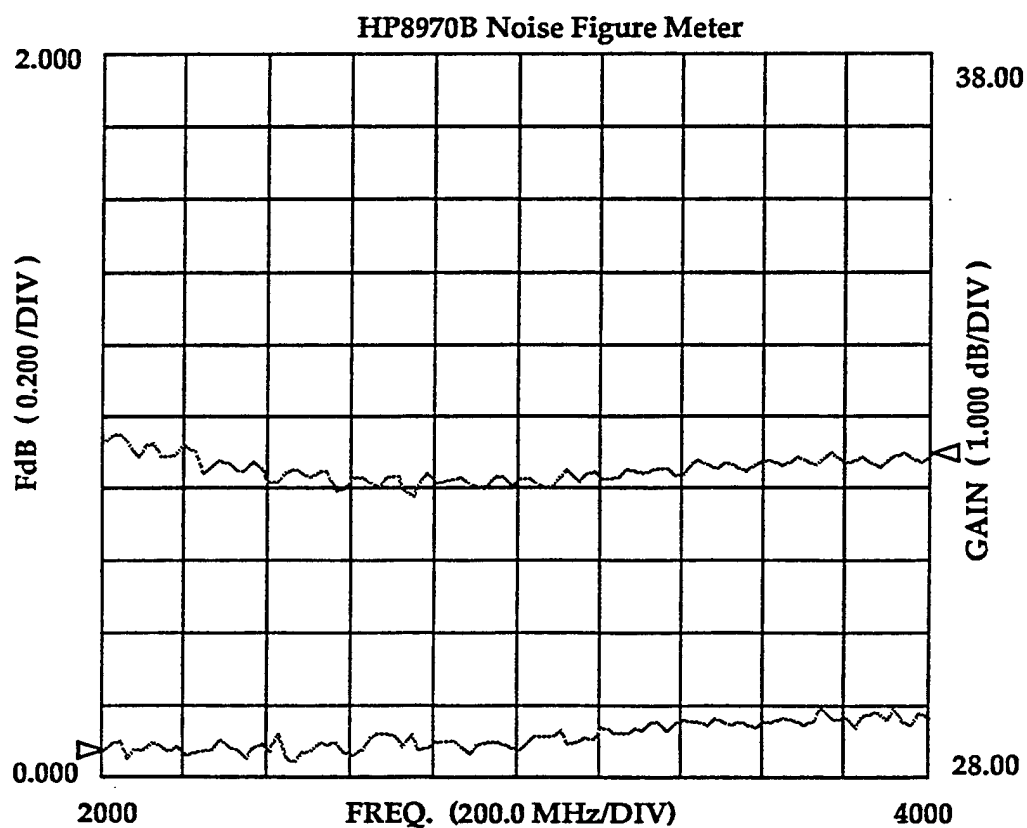
Figure 5.   Noise Figure and Gain of Amplifier at -45
Degrees C Operating 2 to 4 GHz
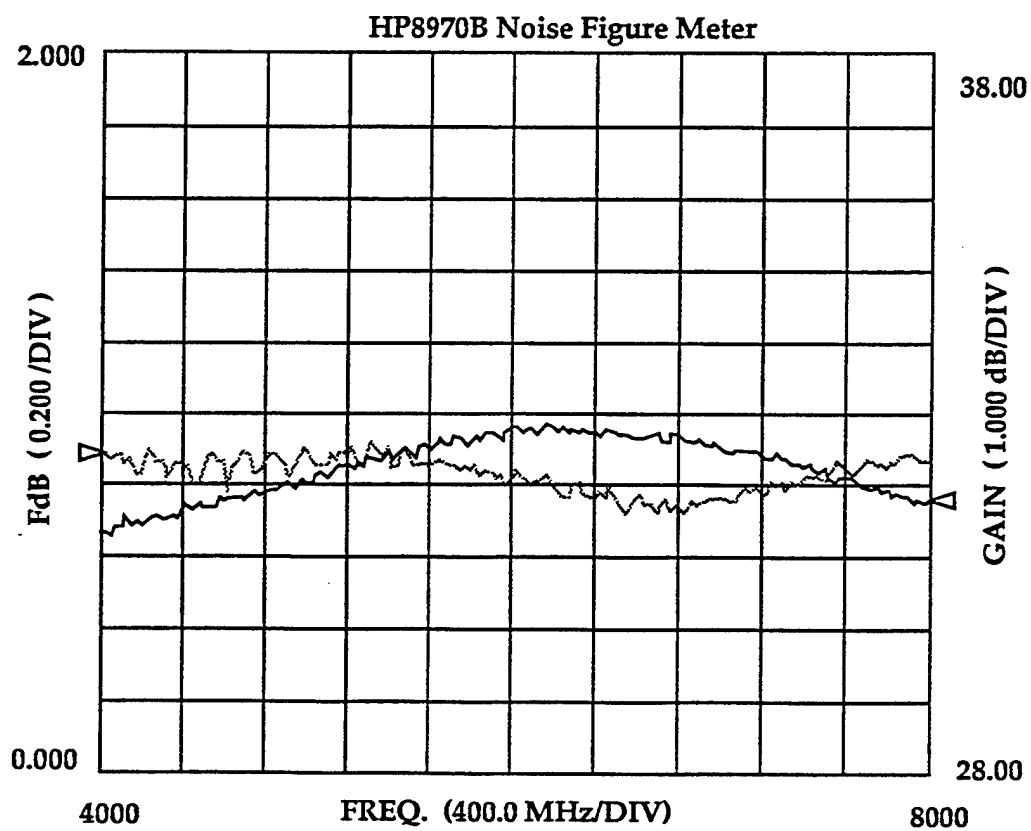
Figure 6. Noise Figure and Gain of Amplifier at 25
Degrees C Operating 4 to 8 GHz
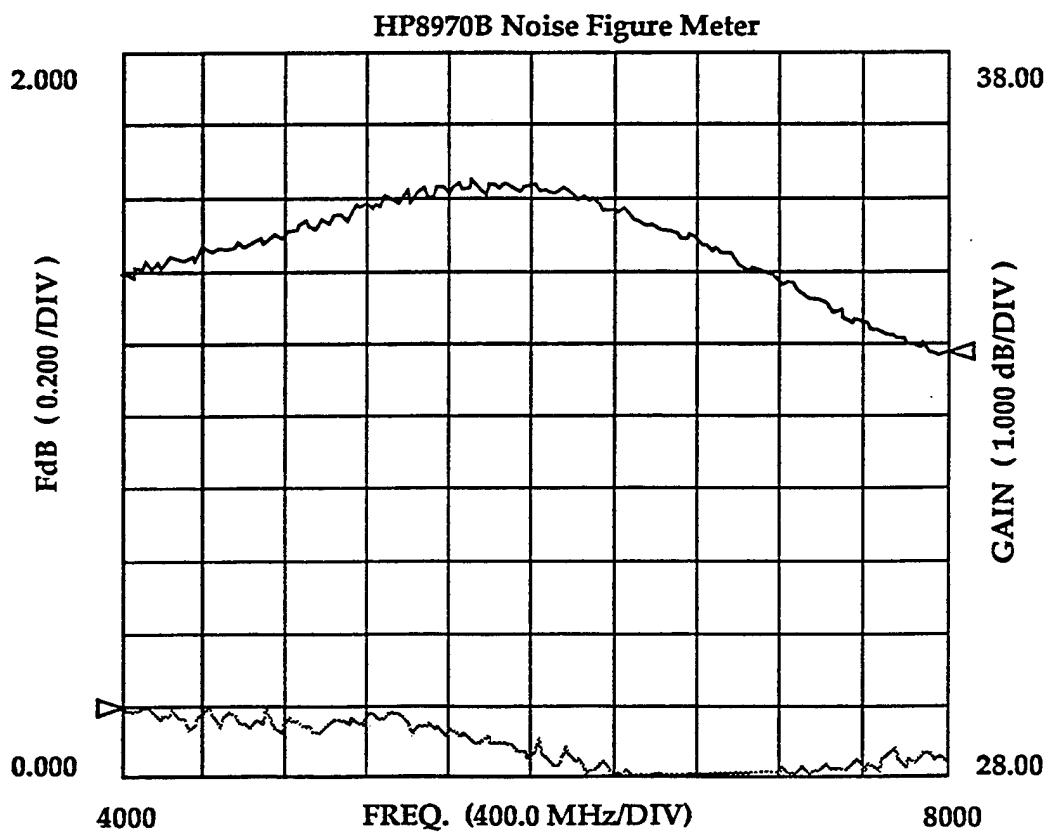
Figure 7. Noise Figure and Gain of Amplifier at -45 Degrees C Operating 4 to 8 GHz
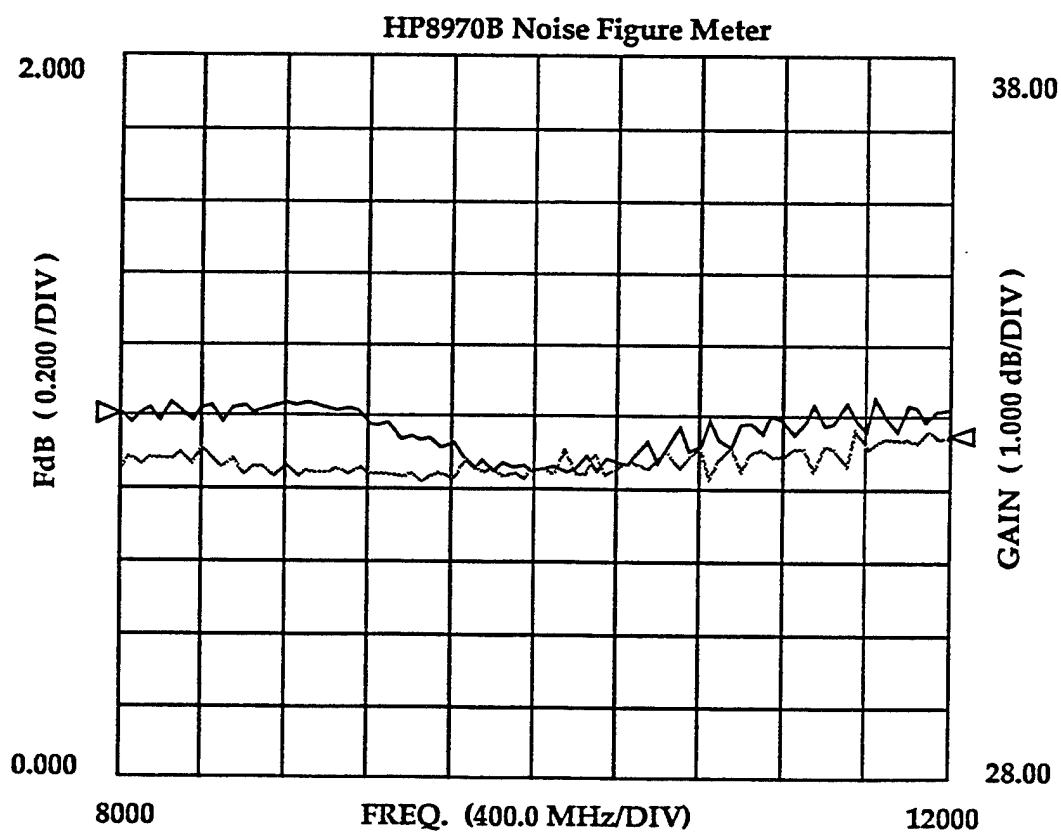
Figure 8.   Noise Figure and Gain of Amplifier at 25
Degrees C Operating 8 to 12 GHz
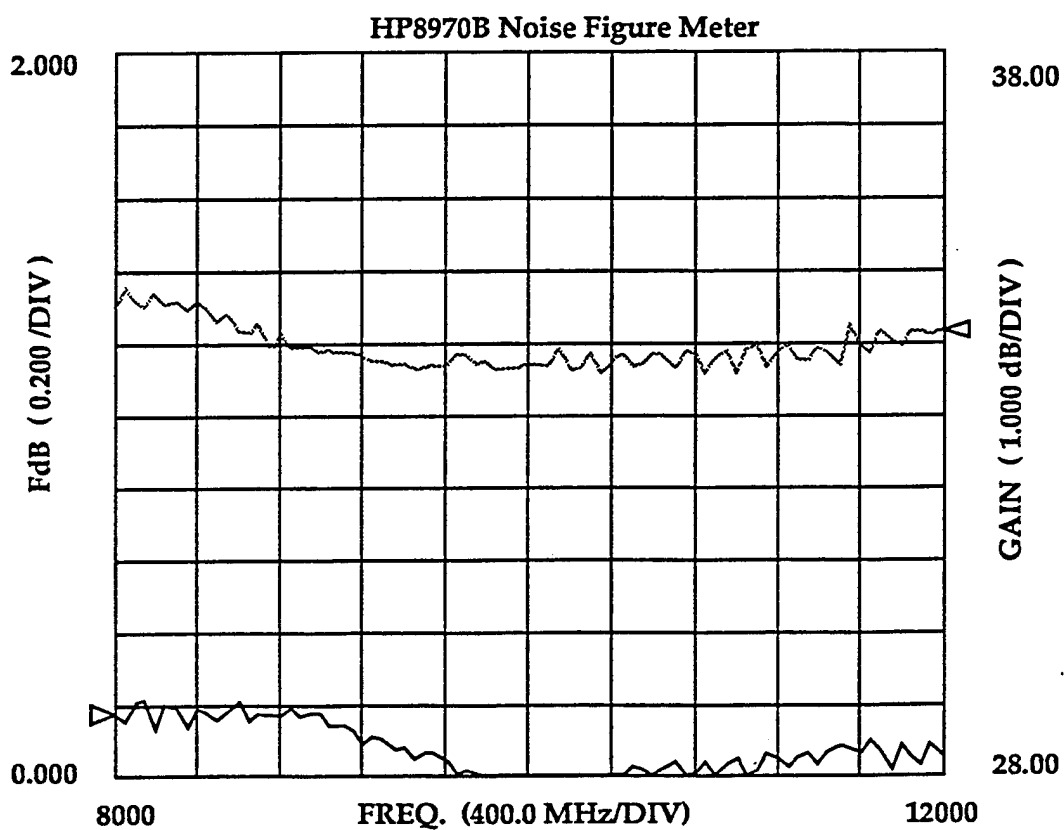
Figure 9.   Noise Figure and Gain of Amplifier at -45
Degrees C Operating 8 to 12 GHz
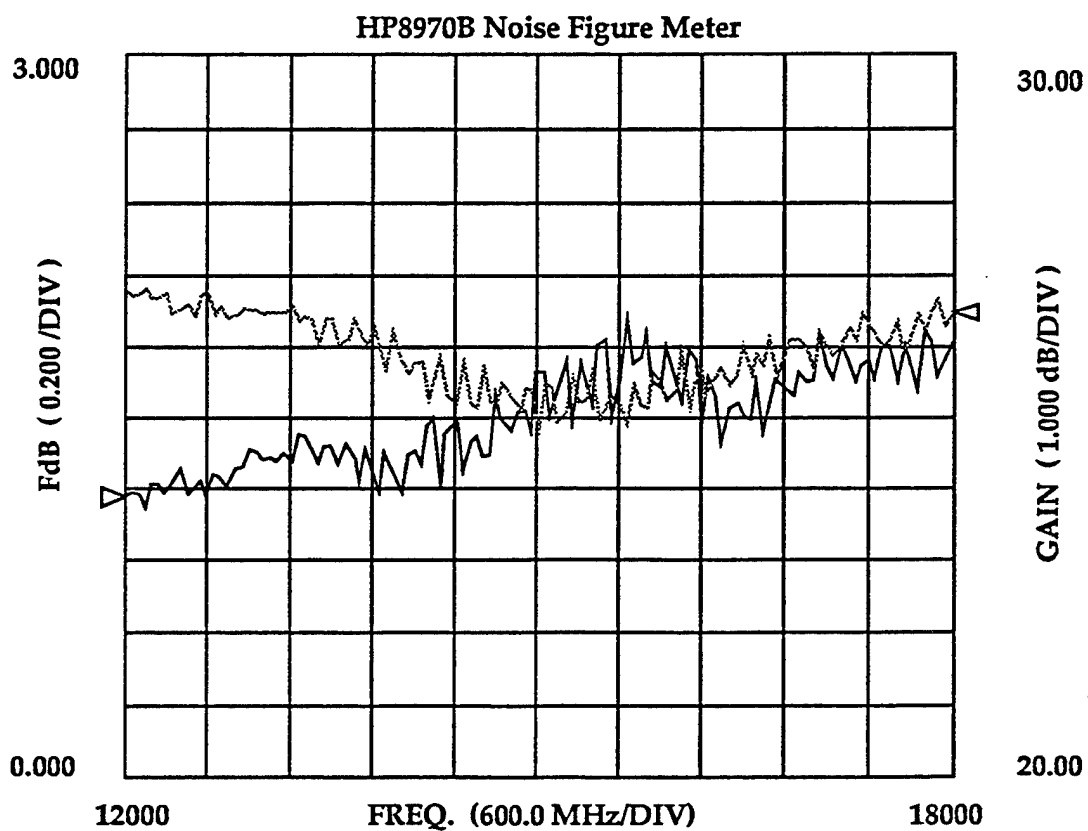
Figure 10.   Noise Figure and Gain of Amplifier at 25
Degrees C Operating 12 to 18 GHz

236
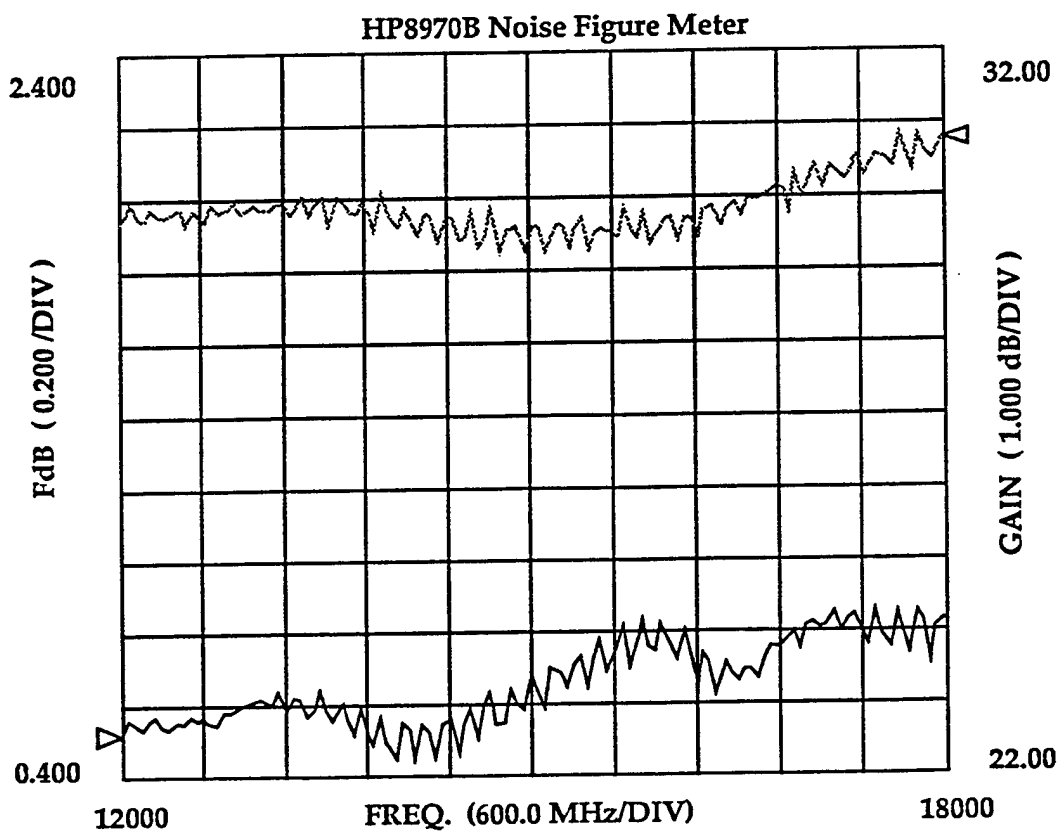
Figure 11. Noise Figure and Gain of Amplifier at -45 Degrees C Operating 12 to 18 GHz

The foregoing data was then entered into the
appropriate replacement points of the various RF
distribution spreadsheets for three systems. The
results of the analysis are summarized by determining
the performance improvements in 2nd and 3rd order
dynamic ranges, system noise figure and system
sensitivity. The data from Table I was used in
performing these analysis. A delta of 0.1 to 0.15 dB
was added to the front of the Low Noise Amplifiers
(LNA) noise figure in order to account for a limiter
(Limiters were not available due to the short schedule
of this effort).

All pertinant data are summarized in additional tables
for the systems analyzed.

There are three methods of optimizing a system which
are independently sensitivity, spur free dynamic range,
and the optimizing of both sensitivity and spur free
dynamic range concurrently. System 1 is optimized for
dynamic range i.e. it is optimized to handle large
amounts of high power interference. Thus the criteria
of importance in the tables for System 1 are second and
third order spur free dynamic range. System 2 is

optimized for maximum sensitivity i.e. it is optimized
to pick up extremely weak or low power interference.
System 3 is concurrently optimized for both sensitivity
and spur free dynamic range i.e. both for weak or low
power interference and large amounts of high power
interference.

Tables II through III provide comparisons to the
reference values of system 1. Delta comparisons for
improvement are tabulated in Table IV. They quickly
show the improvements that are obtained. Positive
numbers are improvements, whereas, negative numbers are
the opposite.

Tabulated data and comparisons for system 2 are shown
in Tables V through VI. Delta comparisons for
improvement are tabulated in Table VII. This is a
sensitivity optimized platform.

Tabulated data and comparisons for system 3 are shown
in Tables VIII through IX. Delta comparisons are shown
in Table X. This is an optimized concurrently
sensitivity and spur free dynamic range platform.

Table II. System 1 Reference Paths

Frequency (GHz)	Sensitivity (dBm)	2nd SFDR (dB)	3rd SFDR (dB)
3.0	−108.2	41.5	52.3
6.0	−108.5	41.6	52.8
10.0	−107.2	40.7	51.6
15.0	−107.9	36.6	46.1

Table III. System 1 Performance Data

Frequency (GHz)	Sensitivity (dBm)	2nd SFDR (dB)	3rd SFDR (dB)
3.0	−111.8	43.5	55.3
6.0	−112.5	42.1	53.5
10.0	−112.4	41.7	53.0
15.0	−110.5	44.0	56.1

Table IV. System 1 Performance Deltas

Frequency (GHz)	Delta Sensitivity (dBm)	Delta 2nd SFDR (dB)	Delta 3rd SFDR (dB)
3.0	+3.6	+2.0	+3.0
6.0	+4.0	+0.5	+0.7
10.0	+5.2	+1.0	+1.4
15.0	+2.6	+7.4	+10.0

Table V. System 2 Reference Paths

Frequency (GHz)	Sensitivity (dBm)	2nd SFDR (dB)	3rd SFDR (dB)
4.0	-108.35	43.71	54.09
8.0	-105.16	42.34	52.33
12.0	-98.98	40.88	50.36
18.0	-94.2	42.86	53.39

Table VI.   System 2 Performance Data

Frequency	Sensitivity	2nd SFDR	3rd SFDR
(GHz)	(dBm)	(dB)	(dB)
4.0	-102.60	48.04	60.36
8.0	-105.93	42.97	53.02
12.0	-104.34	43.57	53.96
18.0	-94.96	43.98	54.88

Table VII.   System 2 Performance Deltas

	Delta	Delta	Delta
Frequency	Sensitivity	2nd SFDR	3rd SFDR
(GHz)	(dBm)	(dB)	(dB)
4.0	+0.84	-1.15	-1.62
8.0	+0.22	+0.47	+0.51
12.0	+6.74	+2.78	+3.78
18.0	+2.21	+0.98	+1.38

Table VIII. System 3 Reference Paths

Frequency (GHz)	Sensitivity (dBm)	2nd SFDR (dB)	3rd SFDR (dB)
4.0	-100.6	47.5	59.2
8.0	-104.5	44.6	55.0
12.0	-102.7	46.8	59.1
18.0	-102.2	43.7	55.7

Table IX. System 3 Performance Data

Frequency (GHz)	Sensitivity (dBm)	2nd SFDR (dB)	3rd SFDR (dB)
4.0	-112.3	43.5	55.1
8.0	-109.0	46.4	58.4
12.0	-106.1	46.54	58.62
18.0	-104.8	46.5	60.4

Table X. System 3 Performance Deltas

Frequency (GHz)	Delta Sensitivity (dBm)	Delta 2nd SFDR (dB)	Delta 3rd SFDR (dB)
4.0	+11.7	-4.0	-4.1
8.0	+4.5	+1.8	+3.4
12.0	+3.4	-0.26	-0.48
18.0	+2.6	+2.8	+4.7

3.0 Conclusions:

The measurements taken and the resultant analyzed data have illustrated that DC cryo-electronics along with cryogenic manufactured amplifiers are viable and in most cases for Systems 1 through 3 produce desired improvements in performance. Care must be taken in the installation of the TEC's by using stacking, cryogenic cables, and external regulators. The added cost of the amplifiers is not excessive and appears well worth the gains in system performance. It is recommended that these class of amplifiers and TEC's be incorporated into system platforms where the greatest benefits from performance improvements occur and certainly at frequencies greater than or equal to 8.0 GHz.

The techniques for installing the TEC's, as used in the study, must be maintained and preference is to locate amplifier and TEC's in a cavity filled with dry air with external heat radiators. Stacking is desireable, as shown in the figures. TEC specifications must be carefully read as the highest delta temperatures specified occur in a closed vacuum.

4.0 References:

[1] A. F. Joffe, "The Revival of Thermoelectricity", Scientific American, vol. 199, no. 5, pp 31-37, November, 1958.

[2] J. McDermott, "Thermoelectric Coolers Tackle Jobs Heat Sinks Can't", EDN, pp 111-117, May 20, 1980.

[3] ASHRAE Handbook of Fundamentals, pp 24-30, ASHRAE, 1988.

[4] L. A. Johnson, "Controlling Temperatures of Diode Lasers and Detectors Thermoelectrically", Lasers & Optronics, pp 88-92, April, 1988.

[5] A. W. Swager, "Methods Converge to Cool Fast and Dense Circuits", EDN, pp 162-168, December 6, 1990.

[6] T. P. Lynch, "Get A Handle on Heat", Design News, pp 102-104, January 21, 1991.

[7] M. A. Levine, "Thermoelectric Refrigeration",
     Refrigeration Service Engineering Society, App.
     Note 630-101, Section 79, pp 1-11, July, 1989.

[8] D. K. C. MacDonald, Thermoelectricity: An
     Introduction to the Principles, New York: John
     Wiley & Sons, Inc., 1962.

[9] A. J. Chapman, Heat Transfer, pp 20-41 and pp 470-
     524, New York: The Macmillan Company, 1968.

[10] Melcor Thermoelectric Coolers Catalog, page 4,
      1995.

A SURVEY OF OPTICAL BEAMFORMING TECHNIQUES

Mark G. Parent

Naval Research Laboratory
Code 5317 Radar Analysis Branch
Washington D.C. 20375

Abstract

With the large availability of wideband components and MMIC devices, the design and development of wideband phased arrays has become practicable. Unfortunately, current microwave beamforming and distribution architectures used in current phased array systems are either too narrowband to fully utilize these component characteristics or become too heavy and bulky when providing wideband performance. These deficiencies in microwave based concepts has led to the development of various optical systems which provide microwave signal distribution as well as beamforming capabilities to the antenna array.

The use of an optical system to provide functionality to a wideband array is possible due to the extreme wideband nature of the optical system. Microwave signals which are modulated onto an optical carrier can either be delayed or given a relative phase shift which, upon detection, maintain their desired responses. The three most common optical methods used to produce time-delay are: switchable optical fiber or air lengths, optical waveguide switching and dispersive optical fibers. Within each method there are various architectures and techniques used to produce these delays. In this paper a survey of these various optical beamforming methods will be presented. The advantages and disadvantages of these methods will be discussed.

1.0   Introduction

The ability of a phased array system to achieve the high performance levels which are available today has been due to the speed and computational power of the computer. It has been this computational capability that has enabled phased array systems to do search, track and analyze vast amounts of information at millisecond rates. The next generation of phased array based systems will no doubt incorporate newer, higher speed computers to improve their current capabilities and will utilize wideband MMIC technology to increase their operational bandwidth requirements. These next generation phased arrays will need to detect and track multiple threats, be used in a multifunction and/or mutlifrequency role and most of all, must be affordable. Current computing power and the availability of inexpensive wideband MMIC components will help to meet these requirements, but for a phased array system to fully achieve all of these characteristics, advancements in wideband beamformers are required. The main emphasis on future beamformer designs will be in developing distribution networks which are wideband, light weight and easily adaptable to conformal surfaces.

Some of the newest and most promising approaches which are being used in developing wideband beamformers are based on optical technology. There have been over a dozen proposed or demonstrated systems which use various optical techniques to generate both amplitude and phase information or time-delays needed to control an array antenna. The earliest modulo 2π optical techniques[1-2] focused on using optical processors which created an equivalent Fourier Transform (both amplitude and phase) of the far-field antenna pattern across an array of fibers. The

251

main drawback to this type of modulo 2π beamformer is that it is by nature relatively narrowband. By being narrowband, the array becomes frequency dependent, i.e.. a scanned beam will move as the frequency of the beam is changed (array beam squint). To remove this frequency dependency, various optical time-delay beamforming techniques have been developed. The use of time-delay beamforming allows the array to transmit and receive large instantaneous bandwidth signals, such as high data rate communications or spread spectrum techniques, without any signal degradation due to beam squint.

Finally, besides the above two techniques, there are other system concepts that incorporate a hybrid of approaches. This includes using both RF and optical delay lines. In this type of design, the largest delays are produced using optical techniques, while the smaller delays are produced with conventional RF delay lines where the losses can be tolerated.

All of the above optical beamforming techniques have their advantages and disadvantages. In order to understand the specific techniques of each method, each system concept will be examined and commented on.

2.0 Modulo 2π Optical Beamformers

Most phased array radars which are in use today[3-4] incorporate modulo 2π phase shifters (such as ferrite devices) in their beamforming networks. These radar systems have proven to be very effective and have impressive performance characteristics. Unfortunately, the deployment of these arrays has been limited mainly to land and sea based platforms due to the extreme weight of the RF distribution and beamforming networks. The use of an optical based beamformer eliminates this limitation.

2.1 Mach-Zender Beamformer

All early optical beamformer designs incorporated modulo 2π techniques to produce the required phase and amplitude distribution across an antenna array. Figure 1 illustrates a typical optical Mach-Zender[1] interferometer type beamformer which is used to provide both phase and amplitude information to the array.
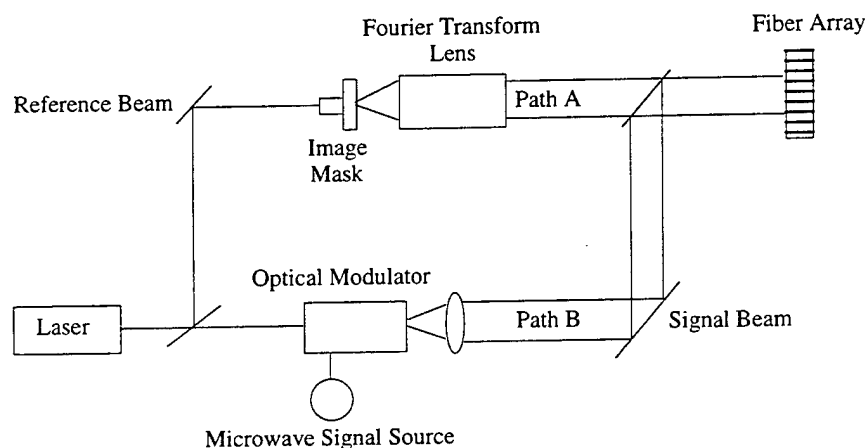
Fig. 1. Mach-Zender Optical Beamformer (after [1]).

This beamformer uses two separate paths of light that are combined and sampled by a fiber optic array. One path, referred as the reference beam (A), passes through an image mask and is focused onto the fiber array by a Fourier Lens arrangement. The second path, called the signal beam (B), is used to modulate a RF signal onto the optical carrier. The role of the image mask and Fourier Transform Lens arrangement is to produce an optical inverse Fourier Transform (FT) of a far field antenna pattern across the fiber array. This mask can be as simple as a pin hole which produces a uniform optical phase and amplitude

253

distribution across the array. In order to steer the array, small lateral movements of the image mask will introduce an interference effect which produces a phase gradient across the optical fiber array. This optical beam deflection, between paths A and B, creates a RF beam deflection from the microwave array after detection. This optical to RF beam deflection is given by

$$\left(\frac{\Delta y}{\lambda}\right) \sin\theta = \left(\frac{\Delta Y}{\Lambda}\right) \sin\Theta \qquad (1)$$

where Δy and ΔY are the spacing of the RF and optical array elements respectively, Θ is the angle between the two optical paths and θ is the resulting beam direction from the antenna array and λ and Λ are RF and optical wavelengths. For a typical optical configuration, the fiber spacing is about 150Λ and the antenna elements are spaced at $\frac{\lambda}{2}$. This produces an overall magnification of 300 for this system. Because of this, less than $.2°$ of relative movement between the two optical beams is required to produce a π phase shift between adjacent elements. This amount of phase shift is capable of steering a beam from broadside to endfire.

In order to produce the microwave signal at the optical detectors, beam (B) is passed through a Bragg Cell or an Acousto Optic Modulator. These devices are used to modulate a RF signal onto the optical carrier. When the optical carrier is detected, a RF signal is recovered which contains any phase or amplitude information transferred by the optical system. Keopf[1] had proposed a design using this type of beamformer and Stilwell[2,5-7] has carried out an extensive

study on using this type of beamformer in a phased array system. Figure 2 shows Stilwell's optical beamformer with a fiber array and RF array elements attached.
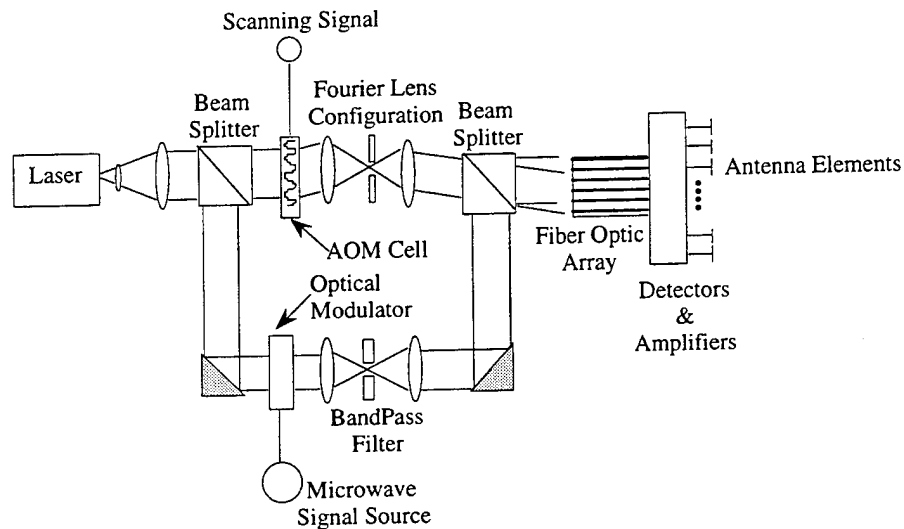
Fig. 2. AOM scanned MZ Optical Beamformer.

Unlike the concept described in Figure 1, the image plane in Figure 2 remains fixed and the variable phase gradient is created by moving the reference beam through the use of an Acousto Optical Modulator (AOM). The AOM deflects the incoming light through an angle θ, which is proportional to an applied RF frequency to the AOM. Since the AOM is also imaged through the FT lens, the steered optical beam generated by the AOM acts as a laterally moving spot in the image plane which creates the variable phase gradient across the optical array.

This system can be made very compact and can be extended to scan in two dimensions by adding an orthogonal AOM deflector to scan in the elevation plane as illustrated in Figure 3.
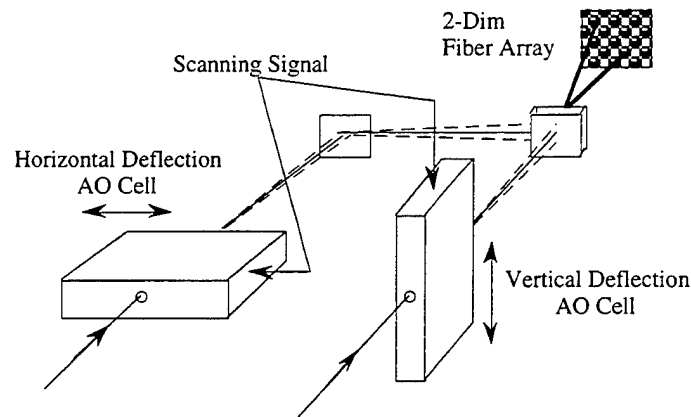
Fig. 3. 2-Dimensional Optical Scanning.

One potential problem of this type of system is due to the interferometeric aspect of combining the two optical beam paths. Since there is a high degree of magnification associated with this system, slight mechanical movements between each path can cause phase modulation to appear across the array and possibly produce unwanted beams from the array. One solution to this problem is to replace the Mach-Zender architecture with an optical device which generates optical phase shifts across the fiber array. Various Liquid Crystal displays have been investigated which have the optical properties necessary to achieve the required phase shifts, as discussed in the next section.

2.2 Liquid Crystal Optical Phase Shifter

There has been various groups investigating techniques[8-9] which use a voltage controlled optical device to create a variable phase shift in an optical beam. These techniques incorporate a Neumatic Liquid Crystal (NLC) to create optical phase shifts on the transmitted light beam. The phase shift produced is equivalent to

the two beam method used in the Mach-Zender beamformer but without the instabilities associated with it.

The NLC is made from a voltage controlled birefringence material which is used in many optical display devices. Because of the birefringence properties of the NLC, the index of refraction in one plane is independent of the applied voltage, while the orthogonal plane's index of refraction is a function of the applied voltage. To understand how this effect can be used to produce an optical phase shift, Figure 4 demonstrates the influence of a NLC on a vertically polarized optical light source.
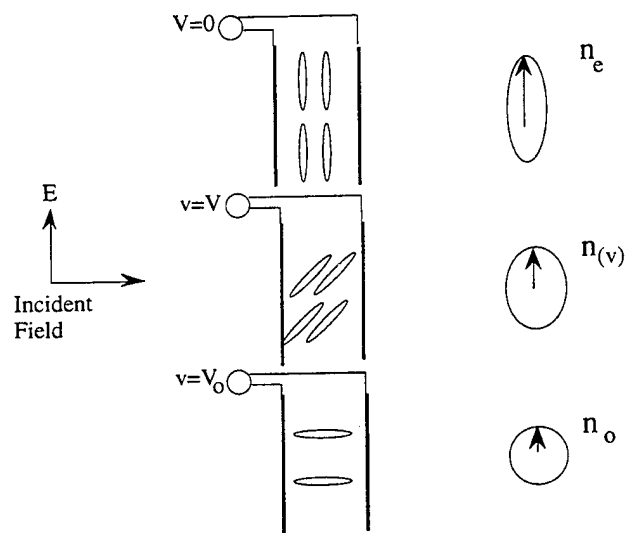
Fig. 4. Neumatic Liquid Crystal voltage controlled concept (after [9]).

When a vertically polarized wave is incident on the NLC in a zero voltage state, the wave passes through the material sensing an index of refraction of n_e. In this state, the long axis of the molecules making up this material are aligned along the axis of the incident polarization and will impart the greatest interaction with the incoming incident field. As voltage is applied to the material, the molecules rotate

away from the vertical position causing the index of refraction of the material to decrease to some value n(v). As the voltage is increased further, the index of refraction approaches the final value n_o which is the same index of refraction as seen by a horizontally polarized wave. Therefore, the maximum phase shift produced by this device is given by

$$\phi_{max} = \left(\frac{2\pi}{\Lambda}\right)(n_e - n_o)d \tag{2}$$

where d is the thickness of the cell and Λ is the optical wavelength. Phase shifts of over 2π have been reported[9] using this technique. Figure 5 shows a typical application of this device used in generating both phase and amplitude distributions for a phased array. Since the phase shift through the material is only a function of the index of refraction, the voltage controlled NLC becomes a very compact method of producing optical phase shifts. The other advantage of using a NLC based system is that it is a natural 2-D system which reduces the complexity in producing both azimuth and elevation scanning capabilities. The only disadvantage in using this system is that it is more optically complex and requires additional alignment procedures.

All of the above optical beamformers generate the phase information using modulo 2π techniques. These techniques are well suited but if large operational bandwidths are required, modulo 2π systems have an inherent problem associated with them. Since a beam position is a function of both the phase gradient and frequency of operation, as one parameter is changed the other must be compensated

for to offset the effects induced on the beam position. Modulo 2π beamformers are unable to compensate for these effects. To use arrays over large bandwidths beamformers must incorporate time-delay instead of modulo 2π techniques. This will allow arrays to operate over large bandwidths without the problem of beam squint. Microwave time-delay beamformers in the past have not been used due to large RF losses associated with them. Current optical techniques provide methods which can be used to offset these losses.
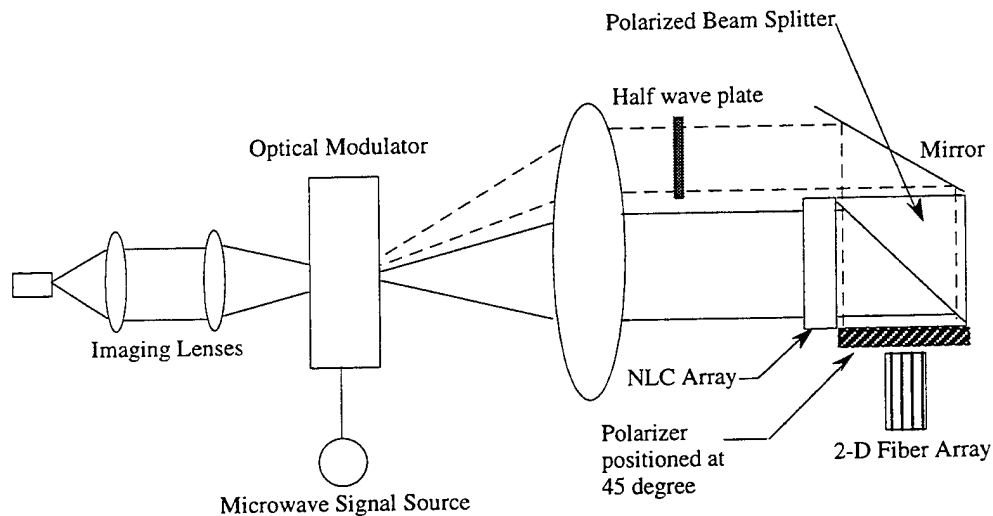
Fig. 5. NLC Optical Beamformer (after [9]).

3.0 Time Delay Architecture

The various optical beamformers which utilize optical time-delay can be divided into two separate approaches. The first, which is most commonly used, is an extension of conventional microwave delay line approach. Instead of using long lengths of coax or waveguide to produce delays, these beamformers replace them with optical fibers. Using optical fibers over microwave cabling has two

advantages. First, for the same amount of delay the fiber is much lighter and second, there is much less transmission loss per unit length when compared to coaxial cable. To produce short time delays however, systems can use either air paths or optical waveguide techniques instead of optical fibers to develop the required time delay. In any case, these methods are a direct extension of convention an RF delay techniques.

The second technique incorporates a completely different approach in producing time delays. This method utilizes the property of a dispersive fiber to achieve a variable time delay and is very analogous to that of an optical prism. In a prism the incoming light is separated into individual colors (wavelengths) of light such that each color propagates through a different path in the prism. By properly arranging a series of dispersive and non-dispersive fibers an equivalent optical prism can be created. This technique, when incorporated with a variable frequency laser, produces a very simple method of producing time delays.

3.1   Switched Fiber Time Delay

One of the most common techniques used to develop time delays employs some form of optically switched fiber line. Figure 6 (a-c) illustrates the various techniques used in producing these delays.

The optical delay shown in Figure 6a resembles its microwave counterpart almost identically. Each bit state is represented by a length of fiber corresponding to a given delay. By arranging these switches in a series fashion, a simple N-bit time-delay unit can be constructed. It is also possible to use free space lengths instead of fibers to produce the same delay effect. Figure 6b shows a parallel approach to achieve various time delays. In this case, a N-way splitter is used with

optical switches to choose a given time delay. This technique does suffer from the

optical loss created by the optical splitters and the need for more delay lines to
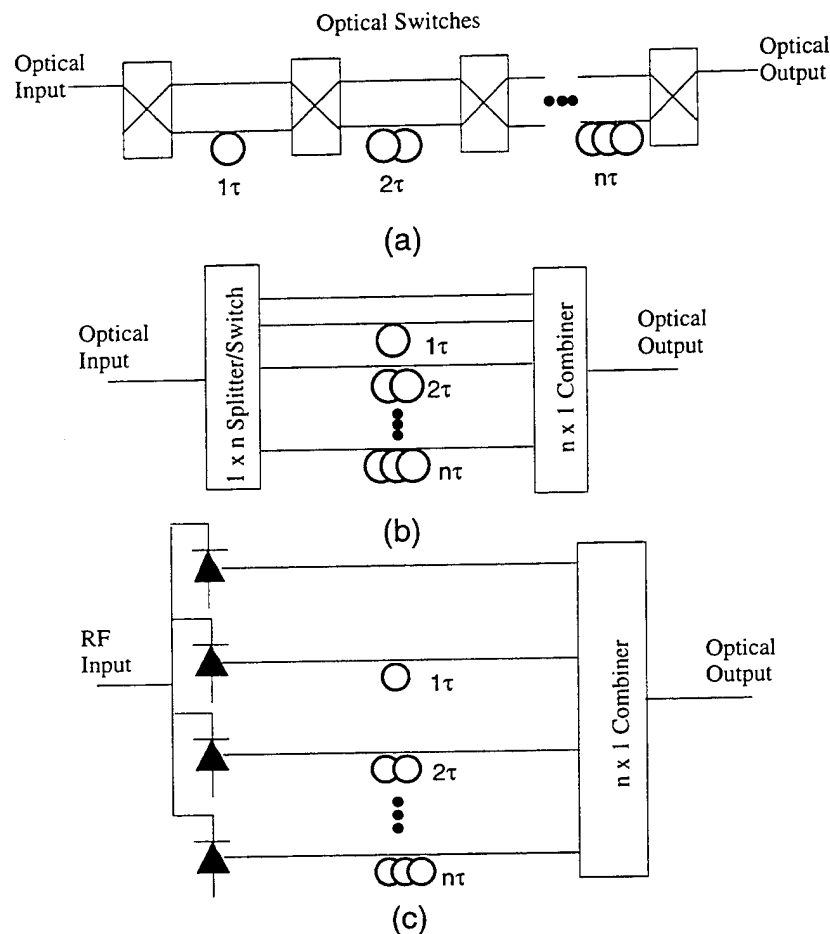
Fig. 6. Various Optical Time-Delay Configurations.

achieve the same amount of delay as a series unit. This loss can be minimized by

configuring the delay unit as shown in Figure 6c. In this case there is a separate

laser used for each bit of the time-delay unit. This technique is feasible for small bit

sizes but becomes impracticable when designed for larger bit sizes. Figure 7

illustrates a time-delay unit which incorporates both serial and parallel techniques. Using this method decreases the total amount of interconnects required when large bit sizes are required and also improves the transmission loss through the delay unit.
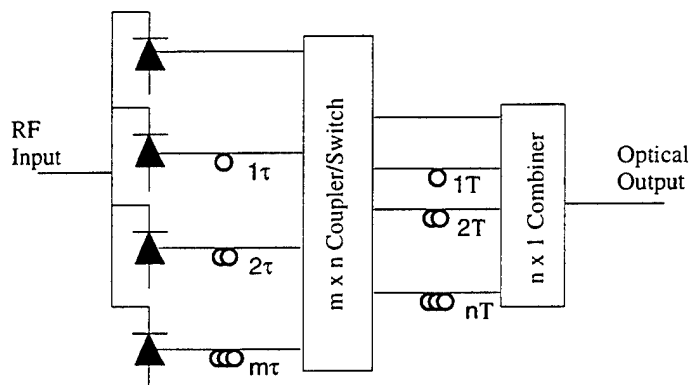
Fig. 7 Serial/Parallel Optical Time-delay Unit

Various other switched delay lines[10-12] are also being investigated based on the development of optical waveguides and switches on LiNbO3 and GaAs substrates. Figure 8 displays a time-delay network developed by GE and AT&T which uses optical waveguide technology with conventional fibers to produce a 6-bit time-delay unit. This approach uses a 4 x 4 matrix switching approach over a 2 x 2 matrix switch arrangement which improves the total insertion loss by over 3 dB. They have also achieved very good electrical performance characteristics with this device with a total insertion loss of 14 dB ±.4 dB over the entire 64 states. Figure 9 displays a typical time-delay network which has been developed on GaAs substrate. In these delay units no external fibers are required for the time delays. All delays are acquired through optical waveguides placed on the substrate. Each unit consists of 2-bit delay which can be cascaded to produce larger bit sizes.
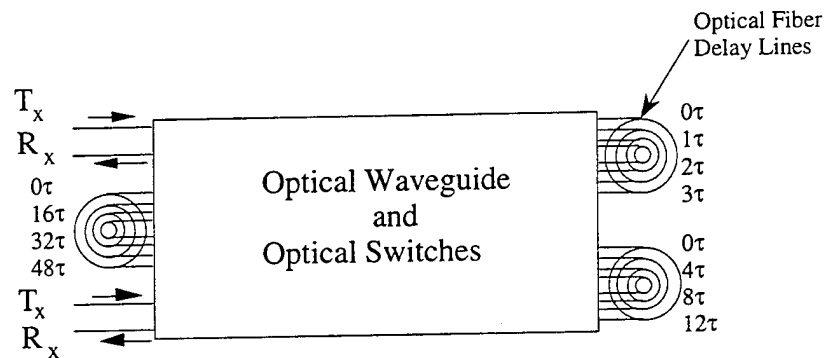
Fig. 8. 6-Bit Optical Time-Delay Unit (after [10]).
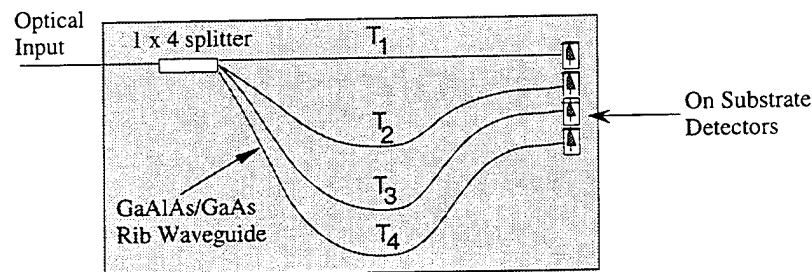
Fig. 9. 2-Bit Optical Waveguide Time-Delay Unit (after [12]).

These devices have two advantages over conventional fiber delays: (1) the control over the exact time delay is more precise due to the photolithography process involved and (2) the integration of the detectors onto the substrate eliminates the interface between the fibers and switching network. Because of the small time delays associated with these devices, these units are more suitable as trimmer delay units or in arrays that are operated above X-band where the array size becomes much smaller.

263

3.2   Hybrid Time-Delay Steering

An alternative architecture to the all optically derived time-delay units is illustrated in Figure 10. In these time-delay devices, both optical and conventional microwave delay lines are utilized to produce large time delays with small resolutions (bits) efficiently.
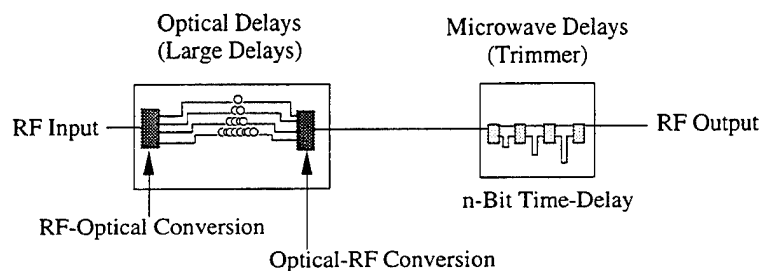
Fig. 10.   Hybrid RF-Optical Time-Delay Unit

As Figure 10 illustrates, the largest delays are produced using optical techniques while the smaller delays are developed using microwave techniques. The smaller delays are produce with conventional microwave methods since there is normally more loss incurred with the optics due to the conversion process than with cable loss. For larger delays, conventional microwave techniques result in a larger loss than the optical-RF conversion losses. There are two main research facilities that have been using this hybrid approach to develop operational phased array systems. Both Westinghouse[13-16] and Hughes[17-19] have been developing optically based beamformers which uses this approach in producing true time-delay beamforming systems.

In the Westinghouse design, they use a combination of subarraying approaches and optical multiplexing to reduce the total amount of time-delay unit

264

required. Their approach is illustrated in Figure 11. Depending upon the array size and the maximum scan angle required, a series of smaller microwave time-delay units are designed ($T_1 \ldots T_n$) in conjunction with a series of larger optical delay units ($O_1 \ldots O_m$). Since the microwave delay units are common to each subarray, optical multiplexing is used to share these delay across the array. This is illustrated in Figure 12. The output of each microwave delay unit is modulated onto a different optical carrier frequency and then multiplexed onto a single optical fiber. This fiber is then sent to a M-way optical splitter which is routed to each subarray optical time-delay unit. The output of each optical delay unit is passed through a N-channel Demux and each channel is detected and connected to the appropriate antenna element. Though this system concept requires less time-delay units, it requires N lasers each operating at a different wavelength.
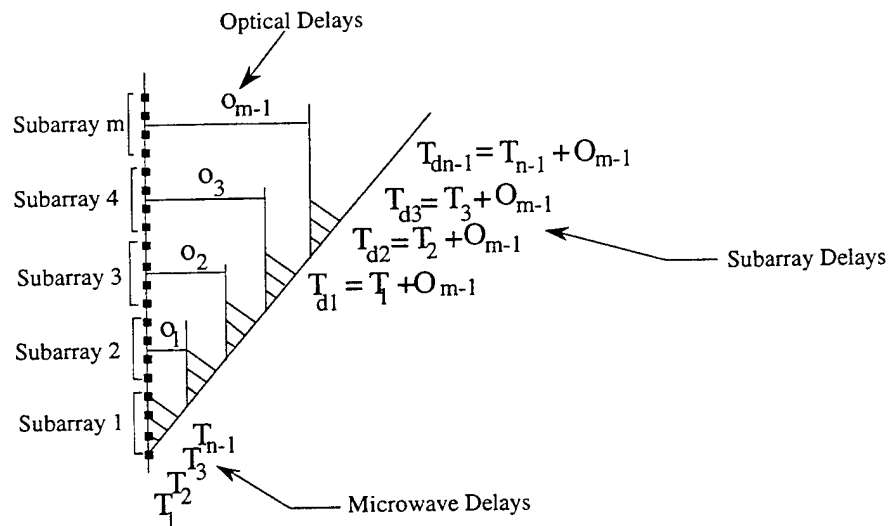
Fig. 11. Subarray Optical-RF Time-Delay Approach (after [16]).

265

Hughes has also developed an optical beamformer using both optical and microwave time-delay units. Figure 13 details the basic concepts used in their optical beamformer. Unlike the Westinghouse approach, this approach uses a microwave time-delay trimmer device at each element instead of optical multiplexing. The microwave time-delay unit is part of the T/R module used at each element and the optical time-delay devices are incorporated into a subarray configuration. The optical time-delay unit shown in Figure 13 is developed from a 4 x 8 fiber coupler network.
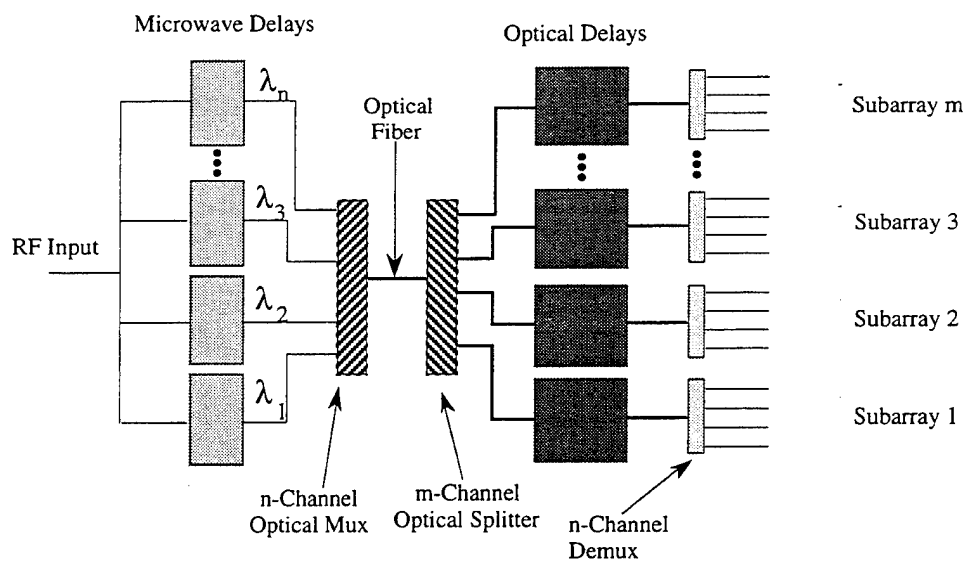
Fig. 12. Westinghouse Optical Multiplexed Hybrid Beamformer (after [15]).

A technique similar to that given in Figure 6 is used in their optical delay unit. Four diode lasers are incorporated into the optical time-delay device. By biasing the correct laser and detector pair, 32 different time-delay states can be obtained. The detected signal is then amplified and routed to the appropriate T/R

module for further processing. A 96 element array using this beamforming technique is currently under test and is being evaluated at the U.S. Air Force's Rome Laboratory.
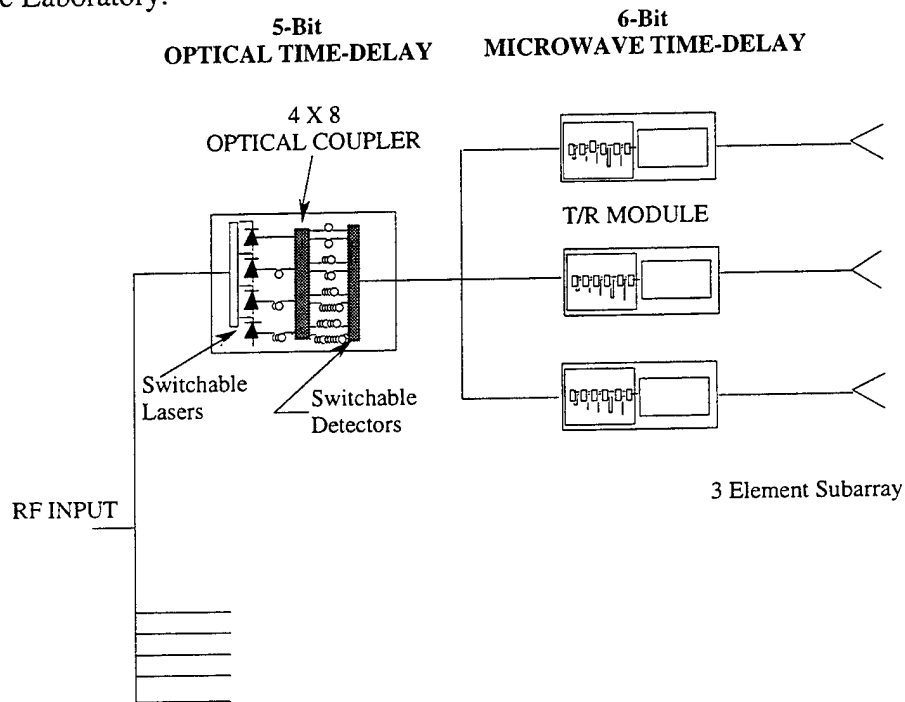
Fig. 13. Hughes 96 element Hybrid Beamformer (after [18]).

4.0 Dispersive Fiber Time-Delay Steering

The final optical time-delay architecture which is discussed here is based on the dispersive nature of optical fibers. Developed at the Naval Research Laboratory[20-22], this technique uses a series of dispersive and non-dispersive fibers together with a tunable laser. The transit time of a signal to propagate down a dispersive fiber is a function of the illuminating optical source and a typical delay of $100\frac{ps}{Km \cdot nm}$ is produced within these fibers. By organizing a series of non-

267

dispersive and dispersive fibers, as shown in Figure 14, a variable time-delay can be generated across the array when used with a tunable laser source. The optical fibers are trimmed such that at a given center optical wavelength, λ_0, all signals propagate down the fibers with equal delay which produces a broadside beam. When the optical wavelength of the laser is decreased, the beam scans to the left since there is a greater delay produced across the left side of the array. As the optical wavelength is increased, the beam scans to the right as the delay is now greater across the right side. Because the delays associated with this technique are independent of the RF frequency, this system can generate scanned beams that are microwave frequency independent. This technique provides a very simple way to produce a variable time-delay beamformer.
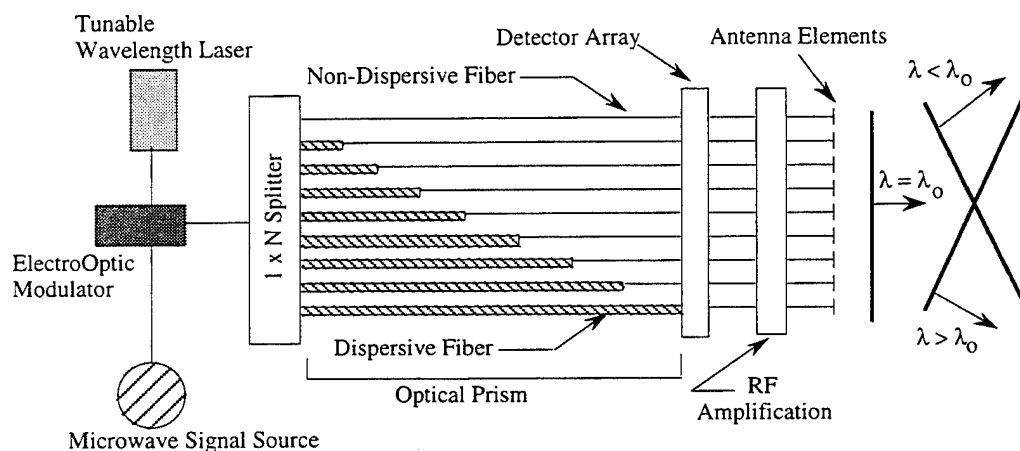
Fig. 14. NRL Optical Prism Time-Delay Beamformer.

5.0   Conclusion

This paper has tried to introduce the reader to the various optical techniques which are being used to control the beam position of a phased array antenna. By no means are the techniques covered in this work a complete listing of all available optical beamforming methods. The concepts described are some of the more common methods which are used. There will continue to be improvements and discoveries of new devices and techniques which will improve the current state-of-the-art of optical beamforming. Optical systems have provided the ability for phased array antennas to beamform over large bandwidths. Most of these techniques have shown substantial improvements in both performance and cost considerations over the last few years and with increasing research now occurring, optical beamformers will remain a viable solution for future wideband phased array systems.

6.0   References

[1] G.A. Koepf, "Optical Processor for Phased-Array Antenna Beam Formation," SPIE Vol. 477, *Optical Technology for Microwave Applications,* 75-81, (1984).

[2] D. Stilwell, L. Goldberg, M. Parent, J. F. Weller, W. Collins, D. Chaplak and G. Sherman: *Confrerence on Lasers and Electrooptics,* San Francisco, 1986, Paper TH03.

[3] Theo Cheston and Joe Frank, "Phased Array Radar Antennas," in *Radar Handbook,* 2nd ed., M.I. Skolnik, Ed., New York: McGraw-Hill, 1990, chap 7.

[4] Eli Brookner, *Practical Phased Array Antenna Systems,* Artech House, 1991.

[5] D. Stilwell, M. Parent and L. Goldberg, "Fiber Optic Feed," NRL Report 6741, Nov. 6 1990.

[6] M. Tamburrini, et al., "Optical Feed for a Phased Array Microwave Antenna," *Electronic Letters,* Vol. 23, pp. 680 - 681, 1987

[7] P.D. Stilwell, "Fiber Optic Feed and Phased Array Antenna", Patent Number: 5,365,239, Nov. 15, 1995.

[8] D. Dolfi, F. Michel-Gaberial, S. Bann and J.P. Huignard, "Two-dimensional optical architecture for time-delay beamforming in a phased-array antenna," *Optics Letters*, Vol.16, no. 4, pp. 255-257, Feb. 1991.

[9] N.A. Riza, "Liquid Crystal-Based Optical Control of Phased Array Antennas," *Journal of Lightwave Technology*, Vol. 10, No.12, December 1992, 1974-1984.

[10] E. Ackerman, S. Wanga, D. Kasemet, W. Minford, N. Thorsten and J. Watson, "Integrated 6-Bit Photonic True-Time Delay unit for lightweight 3-6 GHz Radar Beamformer," *MTT-S Digest*, pp. 681-684, 1992.

[11] C.T. Sullivan, et. al., "Switched time delay elements based on AlGaAs/ GaAs optical waveguide technology at 1.32 μm for optically controlled phased array antennas," *SPIE Conf Proc.*, Vol. 1703, pp. 264 - 271, 1992.

[12] W. Ng., D. Yap, A. Narayana, and A. Waltson, " High-Precision Detector-Switched Monolithic GaAs Time-Delay Network for the Optical Control of Phased Arrays," *IEEE Phontoics Technology Letters*, Vol. 6, No. 2, Feb. 1994, pp. 231 - 234.

[13] A. Goutzoulis, K. Davies, J. Zomps, D. Hrycak and A. Johnson, " A Hardware-Compressive Fiber Optic True-Time Delay Steering for Phased-Array Antennas," *Microwave Journal,* Sept. 1994, pp. 126 - 140.

[14] A. Goutzoulis and K. Davies, "All- optical hardware-compressive wavelength-multiplexed Fiber optic architecture for true time delay steering of 2-D Phased Array Antennas," *SPIE Conf. Proc.*, Vol. 1703, pp. 604 - 614, 1992.

[15] A. Goutzoulis, K. Davies and J. Zomps, "Hybrid electronic fiber optic wavelength-multi[plexed system for true time-delay steering of Phased Array Antennas," *Optical Eng.*, Vol. 31, No. 11, pp. 2312 - 2322, Nov. 1992.

[16] D.K. Davies and A.P. Goutzoulis, "Wavelength-multiplexed analog fiber optic link for wideband radio-frequency and local oscillator signal transmission," *Optical Engineering,* Vol. 31 No. 11, 2323-2329, Nov. 1992.

[17] W. Ng, A. Waltson, G. Tangonan, J.J. Lee, I.L. Newberg and N. Bernstein, " The First Demonstration of an Optically Steered Microwave Phased Array Antenna using True-Time-Delay," *Journal of Lightwave Technology,* Vol. 9, no. 9. Sept. 1991, pp. 1124 - 1131.

[18] J.J. Lee, S. Livingston, B. Loo, V. Jones,C. Foster, H.W. Yen and G. Tangonan, "System Design and Performance of a Wideband Photonic Array Antenna", *SPIE Conf. Proc.*, Vol. 2155, pp. 287 - 95, 1994.

[19] H. Yen, R. Loo and J.J. Lee, "Development of an Optically Controlled Phased Array",*SPIE Conf. Proc.*, Vol. 2236, pp. 76-80, 1994.

[20] R. Esman, et al., "Fiber Optic Prism True Time-Delay," *IEEE Photonics Technology Letters,* Vol. 5, no. 11, Nov. 93, pp. 1347 - 1349.

[21] R. Esman, M.Y. Frankel and M.G. Parent, "True Time-Delay Fiber Optic Control of a Phased Array Transmitter with Three Octave Bandwidth," *1995 MTT-S International Symposium,* Orlando, Fl, 1995.

[22] M.Y. Frankel, R. Esman and M. G. Parent, " Fiber Optic True Time Delay Control of an Array Antenna," *Conf on Optical Fiber Communications,* San Diego, Ca., Vol. WH3, pp. 125 - 127, 1995.

Structurally-Integrated Optically-Reconfigurable Antenna Array[⊥]

Sanders, A Lockheed Martin Company

R. Gilbert, G. Pirrung[*], D. Kopf, P. Hoefler, F. Hayes

Nashua, NH 03061-0868

ABSTRACT

A conformal broadband reconfigurable array concept for use with integrated, multifunction avionics and communication systems is described. Photonically-activated switches are utilized to alter the dimensions of simple antenna elements over a passive, frequency-independent ground plane. A unique feature of the array is its ability to scan grating lobe-free beams over several octaves while maintaining near $\lambda/2$ spacing between elements. Feeds to unused elements in the array are terminated with broadband impedance loads that minimize their interaction with active elements. Performance data of an array operating over the 500 MHz to 2 GHz band is presented.

INTRODUCTION

Advancements in avionics and communication technologies have resulted in many antennas competing for very limited real estate on military and commercial aircraft. Whereas advancing electronics technologies permit the packaging of more functionality in smaller volumes, the wavelength dependency of antennas continue to resist miniaturization. Since the dimensions of conformal antennas in the VHF, UHF, and L-bands are large in the context of an aircraft installation, their usage for multifunction systems has been limited to frequency and time sharing of single element antennas with omni azimuthal coverage. Most of the research with multifunction arrays has been in the microwave and millimeter wave bands where array dimensions are small enough for installation between structural members of the fuselage and wings or behind the nose cone radome of an aircraft. Some elements, such as the tapered notch, can be arrayed with the critical spacing needed for multi-octave, grating lobe-free beam scanning at the shortest wavelength. With most elements, however, the penalty for close spacing is a reduction in gain, increased VSWR, distorted radiation patterns as a result of the strong mutual coupling and, in some cases, blind angle phenomena. An antenna array technology where frequency, polarization, and element spacing can be reconfigured in real time would overcome many of these obstacles while allowing for a reduction in the size and weight needed for the conformal array.

---

[*] Mr. Pirrung is with the Naval Air Warfare Center, Aircraft Division, Warminster, Pa.

A reconfigurable antenna array concept is presented which is comprised of simple radiating elements whose dimensions can be altered with photonically-activated RF switches. These elements are integrated into the top layer of a multilayered composite structure comprised of passive frequency selective surfaces (FSS) that form a broadband ground plane system. The construction lends itself to conventional bolt-in installation in the form of a lightweight and potentially load-bearing panel or to direct integration with composite aircraft structure. Methods to integrate feed baluns, optic fibers, and antenna/FSS layers into and in between aircraft structural members are currently being developed to allow arrays to extend over large areas. A reduction in the overall array thickness is also creating an interest in installing apertures in locations such as the wing tips which were previously not considered since they were not voluminous enough for the conformal, cavity-type, UHF and L-band antennas.

This paper presents the reconfigurable aperture concept, some design considerations, and performance data from a 500 MHz to 2 GHz, 3x3 array panel.

RECONFIGURABLE ARRAY CONCEPT

The three major design parameters which affect the radiation performance and impedance of a dipole array over a ground plane are: 1) the dimensions of the dipole arms; 2) the dipole-to-ground plane spacing; and 3) the spacing between dipoles elements. The reconfigurable array concept shown in Figure 1 utilizes active and passive methods to physically and electrically configure antenna arrays to function over as much as 4 octaves of bandwidth. The instantaneous bandwidth of the dipoles is about 50% around its half wavelength resonant frequency within the operational band. The instantaneous bandwidth is sufficiently wide for most avionics and communications application.

Dipole Length Configurability

The dipole length is modified by adding conductive segments to the arms using a switch. Since the dipole is part of an array, the arms of adjacent dipoles can be connected together to form one larger dipole. The process is simply illustrated in Figure 2. At the highest frequency of operation, all the dipoles are active and the switches are in their "off" (high impedance) state. At midband, the arms of the dipoles are lengthened by turning on one set of switches. At the lowest frequency band, another set of switches is turned on connecting adjacent dipoles to create a larger dipole. The intrinsic silicon switch that connects the dipole segments together has an "on" resistance which can be varied over a wide range of values. Setting the switch to a particular value is sometimes beneficial to increase the dipole's instantaneous bandwidth.

The number of switches and feed points in an array can sometimes be minimized if the spacings between elements are harmonically related. The optimum design in terms of performance is not usually obtained in this manner, however. The approach is to determine the number of reconfigurable subbands, based on 40% to 50% instantaneous bandwidths, which are needed to cover the total operational frequency band of the array. Separate arrays are laid out for each subband assuring that the critical spacing for element spacing is observed for the maximum desired scan angle. The array layouts are then overlaid to line up as many feed points as possible.

273
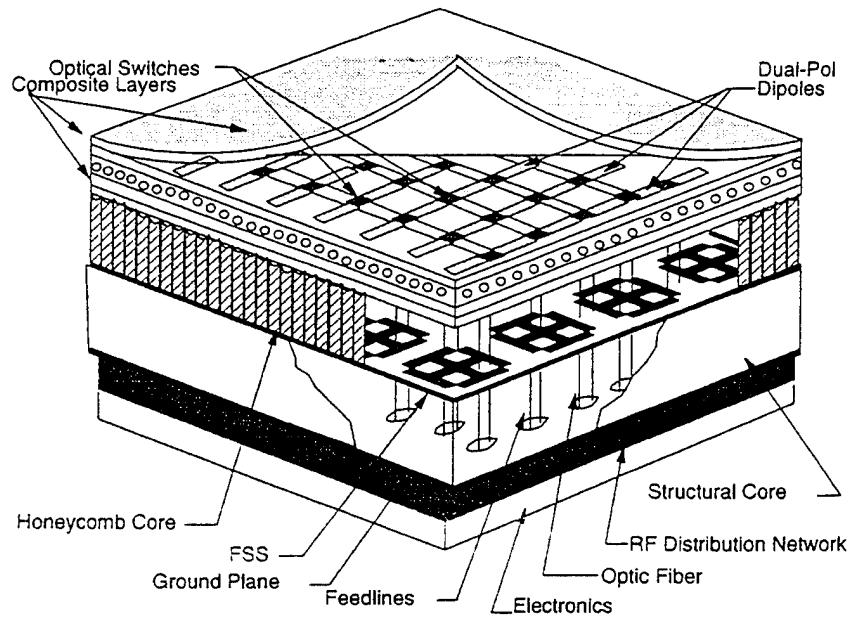
Figure 1: Reconfigurable dipole array concept
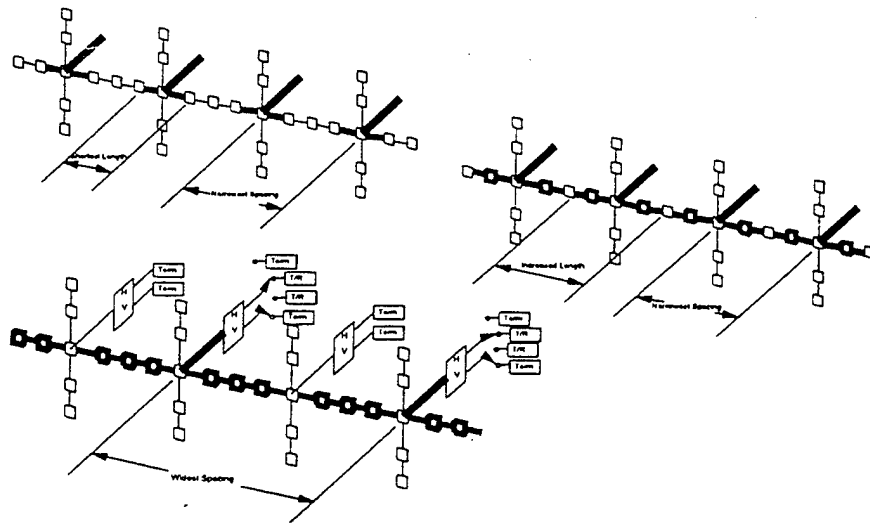
Figure 2:   Reconfiguration process which lengthens the arms of a dipole by connecting through
a switch the conductive segments from the arms of adjacent dipoles.

For those points which are far apart, a separate feed will be required in the combined layup, while those points which nearly line up are combined into one feed point. An optimization of the array spacings for each subband is then performed to accommodate the "common" feed points.

During the reconfiguration process one cannot avoid having inactive feed points of adjacent dipoles in the arms of active dipoles. The impedance of the feed termination, which is frequency dependent, is reflected to the dipole arm as shown in Figure 3 where it has the tendency to load the switch there. When the switch is "off," the impedance loads the dipole arm creating a current imbalance in the dipole which skews the radiation pattern If the reflected impedance presented an open circuit, it would have no impact on the switch or dipole performance. Several feed termination concepts have been studied that would reflect an "open circuit" condition at the unused feed point. The simplest includes adding switches directly in series with the feed balun at the dipole. This concept increases the number of switches to be controlled in the array and the number of optic fibers penetrating the composite. The second concept is to place a frequency independent feed termination (FIFT) at the input of the balun leading to the feed point. The impedance of the FIFT, when combined with the effects of the transmission line and balun, is reflected as a broadband high impedance load at the dipole feed point.

Active circuits employing negative impedance have been examined for their potential use as FIFTs. These will be feasible when operational amplifiers become available which have an f_t of 30 GHz or higher. Passive bandpass filters are currently used as FIFTs. An extra layer of switching is required to switch in the FIFTs when corporate beamformers and switch matrices are employed. For those arrays which are fed with transmit/receive (T/R) modules behind each element, the FIFT is included into the T/R module package and is switched in line when the module is not needed.

FSS Ground Plane

The resonant length of a dipole is not sufficient to ensure efficient wide band performance. The spacing (electrical height) between the dipole array plane and the ground plane is a major parameter that strongly influences the VSWR, gain, and the shape of the dipole radiation pattern. The effective electrical height should remain constant as the operating frequency changes. In other words, the phase of a signal reflecting from the ground plane system remains constant. However, the physical separation between the dipole and the ground plane is fixed. Therefore an electrical height change must be accomplished by either changing the effective dielectric constant of the material between the dipole and the ground plane or by artificially moving the ground plane.

A passive ground plane system comprised of low pass frequency selective surfaces (FSS) is installed underneath the dipole array layer. These FSS behave as filters to provide for transmissive and reflective responses. Each FSS layer has its cutoff frequency (reflective frequency) and phase rolloff designed such that, when combined with other FSS layers with different cutoff frequencies, the combined response is relatively flat in amplitude and phase as referenced from the dipole array plane. The functional principle is illustrated in Figure 4. At the high end of the band, the first FSS layer below the dipole array is conductive and functions as the

DIPOLE ARM

OPTICAL SWITCH

R_{ON}

BALANCED T-LINE

BALUN/ TRANSFORMER

STRIP LINE

RF SWITCH

TERMINATION

$Z_{in} \approx \infty$

DIPOLE CURRENT REMAINS ON SURFACE WHEN OPTICAL SWITCH IS "ON" AND FEED IS PROPERLY TERMINATED
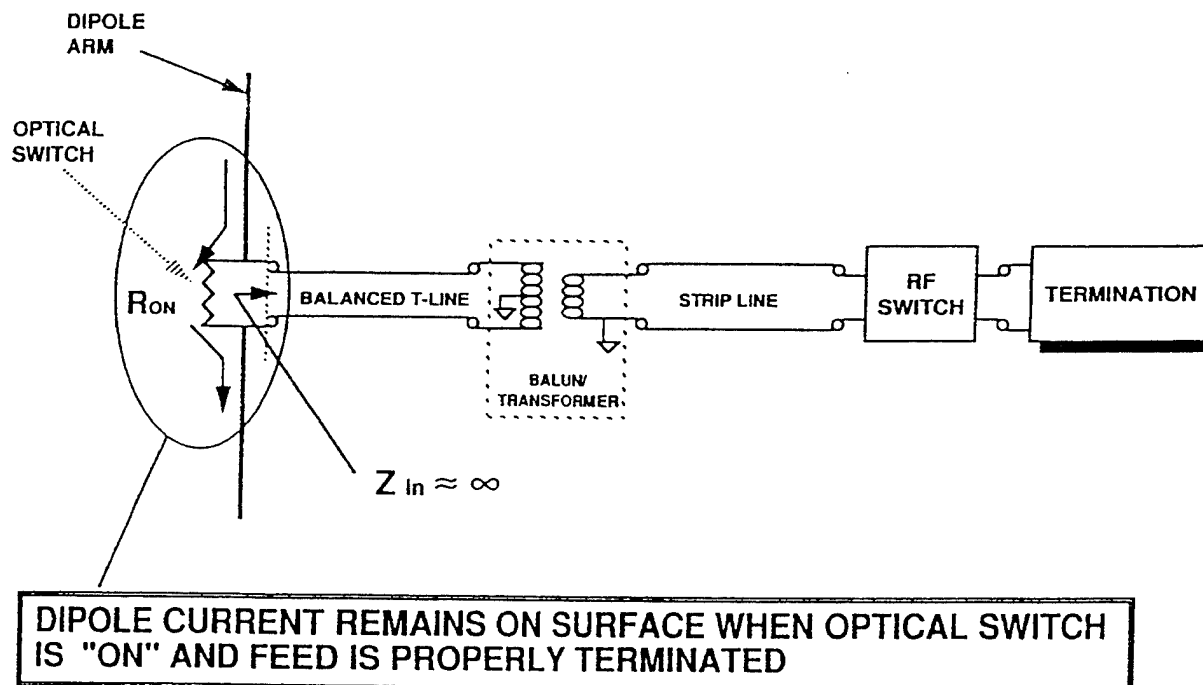
Figure 3:   A high impedance termination must be reflected from a load to the feed point of a dipole when it is incorporated into a larger dipole.

E

Switches

Radome

F_{max} F_{mid} F_{min} e_4

e_3

FSS

e_2

FSS

e_1
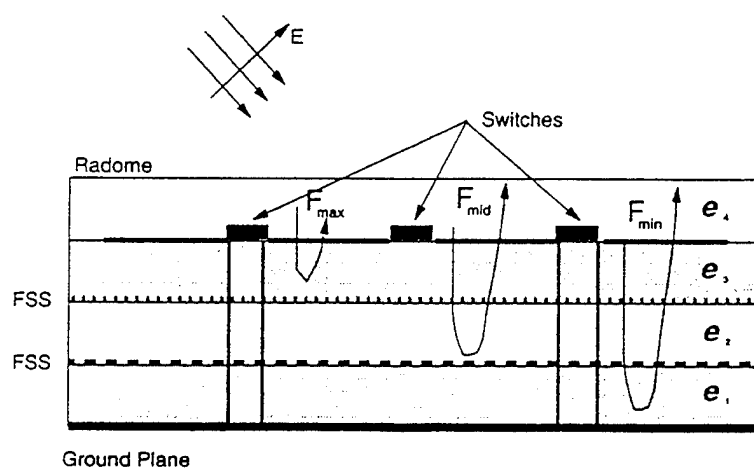
Ground Plane

Figure 4:   Functional principle of a broadband, passive ground plane system

276

ground plane. At midband, this FSS layer is transparent and the one below it functions as the ground plane. Finally at the low end of the band, the actual ground plane acts as the reflective surface while the FSS layers are all transparent. The advantage of this concept over other approaches is that the antenna is totally passive except for the optical switches.

The total band over which the ground plane must reflect a constant phase is also divided into subbands of between 35% and 45% bandwidth. These subbands are independent of those for the dipole array above it. Each subband is represented in terms of an FSS layer. The cutoff frequency of a particular subband is designed to be the geometrical mean of the band edges. These bandwidths and cutoff frequencies in addition to desired FSS rolloff characteristics (which are dependent on the FSS element types) provide good initial estimates for a computer model to optimize the design. When panel thickness reduction becomes a parameter to optimize, mutual coupling between FSS layers becomes a predominant factor. Individual FSS resonant frequencies change and broadband performance is achievable with fewer FSS layers. However, the panel becomes more susceptible to manufacturing tolerances.

An array designed to operate over a 10:1 frequency band would have four or five FSS layers. For a 4:1 band, two or three FSS layers are sufficient. The number of FSS layers needed is a function of parameters identified above, embedded material, and dipole interactions. Even when an FSS is transparent at a particular portion of the frequency band, it still has interaction in the form of mutual coupling with the dipole array layer above and the FSS layers above and below it. It even has interaction with its image and images of other layers from the solid ground plane. It has been observed that low Q FSS designs provide the best overall broadband performance. Thin films with a resistivity of 2000 to 3000 ohms/■ can be placed or deposited on the intermediate FSS layers to absorb higher order modes and surface waves without causing significant reduction in the efficiency of the system. Losses can be minimized by placing "discrete" films between the tips of FSS elements themselves.

Reconfigurable Array Spacing

The array performance with scan angle is dependent on element spacing and array geometry. Array spacing reconfiguration is achieved by selecting those dipoles and feed points which avoid or minimize grating lobes throughout the entire operating band. Hence the concept of reconfiguration is extended to the feed network. For an implementable design, the number of feeds and switches must be kept to a minimum to reduce cost, complexity, and optical power needs. The tradeoff between element spacing, instantaneous bandwidth, array gain and beamwidth, and physical layout of the feeds and switches will be driven by the instantaneous requirements of the functions being serviced in addition to physical/mechanical constraints.

There are many potential methods of connecting an antenna array to a beamforming network or manifold. Notwithstanding application-specific variations, conventional beamformers coherently sum all the outputs of the array elements and in-line T/R modules (if present) through a corporate feed network. In the case of the reconfigurable array, the concept requires a complex switch matrix to permit access to particular elements and restrict others. For multifunction applications, the switch matrix also routes signals to various portions of an array. A sophisticated

cross-point matrix switch would allow for multiple beams by adding or deleting RF ports on a complex RF bus. Optical beamforming and optical modulators/demodulators are also applicable to this smart skins concept.

Dipole Feed/Balun

An important element in the design of dipoles is the feed. The transmission line needs to be "balanced" to deliver equal but opposite currents to the dipole arms. "Unbalanced" currents cause the radiation pattern to be skewed and it increases the mutual coupling between the dipole arms and the feed line. Besides selecting a "balun" whose electrical performance extends over the total operational frequency band of the reconfigurable array, its inclusion into the array panel must not impair the mechanical load carrying capability of the structure. Our approach has been to make the baluns into structural members of the array onto which shear loads across the top laminates can be transferred through the structure. Also, the attachment of the balun to the dipole must allow for movement of the outer aircraft skin while maintaining electrical contact.

A slotline balun, excited by a stripline or coaxial feedline, supplies a voltage across the dipole feed gap. The fields are tightly coupled to the slotline thereby reducing mutual coupling with adjacent baluns. The baluns are capable of operating over more than 10:1 bandwidths. Baluns as short as $\lambda/15$ have been demonstrated to operate with VSWR less than 2:1. When panel thickness is less than $\lambda/12$ it is recommended that a balanced feedline such as twin lead be brought up to the dipoles. T/R modules can easily be designed with balanced output ports.

The dual-polarized balun uses the same concept. The crossed-slot baluns have cross polarization isolation that varies from -15 dB at the low end of the band to -30 dB at the high end of the band.

OPTICAL SWITCHES

The switches that reconfigure the dipole elements must withstand the composite embedment and curing process, the aircraft environment, and be highly reliable. The switches should be capable of withstanding high power and an electrostatic discharge or indirect lightning strike without damage. Most active semiconductor devices (PIN diodes, FET's, and other junction devices) are temperature sensitive and susceptible to voltage pulses. Mechanical switches require wires to power and control them which causes interference with the RF performance of the panel. There are FET switches which are optically activated and hence do not require a bias line to the gate. A small solar cell is illuminated to create the biasing voltage to the gate. Conductive polymers and ferrielectric materials require an electric field for activation which necessitates wires or thin conductive/resistive films. These devices require "charge-up" time and could limit switching speeds.

The important parameters in designing the switch are saturation current, "off" isolation, high voltage susceptibility, switching speed, RF insertion loss, optical power requirements, and switch geometry. The Sanders switch was designed to operate under high peak and average power

conditions. The switch is 85 mils square, with 20 mils by 85 mils ohmic contacts on opposite ends. The switch has a DC resistance less than 1.75 ohms with a saturating optical power of 120 mW at 0.82 micron wavelength. The RF insertion loss is less than 0.3 dB from 100 MHz to 20 GHz. The "off" state RF isolation is better than 30 dB at UHF band, 25 dB at L-band, and 15 dB at 6 GHz. The switch isolation at the higher frequencies decreases as a result of increased capacitive coupling across the dipole gaps caused by the high dielectric constant (ε_r=11.8ε_0) of silicon. A change in contact geometry is helpful in reducing the capacitive coupling at X-band and higher frequencies. The switch has a DC saturation current of 2.2 amps and slightly higher at RF due to displacement current. In power handling tests, the switch has been demonstrated on a dipole radiating 100 watts CW for 30 minutes and microsecond pulses at 1 kilovolt. No switch deterioration was observed. Finally, the switch recombination time ("turn off" time) was measured to be about 1 millisecond thereby limiting reconfiguration rates to 1 millisecond. The "turn on" time is less than 100 nanoseconds.

500 MHZ TO 2 GHZ PANEL

As part of an aperture technology program to demonstrate the reconfigurable array concept described above, a 500 MHz to 2 GHz reconfigurable array panel was designed and tested. The design guidelines were to construct a panel which would not exceed 4 inches thickness and would operate across the frequency band in 3 reconfigurable subbands. The array form factor would comprise 3x3 active elements in any given subband surrounded by at least one row or column of passively terminated elements. The elements would be spaced as to prevent grating lobes up to 60° off boresight. An objective was to determine the effects of mutual coupling in a densely packed array. The design was to take into consideration common CNI and EW avionics functions. . After a brief requirements analysis, it was determined that the subbands should be defined as: 500-900 MHz, 900-1200 MHz, and 1.2-2.0 GHz to minimize the need of having to reconfigure the array between two subbands for any one given avionics function. It should be noted that the instantaneous bandwidth of the lower and highest subbands far exceed the recommended 40% to 50% bandwidth. A four subband design would have provided for a smoother VSWR especially at the low end of the band.

During the course of the program, there were motivating factors to determine how thin a panel could be achieved, and consequently an interesting phenomena was discovered. Utilizing the effects of mutual coupling between closely spaced FSS layers, one can also create the effect of near-λ/4 spacing between the ground plane system and the dipole over the operational band. Initially, previously developed computer modeling software was very useful in predicting the performance of the FSS layers and dipole array, including mutual coupling, for a 4 inch thick panel. Empirical methods were utilized to obtain a design for a 2.5 inch thick panel. There are indications that a panel as thin as 1.5 inches can be achieved.

Under an earlier feasibility study, a simple 3x3 element dipole array with optical switches to lengthen the dipole arms but with fixed feed point spacings was fabricated and tested. Good VSWR and element patterns were obtained with a two FSS layer, 4 inch thick design. The VSWR vs. frequency of the center element of the array with surrounding elements terminated in 50 ohms is given in Figure 5, showing the effect as the dipole arms are lengthened with the optical
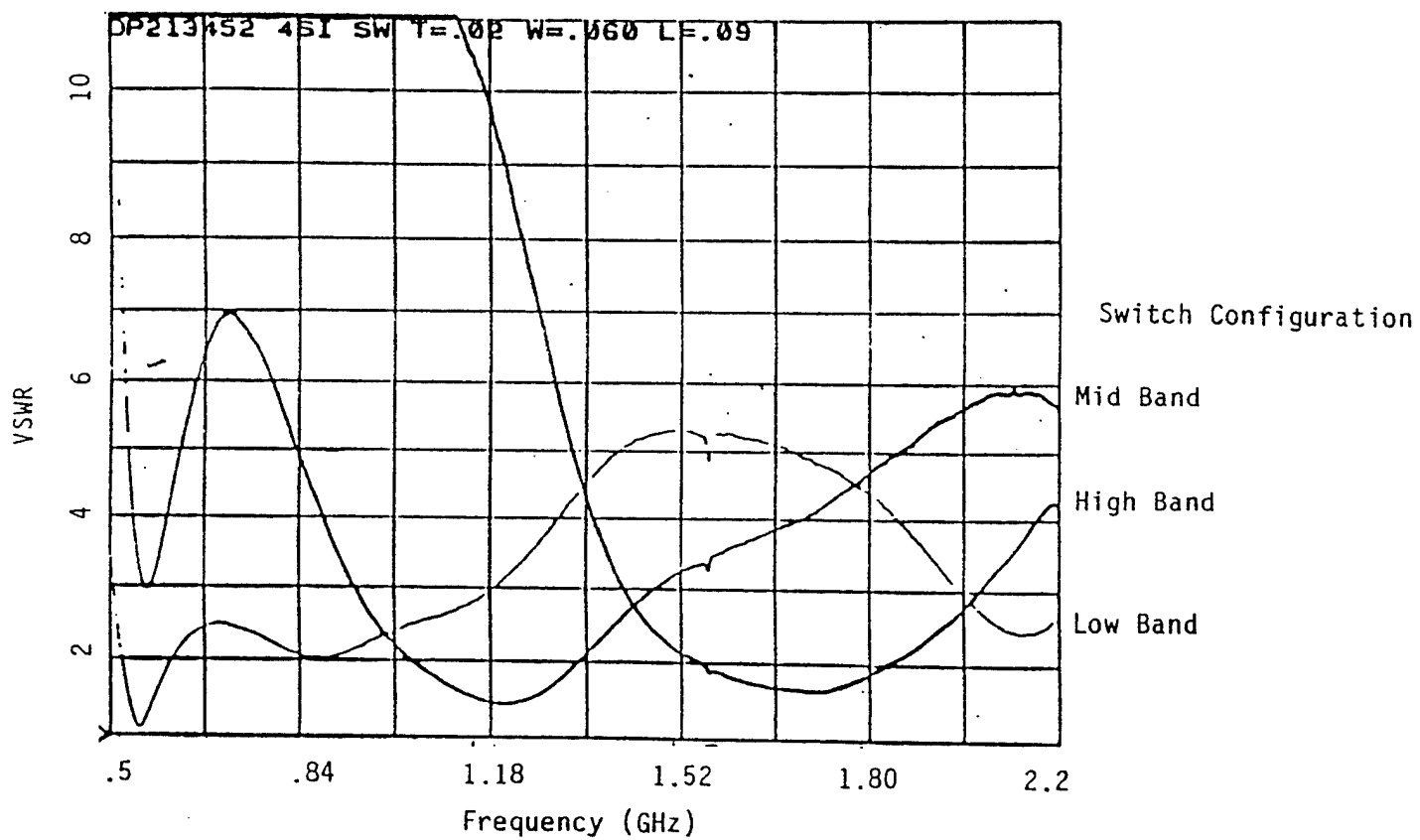
Figure 5:   VSWR vs. Frequency of a dipole over a two FSS ground plane system as it is
reconfigured through three operational subbands.

switches. The frequency band is covered in three dipole configurations. The H-plane radiation patterns of the same element are plotted for every 100 MHz increment in Figure 6. This early prototype and data from other panels provided the starting point design for the reconfigurable panel.

Panel Design

Early experiments and computer modeling indicated that a three FSS layer reconfigurable array panel design would improve the gain of individual dipole elements. The three FSS layer ground plane system is comprised of four frequency subbands. The first band is related to the solid backplane which will reflect signals are the lower frequencies. The second band is related to the reflectivity of the lower FSS. The next two bands are related to the upper two FSS layers respectively. The subbands were initially assigned equal percentage bandwidths from 500 MHz to 2 GHz. The frequencies which defined the subbands were 500-707 MHz, 707-1000 MHz, 1000-1414 MHz, and 1414-2000 MHz. The mean frequency in each subband that constituted the optimization starting point for tuning each FSS layer was 1707 MHz for the top FSS, 1207 MHz for the second, and 853 MHz for the lower FSS. After the optimization for a constant phase reflection from the ground plane system was completed, the subband limits over which each FSS layer has influence were changed to the limits shown in Figure 7. From this optimization were also obtained the dimensions for the "crossed dipole" elements, the discrete resistive loadings, and the grid constituting the FSS patterns.

Utilizing the same FSS designs, the spacings between the layers were varied to minimize panel thickness. The loadings between FSS elements were also changed to improve the flatness of the phase vs. frequency of the reflected signals from the ground plane system. The films have a resistivity of 2100 ohms/■.

The dual-polarized dipole array layout for each subband is given in Figures 8-10. The horizontal rectangles represent the switches associated with the vertically polarized dipole elements and the vertical rectangles represent the horizontally polarized elements. The locations of FIFTs are indicated in the legends.

The spacing between dipole elements when configured for the high subband is $\lambda/2$ at 1800 MHz. The spacings for the other two subbands are $\lambda/2$ at 1200 and 900 MHz respectively. These spacings were chosen to minimize the number of feed points, switches, and FIFTs needed. The spacings are multiples of $\lambda/4$ at 1800 MHz.

The dipole array and FSS patterns were etched out of copper coated, 10 mils thick G-10 substrates. The sheets were bonded to and separated by low density, closed-cell foam material. The spacings between layers are shown in Figure 11. During assembly of the panel, care was taken to assure that the baluns were well grounded to the backplane and that they did not make electrical contact with any FSS element. In two or three cases where FSS elements were cut by the baluns, they were reattached by jumpers.

281
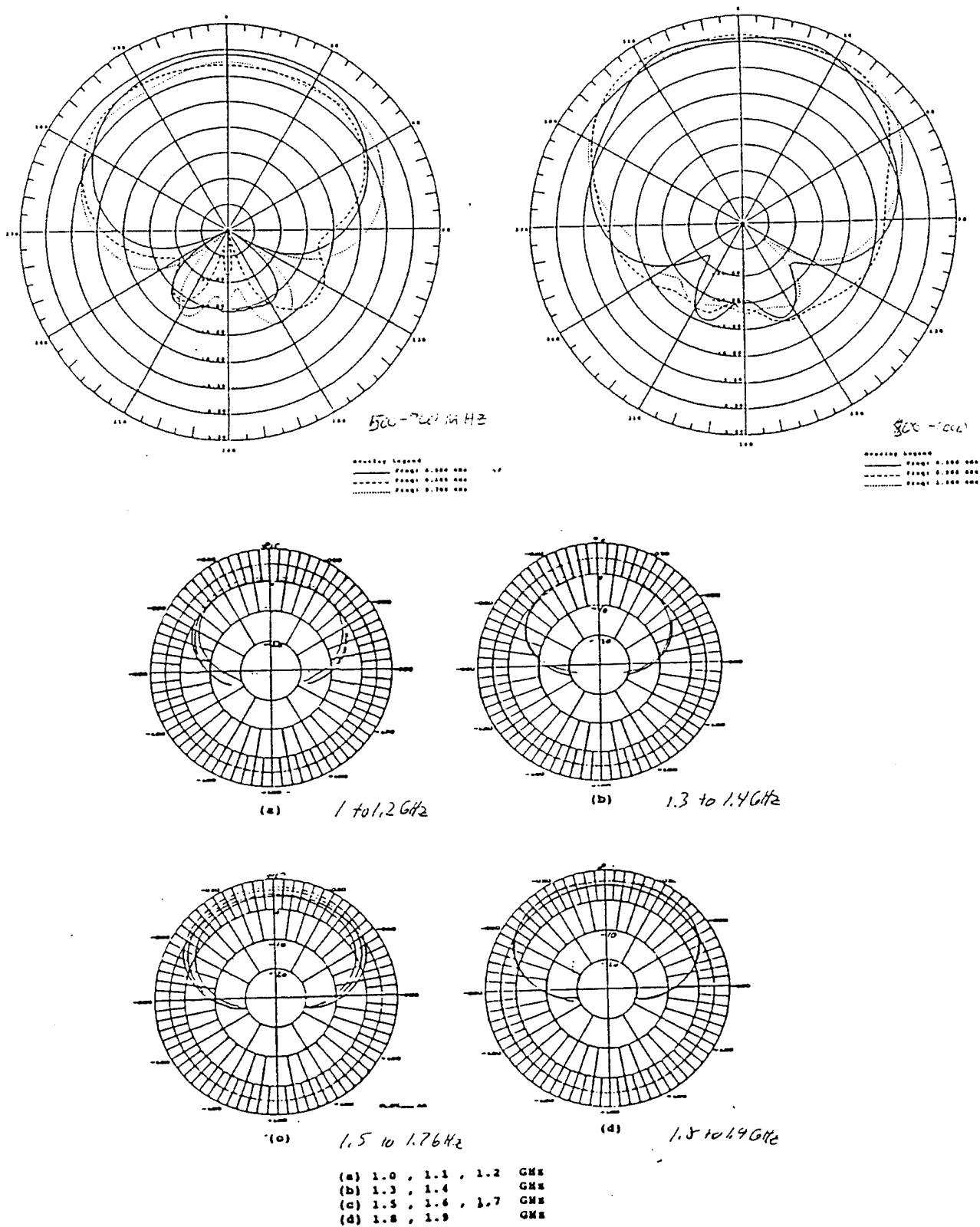
Figure 6: H-plane radiation patterns of center element of a 3x3 dipole array over a two FSS ground plane system. The gain can be read directly in dBi.

282
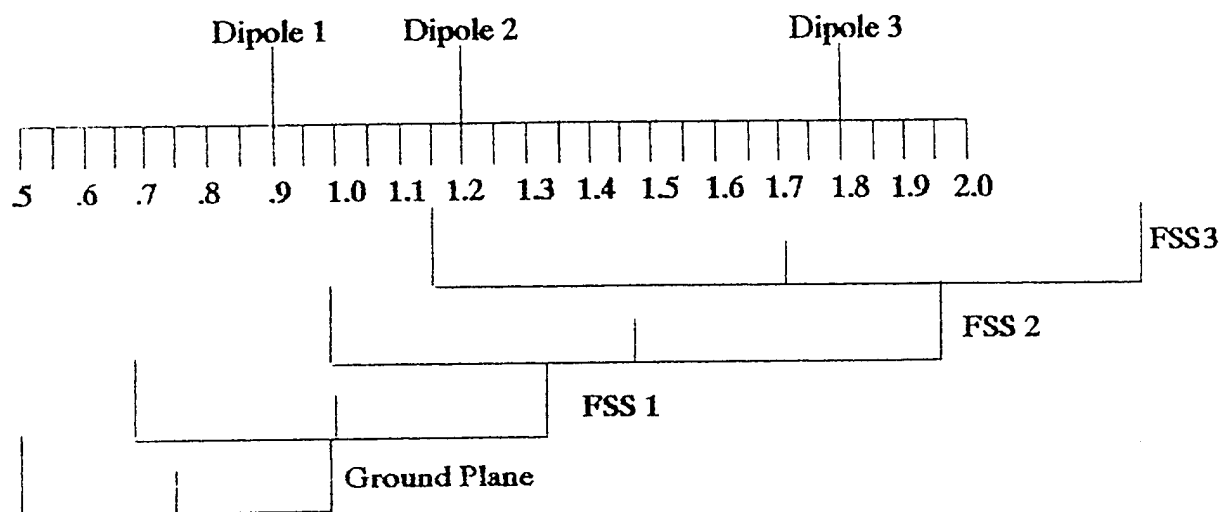
Figure 7: Subbands over which each FSS layer has influence over the reflectivity of the ground plane system.

5 x 5 Element, V-pol, Band 3 Array
3 x 3 Element Active Subarray

- All baluns terminated in 50 ohms except when specified otherwise.

- All optical switches set to dark state except for those needed to configure array.

- Switches which need to be illuminated for V-pol, band 3 operation are:

  v9, v13, v16, v20

- The active portion of array has the following baluns connected to the RF beamformer

  E2, E3, E4
  F5, F6, F7
  G2, G3, G4

- FIFT's are connected to baluns:

  D3, H3
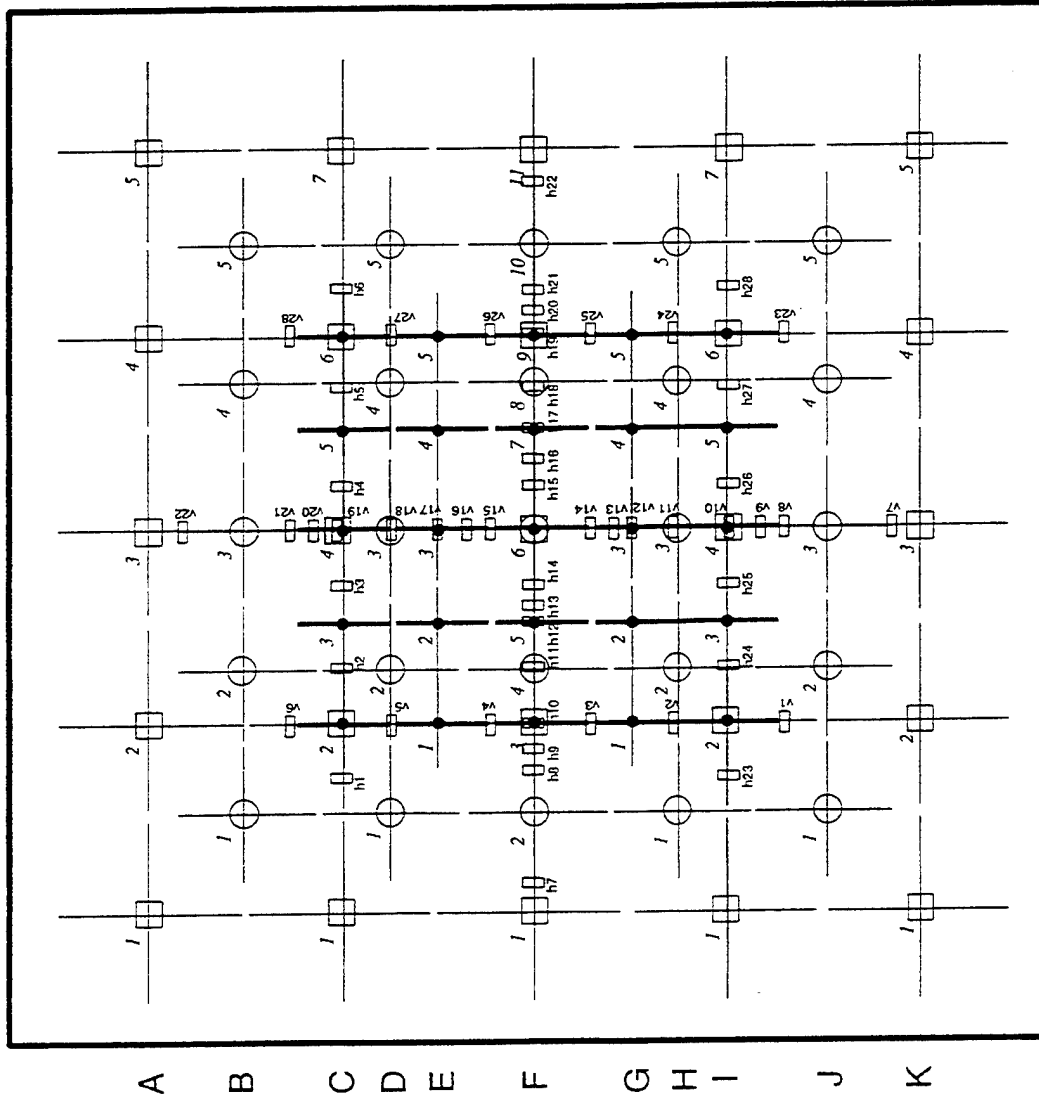
Figure 8: Dipole array layout for the test panel configured to operate over the 1200 MHz to 2000 MHz subband.

284
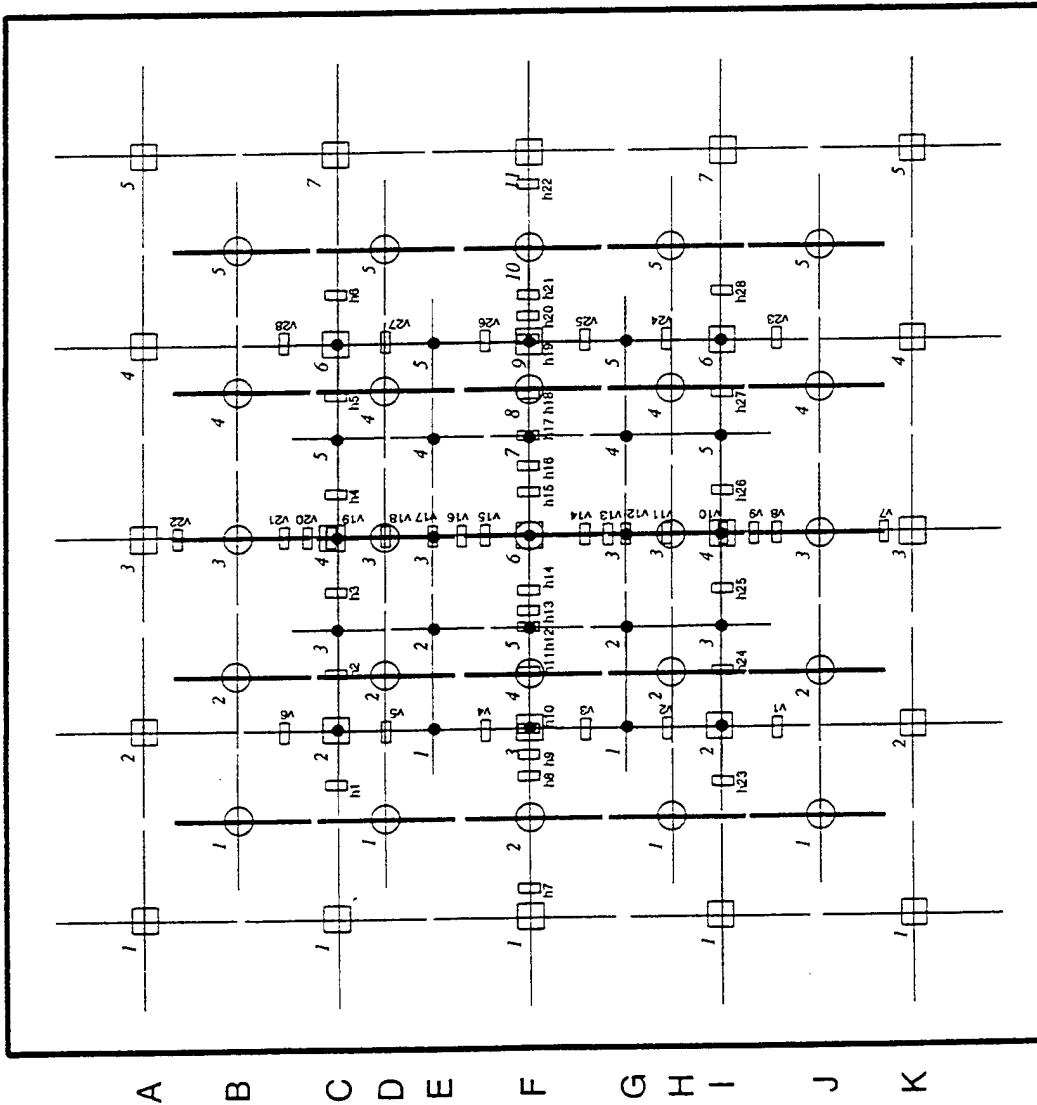
5 x 5 Element, V-pol, Band 2 Array
3 x 3 Element Active Subarray

- All baluns terminated in 50 ohms except when specified otherwise.

- All optical switches set to dark state except for those needed to configure array.

- Switches which need to be illuminated for V-pol, band 2 operation are:

  v8, v10, v12, v14, v15, v17, v19, v21

- The active portion of array has the following baluns connected to the RF beamformer

  D2, D3, D4
  F4, F6, F8
  H2, H3, H4

- FIFT's are connected to baluns:

  C4, E3, G3, I4

Figure 9: Dipole array layout for the test panel configured to operate over the 900 MHz to 1200 MHz subband.

5 x 5 Element, V-pol, Band 1 Array
3 x 3 Element Active Subarray

- All baluns terminated in 50 ohms except when specified otherwise.

- All optical switches set to dark state except for those needed to configure array.

- Switches which need to be illuminated for V-pol, band 1 operation are:

  v1, v2, v3, v4, v5, v6, v7, v8, v9, v11
  v13, v14, v15, v16, v18, v20, v21,
  v22, v23, v24, v25, v26, v27, v28

- The active portion of array has the following baluns connected to the RF beamformer

  C2, C4, C6
  F3, F6, F9
  I2, I4, I6

- FIFT's are connected to baluns:

  G1, E1, G5, E5, J3, H3, G3, E3, D3, B3
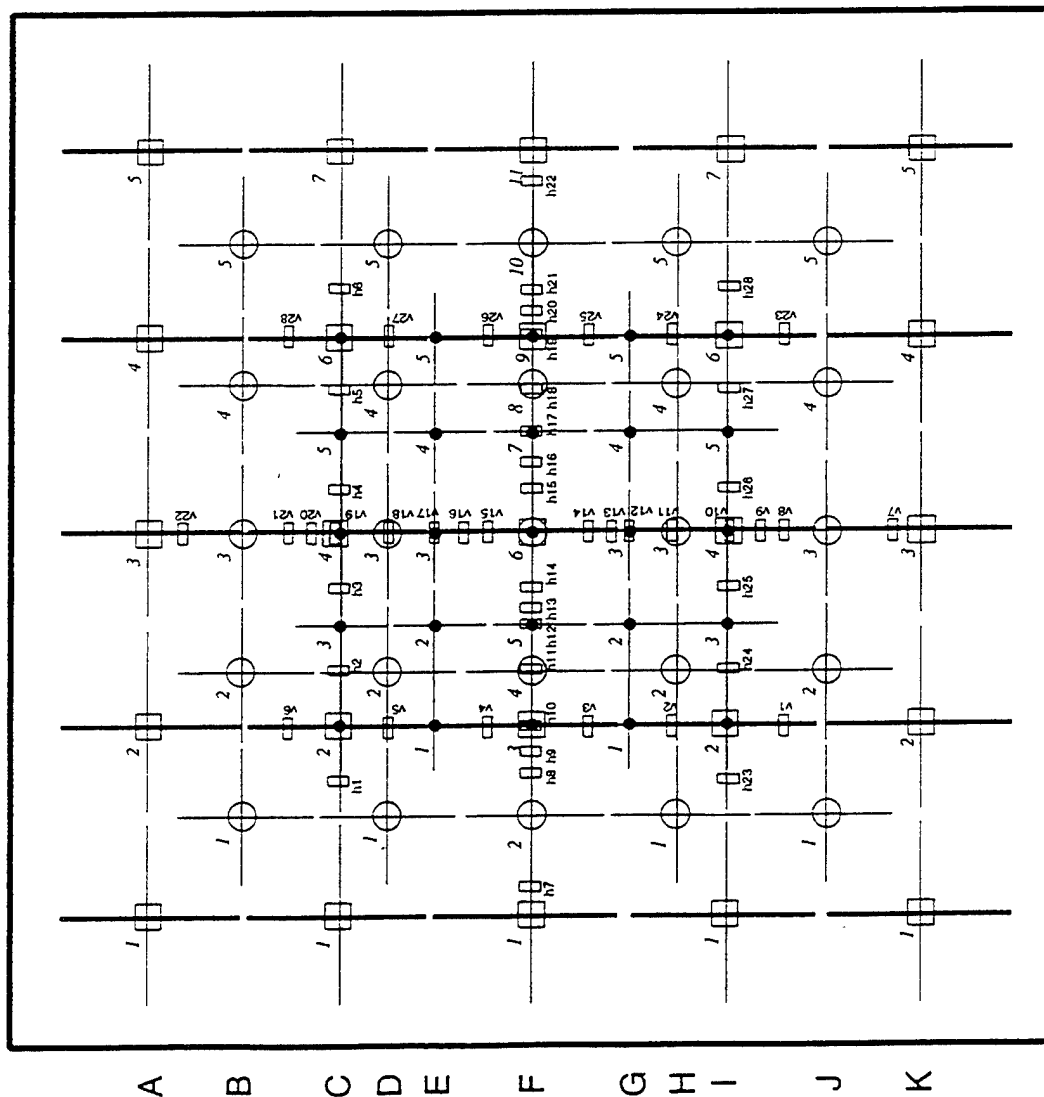
Figure 10: Dipole array layout for the test panel configured to operate over the 500 MHz to 900 MHz subband.

286

Performance Data

Measurements were taken on each unique configured dipole. The VSWR plots were very similar for all the elements whether they had switches or not on them. The radiation patterns of the active elements were also measured and verified that they were similar. Typical mutual coupling data between adjacent E-plane and H-plane elements and cross-polarization isolation are presented in Figure 12. Typical radiation patterns of the central element configured in the three subbands with all surrounding elements terminated are given in Figure 13. Typical arrayed patterns for 3x3 array are shown in Figure 14. The gain of the array is slightly higher than what would be expected for a nine element array. This is caused by crossed dipole elements in the FSS layers acting as passive director elements. The VSWR vs. frequency of the central dipole element as it is configured to each of the three subbands is given in Figure 15. Over all the arrayed patterns were what would be expected of a 3x3 array.

CONCLUSION

The feasibility of a reconfigurable dipole array antenna was demonstrated. The array was designed to operate over two octaves in three subbands. The instantaneous bandwidth of each dipole extended from 50% to almost 90% which covers the instantaneous bandwidth of many avionics functions. With further optimization it should be possible to decrease the thickness of the panel by almost an inch.

The benefits of a broadband ground plane system can be extended to other types of array elements. Printed bowtie dipoles have be demonstrated to have instantaneous bandwidths of more than two octaves without reconfiguration. Bowties do not lend themselves to be connected together by switches. Smoother VSWR and pattern performance over a broader bandwidth have also be observed with printed log periodic dipoles over the ground plane system. Currently, reconfigurable slot elements are being developed which would be more amenable for installation on aircraft. Slots have the ability to look down to the horizon with vertical polarization when they are mounted on the top of a fuselage or top of wings.
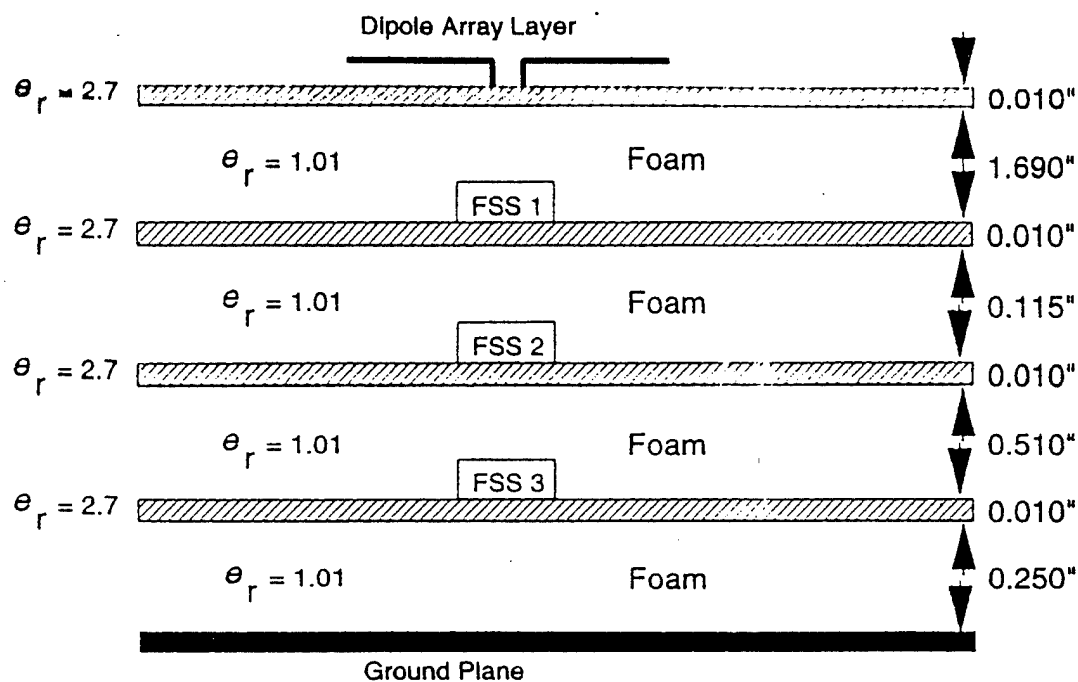
Figure 11:   Dipole array spacings between laminates
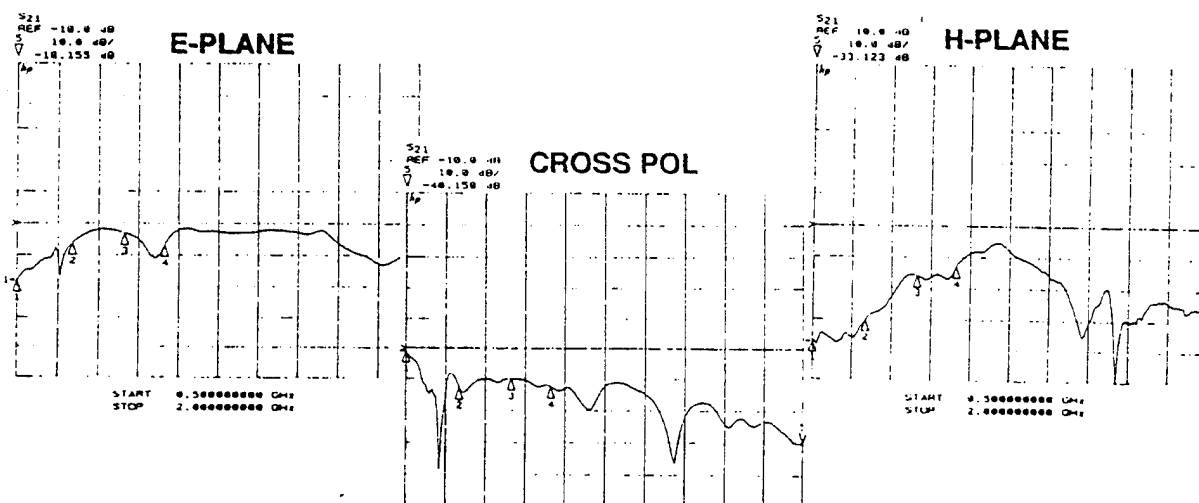
Figure 12:   Mutual coupling between adjacent co-polarized dipole elements and cross-polarized
isolation of a dual-polarized element.

1 800 GHz

Freq

1800 MHz

900 MHz

500 MHz
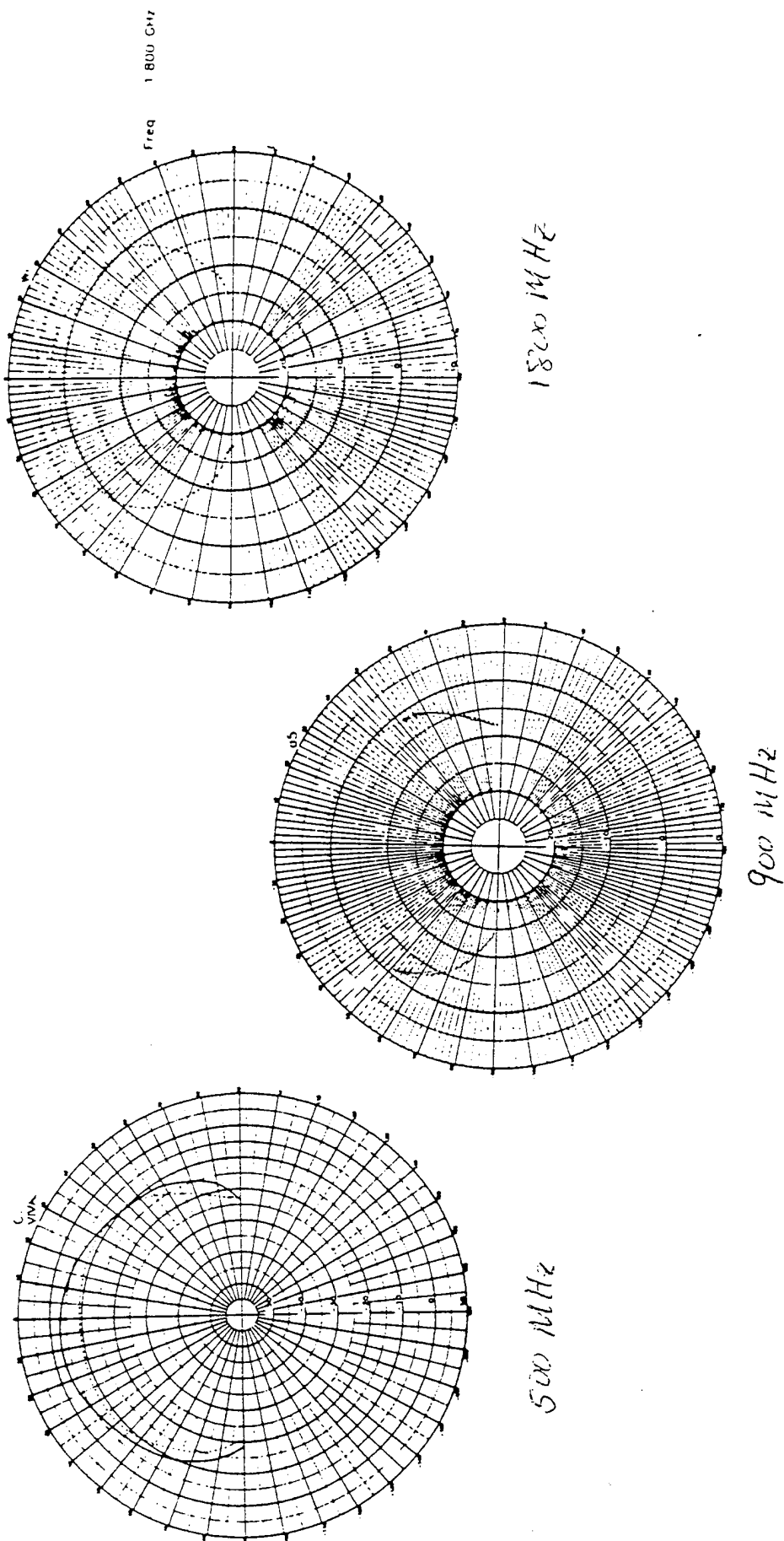
Figure 13:   Typical radiation patterns of central element for the three FSS layer panel

289
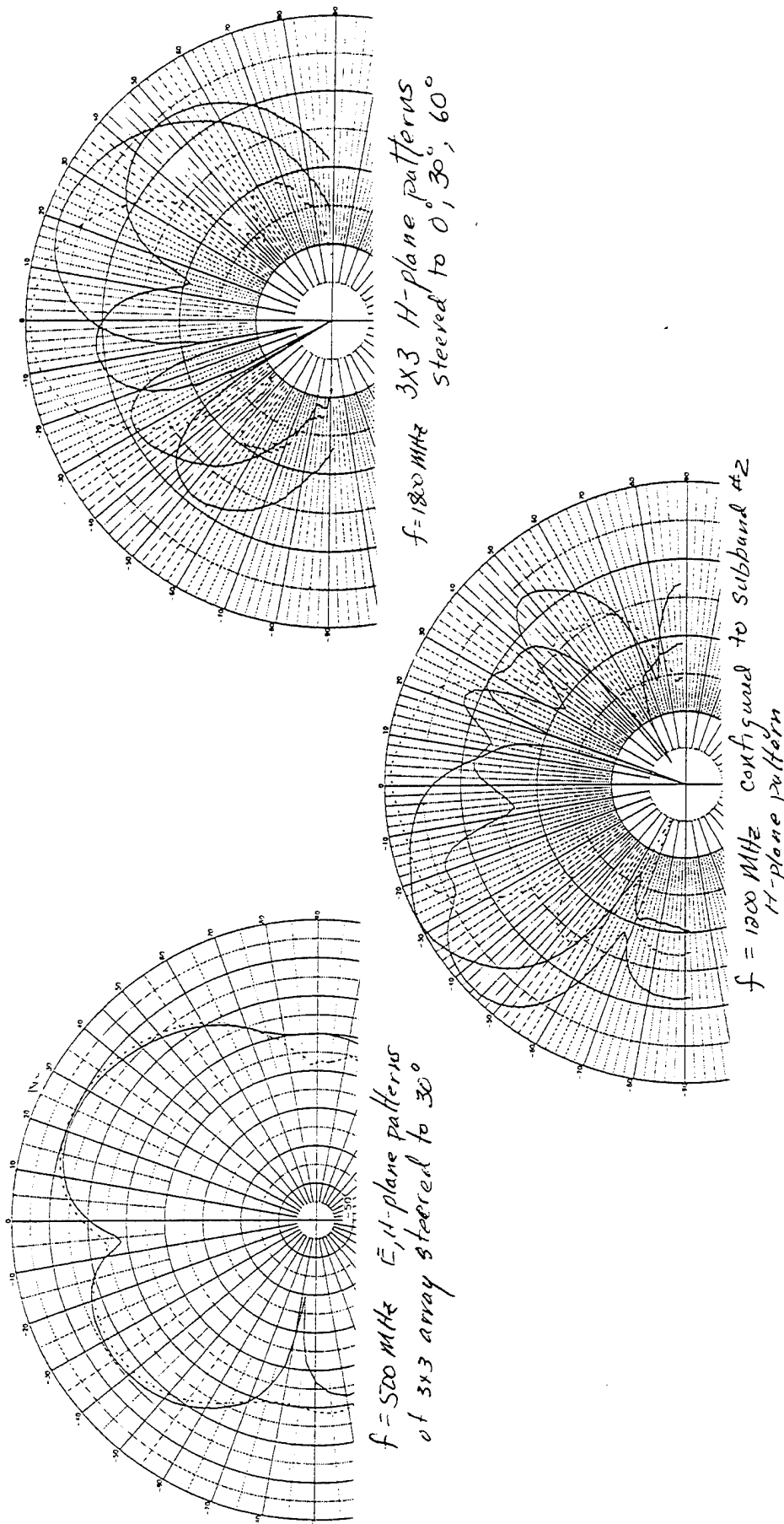
Figure 14: Typical 3x3 array radiation patterns with array beam steered to 0°, 30°, and 60°.

VSWR, CENTER ELEMENT
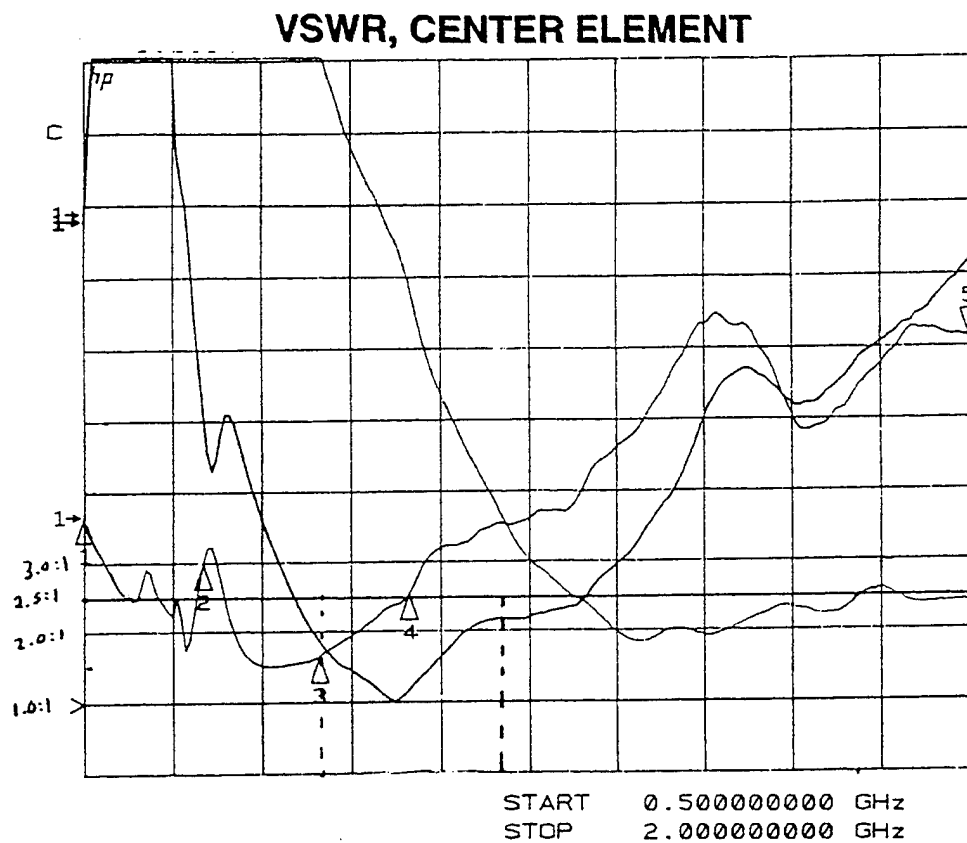
Figure 15: VSWR vs. frequency of central dipole element of the three FSS layer panel with all the other elements in the panel terminated in a matched load as it is configured to each of the three subbands

THE DESIGN OF WIRE ANTENNAS USING GENETIC ALGORITHMS

Derek S. Linden
Edward E. Altshuler
U.S. Air Force
Rome Laboratory
Electromagnetics and Reliability Directorate
Hanscom AFB, MA 01731-3010

ABSTRACT

There is a large class of electromagnetic radiators designated as wire antennas. In the design of these antennas an inductive process is used, that is, an integral equation for the current distributions on the wires that make up the antenna is formulated so that the electromagnetic properties of the antenna can then be determined. However, using an electromagnetics code in conjunction with a Genetic Algorithm (GA), it is possible to design an antenna using a completely deductive approach; that is, the desired electromagnetic properties of the antenna are specified and the wire configuration that most closely produces these results is then synthesized. As a result, it is possible for there to be few constraints on the antenna design, and one can even dispense with having an initial design to feed into the optimization.

For typical wire antennas there is a population of trillions upon trillions of possible wire configurations that fall within a specific volume. The GA randomly selects a small set of potential solutions from this population and rates each member. As in the evolutionary process of "survival of the fittest," high quality solutions mate and produce offspring; poor quality strings perish. With succeeding "generations," the quality of the solutions continually improve and an optimal solution is ultimately obtained. The GA method of antenna design is analogous to a method of breeding mice to run a maze, only the "mice" are antenna designs and the "maze" is a simulation to determine its performance.

We have designed several antennas using this new process. In this paper, we describe antennas that we specified should radiate a circularly polarized field in all directions 10 degrees or more above the horizon at a frequency of 1.6 GHz. The constraints on the optimizations were the volume of the search space (a cube one-half wavelength on each side); the resolution of the search space grid (32 points per axis was chosen), the presence or absence of a ground plane, and the number of wires connected in series (best results were found with 7). No particular design or theory of operation was specified. We built and tested the resulting so-called "genetic antennas"; agreement with the computational results was very good. The antennas that have been designed with this process have a very weird shape with wires going in haphazard directions. It is obvious that these

designs could never be obtained using the inductive approach that has been used in the past. We believe that this new process may revolutionize the design of wire antennas.

1. Introduction

Since the time wire antennas first appeared, a variety of useful designs have emerged: e.g. the dipole and its counter-part monopole over a ground screen, rhombic, beverage, yagi, log periodic, loop, helix, and spiral antennas. These antennas were designed, and continue to be designed, using an inductive process, that is, an integral equation for the current distribution on each of the wires is formulated and the electromagnetic properties of the antenna are then calculated. This design approach is generally limited to relatively simple wire structures. In general, an engineer finds an existing design that may have the desired electromagnetic characteristics, works with appropriate equations, if any exist, to determine its proper dimensions and parameters, and uses a simulator, which is often available, to predict its performance. If the performance is not good enough, the engineer redesigns and resimulates the antenna, using intuition to determine which parameters to change to improve performance. This design cycle has produced, over time, many different antenna designs with different characteristics, but it is time-consuming, and, if there are many unknowns, unlikely to produce truly optimum results. It requires that the engineer be familiar with the many different designs that exist, and have enough experience so an acceptable solution can be reached in a reasonable amount of time.

When the high speed digital computer became available in recent years, it was then possible to analyze more complex wire structures in shorter times, and also to optimize wire antennas using computer aided design technologies. In most, if not all, cases, the general shape of the wire antenna is still predetermined and the individual wires that constitute that particular configuration are optimized. While the computer allows for greater design complexity, there are still no automated design tools available. This lack of tools means the engineer must still use intuition to design an antenna and optimize it. It is faster than using pen and paper or a calculator, but there are too many variables in even simple designs for a person to keep track of effectively. "Folklore" develops with such a system: certain factors are seen to affect certain antenna characteristics, yet they may or may not. Even years of experience may not result in useful intuition about certain aspects of electromagnetic problems.

In addition, this design cycle limits the types of designs that are tried to those that have an intuitive logic about them. Symmetry is often present, and structures are kept relatively simple to allow for easier understanding and analysis. Nearly all of the designs produced by engineers have the characteristic of "making sense" when one looks at them or their circuit schematics. Most all of them look like they should work. However, non-intuitive configurations can sometimes work as well as or better than intuitive ones. As an example, note that people use bent coat hangers, aluminum foil, and antennas in strange-

293

looking configurations to get good radio or TV reception, unhindered by knowledge of EM theory. It is therefore of interest to find a way to search for such counter-intuitive solutions using a well-validated optimization methodology. One technique in particular, the Genetic Algorithm (GA), is sufficiently powerful to search this kind of counter-intuitive solution space, as we will show later.

As for motivation to find a new process of antenna design, there is a pressing need for increased antenna performance. For instance, current and future earth-to-satellite communication and navigation systems require ground-based antennas that are circularly polarized and have near-hemispherical coverage. Circular polarization is necessary for systems operating at frequencies below about 3 GHz since the faraday rotation produced by the ionosphere can cause a linearly polarized wave to be rotated such that it may not be aligned with the receiving antenna; a worst case scenario could find the incoming wave cross polarized so that no signal is received. A circularly polarized signal averts this from happening. Near hemispherical coverage is desirable since the ground antenna is often required to receive a signal from a satellite anywhere in space, except at low elevation angles where signals have a multipath component which has a time delay that may disrupt the system performance.

Currently helical or patch antennas are often used for the above-mentioned systems. We have experimented with monopole antennas loaded with modified folded dipoles [1,2] or loops [3]. We have shown that it is possible to achieve nominal circular polarization and near-hemispherical coverage with these configurations; the monopole radiates a vertically polarized wave and provides coverage at the lower elevation angles while the folded elements or loop radiate a horizontally polarized wave and provide coverage at the higher elevation angles. The main limitations of these antennas are that they are relatively narrow band. In addition, the helical and patch antennas require a phasing network.

In this paper we describe a new and revolutionary process for designing antennas using a genetic algorithm in conjunction with an electromagnetic code. We have used this process to optimize a monopole loaded with a modified folded dipole for uniform power over the hemisphere [4]. We will show that it is possible using this approach to synthesize the design of a wire antenna that is circularly polarized, has near hemispherical coverage and is broad band. In this paper we describe two such antennas: one to be used over a ground plane, the other without a ground plane.

2. Approach

It is useful to briefly describe the operation of GAs. The GA, which utilizes the mechanisms of evolution, starts with a large population (trillions upon trillions for typical problems) of potential wire configurations. It randomly selects a small set, or sample population, of wire configurations and, through an encoding scheme, maps all

configuration information (e.g. start and endpoints, wire sizes) into a binary string of 1s and 0s called a chromosome. The performance of each member of the sample population is computed using an electromagnetics code. Using an iterative method it moves toward more optimal solutions. Partial solutions to the problem are obtained by combining parts of strings (i.e. mating two strings) into a new string, i.e. their offspring. As in the evolutionary process of "survival of the fittest," high quality strings mate and produce offspring; poor quality strings perish. With succeeding "generations," the quality of the strings continually improve and an optimal solution is ultimately obtained. The GA method of antenna design is analogous to a method of breeding mice to run a maze, only the "mice" are antenna designs and the "maze" is a simulation to determine its performance. In this manner, after only a few thousand antenna simulations out of the trillions (or more) possible, a good solution is usually obtained. This method is very resistant to being stuck in local maxima, which allows it to work well for antenna design problems. Our experience so far seems to indicate the search space for antenna problems has many comparable maxima in a given search space. Antennas produced with the GA can have similar performance and also be radically different from one another.

The antenna design program we created employs a so-called steady-state GA (i.e. a portion of the current population carries over to the next generation). A top percentage of the population--between 10% and 50%--is saved from each generation after all chromosomes have been evaluated. (In the designs at hand we chose to save the top 50% of the population of 500 chromosomes.) These chromosomes are used to generate the offspring that will fill the rest of the population. A virtual "weighted roulette wheel" is filled according to each chromosome's fitness as compared to all the others'. The more fit a chromosome is, the larger its share of the wheel. For each new position to be filled in the population, the wheel is spun and the first parent is chosen. The wheel is spun again and the second parent is chosen, unless the wheel points to the same member of the population, in which case it is spun again. It should be noted that although the parents are constrained not to be the same member of the population (i.e. clones are not allowed), they can be the composed of the same genetic material (a case that occurs as the population converges to a single optimal chromosome). A single crossover site is chosen at random, and the child is produced from the first part of the first parent's chromosome, up to the cross-over point, and the second part of the second parent's chromosome. This process is repeated until the population is full again. For each generation, between 0 and 20 bit-flip (0 to 1 or 1 to 0) mutations occurs in the new children (much less than 1% of the bits are affected, and no more than about 8% of the children, depending on the size of the chromosomes and the population size). The new population members are evaluated, and the generation process is begun anew. There is one other feature that has been added that saves time. The program remembers evaluations it has done, so that if a chromosome is exactly like a chromosome it has evaluated or saved, it will copy the score from it and move to the next one. This is very helpful as the population converges to a small number of genetically different chromosomes. For more information on basic GAs see references [5] and [6].

In order to implement the GA, it is first necessary to define the constraints of the design. One such constraint is antenna size. Since near-hemispherical coverage is desired the antenna should obviously be relatively small. We chose to start out by confining the antenna to a cube 0.5λ on a side. This design space is shown in Figure 1. As the GA uses binary strings to store configuration information, we had to encode the location of each wire using a binary system. We allowed 5 bits for each component of the (X,Y,Z) coordinate for the beginning and end of each wire. In other words, each axis of the design space had 32 levels, and there was therefore 32^3 possible vertices at which the wires could be connected.

Next we had to specify the number of wires and the connection scheme that a configuration could use. We initially chose to investigate antennas consisting of 5,6,7 and 8 connected wire segments. The preliminary results showed the 7-wire antenna to perform slightly better than the 5, 6 and 8 wire antennas, so that is the focus of this paper. In addition, we decided to make all wires connect in series for simplicity.
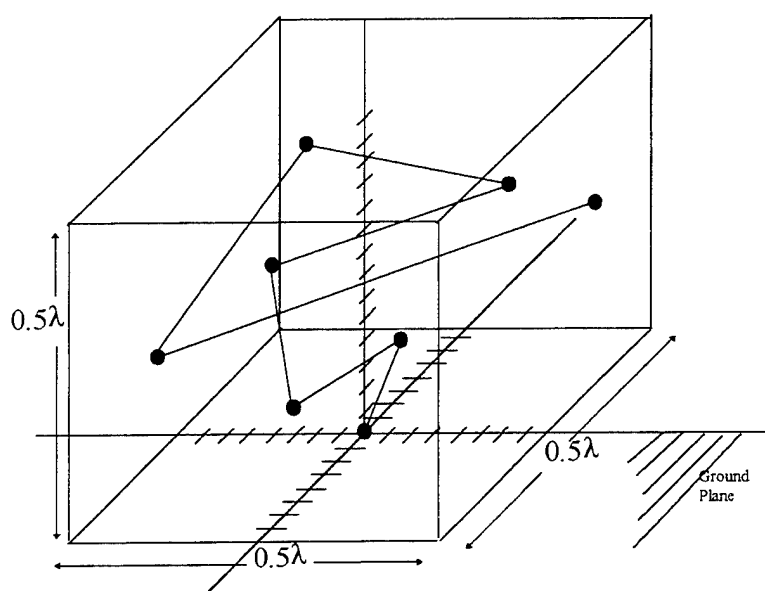
Figure 1. Genetic Antenna Design Space. 3-D cube of space with 32 levels possible in each of three dimensions for a designated number of points. Wires are connected in series only, from the origin to each successive point. The 0.5λ (i.e. 1/2 wavelength) limit is arbitrary and loosely based on the problem to be solved. For uniform gain characteristics, 0.5λ seems a good length. The ground plane can be removed if desired.

As there were 5 bits for each axis coordinate, 3 axis coordinates per point, and 7 points to be designated (1 point per wire, as each wire starts at the previous wire's endpoint, and the first wire begins at the origin), each 7-wire antenna required a chromosome with 5x3x7 = 105 genes (or bits).

After determining the constraints, which gives the chromosome mapping to the antenna configuration, it is necessary to determine the function for evaluating the resulting antennas. This function is called the cost function, which returns a single number to the GA that is a measure of its fitness. As a first step in this evaluation, we used the Numerical Electromagnetics Code (NEC) [7] to get an antenna pattern of each configuration. We computed the hemispherical radiation pattern at increments of 5° in elevation (from θ= -80° to +80°)and 5° in azimuth (from ϕ=0° to ϕ=355°).

Our goal was to obtain right hand circular polarization 10° above the horizon over the hemisphere at a frequency of 1.6 GHz. The cost function for this system was therefore simple: the program read the output from NEC2, calculated the average gain, and calculated the sum of squares from all the points. In equation form,

$$\text{score} = \Sigma_{\text{over all } \theta,\phi}(\text{Gain}(\theta,\phi) - \text{Avg. Gain}) \qquad (1)$$

If the average gain was less than -10dB, the average gain was set to be -10dB. This allows us to get rid of antennas that are very poor radiators in general. The system's goal was to minimize this score. A perfectly uniform gain pattern would receive a score of zero.

The radiation patterns were measured in an anechoic chamber. The test antenna was illuminated by a circularly polarized horn antenna. θ-plane cuts were measured for azimuth angles of 0°, 45°, 90° and 135° and for frequencies from 1.2 to 2.0 GHz.

Before discussing the results, it seems appropriate to briefly discuss a name for these types of antennas. We have called the outcome of the design process we have described above a genetic antenna. A genetic antenna is an antenna that comes directly from a GA optimization, and is not constrained by a pre-existing design. While the GA has been used previously to help determine unknowns in existing designs [8,9,10,11], it has not, to the best of our knowledge, been used to create a completely new design with its own unique theory of operation. The resulting antennas we will describe in the next section are unique and distinct from all existing antenna designs, yet were not designed in the traditional sense of the word. As the antennas designed this way seem to take on shapes that are different from one another but all equally unusual and non-intuitive, it seems more appropriate to give them a name that describes their origin rather than their particular shape.

3. Results

For antennas with and without a ground screen, the GA produced 7-wire configurations having vertices at the coordinates shown in Table 1. These genetic antennas have a very unorthodox shape, as shown in Figures 2 and 3. The computed radiation patterns of the antenna over a ground plane are shown in Figure 4 for elevation cuts corresponding to

297

azimuth angles of 0°, 45°, 90° and 135° at a frequency of 1.6 GHz. Note that the response to a circularly polarized wave varies by less than 4 dB for angles above 10° over the horizon. The frequency dependence of the radiation pattern is shown in Figure 5 for the range of 1.2 to 1.9 GHz for an elevation cut with an azimuth angle of 0°. It is seen that these patterns are relatively flat from 1.3 to 1.9 GHz. This corresponds to an over 30% bandwidth which is excellent for a circularly polarized antenna having near hemispherical coverage. Patterns for other elevation cuts were comparable to these.

(It should be mentioned that true circular polarization is not achievable over large angles. From a practical standpoint we have elliptical polarization for which the magnitudes of the orthogonal signals approach unity and their respective phases approach quadrature. Note that as long as the receiving antenna has the same sense polarization as the transmitter, the maximum polarization loss of 3dB occurs when the receiver is linearly polarized. If however the receiving antenna has the opposite sense polarization, the polarization loss can become very large.)

7-wire genetic antenna with ground plane					
Startpoint (coordinates in meters)			Endpoint (coordinates in meters)		
X	Y	Z	X	Y	Z
0.0000	0.0000	0.0000	-0.0166	0.0045	0.0714
-0.0166	0.0045	0.0714	-0.0318	-0.0166	0.0170
-0.0318	-0.0166	0.0170	-0.0318	-0.0287	0.0775
-0.0318	-0.0287	0.0775	-0.0318	0.0439	0.0140
-0.0318	0.0439	0.0140	-0.0318	0.0045	0.0624
-0.0318	0.0045	0.0624	-0.0106	0.0378	0.0866
-0.0106	0.0378	0.0866	-0.0106	0.0257	0.0230

7-wire genetic antenna without ground plane					
Startpoint (coordinates in meters)			Endpoint (coordinates in meters)		
X	Y	Z	X	Y	Z
0.0000	0.0000	0.0000	-0.0197,,	0.0045	0.0140
-0.0197	0.0045	0.0140	0.0408	0.0378	0.0321
0.0408	0.0378	0.0321	-0.0348	0.0257	0.0321
-0.0348	0.0257	0.0321	0.0408	0.0166	0.0291
0.0408	0.0166	0.0291	0.0318	-0.0076	0.0714
0.0318	-0.0076	0.0714	-0.0197	-0.0045	0.0745
-0.0197	-0.0045	0.0745	-0.0136	-0.0378	0.0775

Table 1: 7-wire genetic antenna coordinates--with ground plane and without ground plane
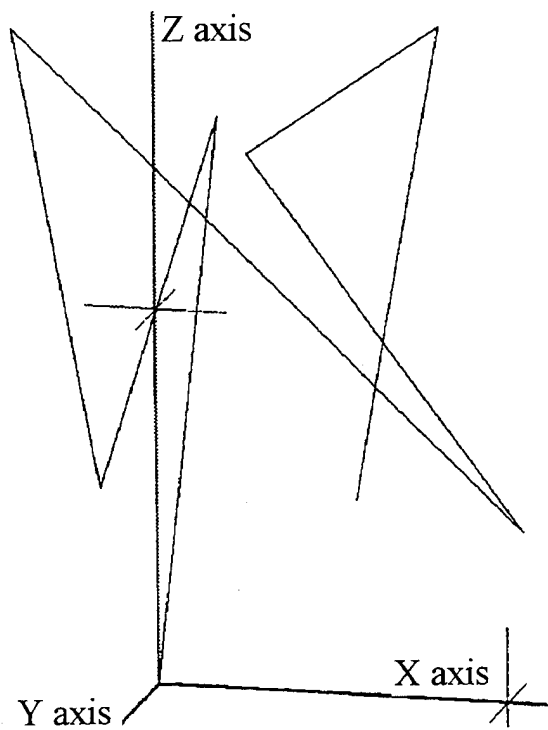
Figure 2. 7-wire Genetic Antenna with ground plane. 3-dimensional view. Hash marks are 5cm apart.
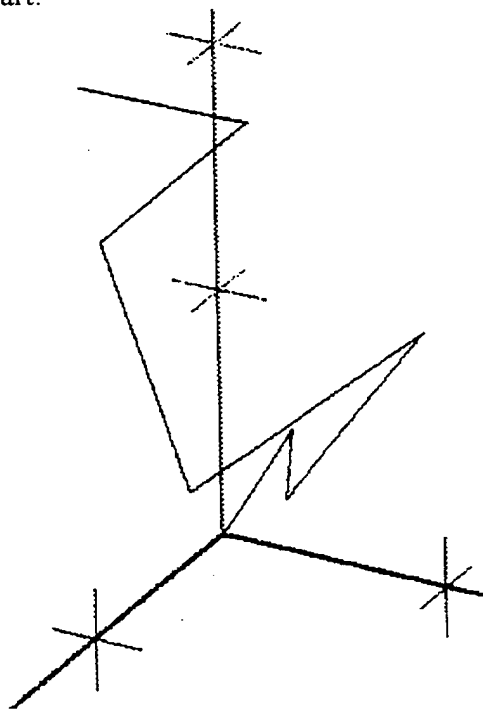
Figure 3. 7-wire Genetic Antenna without ground plane. 3-dimensional view. Hash marks are 5cm apart.
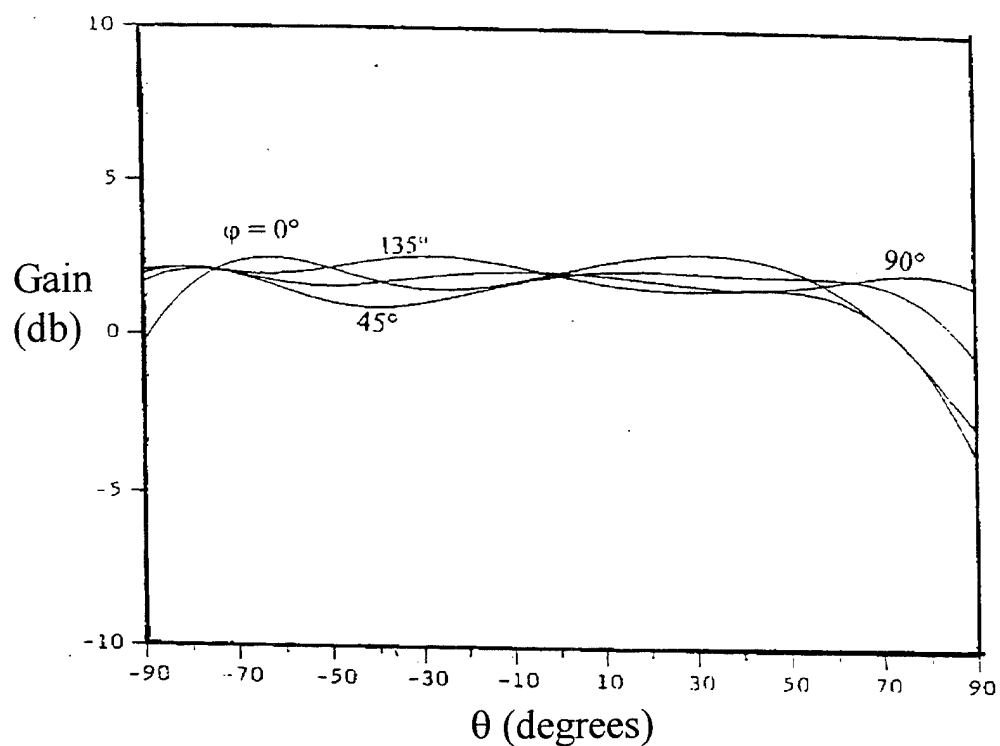
Figure 4. 7-wire genetic antenna with ground plane computations: φ dependence for RH circularly polarized wave.
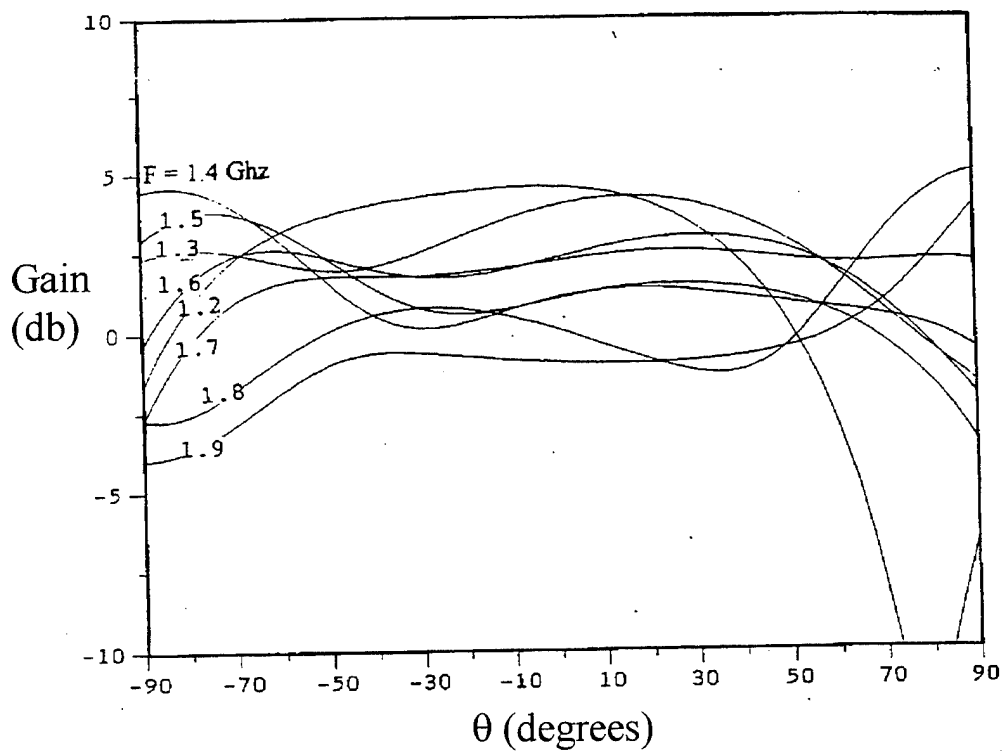
Figure 5. 7-wire genetic antenna with ground plane computations: frequency dependence for RH circularly polarized wave.

300

The computed radiation patterns for the genetic antenna without a ground plane are shown in Figure 6 for elevation cuts corresponding to the same azimuth angles as before, 0°, 45°, 90° and 135°. The 90° and 135° cuts are flat to within slightly over 1 dB above an elevation angle of 10°. The 0° and 45° cuts fall off at the low elevation angles so they have a variation of close to 5 dB above 10°. The frequency dependence of this antenna is shown in Figure 7 for 1.1 to 1.9 GHz for an elevation cut corresponding to an azimuth angle of 0°. Note that this antenna provides very good coverage over the range from 1.2 to 1.8 GHz.
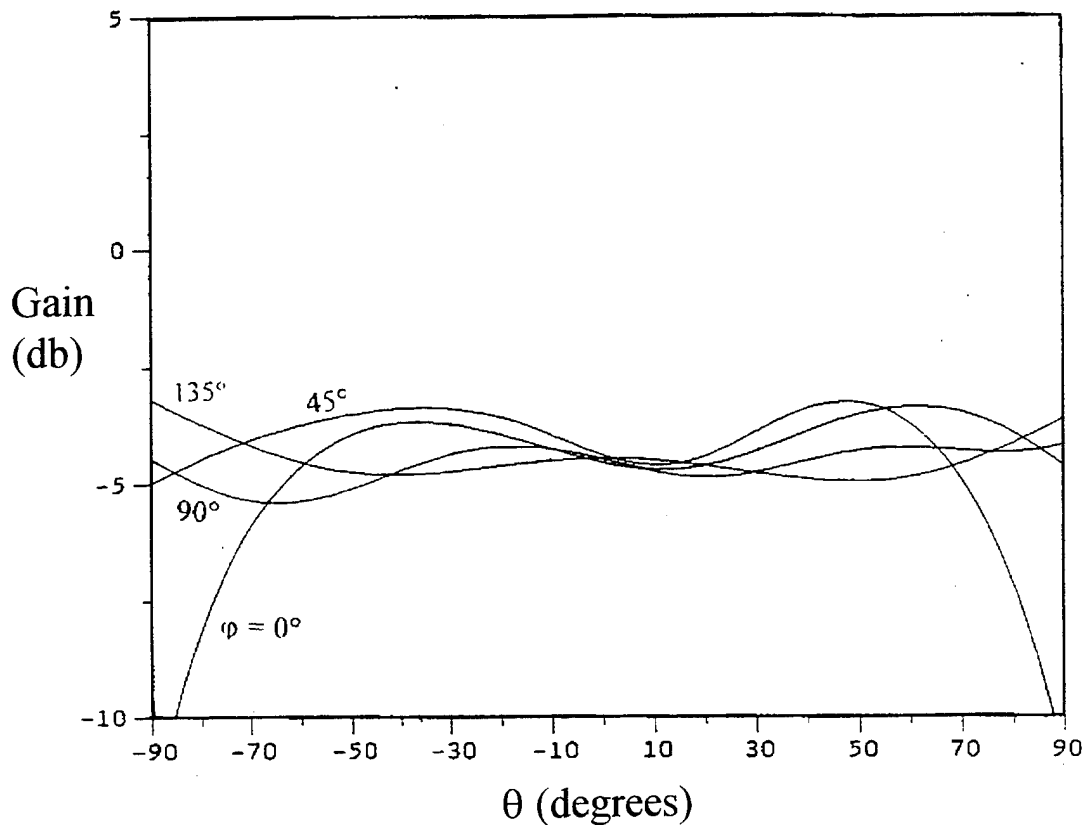
Figure 6. 7-wire genetic antenna with no ground plane computation: φ dependence for RH circularly polarized wave.
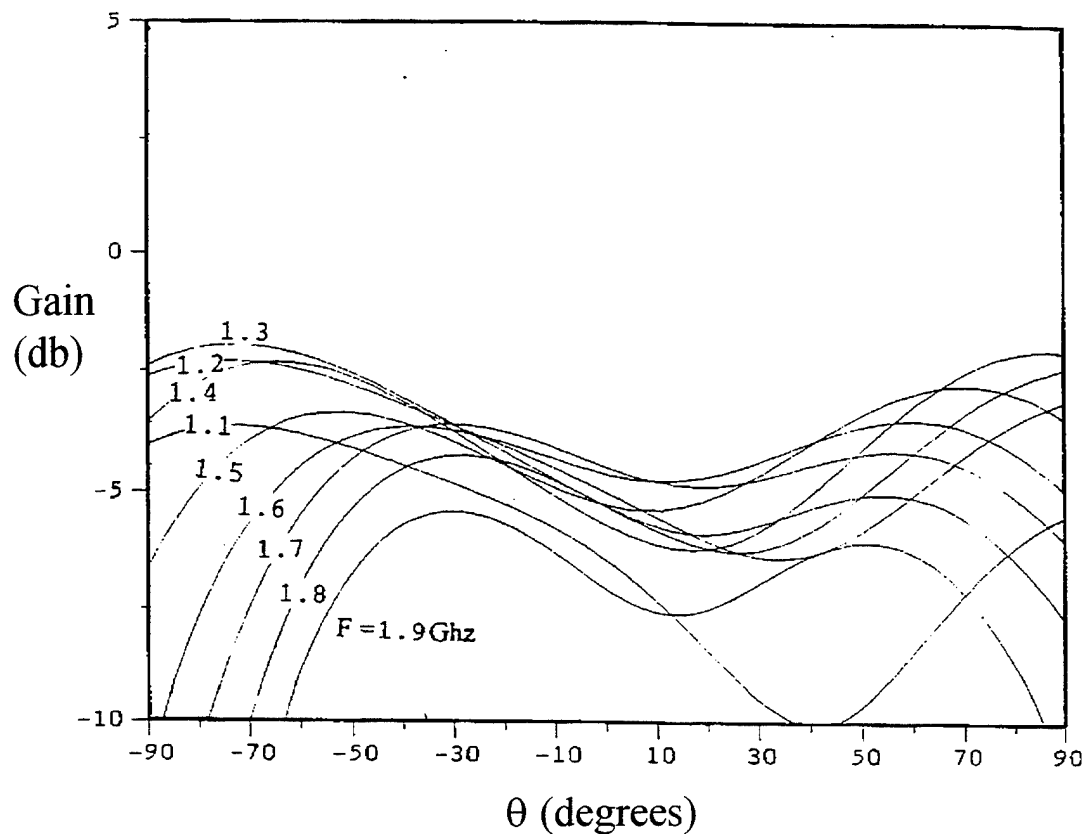
Figure 7. 7-wire genetic antenna with no ground plane computation: frequency dependence for RH circularly polarized wave.

The measured, normalized radiation patterns for the genetic antenna over a ground plane are shown in Figure 8 for the same elevation cuts that were previously used at a frequency of 1.6 GHz. There is approximately a 6dB variation in the field above an elevation angle of 10° as compared to the computed variation of about 4dB. This discrepancy can for the most part be attributed to the fact that the measurements were made over a 4 ft x 4 ft ground plane whereas the computations were done for an infinite ground plane. The ripples in the pattern arise for the most part from reflections from the edges of the ground plane. In addition, the antenna was hand made and it was difficult to produce the exact configuration that was computed. (As evidence of this problem, another antenna was made with the same design but with thinner wire and more accuracy, and preliminary measurements show its pattern only varies 4.5dB and that it has a flatter frequency dependence.) The patterns were also measured over the frequency range from 1.25 to 1.9 GHz for an elevation cut corresponding to an azimuth angle of 0° and are shown in Figure 10. It should be noted that these are only relative gain patterns so only the directional properties are valid; no attempt was made to calibrate the transmitting antenna at all frequencies. As was the case for the computed patterns, these patterns show good coverage for 1.3 to 1.9 GHz.
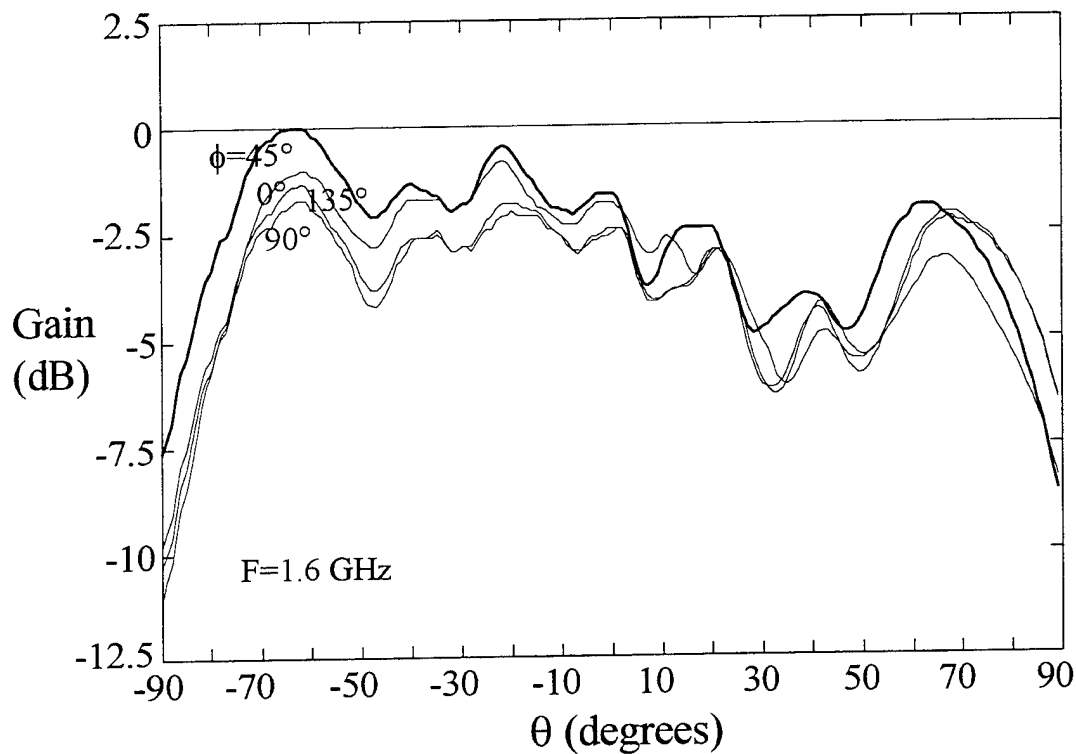
Figure 8. 7-wire genetic antenna with ground plane results: φ dependence. Response is to a circularly polarized wave.
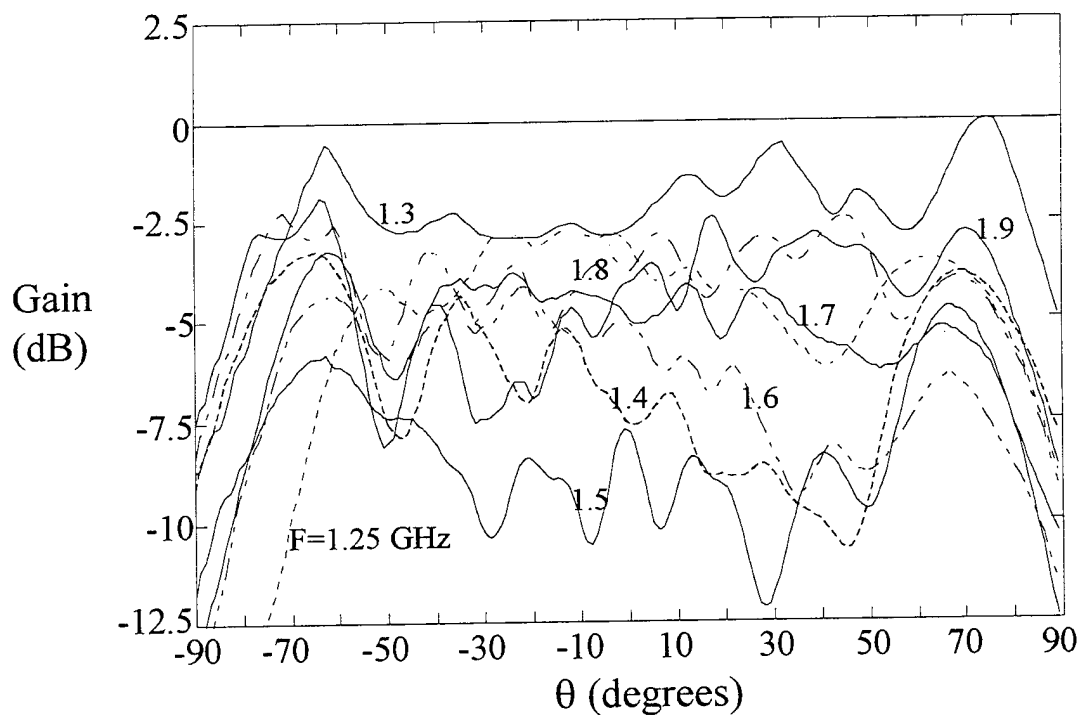
Figure 9. 7-wire genetic antenna with ground plane results: frequency dependence. Response is to a circularly polarized wave.

303

The measured radiation patterns for the 7-wire genetic antenna in free space (no ground plane) are shown in Figure 10 for the same elevation cuts previously computed at a frequency of 1.6 GHz. These results are somewhat poorer than the computed patterns, particularly for the elevation cuts corresponding to azimuth angles of 45° and 135°. We suspect that this lack of agreement is due in part by reflections from the cable from the test equipment to the receiver and from the pedestal itself. Also, as before, the test antenna was not identical to the antenna for which the computations were made. Note that the larger ripples that were present in the radiation patterns for the antenna over a ground plane are not present. The frequency dependence of the directional properties of this antenna are shown in Figure 11 for an elevation cut corresponding to an azimuth angle of 0°. Once again, the measured patterns are not as good as the computed patterns particularly at the lower frequencies; however, the higher frequency patterns are very good. We assume that these differences arise for the same reasons stated earlier.
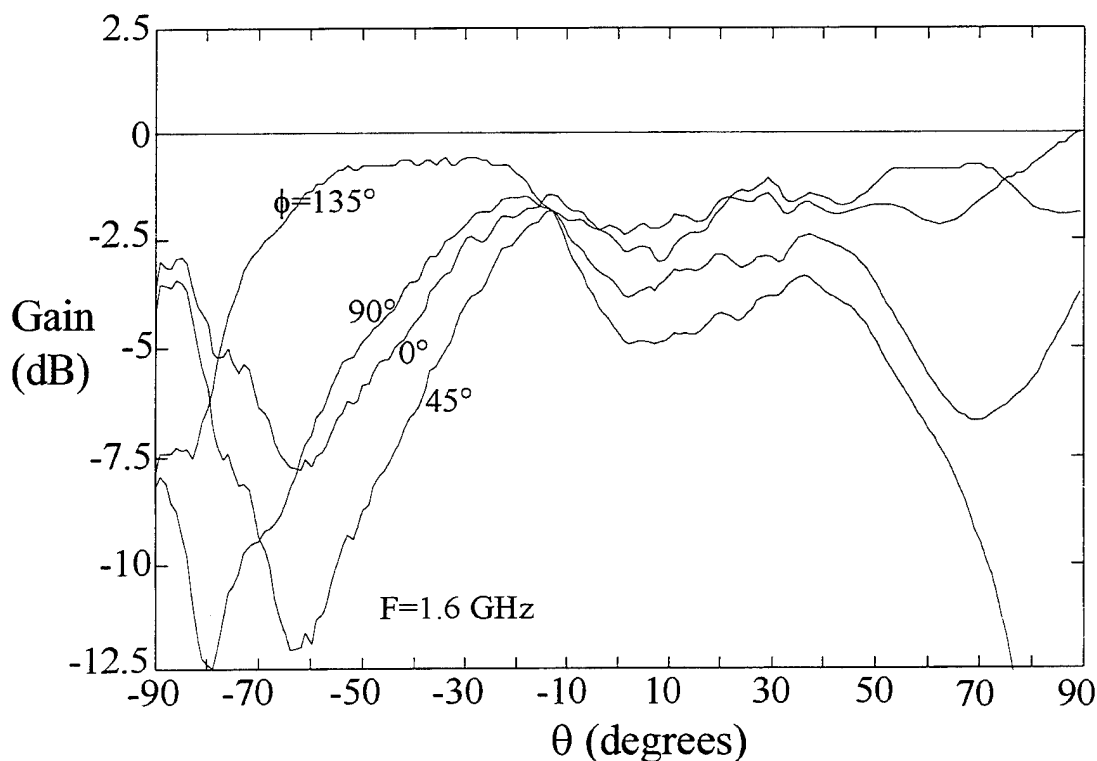
Figure 10. 7-wire genetic antenna with no ground plane results: ϕ dependence.
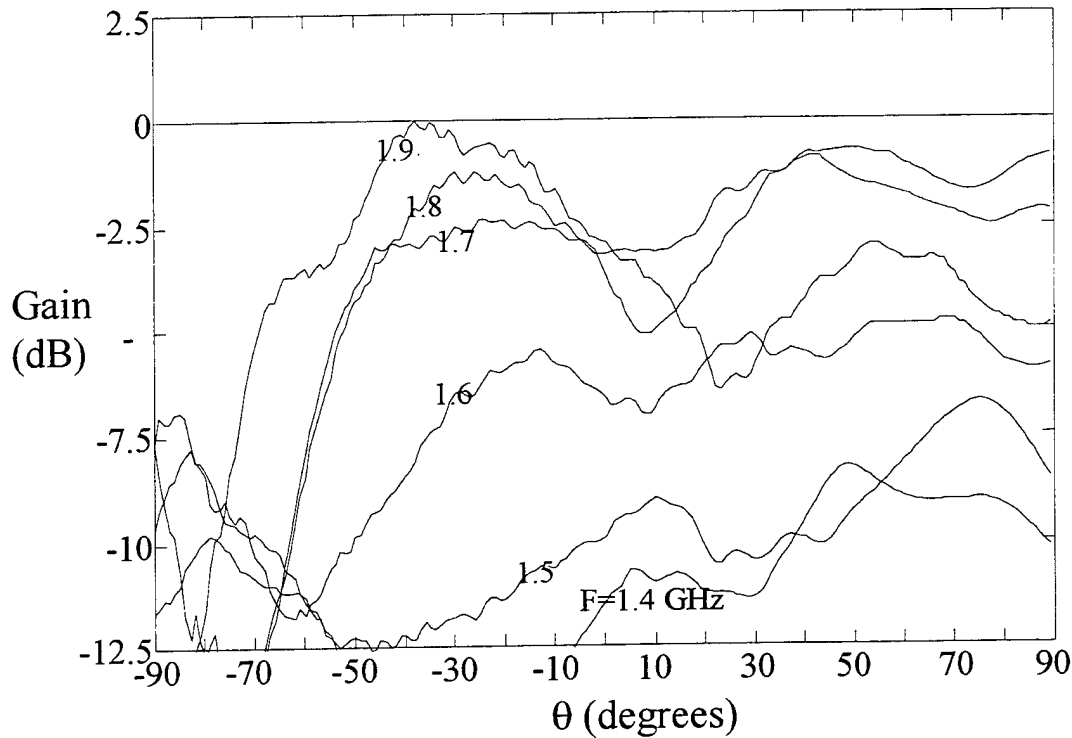
Figure 11. 7-wire genetic antenna with no ground plane results: frequency dependence.

4. Conclusions

The preliminary results of this new process for designing wire antennas are very encouraging. We have shown that it is possible to synthesize the design of an antenna that is nominally circularly polarized over most of the hemisphere using a GA in conjunction with the Numerical Electromagnetics Code. The genetic antenna designs have been quite counter-intuitive. Though they do work in simulation and actual measurement, it does not appear logical or reasonable that they should work. They are quite different from those a rational human designer would have ever thought of, let alone tried to optimize.

Although these genetic antennas were optimized to operate at a single frequency they turned out to be more broadband than expected. For this reason it appears that the antenna is non-resonant and the dimensions of the wires are not too critical. We were pleased that the agreement between the computations and measurements was so good, particularly for the genetic antenna over a ground plane.

In this paper we limited our investigation to the directional properties of the genetic antenna. In the future other parameters such as input impedance and bandwidth will be included in the optimization process.

This procedure of simply defining constraints and cost functions and allowing a blind algorithm like the GA to find the proper design appears to show remarkable promise. Using different cost functions and coding schemes, it seems that this new design procedure is capable of finding genetic antennas able to effectively solve difficult antenna problems, and will be particularly useful in situations where existing designs are not adequate.

Acknowledgment

References

[1] E.E. Altshuler, "A monopole antenna loaded with a modified folded dipole," IEEE Trans. Antennas Propagat. Vol. 41, pp. 871-876, July 1993.

[2] E.E. Altshuler, "Hemispherical coverage using a double-folded monopole," (to be published).

[3] E.E. Altshuler, "A monopole loaded with a loop antenna," (to be published).

[4] E.E. Altshuler and D.S. Linden, "Design of a Loaded Monopole Having Hemispherical Coverage Using a Genetic Algorithm," (to be published).

[5] J.H. Holland, "Genetic Algorithms," Scientific American, pp. 66-72, July 1992.

[6] Goldberg, David E., *Genetic Algorithms in Search, Optimization & Machine Learning*, Addison-Wesley (1989).

[7] G.J. Burke and A.J. Poffio, "Numerical Electromagnetics Code (NEC)-Method of Moments, " Rep. UCID18834, Lawrence Livermore Lab. CA, Jan 1981.

[8]Bahr, M. et al. "Design of Ultra-Broadband Monopoles." IEEE AP-S Symposium, Seattle, WA June 1994.

[9] Haupt, R.L. "Thinned Arrays using Genetic Algorithms." IEEE Trans. Antennas and Propagation, Vol. 42, July, 1994., pp. 983-999.

[10] Johnson, M.J. and Rahmat-samii, Y. "Genetic Algorithm Optimization and its Application to Antenna Design." IEEE, 1994. pp. 326-329.

[11] R.L. Haupt, "An introduction to genetic algorithms for electromagnetics," IEEE Antennas Propagat. Magazine, vol. 37, pp.7-15, April 1995.

ISOIMPEDANCE INHOMOGENEOUS MEDIA IN ANTENNA APPLICATIONS

A.I.KNYAZ

Ukrainian Telecommunication Academy
(Ukraine, Odessa Tel/Fax (0482) 445707)

Abstract. Inhomogeneous medium is isoimpedance one if the equality between ratio permittivity and permeability takes place. Electrodynamics and antenna applications of these materials are considered.

INTRODUCTION

There are well known the use of dielectric rods, lens, dielectric coatings for wires in the antennas constructions. This paper is devoted to justification of the main principle - so wave device as antenna demands application of the wave material which is the inhomogeneous isoimpedance medium (IIIM). At first (p.1), the wave effects in the IIIM have been described. In p.2, the similarity and conservation theorems for immersed antennas are given. Part 3 deals with the IIIM fabrication methods. Part 4 is devoted to the results review and further perspectives.

PART 1. The IIIM is determined with the equation $\sqrt{\mu/\varepsilon} = Z_0 = \text{const}$ when

$$\varepsilon_r(x,y,z) = \mu_r(x,y,z) = \alpha(x,y,z) \tag{1}$$

The using curvilinear plane-basis and sphere-basis coordinates systems are :

$$A \begin{cases} \text{PBI} \quad x_3 = z, x_1 + ix_2 = f(x+iy), h_3 = 1; \\ \text{SBI} \quad x_3 = r, x_1 + ix_2 = f[(x+iy)/(r+z)], h_3 = 1; \end{cases} \tag{2}$$

$$B \begin{cases} \text{PBII} \quad tgx_3 = y/x, h_3 = \rho; \\ \text{SBII} \quad x_3 = az/r^2; \\ \text{SBIII} \quad x^2 + y^2 + (z - a\ ctgx_3)^2 = a^2/\sin^2 x_3; \\ \text{SBIV} \quad x^2 + y^2 + (z - a\ cthx_3)^2 = a^2/sh^2 x_3; \end{cases} \tag{3}$$

In group B the functions (1) are linked with Lame's coefficients : $\alpha(x_1, x_2, x_3) = h_{3c}/h_3(x_1, x_2, x_3)$, $h_{3c} = \text{const}$ and in group A $\alpha = \alpha(x_3), \alpha = \alpha(x_1, x_2), \alpha = \alpha(x_1, x_2, x_3)$ are arbitrary functions with variants: a) partly homogeneous, b) smoothly homogeneous, c) hybrid. As example, Fig. 1 shows the IIIM characteristic $\alpha(z)$ and constancy of the IIIM impedance $Z = Z_0 = 120\pi$ Ohm.

$$\alpha(z)$$

$$Z = Z_0 = 120\pi \ \text{Ohm}$$
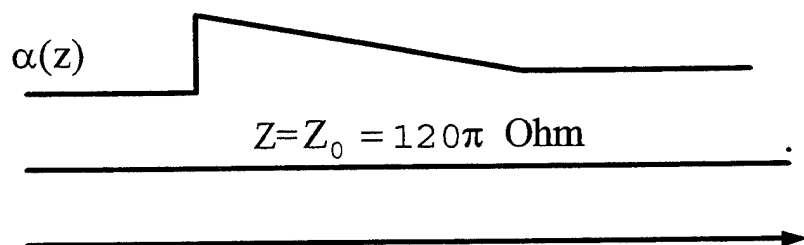
z   Fig. 1

Previous author's works [1-4] were devoted to the circular waves and coordinates of group B. It was shown that additionally to known T, E, H, EH-waves in the cylinder waveguides the similar ones take place in the channels waveguides with transverse intensities:

$$h\overline{E}_\perp = \overline{A}(x_1, x_2)e^{-jk_3 h_{3c} x_3} \quad , |\overline{H}_\perp| = |\overline{E}_\perp|/W \tag{4}$$

Simplest examples are attached with the plane-axis coordinates PBII $z, \rho, \varphi = \text{arctg}(y/x)$, $\alpha = a/\rho$ where a-radius of IIIM cylinder with solution

$$E_\perp = E_z(\rho)e^{-jk_0 a\varphi} \quad , H_\perp = H_\rho(\rho)e^{-jk_0 a\varphi} \tag{5}$$

TE circular waves (5) describe the principally new effect "refraction without reflection" (invisible cylinder , sphere) [5] when outer and inner fields are equal

$$E_z^0 = e^{-jk_0 \rho \cos\varphi}, E_z = \sqrt{a/\rho} \sum_{-\infty}^{\infty} (-j)^n e^{jn\varphi} f_n(\rho), \tag{6}$$

$$f_n = J_n(\xi)\cos\eta + b_n^{-1}(0.5 J_n + J_n')\sin\eta, \xi = k_0 a, \eta = \ln(\rho/a) \tag{7}$$

Formulae (6), (7) correspond to the situation when incident plane wave smoothly, without reflecting field, transmits through the IIIM cylinder.

In the article [6], the different variants of transmission without reflection with the cylinder and conical coordinates application have been investigated. The arbitrary longitudinal characteristics $\alpha(z)$ and normally to plane boundary z=0 incident wave are simply analyzed with the substitution

$$\exp(\pm jk_0 z) \rightarrow \exp[\pm jk_0 \int_0^z \alpha(z)dz] \tag{8}$$

It is important that any view $\alpha(z)$ doesn't disturb the boundary conditions fulfillment.

Next example is the guided wave which is going without reflection in the rectangular waveguide when space z>0 is filled with IIIM media. Appropriate solution is

$$z < 0 \quad E^0 = \sin Mx e^{-j\sqrt{k_0^2 - M^2} z}$$

$$z > 0 \quad E = \sin Mx e^{\int_{}^{z} \alpha\beta_i dz} \ e^{\int_{}^{z} \alpha\beta_r dz} \tag{9}$$

308

Application of the IIIM allows to create arbitrary amplitude distribution on the wave front. Sliding along x=o plane wave with arbitrary amplitude distribution in the IIIM may be represented with the formulae

$$x > 0 \quad E^0 = \exp(-jk_0 z)$$

$$x < 0 \quad E = e^{\displaystyle -k_0 \int_0^{k_0 x} \alpha\beta dx} \, e^{-jk_0 z} \tag{10}$$

$$\alpha = [\beta' + \sqrt{\beta'^2 + 4(1+\beta^2)}]/2(1+\beta^2) \tag{11}$$

The expressions (10), (11) with small changes describe [6] the wave without critical wavelength in the rectangular waveguide (Fig.2).

| IIIM |
| the air |
| IIIM |

x $\alpha(x)$ Fig.2
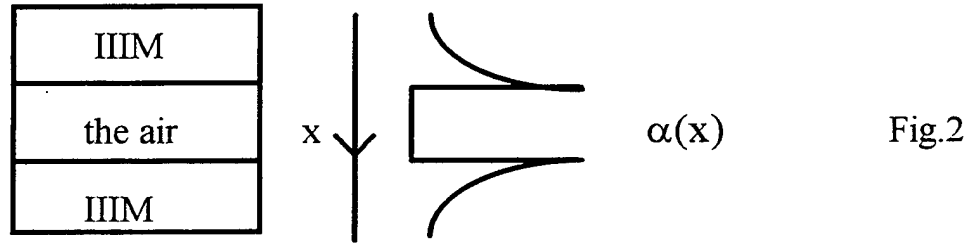
The IIIM synthesis methods are suggested in [7] where it is counted the influence of the IIIM characteristic on the oblique incident wave only. For example, the intensities in the problem about oblique incident plane wave and the plane boundary z=0 are

$$E^0 = E_y^0 = \exp[-jk_0(x\sin\theta_0 + z\cos\theta_0)] \tag{12}$$

$$E_y^R = R \ \exp[-jk_0(x\sin\theta_0 - z\cos\theta_0)]$$

$$E_y^T = T \ \exp[-jk(x\sin\theta_0 + \int_0^z \alpha\beta dz)] \tag{13}$$

$$\alpha^2(1-\beta^2) - jk_0^{-1}\alpha\beta_z' - \sin^2\theta_0 = 0$$

where (13) corresponds to reflected and transmitted waves.   Fig.3

The IIIM has different selectivity for different spectrum components of the normally incident wave beam :

$$E^0(x,z) = \int_{-\infty}^{\infty} F(v)\exp[j(vx - z\sqrt{k_0^2 - v^2})]dv \tag{14}$$

$$E^R(x,z) = \int_{-\infty}^{\infty} R(v)\exp[j(vx + z\sqrt{k_0^2 - v^2})]dv \tag{15}$$

$$E^T(x,z) = \int_{-\infty}^{\infty} T(v)\exp[j(vx - \sqrt{k_0^2 - v^2})\int_0^{\cdot}\alpha(z)\beta(z,v)dz]dv \tag{16}$$

1.5. List of the wave effects in presence of the IIIM :1) Multiplex superposition of the plane (sphere) fronts of the circular waves, 2) Refraction without reflection by special isoimpedance bodies, 3) Transmission without reflection for any IIIM characteristic $\alpha(z)$ view, 4) Independent amplitude and phase controls on the plane (sphere) wave front, 5) Angle selectivity change without influence on normal transmission, 6) Minimization of direct portion of the transmitted energy in the wave beam, 7) Formal calculating analogies for the known and new wave's types.

PART 2. Let us consider the immersion of the antennas in the IIIM. General recognition of the problem consists of combination of the Maxwell's equations and boundary equations for perfect conducting surfaces. There are considered two theorems: Proportional change (similarity) theorem and Conservation one. It is need to immerse an antenna wholly in the IIIM and then to produce the "Cut-off "procedures. In the paper, these theorems are considered with help of monopole field transformation (Fig. 4).
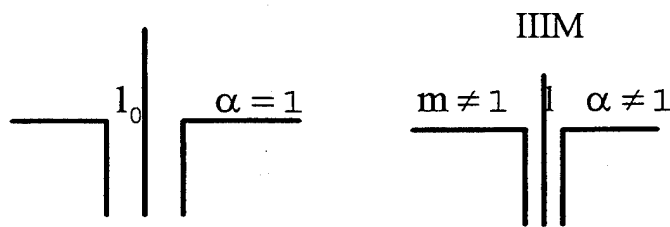
Fig.4

With using of the denotations

$$\alpha = \varepsilon_r = \mu_r \ , m = 1/l_0 \tag{17}$$

the proportional change (similarity) theorem is the following: Electrical characteristics of an antenna are changed in: a) m times if m $\neq$ 1, α = 1 ; b) α times if m = 1, $\alpha \neq$ 1 ; c) mα times if m$\alpha \neq$ 1.

Conservation theorem is used for mα = 1: Electrical characteristics of an antenna are unchanged if the dimensions decrease in α times is following with the concerted increase of medium characteristic in α times.

"Cut-off" procedures are specified as the problem: To find $\alpha = \alpha(r, \theta, \varphi)$ and the perfect metal boundary configuration in order to have proportional change or constancy of the input and output electrical characteristics when the IIIM has finite sizes. In order to have the solution, one can to combine the above mentioned wave properties and the similarity-conservation theorems (finite IIIM synthesis).

On contrast to known publications we use the condition (1) obligatory that allows as theoretically so in an experiment to use not only small values of permittivity , permeability but very great ones. It is very important for practice as the possibility to create small antennas in any frequency bands. Fig. 5 shows the potential properties of real magnetic materials for antenna's sizes decrease.

$\lg \mu_r$

1Hz 1kHz 1MHz 1GHz

1- amorphous alloys
2- high permeab. ferrites
3- ferrites
4- electrotech. steel
5- magnetodielectrics
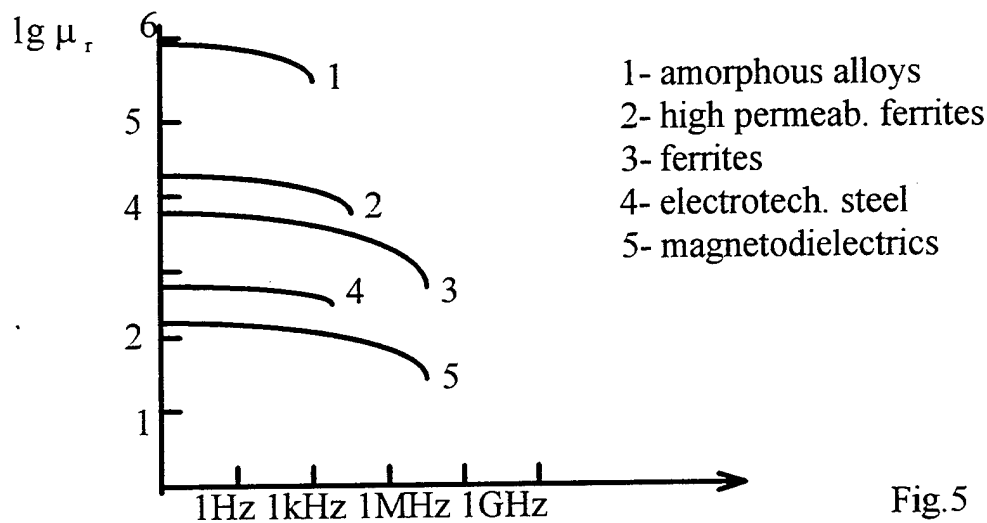
Fig.5

PART 3. The problem of the isoimpedance materials fabrication with details is considered in [5]. We can to use following methods:1. Ferro-dielectric compositions (Particles of the magnetic and dielectric materials), 2. Ferro-aluminum compositions (Particles (rods, strips) of the magnetic material and perfect conducting metal), 3. Lumped metal-air realization (Particles of the perfect conducting metal and special turns),.4. Wave metal-air realization (Combination of the metallic plates, strips). Shown realization techniques have two variants of justification. First of them is the quasistatic method where the IIIM parameters are tested separately in the electrical and magnetic fields:

$$\varepsilon_r = 1 + P / E\varepsilon_0 \ , \mu_r = 1 + M / H\mu_0 \tag{18}$$

According to second (wave) method it is necessary to find for travelling wave the refraction coefficient n and ratio impedance z_c :

$$\varepsilon_r = n / z_c, \mu_r = nz_c, \ n = c_0\beta / \omega, z_c = E_\perp / H_\perp Z_0 \tag{!9}$$

The different artificial materials are given in the Table 1.

№	Medium	ε_r	μ_r	n	Z_c
1	Decelerating dielectric	>1	1	>1	<1
2	Accelerating dielectric	<1	1	<1	>1
3	Accelerating magnetic	1	<1	<1	<1
4	Decelerating magnetic	1	>1	>1	>1
5	Decelerating MD	>1	>1	>1	1
6	Accelerating MD	<1	<1	<1	1
7	MD with small impedance	>1	<1	1	<1
8	MD with great impedance	<1	>1	1	>1

311

PART 4. The IIIM applications for the antennas optimization problem solutions have the great perspectives. Appropriate benefits are:

1. Conservation of the optimum characteristics for shorten antennas
2. Invisible lossless bodies
3. New lens ideology for beam pattern forming
4. IIIM bodies as buffers for wave (laser or acoustic) beams
5. Mobile VLF, LF, MF antennas
6. Antennas for the energy relay transmission
7. New types of the guide systems.

Of course, we have many problems. Some of them are the following :

1. Who will make the invisible body first ?
2. What types of antennas are necessary to realize with IIIM application primarily?
3. How to combine the great advantages of the Microelectronics Technology with new demands of the IIIM realization ?

CONCLUSION

RIGID LOGICAL CHAIN : ANTENNA IS WAVE TRANSFORMER - TRANSFORMATION TAKES PLACE IN ELECTROMAGNETIC VOLUME - THIS VOLUME MUST BE FILLED WITH WAVE MATERIAL = ISOIMPEDANCE INHOMOGENEOUS MEDIUM

REFERENCES

1. Knyaz A.I. Electrodynamical Boundary Problems. Odessa: Pub. of Odes. Electrotechn. Instit. of Svyazi (OEIS),1991.-120 p. (R)

2. Knyaz A.I. Circular Waves In Channels Waveguides / book "Devices and Methods of Applied Electrodynamics"(Proc. of second All-union science-techn. Conf.). - Od.-Moscow: Pub. of Mosc. Aviat. Inst., 1991, p. 22. (R)

3. Knyaz A.I. Circular Waves in the Channel Waveguides // Trans. of 14th Intern. Sympos. on Electromagnet. Theory, Australia, August,1992, p. 248-250.

4. Knyaz A.I. Information Systems Electrodynamics. - M.: Radio i svyaz, 1994. - 392 p.(R)

5. Knyaz A.I. Binary Materials In Radio Electronic Devices, Ukranian state Academy of Telecommunication, Odessa, 1994, 80 p.

6. Knyaz A.I. Non-reflecting Action of Inhomogeneous Isoimpedance Media, in book "Telecommunications Problems" Kiev : Tehnica ,1995 ,p.10-14

7. Knyaz A.I. Inhomogeneous Isoimpedance Media Synthesis, Proc. of Ukr. scient. radio and television institute, N 4, Odessa,1995

The Multifunction Mast Antenna for Submarines - covering from VLF to L-band

by

Jack Bryan, Joseph Blais and Naftali I. Herscovici

Spears Associates, Inc.
Norwood, MA USA

Abstract The multitude of communication tasks involved in a submarine mission together with the extraordinary space limitations present the antenna engineer with a unique design challenge.

This paper presents an optimized solution whose main goal is the maximization of the number of simultaneous bands of coverage. This Multifunction Mast Antenna was designed, built, and successfully tested and its first version is currently in operation in the US Navy.

1. Introduction

Techniques for the interception of radio frequency energy encompassing VLF to L-band frequencies, (Multi-Range Antennas) have been well known for a number of years. However, modern radio systems often rely on spread-spectrum or frequency agile techniques. Therefore, much of the thrust of modern antenna design has been towards the achievement of broadband antenna structures. In addition, reduction in the required size of antenna elements has also been a goal of many antenna improvement programs. For a submarine application, achievement of multi-band performance in a compact design is of particular importance. In the United States Navy Advanced Mast Development Program, considerable effort was spent in the development of compact, broadband antenna elements which

could be arrayed in a radome no larger than the antenna radome previously utilized for older generation mast antennas. Therefore, all the antennas (including radiating elements, matching networks and some active circuitry) are located in a mast less than 5 meters long with a cross section of 140 mm (excluding the radome). The Multi-Range Antennas which are the subject of this paper are to be fitted onboard United States Navy Submarines and possibly with small modifications on other submarines currently in service.

2. The Description of the Antenna System

The Multifunction Mast Antenna System comprises five units as follows (Figure 1):

1. Unit 1 - The Antenna/Radome Assembly: A multi-range, multi-element antenna array housed in a non-penetrating, radome assembly.

2. Unit 2 - Outboard Cable Assembly: A single, multi-conductor Outboard Cable Assembly carrying all required RF, power and control lines between inboard and outboard elements.

3. Unit 3 - Hull Penetrator: A hull penetrator allowing a sub-safe interconnection between inboard and outboard antenna elements.

4. Unit 4 - Junction Box: A Junction Box which provides both filtering of DC and control lines and EMP hardening at the point of entry into the submarine's hull.

5. Unit 5 - Antenna Control Unit (ACU): An Antenna Control Unit which allows local control of all antenna function, observation of system status, the running of built-in test routines and the observation of results, and a remote control port allowing remote control and remote monitoring of the antenna by way of

RADOME
(UNIT 1)

NOMINAL
SEA HEIGHT

ERECTING
MECHANISM
(SHIPBUILDER
SUPPLIED)

JUNCTION BOX
(UNIT 4)

OUTBOARD
CABLE
ASSEMBLY
(UNIT 2)

HULL
PENETRATOR
(UNIT 3)

ANTENNA CONTROL UNIT (ACU)
(UNIT 5)

GPS/INMARSAT—C/
MIDS/IFF
ANTENNA HEAD

GPS/INMARSAT—C/
MIDS/IFF
ELECTRONICS
PACKAGE

VLF/LF/MF
ANTENNA

VHF MARITIME/
UHF
ANTENNA

UHF
ELECTRONICS

RADOME

5 METERS
MAXIMUM

HF/VHF
ANTENNA

FEED
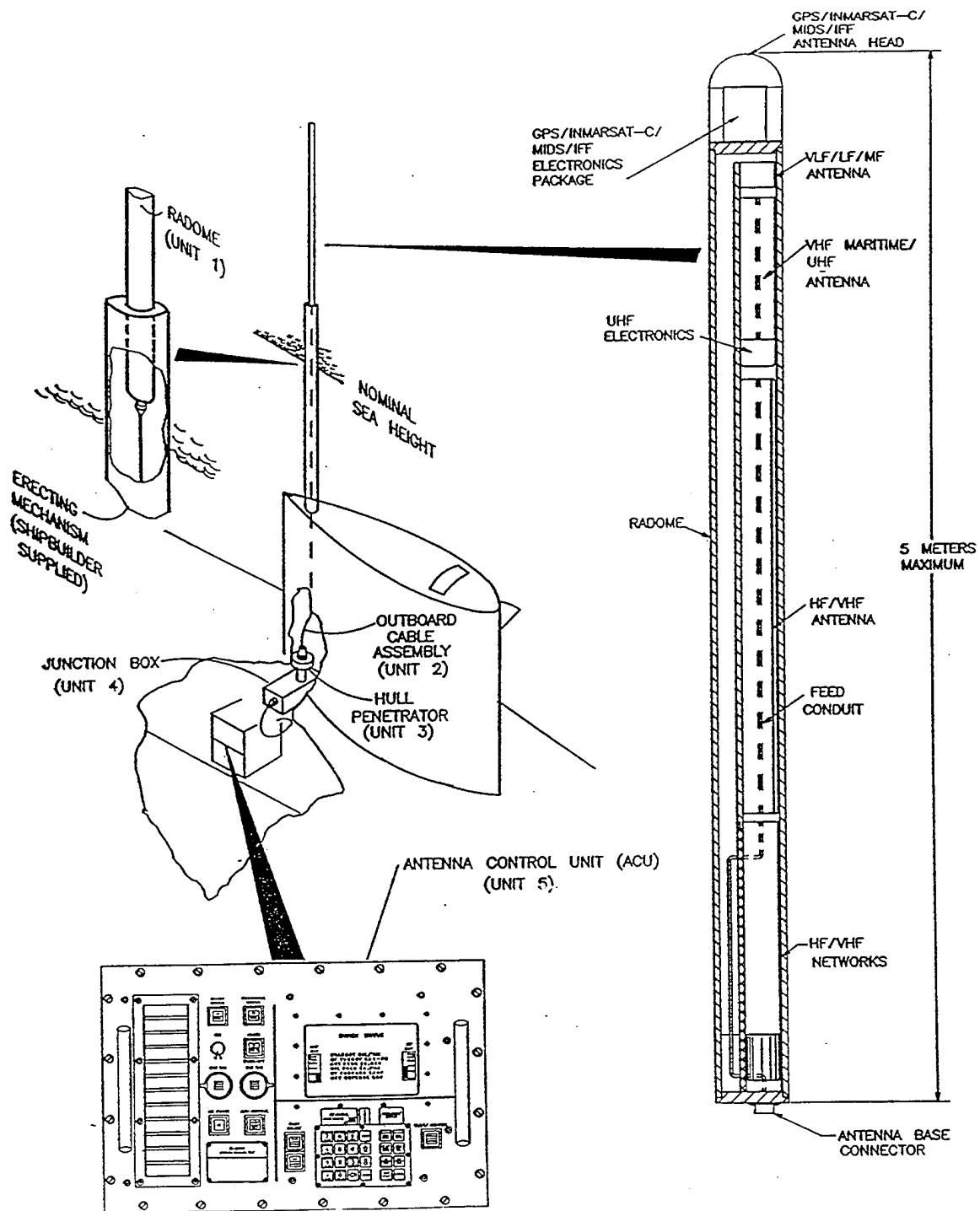CONDUIT

HF/VHF
NETWORKS

ANTENNA BASE
CONNECTOR

FIGURE 1
MULTIRANGE ANTENNA SYSTEM UNITS

315

a standard, computerized interface compatible with PCs and work stations. Unit 5 also provides input and output ports for external receivers and transceivers. In addition, it provides all required system operating power.

The Multi-Range Antenna system described in this paper supports navigation and communication in frequencies ranging from VLF to L-band. This includes continuous coverage of VLF reception from 10 KHz to 30kHz, including Omega Navigation; continuous coverage of LF frequencies from 30kHz to 300kHz, including Loran Navigation coverage; continuous coverage of MF frequencies in the range 250 KHz to 500 KHz; HF transmission and reception in both narrowband (tuned) and broadband modes covering the 2MHz to 30MHz band; transmission and reception coverage of the VHF SINCGARS band from 30MHz to 88 MHz; transmission and reception in the Maritime Radio band from 156MHz to 163MHz; 225MHz to 400MHz UHF coverage, including Satellite (SATCOM) and Line-of-Sight (LOS) Modes; JTIDS transceive coverage over the 960 MHz to 1215 MHz band; IFF transpond with coverage within 980 MHz to 1120 MHz; GPS Navigation Receive coverage; and INMARSAT-C transmission and reception.

An overall block diagram of the system is shown in Figure 2. This figure depicts both unit interconnections and details of functions within each unit. As shown in this figure, the Antenna/Radome Assembly contains four higher frequency antenna elements (HF/VHF, VHF Maritime/UHF, GPS/INMARSAT-C, and IFF/JTIDS) utilized for both receive and transmit. Each of these antenna elements is used for more than one band of frequencies. Use of such broadband, dual use antenna elements allows for reduction in the required size of the antenna system.
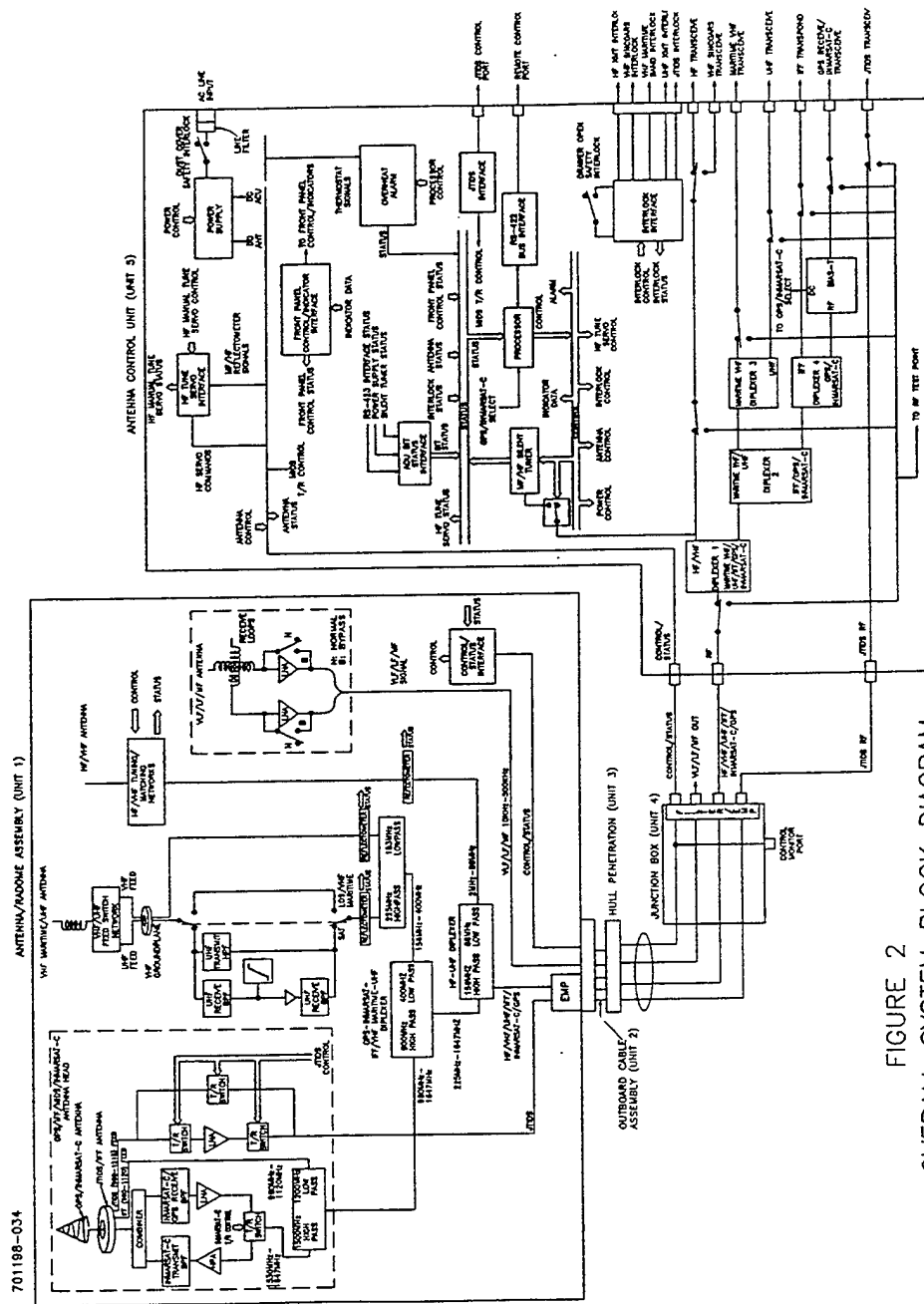
FIGURE 2
OVERALL SYSTEM BLOCK DIAGRAM

Signals are routed to and from the antenna elements via appropriate matching networks, bandpass filters, switching networks, and amplifiers. The JTIDS band is delivered on a dedicated coaxial cable line to the base of the antenna assembly. Since the JTIDS band overlaps the IFF band, it cannot be band-separated using diplex filter assemblies. All other higher frequency RF signals are multiplexed onto a single, coaxial RF line by three diplexers, and are subsequently routed to the connector at the base of the antenna via an EMP protection network.

VLF, LF, and MF reception is accommodated via a crossed loop antenna assembly with integral preamplifiers. The 10 KHz to 500 KHz band is covered by these elements. These signals are routed on dedicated, twisted-shielded pairs through the antenna base connector.

Operating power, control and status information to and from the Antenna/Radome Assembly is routed to and within the radome via separate, dedicated conductors. All of the above signals are routed through a connector at the base of the Antenna/Radome Assembly to the Outboard Cable Assembly (Unit 2) and then to the hull penetrator (Unit 3). A Junction Box (Unit 4) is intended for mounting directly at the hull penetrator, although it can be mounted within a few feet of this penetration point. A Junction Box is included to provide the following functions:

1. The Junction Box provides an EMP hardening point for the input and output signal lines to and from the Antenna/Radome Assembly.

2. The Junction Box provides filtering of power and control signals to and from the Antenna/Radome Assembly. This ensures that electrical activity inboard is isolated from electrical activity outboard. This has been found to be an

important consideration from an electromagnetic interference/electromagnetic compatibility viewpoint.

3. The Junction Box provides a separate output connector/breakout point for the VLF through MF signals. This has been done to allow separate signal distribution of these low level, highly sensitive signals.

4. The Junction Box provides a control monitoring port which allows measurement of control and status signals to and from the Antenna/Radome Assembly as an aid in system troubleshooting.

RF signals from the Antenna/Radome Assembly, as well as control and status information, are routed through the Junction Box to the Antenna Control Unit. The Antenna Control Unit separates the single, multi-band RF signal into five separate signals: HF/VHF, Maritime VHF, UHF, IFF, and GPS/INMARSAT-C. The dedicated coaxial line for JTIDS transceive is also routed through the Antenna Control Unit to a dedicated port on the rear panel of the ACU.

The Antenna Control Unit includes power generation circuitry for the Antenna/Radome Assembly and for all Antenna Control Unit circuits. It also includes features to allow compliance with electromagnetic compatibility specifications.

The Antenna Control Unit includes those circuits necessary to effect both local and remote control of the Antenna/Radome Assembly, as well as for presentation of system status on front panel system status displays, or at a remote location via a control/monitoring port. The ACU also provides safety interlock control for the high power transceivers (HF, VHF SINCGARS, VHF Maritime Band, UHF (both Line-of-Sight and Satellite modes), and JTIDS. Finally, the ACU incorporates built-in-test circuitry which allows monitoring of system status, via on-line, built-

in-test routines, and allows for performance of off-line built-in-test routines for system troubleshooting.

3. Antenna/Radome Description

The block diagram of the Antenna/Radome Assembly, Unit 1 of the system, is shown in the pictorial diagram of Figure 3. With reference to this figure, this assembly comprises a multi-band antenna array housed within a pressure-proof, fiberglass radome. Antenna elements housed within this radome include a VLF/LF/MF receive antenna located at the top of the antenna structure, a VHF Maritime/UHF (Line-of-Sight and SATCOM) Antenna Assembly with corresponding feed networks and interface electronics located below the VLF/LF/MF Antenna Assembly, an HF/VHF Antenna located below the UHF networks, and an HF/VHF network assembly located below the HF/VHF Antenna. At the very top of the antenna assembly is a combination GPS/INMARSAT-C/JTIDS/IFF antenna head which is housed in its own pressure-proof radome. A feed conduit is used to route radio frequency (RF), power and control signals from the interface connector located at the base of the radome, through the center of the HF/VHF Antenna, to the upper antenna elements.

A more detailed drawing of the physical stack-up is shown in the section views of Figures 4A and Figure 4B. With reference to these figures, the lower half of the Antenna/Radome Assembly is primarily occupied by elements of the HF/VHF antenna matching networks. Starting at the very bottom of this lower section, the Antenna/Radome baseplate provides a mounting surface for the base connector which is the electrical interface point for the Antenna/Radome Assembly. Just

320

701196-033

FIGURE 3
ANTENNA/RADOME
BLOCK DIAGRAM

FIGURE 4a

ANTENNA/RADOME ASSEMBLY— LOWER HALF
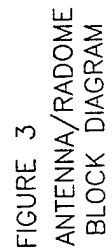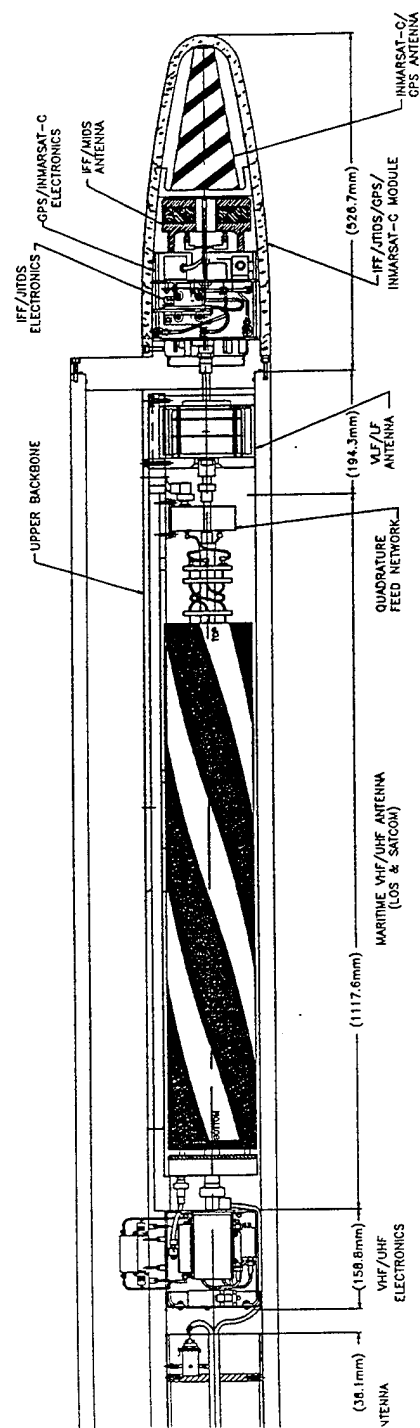
UPPER SECTION

FIGURE 4b
ANTENNA/RADOME ASSEMBLY- UPPER HALF

701194-033

323

above the antenna baseplate is an HF/VHF coaxial switch assembly. This module houses input switching coaxial relays which steer the HF/VHF transceive signal to the input of the desired matching network. This assembly also includes a terminal board for distribution of control and power signal wiring, a filter board which filters DC power lines to a coolant circulating pump discussed later in this section, and a HF/VHF reflectometer and its corresponding amplifier circuits. Next to the HF/VHF coaxial switch assembly is a coolant pump. This coolant pump forms a part of a copper heatsink/backbone and reservoir assembly utilized to cool resistive elements associated with the HF/VHF antenna system. These elements are required because the HF/VHF antenna is electrically short at the lower frequencies in this band. The use of an erectable long whip could be possible; however, a mechanism for the adjustment of the whip length would be needed (as a function of frequency), this would increase the RCS of the antenna, and somewhat reduce the reliability of the system.

Electrically short antennas are by their very nature very high Q elements. In order to achieve broadband operation, it is necessary to utilize matching networks. Practically it is very hard if not impossible to realize a matching network for such a high Q antenna structure. Therefore, Q-spoiling resistors were used to lower the antenna element Q such that a matching network can be realized. Unfortunately, at the very lowest of frequencies, a substantial amount of the input power to the system is dissipated in these Q-spoiling resistors. It is therefore necessary to cool these elements. To avoid the need for radome penetrations which can reduce system reliability (increased risk of water intrusion) and which also can increase thermal and radar signature, a heat storing, copper heatsink backbone and reservoir with an associated coolant pump is included in the system. The heatsink assembly comprises a copper heatsink backbone and reservoir which contains a

eutectic metal. The eutectic metal absorbs heat generated by the Q-spoiling resistors. This heat is uniformly spread throughout the entire reservoir by a fluid circulated by the coolant pump. Therefore, resistor cooling is accomplished by utilizing the latent heat of fusion of the phase change material (eutectic metal) and by spreading this heat throughout the volume of this material via the coolant lines.

Again with reference to Figure 4a, six matching network assemblies are located along the heatsink assembly just above the coaxial switch assembly. These networks provide both narrowband and broadband modes of operation for the HF/VHF antenna system. These modes include a broadband, 9-30 MHz mode, two broadband 2-10 MHz modes, two broadband 2-30 MHz modes, a tuned 2 MHz through 30 MHz mode, and a 30-88 MHz SINCGARS mode.

The antenna system has been designed to supply two different operating modes; a Multifunction mode and an HF Only mode. In the Multifunction mode, the upper antenna elements which provide both VLF through MF communications and UHF and higher band communications are available for use. However, if it is desired to optimize operation in HF tranceive mode, a mode switch assembly may be energized which breaks all feedlines to these upper antenna elements The top of the HF cylinder is also connected to the conduit assembly, extending the effective length of the radiating structure. This minimizes loading of the HF antenna system and improves the overall system gain in the HF band.

In Figure 4A, the HF/VHF SINCGARS Band Antenna is shown just above the mode switch. This antenna element comprises a 140 mm diameter metallic cylinder with a conduit assembly through its center. It also includes a relay which places an open or a short at the top of the antenna assembly between this conduit and the HF cylinder. This is utilized to optimize gain in some bands such as the 9-30 MHz band. In actuality, the radiating structure of this antenna at HF/VHF

frequencies includes not only the 1524 mm cylinder, but also the backbone structure located below it along which are mounted various matching network elements as described in the preceding paragraphs. In HF Only mode, it also includes the ground structure of the upper antenna elements. The antenna functions as a raised feed monopole or somewhat as a folded monopole depending upon operating mode utilized and band selected.

Figure 4B also depicts those elements utilized to achieve communications in VHF and higher frequencies. The upper antenna section includes those elements necessary for VHF Maritime transceive, UHF Line-of-Sight and SATCOM transceive, IFF transpond, JTIDS transceive, INMARSAT-C transceive, GPS Navigation receive, and VLF through MF receive coverage.

The first module located above the HF/VHF antenna is a VHF/UHF electronics module. This module contains the interface electronics necessary to effect VHF Maritime transceive, full duplex UHF SATCOM transceive, allow switching between Line-of-Sight and SATCOM modes, reflectometer circuitry for measuring the status of these antenna elements, and two diplex filters which separate VHF Maritime through UHF frequencies from higher frequencies, that is, separates the 156 MHz to 163 MHz and 225 MHz to 400 MHz bands from the band above 900 MHz. The VHF Maritime/UHF antenna element is located just above the VHF/UHF electronics module. This assembly provides both Line-of-Sight (LOS) and Satellite UHF transceive capability. Via a separate feed and small local groundplane, it also provides for Maritime VHF transceive coverage. A conduit assembly is routed through the center of this antenna element to provide an isolated feed structure for elements which are located above it.

The VLF/LF/MF antenna module is located just above the Maritime VHF/UHF Antenna Assembly. This is an active, ferrite loaded, crossed-loop antenna

assembly which provides crossed figure-eight reception of frequencies between 10 kHz and 500 KHz. It includes not only the antenna elements, but also those filters, phase compensation networks, and amplifiers necessary to allow coverage of the VLF, LF, and MF. This assembly also includes bypass relays which bypass all active circuits in the event of either preamplifier or system power failure. This allows achievement of a fallback mode wherein it is still possible to receive frequencies in this band. The above described elements are shown in the sectional view of Figure 4B and in the block diagram of Figure 3.

Coverage of IFF transpond, JTIDS transceive, INMARSAT-C transceive, and GPS receive is obtained through a mast head assembly as shown in Figure 4B. This separate module includes all electronics, switching elements, and antenna elements necessary to achieve operation in these bands. These elements are housed in a separate, pressure-proof radome at the top of the antenna assembly.

3. The VLF/LF/MF Antenna System

The VLF/LF/MF antenna system provides coverage of the 10 KHz to 500kHz band including Omega and Loran Navigation through the use of an active (preamplified), ferrite loaded, crossed loop antenna assembly. This receive antenna is located at the top of the antenna structure. Receive signals are captured by the outboard, active, crossed-loop antenna assembly located within the outboard Antenna/Radome Assembly. Two separate receive channels, one for fore-aft and one for athwart, are accommodated via two, ferrite loaded loop windings. These are coupled to independent low noise amplifiers which include bypass provisions which allow amplifier bypassing in the event of outboard preamplifier failure or system power loss. Signals amplified by the low noise

amplifiers (or signals directly from the loops in the bypass mode) are carried via dedicated twisted shielded pairs through the Antenna/Radome Assembly, to the base connector of this unit. They are conducted inboard through the Unit 2 and Unit 3 conductor paths to the Junction Box Assembly. Within the Junction Box, they are routed through transorb-type, EMP protection circuits which limit energy throughput to inboard units of the ship's signal distribution system.

The intended use of the antenna system is on the surface or at periscope submergence depths. It is also desirable to allow VLF/LF reception while the antenna is submerged. This being the case, a loop antenna is utilized. This is because such devices allow reception of these signals when the antenna is underwater. By contrast, an electric field antenna, such as a whip, is shorted out by the surrounding conductive medium of the seawater. A loop antenna allows reception of the magnetic field component of the signal at the surface even if the receive antenna is operated underwater.

The loop antenna system sensitivity is shown in Figure 5. The equivalent input noise level is approximately 0.3 nanovolts per square root of Hertz.
Over the Omega Navigation band, in fact, over the entire VLF band, the output amplitude response is flat within a few tenths of a dB: The phase response is typically such that the maximum deviation between a least mean square fit line and the phase response curve is less than $\pm 0.6^\circ$ from 10 KHz to 14 KHz.
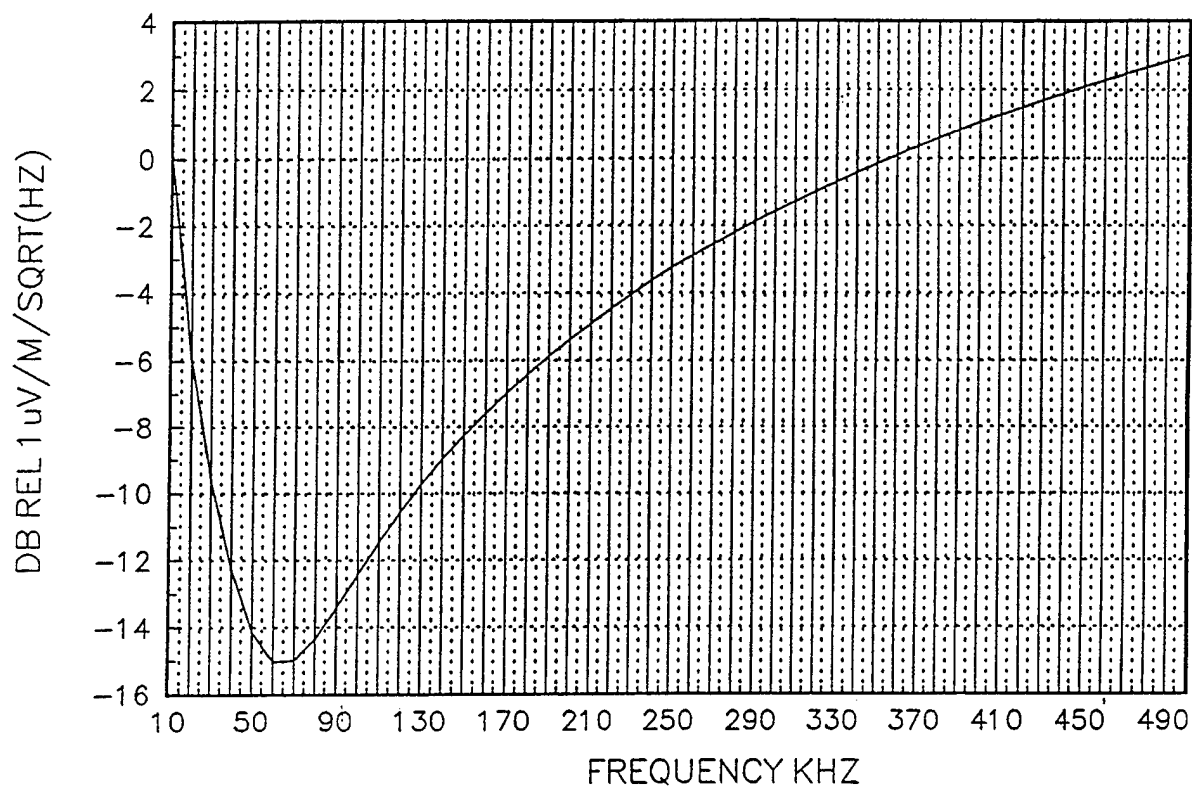
FIGURE 5
MAST MOUNTED LOOP ANTENNA SENSITIVITY VS. FREQUENCY
ACTIVE PREAMPLIFIER OUTBOARD

4. LF Antenna System

The LF band covers the 30kHz to 300kHz. The loop antenna system above covers this entire band with a very flat amplitude response and good phase linearity characteristics. For the Loran Navigation band, the response is typically flat to within $\pm$ 0.3 dB over the 70 KHz to 130 KHz range. The phase variation is within $\pm$ 2° (approximately 80 nanoseconds) over the 70 KHz to 130 KHz band. In addition, the maximum phase difference between the orthogonal loop channels is 20 nanoseconds maximum. Further, the maximum and standard deviations of the phase delay variation from the input to the output of the antenna system are less than 90 nanoseconds and 30 nanoseconds, respectively.

The same loop antenna is utilized for MF reception. The loop antenna system includes coverage of the 250kHz to 500kHz range. The frequency response is flat over the entire 10 KHz to 500kHz range within 3dB.

5. The HF system

5.1 Design Considerations

It was noted in preceding Section 3, which provides an overall description of the Antenna/Radome Assembly, that the HF antenna must, is electrically short at the lower part of the HF band.

Erectable whip antennas have been utilized in some applications as part of a mast antenna system. It was decided not to use such an erectable whip assembly for the following reasons:

1. An additional mechanism would be required as the length of the whip must be adjusted as a function of frequency.

2. It would result in a significant increase in the Radar Cross Section.

3. It would significantly affect the system reliability.

5.2 HF Antenna System Description

The basic antenna system consists of an aluminum cylinder 140 mm in diameter fed against a grounded backbone assembly. These two elements may be seen in Figure 4a, which shows a sectional view of the Antenna/Radome Assembly. The backbone assembly is shown in the lower section, and is the element along which the MF/HF/VHF antenna networks are arrayed. The cylinder is shown in the mid-section view, and is a round section with a conduit through its center. The length of the cylinder is 1,524 mm. This length was found to represent an optimum length based on the need to accommodate the other required bands in a compact antenna system while still maintaining the best possible HF performance.

A number of elements are required to achieve the required HF band transmit/receive functions. Figure 6 provides a graphical description of these elements. The following is a physical description of the HF assembly: The RF input from the antenna base connector is routed through a gas discharge suppressor which limits energy throughput to inboard sections of the Multifunction Mast System. The signal passing through this gas discharge suppressor is applied to an RF diplexer which splits the HF/VHF SINCGARS signal from the GPS/IFF/JTIDS/INMARSAT-C/UHF signal. The HF/VHF signal is applied to the power sensing elements of the reflectometer circuits which are located in an RF coaxial switch assembly. These sensing circuits allow detection of the forward and

reverse power components of the signal. These forward and reverse power signals are routed inboard for subsequent display on the front panel of the ACU and for use by the ACU processor for remote operations. The HF signal is routed through this power sensing element to a one of eight, RF switch matrix which is part of the HF coaxial switch assembly of the Antenna/Radome. This one of eight, RF switch steers the RF signal to the selected, HF or VHF antenna matching network, or directly to the antenna element for direct, unadapted HF reception. The outputs of the matching networks are arranged in series as shown in Figure 6. As can be seen in this figure, the output of the 9-30MHz network is routed through six sets of relay contacts at the outputs of the follow-on matching networks.

Figure 6 also depicts the mode switch assembly which allows the HF/VHF antenna to be switched between Multifunction and HF Only modes of operation. When set to the Multifunction mode, the conduit through the upper HF antenna cylinder is bonded to the copper backbone/phase change material heatsink assembly. In addition, power, control, and RF feed signals to the upper antenna elements, which are routed through the lower conduit, are connected through the mode switch assembly to the upper antenna elements. When the system is operated in the HF Only mode of operation, the winch motor/clutch arrangement shown in Figure 6 pulls apart the connectors which feed the upper antenna elements and opens the lower conduit to copper backbone bonding short. Further, the length of the HF antenna is physically increased by connecting the top of the HF/VHF antenna cylinder to the upper conduit structure. With reference to Figures 4a and 4b, this antenna length extension is actually formed by the VHF/UHF electronic module; the VHF/UHF antenna, the ground structure of the VLF/LF antenna assembly, and the ground structure which extends above the VLF/LF antenna to the base of the GPS/INMARSAT-C antenna. The modes in
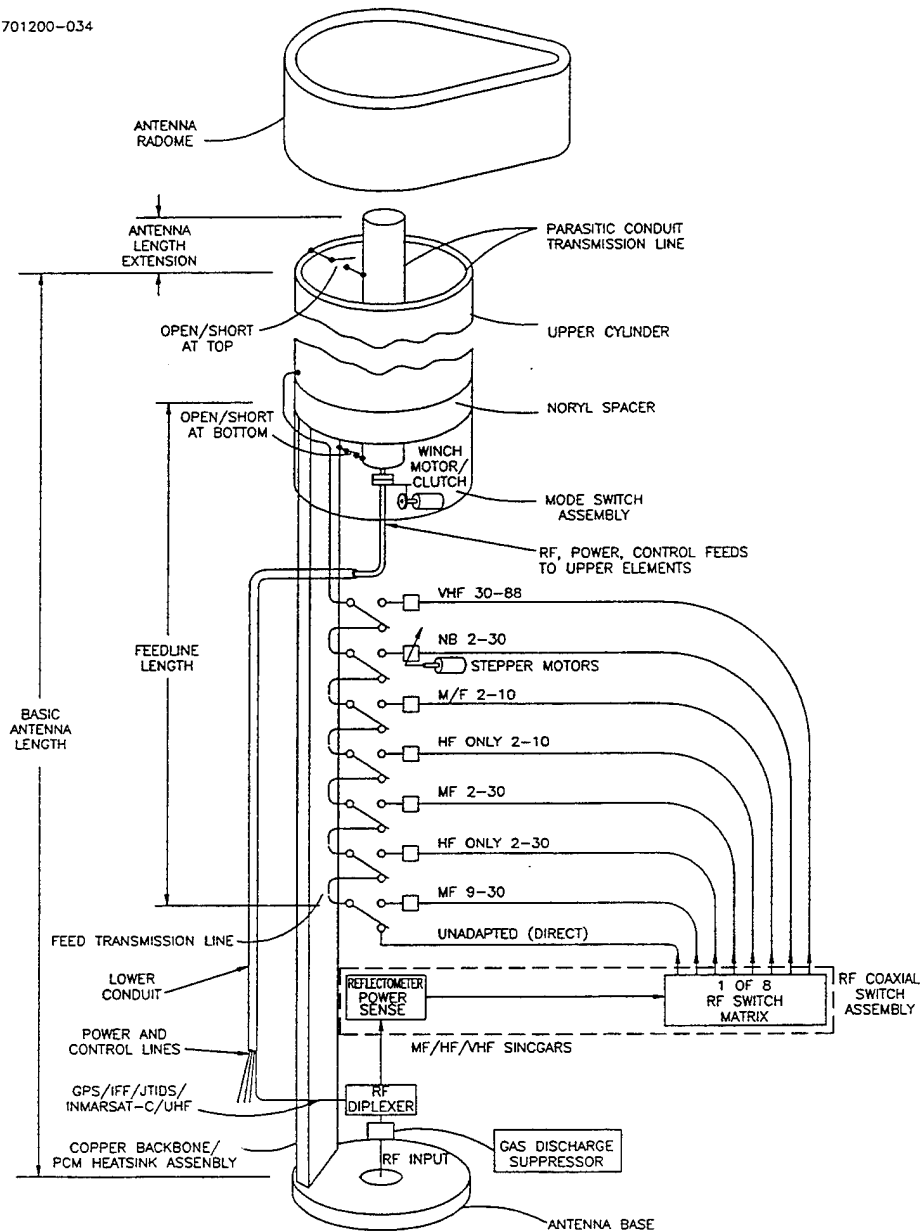
701200-034

ANTENNA
RADOME

ANTENNA
LENGTH
EXTENSION

PARASITIC CONDUIT
TRANSMISSION LINE

OPEN/SHORT
AT TOP

UPPER CYLINDER

NORYL SPACER

OPEN/SHORT
AT BOTTOM

WINCH
MOTOR/
CLUTCH

MODE SWITCH
ASSEMBLY

RF, POWER, CONTROL FEEDS
TO UPPER ELEMENTS

FEEDLINE
LENGTH

VHF 30-88

NB 2-30

STEPPER MOTORS

BASIC
ANTENNA
LENGTH

M/F 2-10

HF ONLY 2-10

MF 2-30

HF ONLY 2-30

MF 9-30

UNADAPTED (DIRECT)

FEED TRANSMISSION LINE

LOWER
CONDUIT

REFLECTOMETER
POWER
SENSE

1 OF 8
RF SWITCH
MATRIX

RF COAXIAL
SWITCH
ASSEMBLY

POWER AND
CONTROL LINES

MF/HF/VHF SINCGARS

GPS/IFF/JTIDS/
INMARSAT-C/UHF

RF
DIPLEXER

COPPER BACKBONE/
PCM HEATSINK ASSENBLY

RF INPUT

GAS DISCHARGE
SUPPRESSOR

ANTENNA BASE

FIGURE 6
MF/HF ANTENNA AND MATCHING NETWORK ELEMENTS

which the length of the HF antenna is physically increased by shorting the top of
the HF antenna cylinder may be reviewed with reference to Table I.

Frequency Band [MHz]	Mode	Top	Bottom	Nominal SWR	Allowable CW Transmit Time	SWR Figure No.	Gain Figure No.
2-10BB[1]	M/F[3]	Open	Short	<3:1	>10 min	7a	7b
2-10BB	HF Only	Short	Open	<3:1	>10 min	8a	8b
2-30 BB	M/F	Short	Short	<3.3:1	>10 min	9a	9b
2-30BB	HF Only	Short	Short	<3.3:1	>10 min	10a	10b
9-30BB	M/F	Short	Short	<3:1	>10 min	11a	11b
2-30NB[2]	M/F	Open	Short	<1.5<1	>10 min	12a	12b
2-30NB	HF only	Short	Open	<1.5:1	>10 min	13a	13b

TABLE I - MF/HF PERFORMANCE SUMMARY

[1] BB = Broadband

[2] NB = Narrowband

[3] M/F = Multifunction

6. VHF Antenna System Description

To provide coverage of the VHF SINCGARS Band from 30MHz-88 MHZ, the
raised feed monopole antenna system which is used for HF transmission and
reception is connected to a special, broadband matching network to provide an
impedance match of the radiating element to the 50 ohm impedance level of the

transceiver. The HF/VHF antenna element has been discussed previously in Section 5.2. Figure 4a depicts the 30-88 MHZ network utilized to achieve a match to the HF/VHF antenna located above. This same HF antenna system described in Section 5.2 is the one utilized to provide the 30-88 MHZ band coverage.

Coverage of the Maritime VHF band from 156MHz-163MHz is provided by a bandwidth extension of the UHF antenna used for Line-of-Sight and SATCOM coverage. The UHF antenna is a quadrafilar helix antenna which has four filars shorted on the end opposed to the excitation end. By feeding the other end of this UHF antenna against a small grounded disc, a quasi-vertical polarized monopole is obtained. The SWR for the Maritime VHF bandwidth required is better than 2:1. The predicted patterns of the VHF antenna are shown in Figure 14. These predictions were made using a Method of Moments Code which has been shown to be quite reliable for predictions of this type on past programs. Examination of the predicted pattern shows pattern lobbing. However, since this antenna system is to be utilized for omni-directional, vertical polarization, Line-of-Sight type communications, these lobes should not be problematic. In point of fact, any dipole-type antenna will exhibit such pattern lobbing when operated over an imperfect groundplane, such as the seawater groundplane beneath the exposed Antenna/Radome Assembly. The imperfect groundplane also results in some pattern elevation, which is an expected characteristic of any vertically polarized, monopole or dipole-type element operated over such a groundplane.
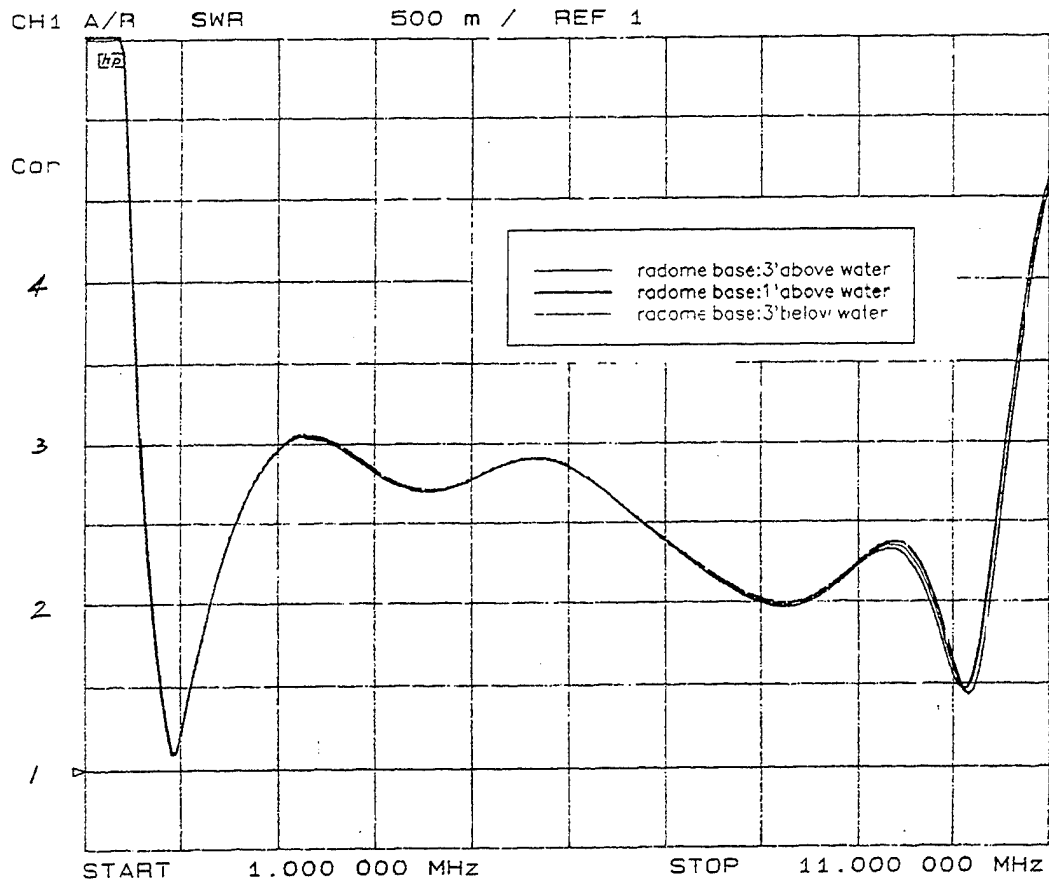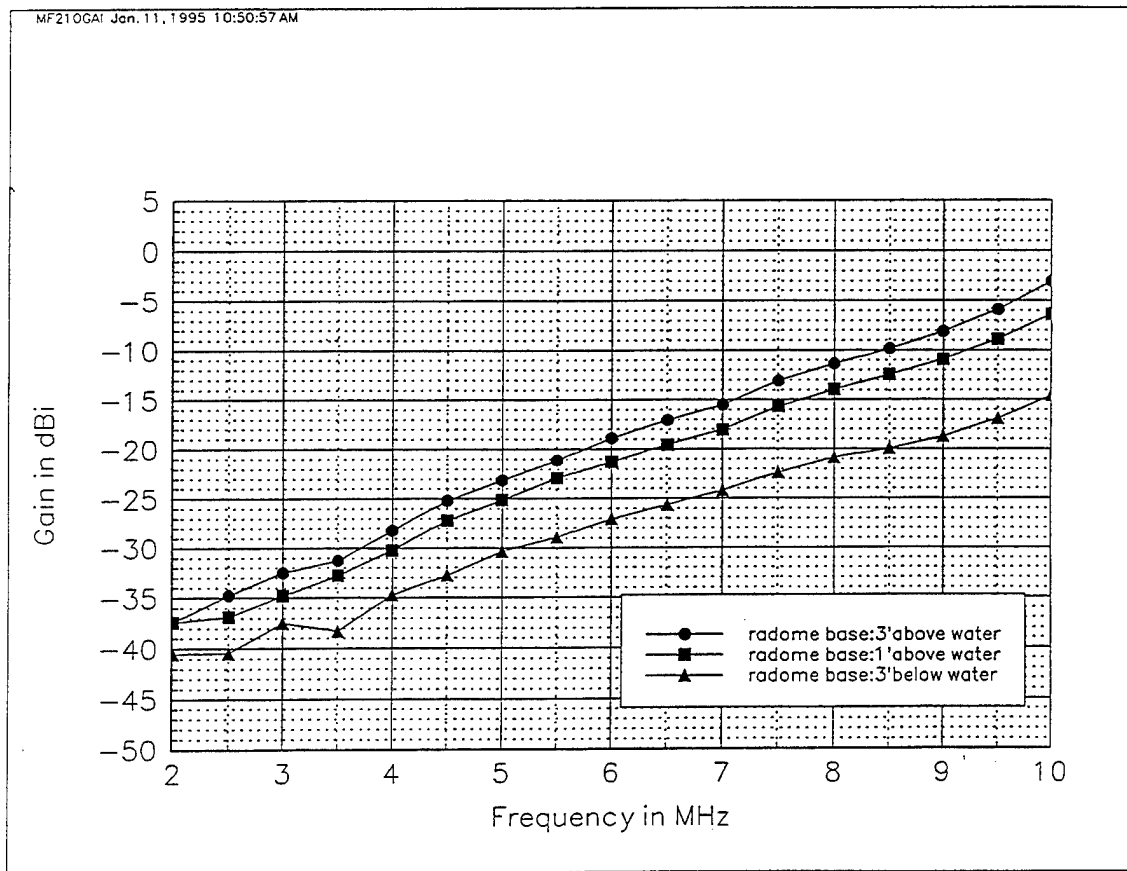
FIGURE 7A
MULTIFUNCTION 2-10MHz - MEASURED SWR

FIGURE 7B
MULTIFUNCTION BROADBAND 2-10MHz MODE
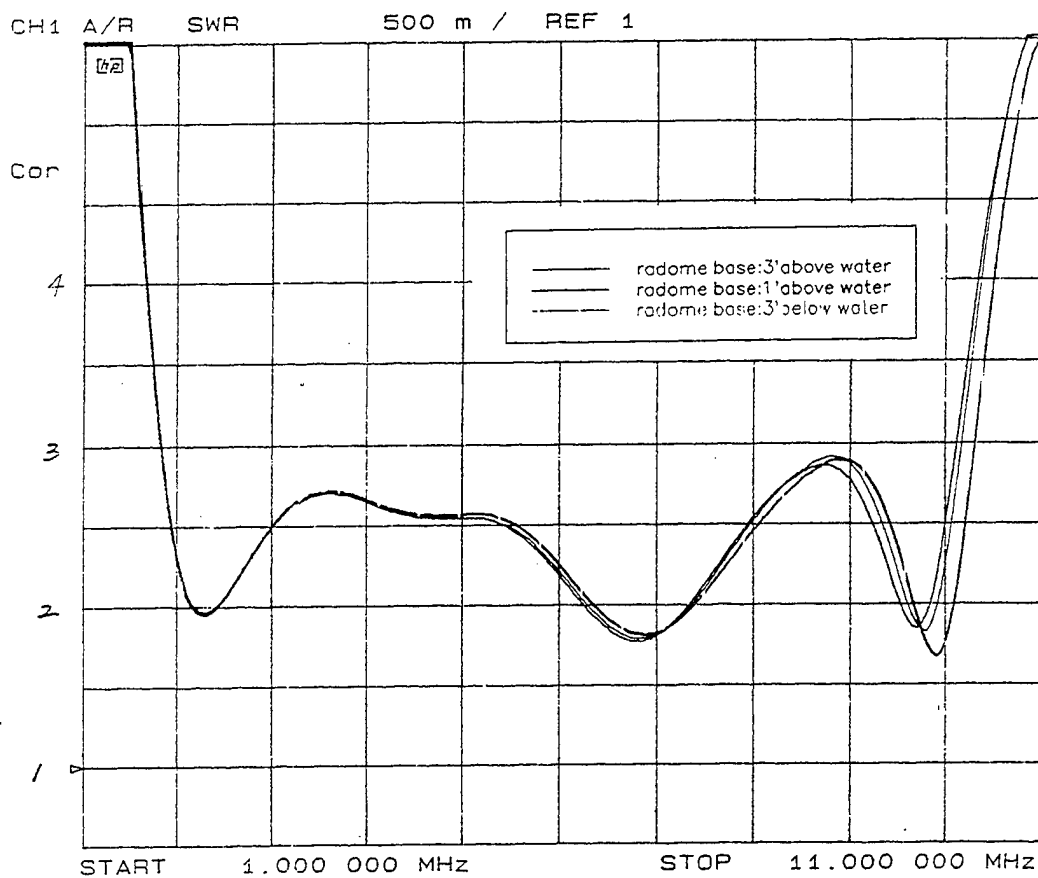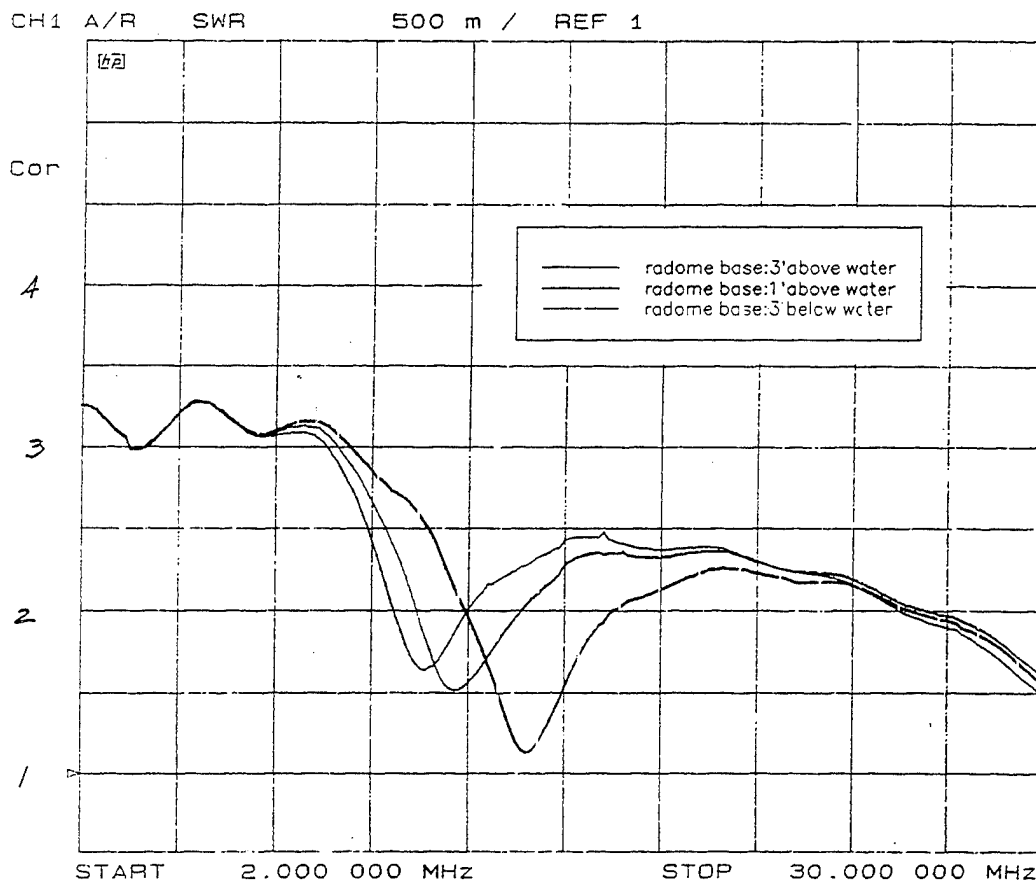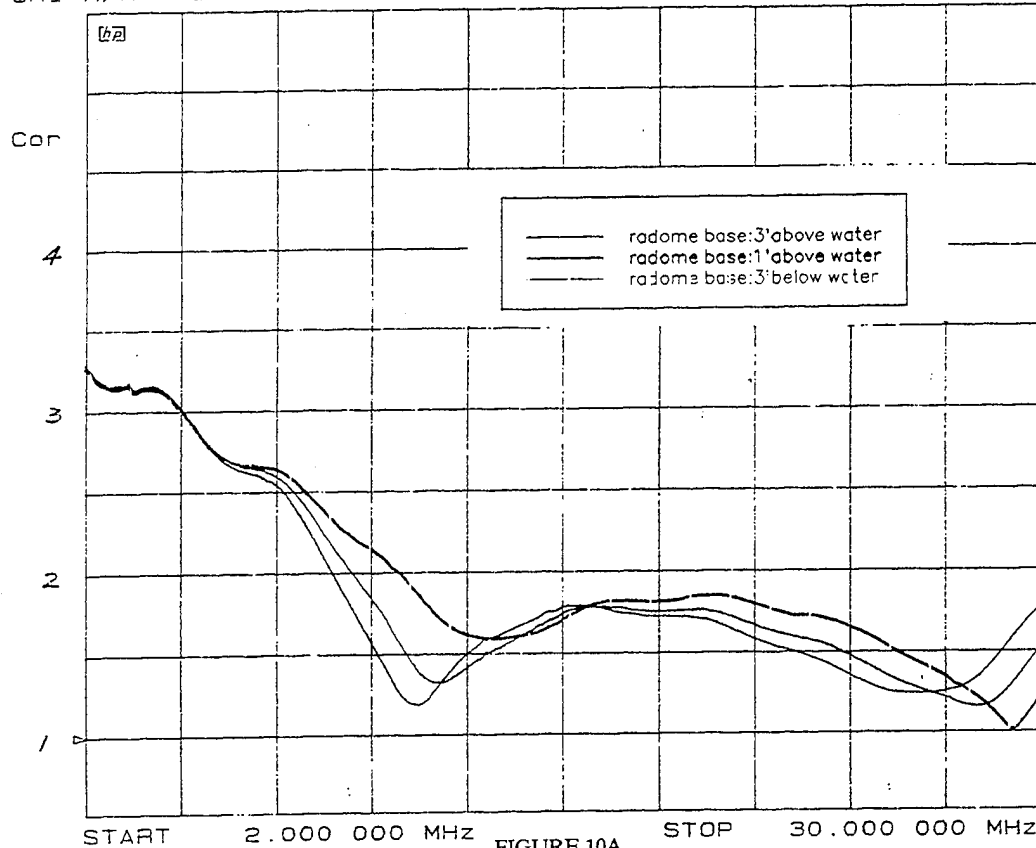MEASURED ANTENNA REALIZED GAIN

Cor

radome base:3'above water
radome base:1'above water
radome base:3'below water

START   1.000 000 MHz   STOP   11.000 000 MHz

FIGURE 8A
HF ONLY 2-10MHz - MEASURED SWR

HF21OGAI Jan. 11, 1995 10:53:57 AM

radome base:3'above water
radome base:1'above water
radome base:3'below water

Gain in dBi

Frequency in MHz
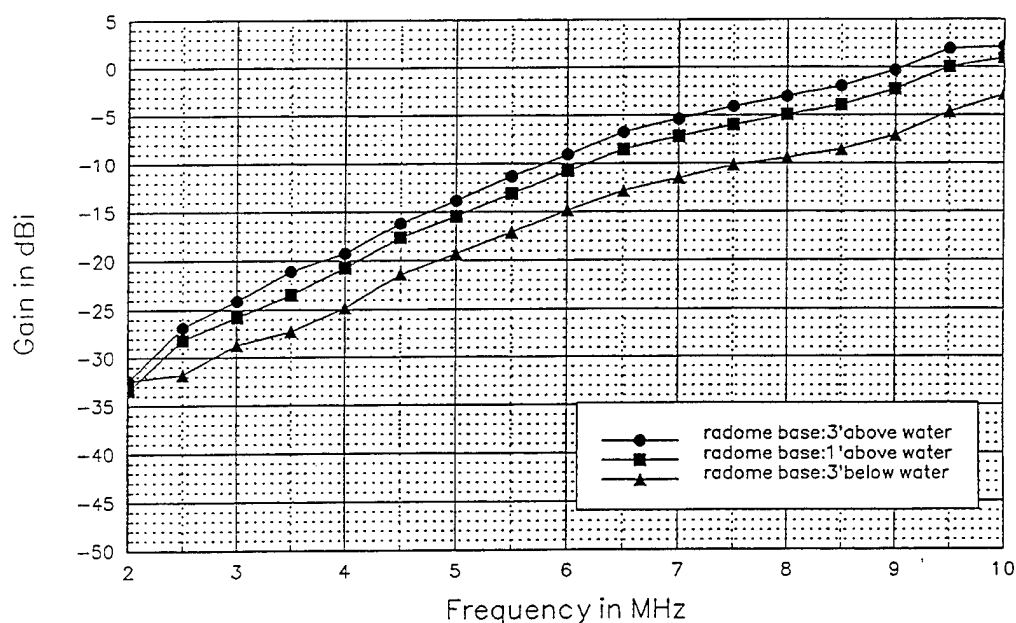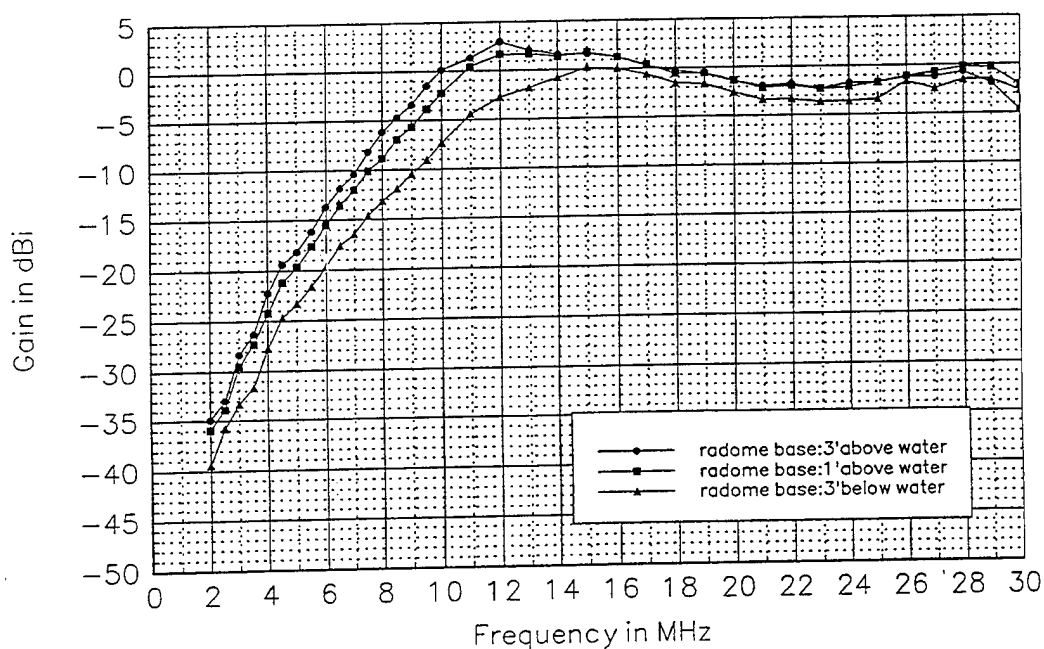
FIGURE 8B
HF ONLY BROADBAND 2-10MHz MODE
MEASURED ANTENNA REALIZED GAIN

FIGURE 9A
MULTIFUNCTION, 2-30MHz - MEASURED SWR
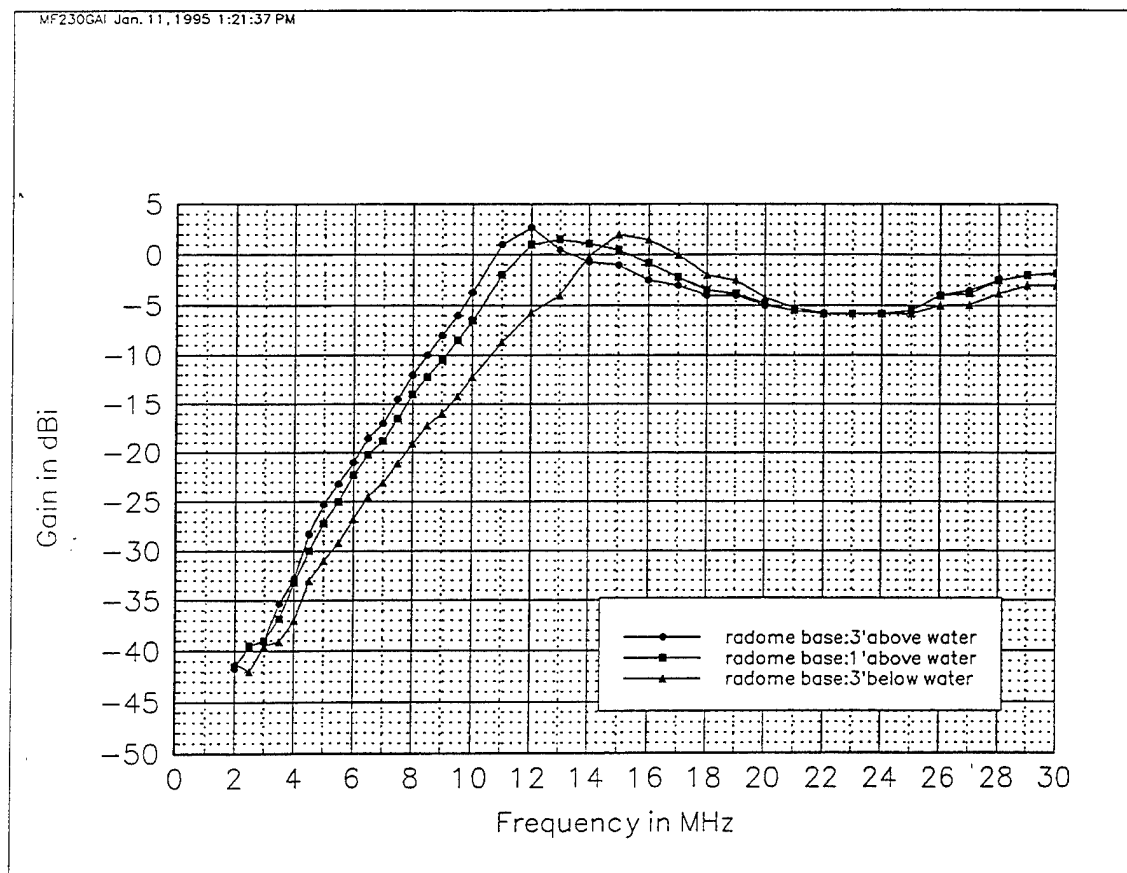
FIGURE 9B
MULTIFUNCTION BROADBAND 2-30MHz MODE
MEASURED ANTENNA REALIZED GAIN

Cor

4

3

2

1

radome base:3'above water
radome base:1'above water
radome base:3'below water

START   2.000 000 MHz   STOP   30.000 000 MHz

FIGURE 10A
HF ONLY 2-30MHz - MEASURED SWR

HF230GAI Jan. 11, 1995 10:57:23 AM

5

0

−5

−10

−15

−20

−25

−30

−35

−40

−45

−50

Gain in dBi

0   2   4   6   8   10 12 14 16 18 20 22 24 26 28 30

Frequency in MHz

radome base:3'above water
radome base:1'above water
radome base:3'below water

FIGURE 10B
HF ONLY BROADBAND 2-30MHz MODE
MEASURED ANTENNA REALIZED GAIN

339

CH1 A/R   SWR   500 m /   REF 1

Cor

4

3

2

1

START   2.000 000 MHz   STOP   30.000 000 MHz

radome base:3'above water
radome base:1'above water
radome base:3 below water
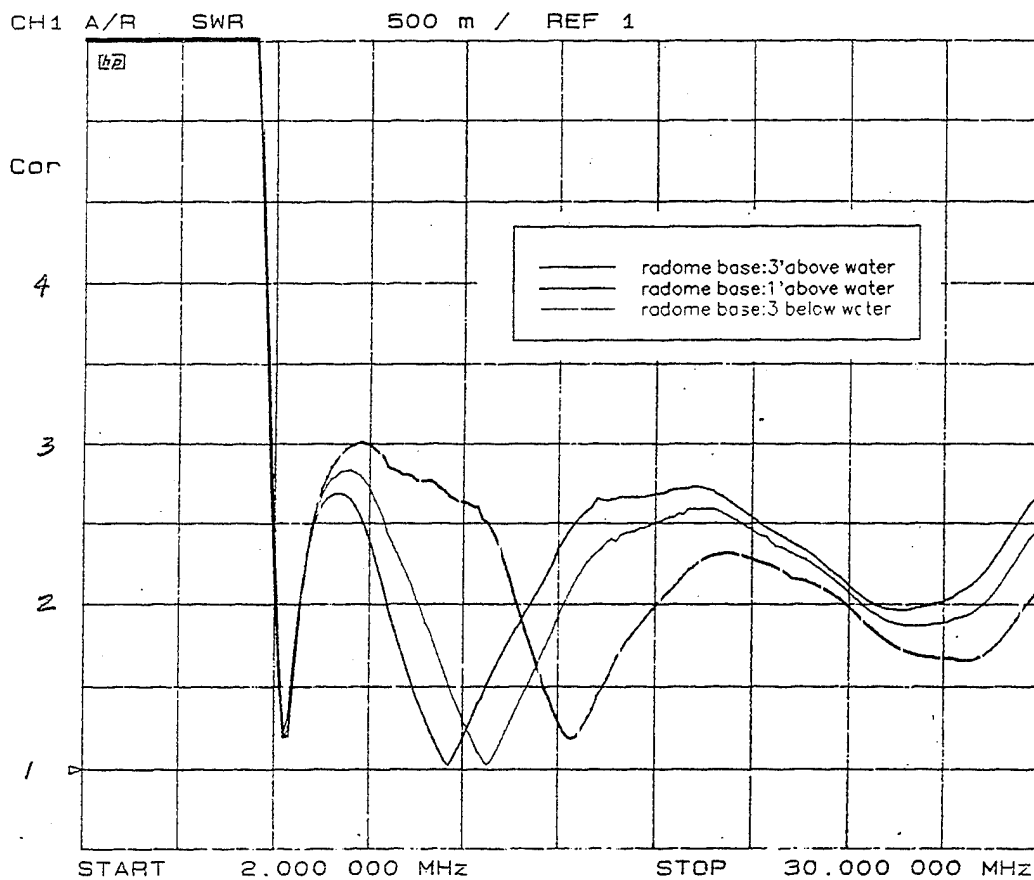
FIGURE 11A
MULTIFUNCTION 9-30MHz - MEASURED SWR

MF930GAI Jan.11,1995 10:59:51 AM

radome base:3'above water
radome base:1'above water
radome base:3'below water

Gain in dBi

Frequency in MHz
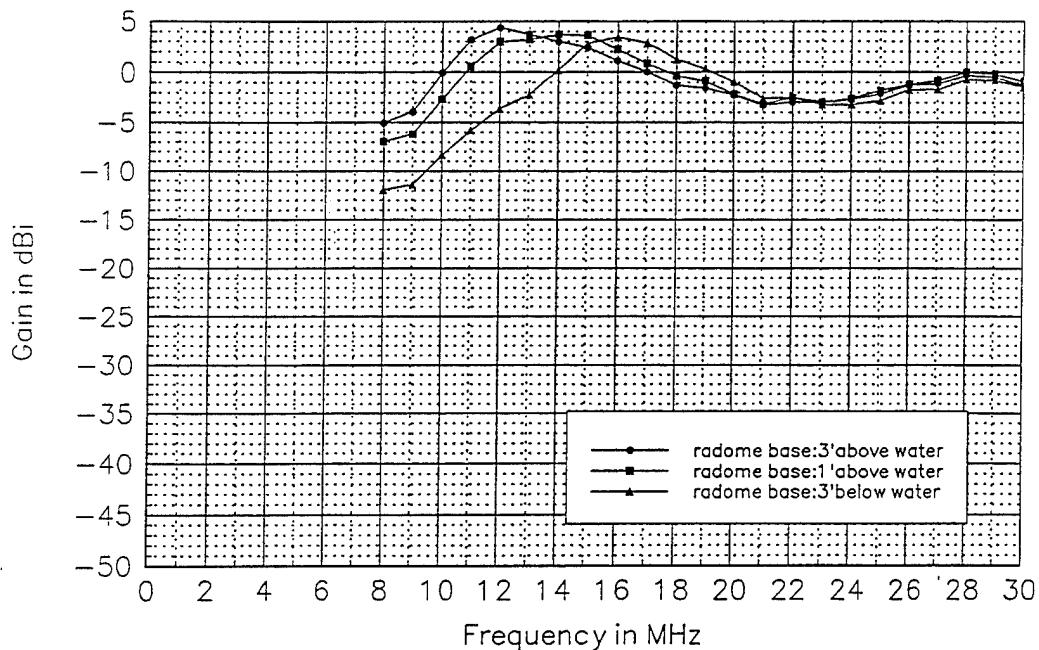
FIGURE 11B
MULTIFUNCTION BROADBAND 9-30MHz MODE
MEASURED ANTENNA REALIZED GAIN
340
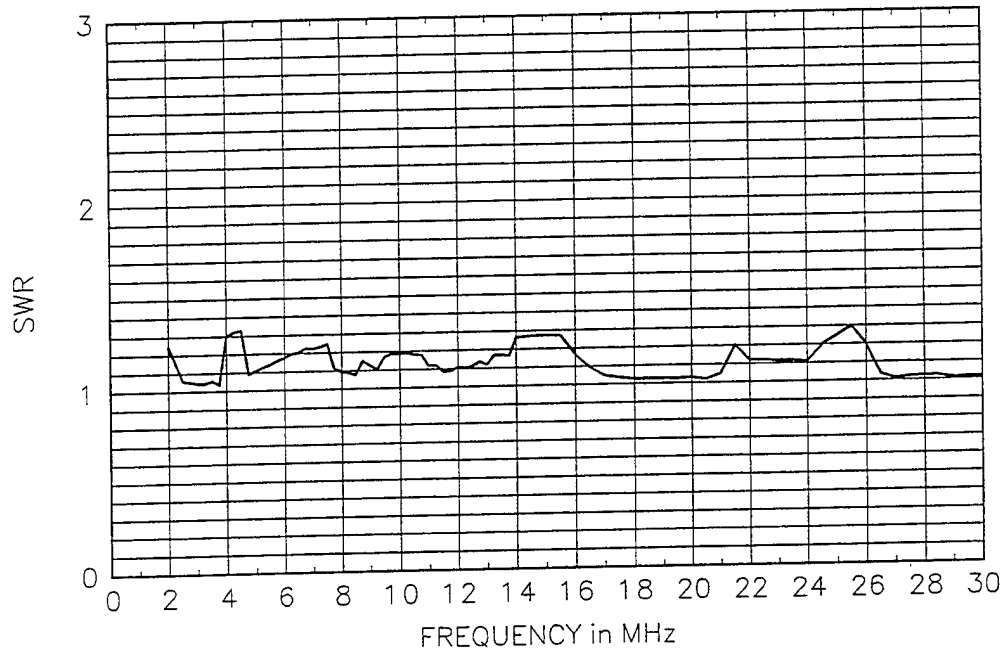
FIGURE 12A
MULTIFUNCTION NARROWBAND PREDICTED SWR
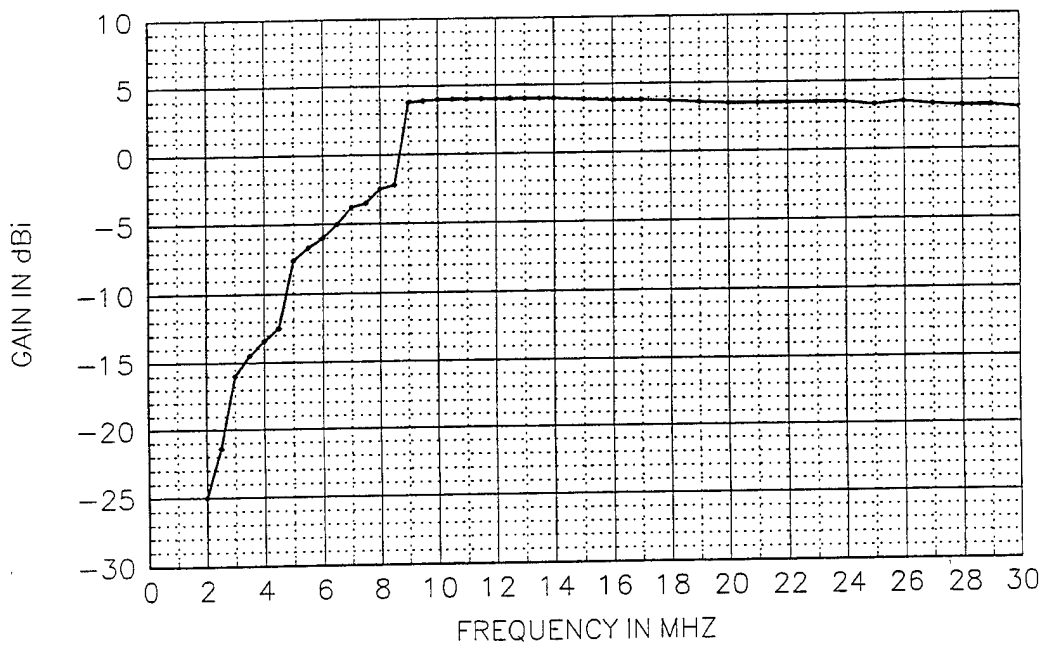
FIGURE 12B
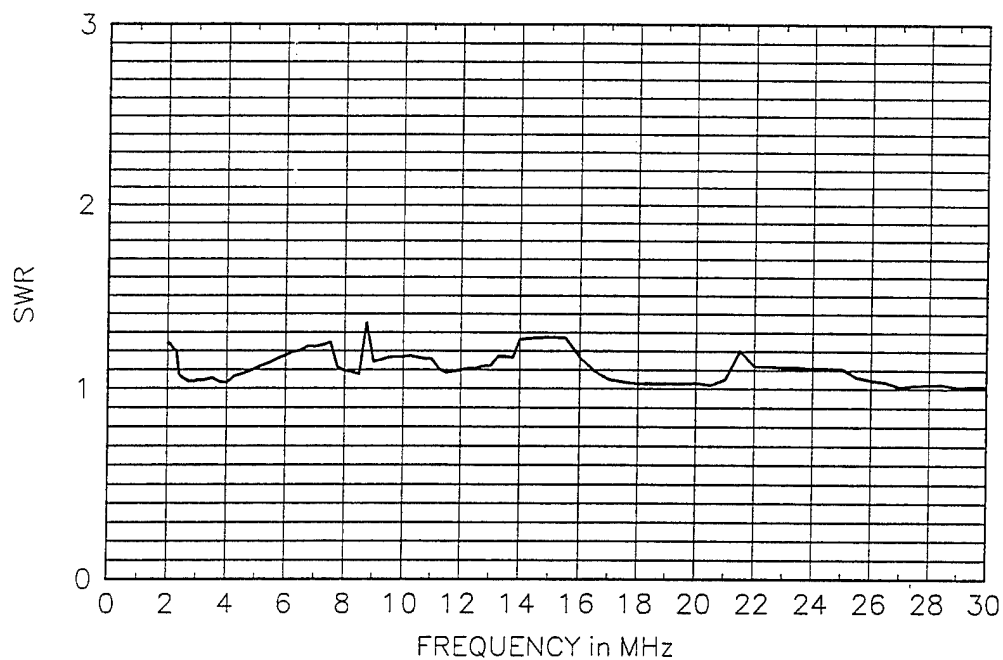MULTIFUNCTION NARROWBAND 2-30MHz MODE GAIN
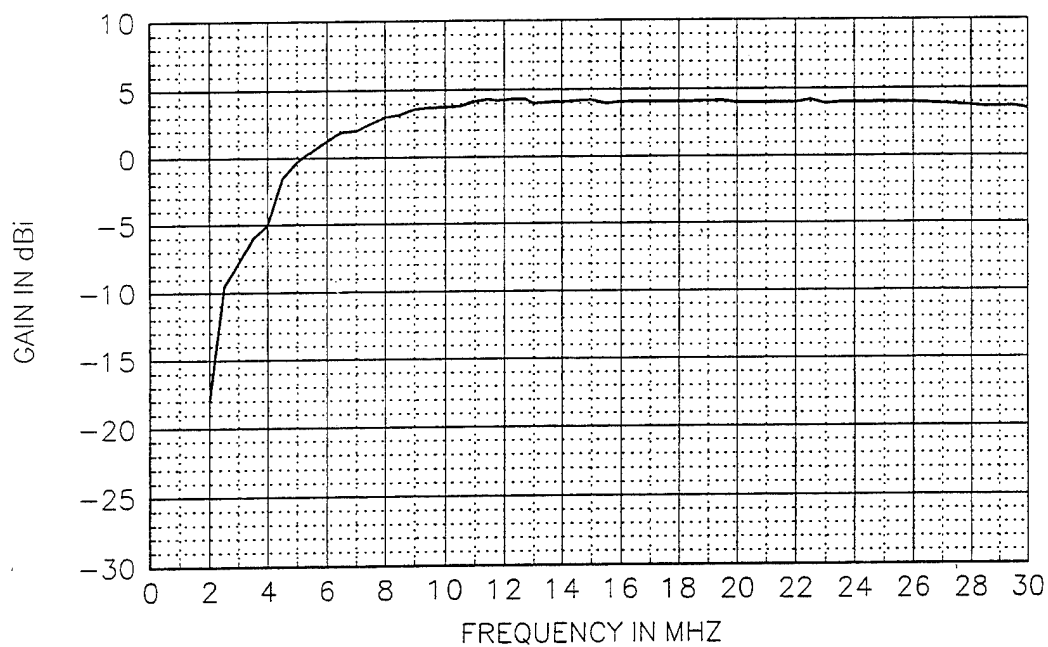
FIGURE 13A
HF ONLY NARROWBAND PREDICTED SWR

FIGURE 13B
HF ONLY NARROWBAND 2-30MHz MODE GAIN

7. UHF Antenna System Description

The Satellite and Line-of-Sight coverage are provided via a single antenna. This antenna and the appropriate feeding network are located above the HF/VHF antenna cylinder assembly, as shown in Figure 1. Figure 4b shows further details regarding the mounting and location of these two assemblies. A pictorial diagram of the proposed UHF antenna system is shown in Figure 15. In arriving at the final UHF antenna design, several different antenna configurations were considered. The final antenna configuration chosen for incorporation in the system comprises a 33 inch long antenna and quadrature network structure as shown in Figure 4b and 15. With reference to these figures, a quadrature feed network located at the base of the antenna assembly feeds four independent helices from the top via coaxial feeds which pass through the center of the helix assembly. The above structure yields a SWR, without hybrid elements, of less than 4:1 from 225MHz to 400MHz. However, the hybrid feeds correct the SWR of the overall assembly to less than 2:1.

In previous studies of similar UHF requirements, over 100 different quadrafilar helix geometries were analyzed using a Numerical Electromagnetic Code (NEC). The analysis included the effects of the salt water groundplane and location of the antenna above this groundplane. Several different configurations were studied and performance with respect to both Line-of-Sight and SATCOM performance cataloged. In addition, numerous models were fabricated to verify measured results. It is based on these studies that this antenna was chosen for this application. The measured SWR of the proposed antenna, in a prototype stage, is shown in Figure 16. A summary of UHF performance is presented in Table II.
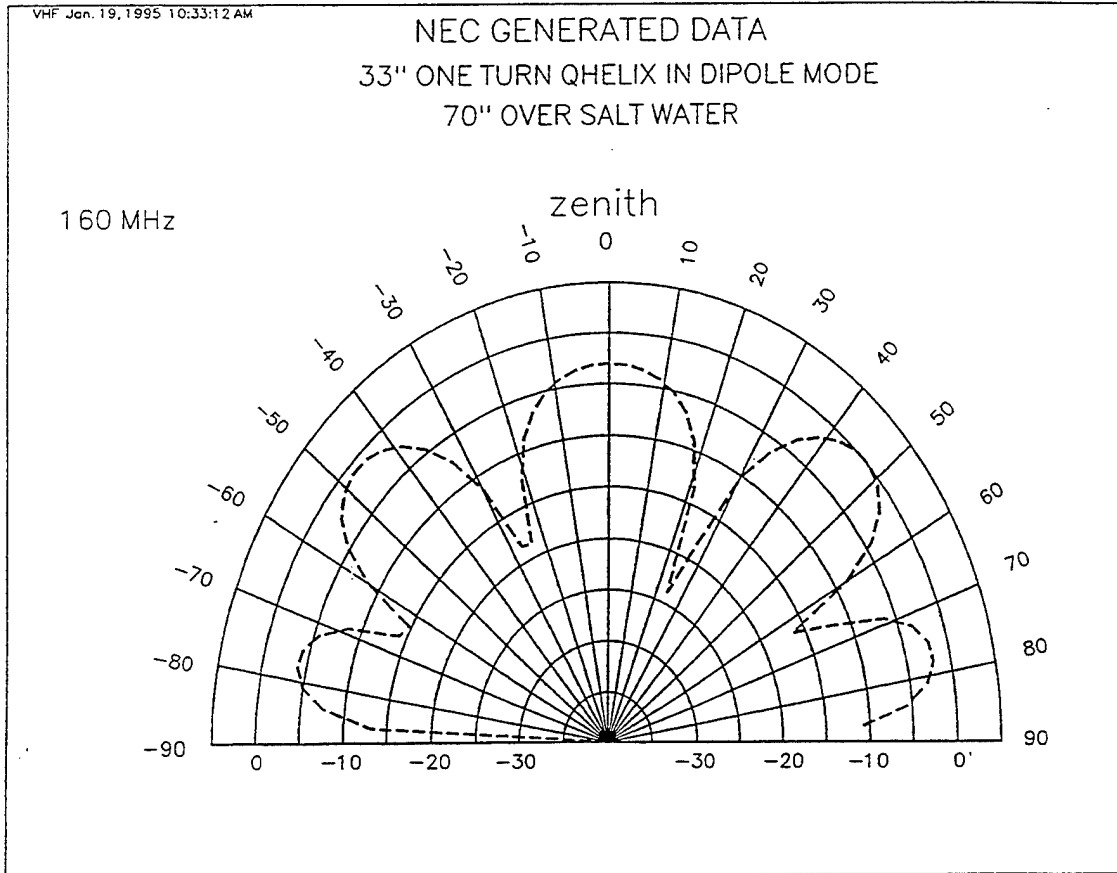
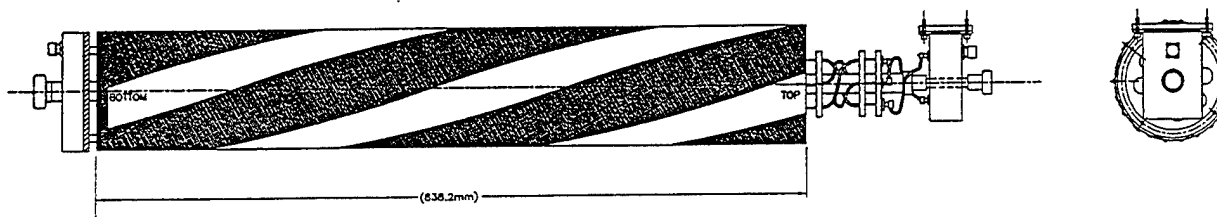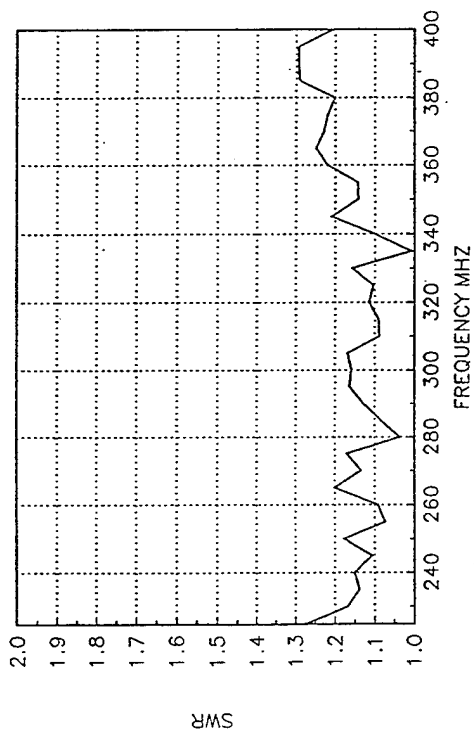NEC GENERATED DATA
33" ONE TURN QHELIX IN DIPOLE MODE
70" OVER SALT WATER

160 MHz

zenith

FIGURE 14

FIGURE 15
THE UHF ANTENNA

344

FIGURE 16
UHF LOS/SATCOM ANTENNA - MEASURED SWR

33" ONE TURN QHELIX FED FROM THE TOP
Measured Data over Salt Water (56")

300 MHz

FIGURE 18

33" ONE TURN QHELIX FED FROM THE TOP
Measured Data over Salt Water (56")

240 MHz
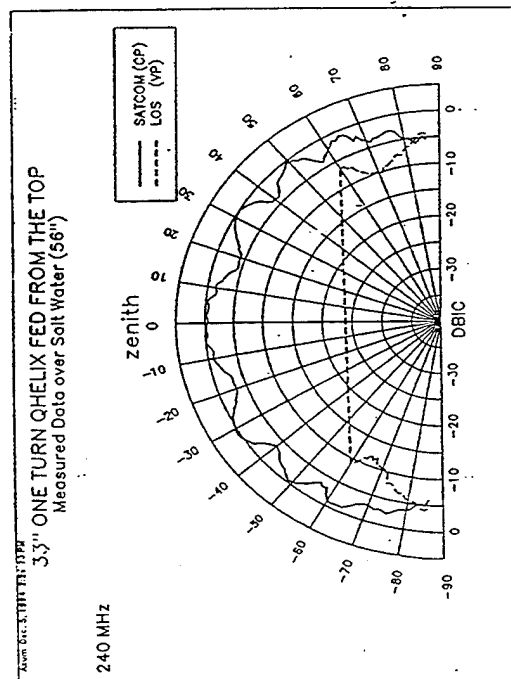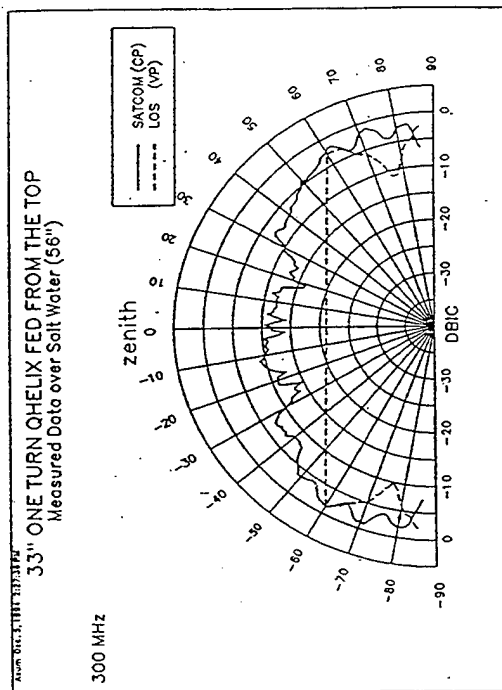
FIGURE 17

Parameter	Performance
Frequency Range	LOS 225 - 400 MHz SATCOM 240 - 400 MHz
Azimuth gain variation	± 2 dB
Front/Back Ratio	>10 dB
Power Handling	100 watts CW
VSWR	<2:1

Table II

Figures 17 and 18 show the antenna patterns (in LOS and SATCOM) at 240 MHz and 300 MHz frequencies when the antenna is located 56 inches over a salt water groundplane.

8. The IFF/JTIDS Antenna System

The Joint Tactical Information Distribution System (JTIDS) is a high capacity, spread spectrum/time division multiple-access (TDMA) information distribution system providing integrated communication, navigation, and identification capabilities. The JTIDS System operates over the 960 MHz-1215 MHz band in a frequency hopping mode. The JTIDS waveform takes a 24 hour day, divides it into 112.5 epochs, divides these epochs into 64 timeframes, which are further divided into 1536 time slots per timeframe. In any particular time slot, a JTIDS System can be in either a transmit or receive mode. Examination of the JTIDS waveform timing indicates that, at maximum range, assuming the full propagation guard time is required, that very rapid switching between transmit and receive modes is required. Further, the system can be transmitting or receiving anywhere in its 969 MHz to 1209 MHz operating band. This then requires the use of

broadband antenna elements which can be switched between transmit and receive modes in a few microseconds. By extension, an antenna system for JTIDS must include the same type of broadband operation and fast switching capabilities.

IFF systems share the same spectral space as the JTIDS System. However, to avoid IFF interference, an IFF slot interference specification is placed on the JTIDS/JTIDS System. This precludes hopping to a band approximately 14 MHz wide around 1030 MHz and 1090 MHz. This being the case, the same antenna system can be used for JTIDS and IFF operation. The IFF/JTIDS Antenna is an annular slot. As shown in Figure 19, it consists of a coaxial cavity fed by two probes. It provides omni-directional radiation through an annular slot in the vertical/outside wall of the cavity. The main advantage of this antenna design is its minimum size, provisions for cable access to the GPS/INMARSAT-C antenna located on top of it, and separate IFF/JTIDS feed as required due to the sharing of the same spectral space.

As discussed above, the pattern of an annular slot antenna is essentially that of a vertical dipole (see Figure 20) and the gain (measured in free space) is approximately that of a dipole.

9. The GPS Antenna System

A similar situation exists with respect to GPS and INMARSAT-C as exists with IFF and JTIDS, i.e. the GPS receive frequency lies within the INMARSAT-C band. GPS coverage requires the receiving of a signal approximately 20 MHz wide centered at 1575.42 MHz. INMARSAT-C uses receive frequencies from 1530 MHz to 1545 MHz and transmit frequencies from 1626.5 MHz to 1646.5 MHz. The close proximity of these services in terms of frequency spectrum
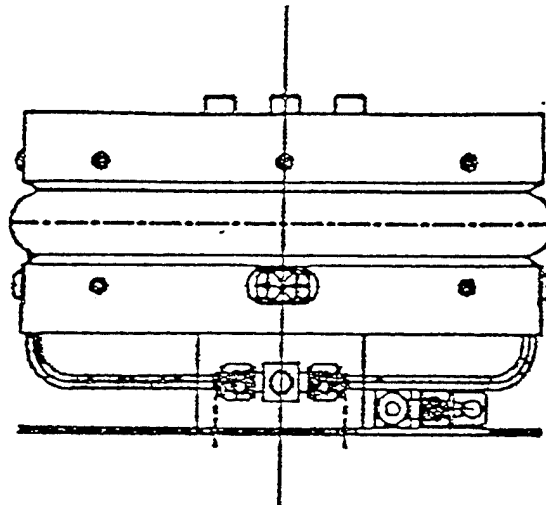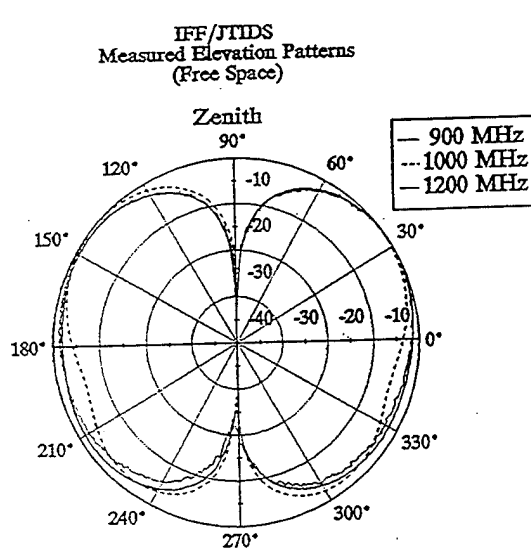
347

FIGURE 19

IFF/JTIDS
Measured Elevation Patterns
(Free Space)

FIGURE 20A

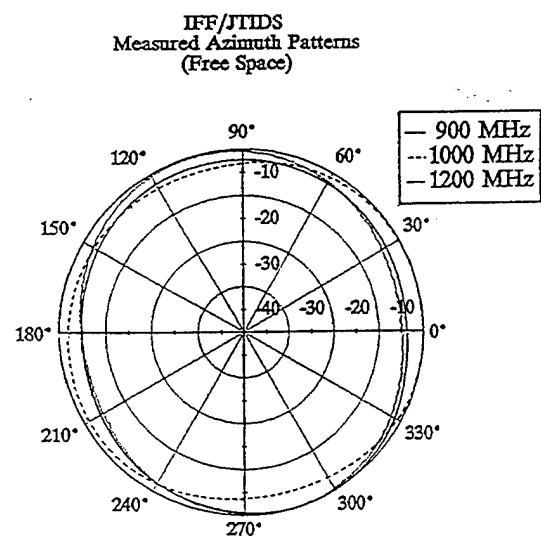IFF/JTIDS
Measured Azimuth Patterns
(Free Space)

FIGURE 20B

occupied is an advantage in terms of design of the antenna element, but a disadvantage in terms of the ability to provide band isolation through the use of filter elements. This implies that the GPS receive and INMARSAT-C receive frequencies must be accommodated by the same electronics. It also implies that simultaneous INMARSAT-C transmit and GPS receive will not be possible, since the same preamplifier used for GPS receive is used for INMARSAT-C receive, and the INMARSAT-C System is a half duplex system utilizing transmit/receive switching.

The four functions, IFF, JTIDS, GPS, and INMARSAT-C cover a 30 percent bandwidth which in principle could have been served by only one antenna. However, there is a definite distinction between the two groups: IFF/JTIDS and GPS/INMARSAT-C. The difference is in the desired pattern (dipole pattern for the first and hemispherical for the second) and the polarization (linear vertical for the first and right-hand circular for the second). For this reason, two independent antenna elements have been used. The IFF/JTIDS antenna has been discussed in the preceding section. The antenna for GPS/INMARSAT-C is a conical-log spiral, which unlike other antennas frequently used in GPS applications, is a relatively broadband antenna. It is approximately 150 mm long with a 10 degree half angle opening and a 76 mm diameter; note Figure 21. This conical-log spiral is essentially a bifilar helix antenna working in the back fire mode. Due to its tapered geometry, it exhibits wideband characteristics, which as mentioned above are important in an electromagnetically crowded environment such as the one here. The antenna is fed through a broadband balun by a coaxial cable. A broadband antenna is critical here since a narrowband antenna, like a patch antenna, could be detuned by the significant impact of the radome, and since it is desired to cover both GPS and INMARSAT-C with a single antenna device.

The antenna system provides omni-azimuthal reception in azimuth and coverage from Zenith down to Horizon. Because of the type of antenna employed, the antenna system is tolerant of ship's roll and heave motion, indicating that satellites located near the horizon will remain available even in the presence of ship's motion. The radiation patterns of this antenna are shown in Figure 22.

10. Conclusion

A Multifuntion Mast Antenna System operating from HF to L-band was described. An earlier version of this system is fully operational in the US Navy. The system described is the next generation version about to be installed on existing submarines.
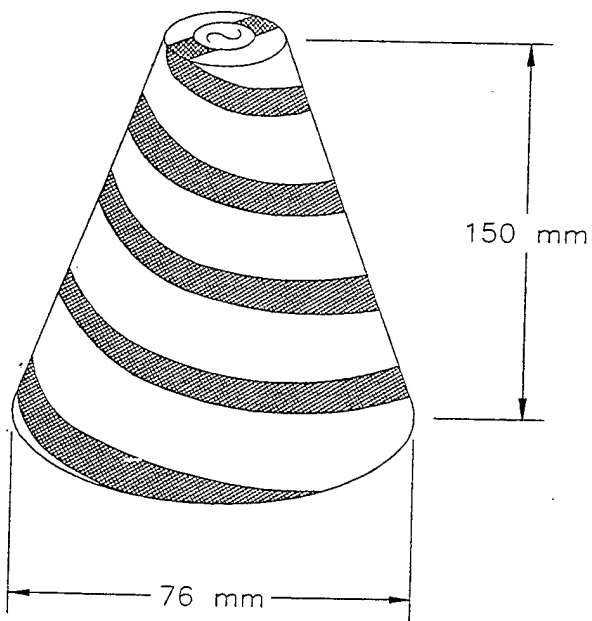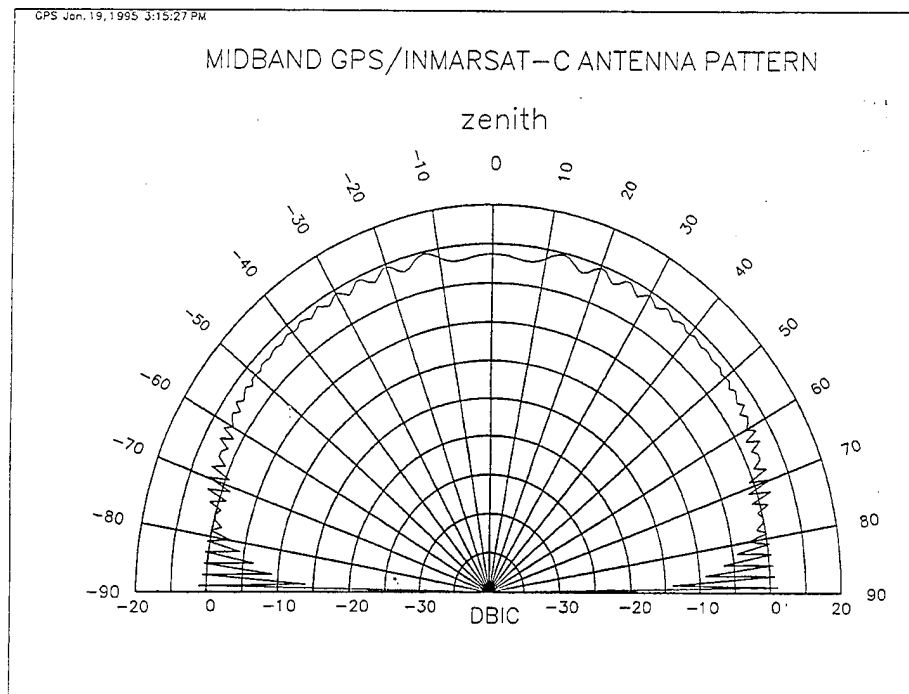
FIGURE 21

GPS Jan. 19, 1995 3:15:27 PM

MIDBAND GPS/INMARSAT–C ANTENNA PATTERN

zenith

DBIC

FIGURE 22

MISSION
OF
ROME LABORATORY

Mission. The mission of Rome Laboratory is to advance the science and technologies of command, control, communications and intelligence and to transition them into systems to meet customer needs. To achieve this, Rome Lab:

a. Conducts vigorous research, development and test programs in all applicable technologies;

b. Transitions technology to current and future systems to improve operational capability, readiness, and supportability;

c. Provides a full range of technical support to Air Force Material Command product centers and other Air Force organizations;

d. Promotes transfer of technology to the private sector;

e. Maintains leading edge technological expertise in the areas of surveillance, communications, command and control, intelligence, reliability science, electro-magnetic technology, photonics, signal processing, and computational science.

The thrust areas of technical competence include: Surveillance, Communications, Command and Control, Intelligence, Signal Processing, Computer Science and Technology, Electromagnetic Technology, Photonics and Reliability Sciences.